Laser Frequency Combs for Astronomy

Rafael Andreas Probst

SIGILL·UNIVERSITAT·LUDOVIC·MAXIM·

München 2015

Laser Frequency Combs for Astronomy

Rafael Andreas Probst

Dissertation
an der Fakultät für Physik
der Ludwig–Maximilians–Universität
München

vorgelegt von
Rafael Andreas Probst
aus München

München, den 8. Mai 2015

Erstgutachter: Prof. Dr. Theodor W. Hänsch
Zweitgutachter: Prof. Dr. Ralf Bender
Tag der mündlichen Prüfung: 10. Juli 2015

Zusammenfassung

Diese Arbeit befasst sich mit der Entwicklung und dem Test optischer Frequenzkämme zur Kalibration astronomischer Spektrographen. Die Genauigkeit der besten Spektrographen war bisher durch ihre Kalibration begrenzt. Die Benutzung von Frequenzkämmen als hochgenaue optische Frequenzreferenz verspricht die Überwindung dieser Limitierung, und damit die Bestimmung von Linienpositionen in astronomischen Spektren mit nie dagewesener Genauigkeit. Dies eröffnet faszinierende neue Möglichkeiten in der Astronomie, wie die Entdeckung erdähnlicher extrasolarer Planeten über Radialgeschwindigkeitsmessungen, die direkte Messung der Beschleunigung der kosmischen Expansion, oder eine genauere kosmologische Suche nach Veränderlichkeit von Naturkonstanten. Auf Basis der vorliegenden Arbeit wurde eine kommerzielle Version des astronomischen Frequenzkamms entwickelt, die derzeit für die Installation und den Routinebetrieb an mehreren Observatorien vorbereitet wird.

Um die Kammstruktur mit astronomischen Spektrographen ausreichend gut aufzulösen, werden Frequenzkämme mit extrem großen Modenabständen von typischerweise > 10 GHz benötigt. Zur Erzeugung von Frequenzkämmen mit derart hohen Modenabständen verfolgt diese Arbeit einen Ytterbium-Faserlaser-basierten Ansatz, der auf der Unterdrückung ungewollter Moden eines Frequenzkamms mit ursprünglich geringerem Modenabstand beruht. Zur breitbandigen Kalibration von Spektrographen muss das erzeugte Kammspektrum über einen großen Teil des sichtbaren Spektralbereichs hinweg verbreitert werden. Bei Pulswiederholraten von > 10 GHz erweist sich dies als sehr herausfordernd, und bringt bis dahin unbekannte Effekte hervor.

Die vorliegende Arbeit entwickelt Strategien zur spektralen Verbreiterung astronomischer Frequenzkämme, und untersucht hiermit verbundene Fragen wie Farbzentren-Bildung im Kern photonischer Kristallfasern. Des Weiteren wird theoretisch und experimentell nachgewiesen, dass spektrale Verbreiterung mit einer drastischen Verstärkung unterdrückter Kammmoden einhergeht, und es wird gezeigt, wie hierdurch bedingte Kalibrations-Ungenauigkeiten begrenzt werden können. Da die Einhüllende des verbreiterten Spektrums stark strukturiert ist, ist es von Nutzen diese abzuflachen. Hierbei werden die Signalpegel aller Kalibrationslinien auf dem Spektrographen angeglichen, was deren Signal-zu-Rausch-Verhältnis maximiert und dadurch die Kalibrationsgenauigkeit erhöht. Mehrere Konzepte zur adaptiven spektralen Abflachung werden entwickelt, wobei über einen Bereich von > 200 nm abgeflachte Spektren erzeugt werden.

Der astronomische Frequenzkamm wird an HARPS getestet, dem bis heute führenden Spektrographen zur Exoplanetensuche, der sich am La Silla Observatorium in Chile befindet. Über kurze Zeitspannen wird hier eine Wiederholbarkeit der Kalibration von 2,5 cm/s erreicht – einen Faktor 4 besser als mit einer Thorium-Lampe, der bis dahin besten Kalibrationsquelle. Erstmals wird der Orbit eines extrasolaren Planeten mit Hilfe eines Frequenzkamms rekonstruiert, und ein Frequenzkamm-kalibrierter Atlas solarer Linien wird aus Beobachtungen von Mondlicht erstellt. Instrumentelle Effekte werden gründlich untersucht, insbesondere Kalibrationsverschiebungen, die von den Signalpegeln auf der Spektrographen-CCD abhängen.

Hinsichtlich seiner Anwendungen in der Sonnenastronomie wird der Frequenzkamm am VTT Sonnenspektrographen auf Teneriffa getestet. Hier wird eine Technik eingesetzt, die den Spektrographen über eine monomode Glasfaser gleichzeitig mit Kalibrationslicht und Sonnenlicht versorgt. Dadurch wird Modenrauschen des Faserkanals als Ursache für Ungenauigkeiten ausgeschlossen, und die Kalibrationswiederholbarkeit verbessert sich um ca. 2 Größenordnungen gegenüber einer zeitlich getrennten Übertragung. Dieses Konzept wird zur Vermessung globaler Sonnenoszillationen und zur Bestimmung der Stabilität von Absorptionslinien aus der Erdatmosphäre angewandt.

Abstract

This work reports on the development and in-field test of laser frequency combs for calibration of astronomical spectrographs. Thus far, the precision of the best spectrographs had been limited by their calibration. The use of a frequency comb as an extremely accurate optical frequency reference promises to overcome this limitation and to allow measuring line positions in astronomical spectra at unprecedented levels of precision. This opens up the door to intriguing new possibilities in astronomy, such as the detection of Earth-like extrasolar planets via radial-velocity measurements, the direct measurement of the acceleration of the cosmic expansion, and a more accurate cosmological search for variability of fundamental constants. A commercial version of the astronomical frequency comb has been derived from this work, and is currently being prepared for installation and routine use at several observatories.

Frequency combs with an extremely large mode spacing of typically > 10 GHz are required to sufficiently resolve the comb structure with astronomical spectrographs. This work pursues an ytterbium-fiber laser-based approach for the generation of such large mode-spacing frequency combs, which works by suppressing unwanted modes of a frequency comb with originally smaller mode spacing. For broadband spectrograph calibration, the generated comb spectrum needs to be broadened to cover a large portion of the visible spectral range. At pulse repetition rates of > 10 GHz, this proves to be very challenging, and discloses many previously unknown effects.

This work develops strategies for spectral broadening of astronomical frequency combs, and investigates associated questions such as color-center formation within the core of photonic crystal fibers. A spectral coverage of > 230 nm in the center of the visible spectral range is demonstrated. Further, it is theoretically and experimentally proven, that spectral broadening is accompanied by a strong re-amplification of the suppressed comb modes, and it is shown how the associated calibration uncertainties can be limited.

Since the envelope of the broadened spectrum is strongly structured, it is useful to reshape it into a flat-top. This equalizes the signal levels of all calibration lines on the spectrograph, and thereby maximizes their signal-to-noise ratio, increasing the calibration precision. Several concepts for adaptive spectral flattening are developed, and flat-top spectra over up to > 200 nm are experimentally obtained.

The astronomical frequency comb is tested at HARPS, the leading spectrograph for exoplanet searches to date, located at the La Silla Observatory in Chile. Over short time horizons, a calibration repeatability of 2.5 cm/s is obtained – a factor of four better than with a thorium lamp, which was the so far best calibration source. For the first time, the orbit of an extrasolar planet is reconstructed by making use of a frequency comb, and a frequency comb-calibrated atlas of solar lines is derived from observations of moonlight. Instrumental effects are closely characterized, in particular calibration shifts related to the signal levels on the spectrograph CCD.

The frequency comb is tested for applications in solar astronomy at the VTT solar spectrograph in Tenerife, Canary Islands. Here, a technique is demonstrated that uses a single-mode fiber to feed the spectrograph simultaneously with both calibration light and sunlight. This excludes modal noise from the fiber delivery as a source of uncertainty, and improves the calibration repeatability by about 2 orders of magnitude over a temporally separated fiber transmission. The concept is applied to measure global solar oscillations, and to assess the stability of absorption lines from Earth's atmosphere.

Contents

Chapter 1

Introduction

Frequency combs have led to revolutionary advances in precision laboratory spectroscopy and beyond, with a remarkable impact on the field of atomic and molecular physics in particular. For this accomplishment, the Nobel Prize in Physics has been awarded to Theodor W. Hänsch and John L. Hall in the year 2005. More recently, implementations of frequency combs for astronomical purposes have emerged. These astronomical frequency combs – or astro-combs – are very likely to pave the way to fascinating new discoveries in astronomy, astrophysics and cosmology.

This chapter provides the basic concepts and prepares the understanding of the working principles of frequency combs and their implementation for astronomy. It explains how astronomical spectrographs work, how they are calibrated, and how frequency combs may be used to replace existing calibration sources for the better. It also discusses several science cases, where astronomical frequency combs are likely to have an important impact. For example, they are likely to enable discoveries of Earth-sized, habitable planets outside of our solar system. They might also contribute to deepening our knowledge on the development of the universe. Moreover, they might allow confirming potential evidence for variability of the fine-structure constant on cosmological scales.

1.1 Frequency combs

Optical frequency combs[1] have revolutionized precision metrology, by providing a direct link between the radio frequency (RF) domain and the optical frequency domain [1,2]. A frequency comb is generated by a passively mode-locked laser that emits an accurately timed train of ultrashort light pulses. The spectrum of this pulse train consists of a very regular pattern of sharp spectral lines at frequencies f_n with:

$$f_n = f_0 + n \times f_r \tag{1.1.1}$$

Here, f_r is the repetition rate of the optical pulses, which determines the line spacing, and n is an integer that is commonly referred to as the mode number. f_0 is the so-called offset frequency, which describes a global shift of the line pattern. The frequencies f_r and f_0 are both in the radio-frequency (RF) range, while the mode number n is large enough to scale f_n to optical frequencies. The spectral lines of a frequency comb are also known as the comb modes, as they represent the longitudinal modes of the laser cavity.

---

[1] The expression “frequency comb” is synonymous with “optical frequency comb” in this work. “Laser frequency comb” (LFC) is another synonym that is frequently encountered in scientific literature.

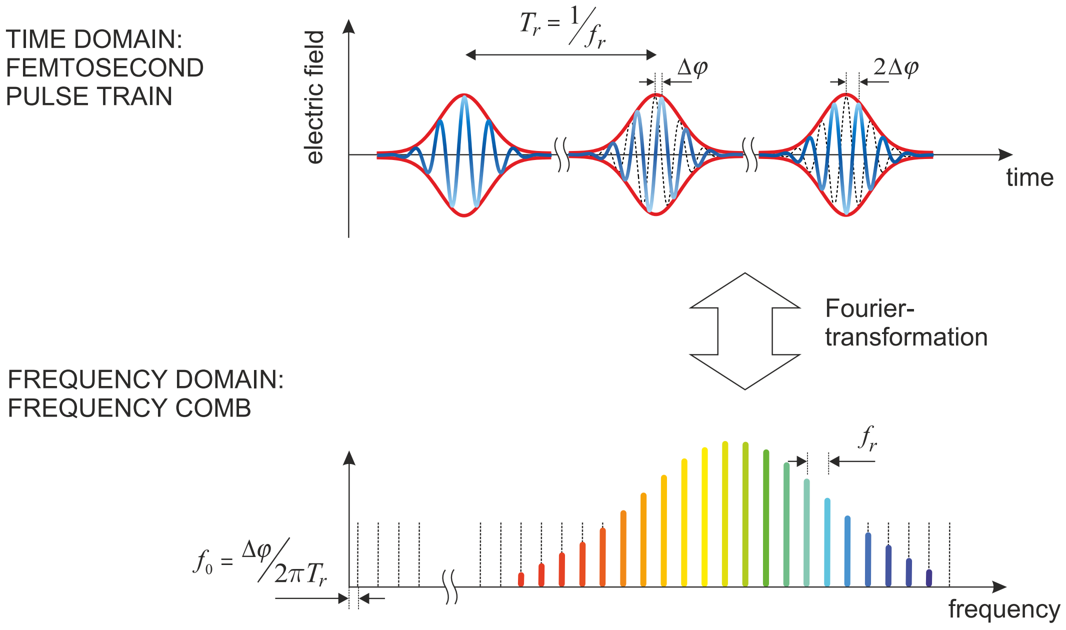

Figure 1.1 – Principle of the frequency comb. In the time domain (upper part), the frequency comb is represented by a train of ultrashort optical pulses, that are separated by a time delay of T_r. From one pulse to the next, there is a continuous shift between the carrier wave (blue) and the pulse envelope (red) of $\Delta\varphi$. The frequency domain (lower part), which is linked to the time domain by Fourier transformation, shows the spectrum consisting of a series of sharp spectral lines, that are separated by the repetition rate f_r of the optical pulses. Extrapolating the comb structure (dashed lines) to zero frequency reveals, that the pattern has an offset from zero of f_0, which is the so-called offset frequency. The relationship between the time domain parameters T_r and $\Delta\varphi$, and the frequency domain parameters f_r and f_0, is expressed by the annotated formulas.

A frequency comb can be understood both in the time domain, and in the frequency domain, which is illustrated in Fig. 1.1. In order to understand the relationship between the two descriptions, we picture a femtosecond laser pulse, that is circulating inside of a laser cavity. After each round-rip in the cavity, a copy of the pulse is emitted from the cavity. Subsequently, the gain medium in the cavity compensates the associated losses. The round-trip time T_r of the pulse is determined by the cavity length, and is the inverse of the repetition rate f_r of the emitted pulse train.

After each round-trip, the temporal pulse shape is exactly restored, which is ensured by an equilibrium between several opposed influences, such as the group-velocity dispersion of the laser cavity and self-phase modulation of the intra-cavity pulse. This results in a stable pulse envelope at the laser output. However, the difference in phase and group velocity within the laser cavity is not canceled out, i.e. the envelope of the intra-cavity pulse and its carrier wave travel at different velocities. This is seen in the emitted pulse train as a continuous shift of the carrier relative to the pulse envelope of $\Delta\varphi$ from one pulse to the next (see upper part of Fig. 1.1). Mathematically, the electric field $E\left(t\right)$ of the emitted pulse train can be described by an infinite sum of time and phase-delayed single pulses $E_1\left(t\right)$:

$$E\left(t\right) = \sum_{n=-\infty}^{\infty} E_1\left(t - n\,T_r\right)\, e^{in\,\Delta\varphi} = \int_{-\infty}^{\infty} E_1\left(t - t'\right) \left[\sum_{n=-\infty}^{\infty} \delta\left(t' - nT_r\right)\, e^{in\,\Delta\varphi}\right] dt' \qquad (1.1.2)$$

In the last step of Eq. (1.1.2), we have converted the sum of pulses into a convolution of a single pulse with a series of Dirac δ-functions. For convenience, we calculate with complex electric fields, whose real part describes the strength of the physical electric fields. In order to compute the amplitude spectrum of this pulse train, we need to Fourier-transform $E\,(t)$. For this we take advantage of the convolution theorem. It states, that the Fourier transform of a convolution of two functions is the product of their Fourier transforms. We can thus transform $E_1(t)$ and the term in square brackets separately, and understand the actual spectrum as a multiplication of the two. The Fourier transform of the single-pulse electric field $E_1\,(t)$ yields the spectral envelope $\tilde{E}_1\,(\omega)$ of the frequency comb, which is smooth function of ω. If for example the pulse envelope is Gaussian, then $\tilde{E}_1\,(\omega)$ is also a Gaussian function. Fourier transforming the term in square brackets in Eq. (1.1.2), on the other hand, yields the comb structure $\tilde{F}_{comb}(\omega)$ of the spectrum:

$$\tilde{F}_{comb}(\omega) = \int_{-\infty}^{\infty} \left[\sum_{n=-\infty}^{\infty} \delta\,(t - nT_r)\; e^{in\,\Delta\varphi} \right] e^{-i\omega t} dt = \sum_{n=-\infty}^{\infty} e^{in(\omega T_r - \Delta\varphi)} \tag{1.1.3}$$

The result can be understood as the Fourier series expansion of a Dirac comb. Reversing the Fourier expansion, we obtain:

$$\tilde{F}_{comb}(\omega) = \frac{1}{T_r} \sum_{n=-\infty}^{\infty} \delta\left(\frac{\omega}{2\pi} - \frac{\Delta\varphi}{2\pi\,T_r} - \frac{n}{T_r}\right) = \frac{1}{T_r} \sum_{n=-\infty}^{\infty} \delta\left(\frac{\omega}{2\pi} - f_0 - n\,f_r\right) \tag{1.1.4}$$

In the last step, we have identified the offset frequency f_0 and the repetition rate f_r with:

$$f_0 = \frac{\Delta\varphi}{2\pi\,T_r}, \qquad f_r = \frac{1}{T_r} \tag{1.1.5}$$

We thus see, that the spectrum of the pulse train consists of a series of evenly spaced δ-functions, that is shifted in frequency by f_0. There are more elegant ways to understand this fact (e.g. in [2,3]), but as we will see in Chapter 4, where the theory is revisited, the description presented here provides a good way to derive the mode structure of the astro-comb. It should also be noted, that in practice the comb modes are not δ-shaped, but are given an finite spectral width by noise mechanisms.

In order to stabilize the frequencies of the comb modes, f_r and f_0 need to be measured and controlled. Measuring f_r is simple: The pulse train is directed on a photodiode that puts out an electric signal with the periodicity of f_r. As f_r is typically between 80 MHz and 1 GHz, it is conveniently accessible to RF electronics. f_0 is also in the RF range, at $< f_r$, but its detection is more intricate, requiring a technique called self-referencing. This is commonly implemented in a device known as f:$2f$-interferometer. Figure 1.2 illustrates the idea. It requires the comb spectrum to span at least an optical octave. As the spectra of most mode-locked lasers are not octave-spanning, they are broadened in a photonic crystal fiber (PCF). PCFs allow exposing laser pulses to very high optical nonlinearities, mainly to four-wave mixing (e.g. self-phase modulation) and stimulated Raman scattering. Spectral broadening by these effects phase-coherently adds new comb modes, and can easily extend the comb spectrum to an optical octave. The low-frequency part of this spectrum is then frequency-doubled in a nonlinear optical crystal. Strictly speaking, what is referred to as frequency doubling in this context, is mainly sum-frequency mixing (SFM) among individual comb modes. This creates a second comb spectrum with the same repetition rate, but twice the offset frequency, which interferes with the high-frequency part of the first comb spectrum. The beat note between the two comb structures displays a frequency of the original offset frequency f_0, that can be detected

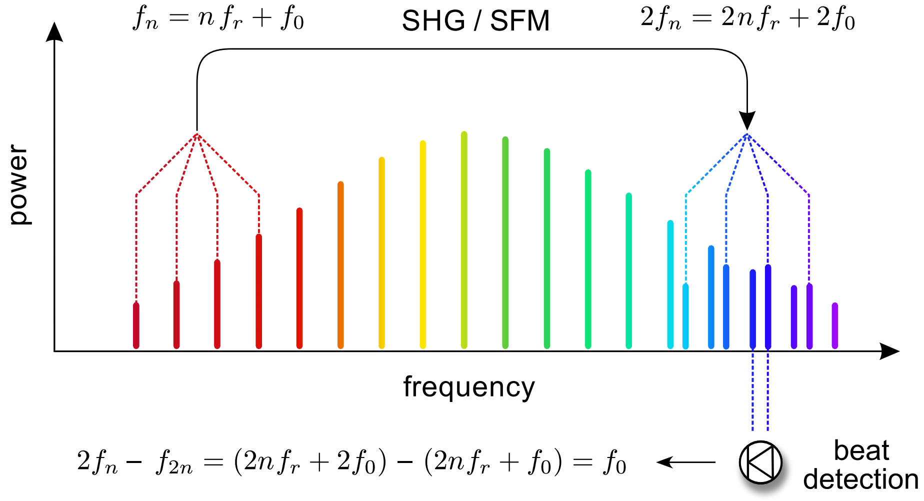

Figure 1.2 – Self-referencing of an optical frequency comb. The low-frequency part of an octave-spanning comb spectrum is frequency-doubled, and overlapped with the high-frequency part. This creates a beat note, equal to the offset frequency f_0, that is detected by a photodiode. Strictly speaking, what we here refer to as frequency doubling, comprises second-harmonic generation (SHG) of individual comb modes, as well as sum-frequency mixing (SFM) among different comb modes. The latter mechanism is the reason, why the mode spacing f_r remains the same, while f_0 is doubled. This generates a second comb pattern, shifted by f_0. The beat detection measures the difference in offset frequency, which equals f_0. The formulas that are annotated to the illustration describe this process, considering only a single comb mode of mode number of n, that is doubled in frequency. It is then beaten with a mode of mode number $2\,n$.

with a photodiode. A practical implementation of an f:$2f$-interferometer will be described in Chapter 2.

f_r and f_0 can easily be controlled by adjusting parameters of the laser. f_r is determined by the laser cavity length, and is usually controlled with a piezo actuator at one of the cavity mirrors. f_0 is determined by the difference between the group velocity and the phase velocity of the intra-cavity laser pulse, which can be acted upon by controlling the cavity dispersion. For slow control, this is usually done by shifting the position of a wedged glass plate in the cavity, adding more or less material dispersion to the beam path. For fast control, the pump power on the gain material is varied, which also has an impact on the net cavity dispersion.

The facts that f_r and f_0 are both radio frequencies, and that they can be measured and controlled, makes it possible to lock them to a stable RF reference, such as an atomic clock. Well-established phase-locked loop (PLL) techniques are used for this purpose, ensuring that the transfer from RF to optical is fully phase-coherent. This assigns optical frequencies to all comb modes with utmost accuracy. It has been shown, that this frequency transfer works with a fractional uncertainty at the level of 10^{-16} [1]. Before its demonstration, it was assumed that this method would not be successful, because RF noise would be vastly increased by the frequency transfer [4]. It can easily be shown, that if the pulse train was randomly phased, its spectrum would not contain any comb modes. This however, does not occur, because the passive stability of the optical resonator is exploited to prevent RF noise from excessively contaminating the control of the cavity length. Above a few kHz, there is no acoustic or thermal noise, and the optical resonator possesses a remarkable stability.

Frequency combs have become simple and compact devices for standard laboratory use.

An important factor that has contributed to this development is their commercial availability. Frequency combs can be used like a ruler in frequency space, to measure optical frequencies with unparalleled accuracy and great simplicity. For example, the frequency of a continuous wave (cw) laser can be measured by a beat note with one of the comb modes. A more coarse wavelength measurement of the cw laser reveals, which of the modes it beats with. Many exciting new applications have been found for the frequency comb, having sparked many important advances in science. The following list compiles a few examples:

Atomic spectroscopy: Frequency combs are used to measure the frequencies of atomic transitions with very high accuracy. Transitions of the hydrogen atom are of special interest, as they constitute an excellent test bed for quantum electrodynamics. Using a frequency comb, the frequency of the hydrogen 1S-2S transition has been measured with a fractional uncertainty of 4.2×10^{-15} [5].

Optical clocks: Optical transitions in trapped ions oscillate at far higher frequencies than microwave atomic clock signals. Hence, they slice time into much finer intervals, enabling higher accuracies. The fractional uncertainty of such optical clocks has reached the 10^{-18} level [6], about two orders of magnitude better than Cs clocks. The frequency comb is used for processing of the clock signal, e.g. to compare clocks of different kinds [7], or to transfer the clock signal to microwave frequencies for comparison with a Cs clock.

Timing dissemination: A frequency comb can be used to transfer the signal of a microwave atomic clock or that of an optical clock to a single-frequency laser that operates at telecom wavelengths. This signal can then be distributed via telecom fiber networks. In a 920 km long fiber link for clock comparisons between Garching (Germany) and Braunschweig (Germany) the timing dissemination has been shown to work down to the 10^{-19} level [8]. On this basis, a Europe-wide network is being built up for dissemination and comparison of clock signals of national standard institutes.

Dual comb spectroscopy: An arrangement of two frequency combs can be used to measure broadband molecular absorption spectra. The resolution of this technique outperforms conventional Fourier-transform spectrometers (FTS). More importantly, typical acquisition times of broadband spectra are of 10 µs, which is about a million times faster than with an FTS [9].

1.2 High-precision spectroscopy in astronomy

The scope of this work is to explore the applications of frequency combs in high-precision astronomical spectroscopy. Enabling higher precision and accuracy, frequency combs could have a deep impact on this field. An important aspect in high-precision astronomical spectroscopy is the detection of shifts of spectral line positions caused by the Doppler effect. This measures the radial velocity v_r of a celestial body, which is the velocity component along the line of sight to the observer. Especially for stars, absolute radial velocities are not measured with very high accuracy, because stellar properties that determine systematic line shifts are not known well enough. These line shifts are caused e.g. by a blue shift due to convection on the stellar surface, or by the gravitational redshift. The scientific interest, however, focuses rather on small radial-velocity changes Δv_r over time. A radial-velocity change of Δv_r shifts the frequency of a spectral line at a frequency f by an amount Δf. For velocities $v \ll c$, where c is the speed of light in vacuum, the frequency shift is given by:

$$\frac{\Delta f}{f} = -\frac{\Delta v_r}{c} \tag{1.2.1}$$

radial-velocity shift	frequency shift @ 600 THz (500 nm)	fractional frequency shift
1 m/s	−2 MHz	-3.33×10^{-9}
1 cm/s	−20 kHz	-3.33×10^{-11}

Table 1.1 – Unit conversion table from radial velocity to frequency shifts. The values given for 600 THz can be used as a rule of thumb for visible wavelengths. When the table is used to quantify uncertainties, the sign is dropped. 1 m/s roughly represents the current state-of-the-art, while 1 cm/s would be desirable for important applications.

By convention, radial velocities (RVs) are positive when they point away from the observer. In astronomy, the concept of RV is so central to high-precision spectroscopy, that all line shifts and uncertainties of line positions are commonly expressed in m/s. This is usually the case even when the line shifts are not caused by the Doppler effect. When using the astronomical frequency comb, we will occasionally use other units, such as Hz, or specify fractional shifts, but generally we will adhere to this convention. To give the reader an orientation, Tab. 1.1 represents a conversion table, where the values given for 600 THz (or 500 nm) can be used as a rule of thumb for unit conversion in the visible region.

A major application of RV measurements is the detection of extrasolar planets. A planet in the orbit of a star imprints a recoil motion on its host star. A periodic modulation of the stellar RV can thus be observed, that carries information on the planet and its orbit. Section 1.4 provides an extensive discussion of this and other scientific applications. Such measurements are of considerable scientific interest, and great efforts are undertaken to improve their precision for the sake of new discoveries. This goal is the basic idea in the rest of this chapter, and the ultimate motivation for this work.

As explained in the previous section, frequency combs have been used to measure the frequency of light. Astronomical spectroscopy, by contrast, measures the wavelength of light rather than its frequency. Such measurements rely on geometrical principles such as diffraction and angular dispersion rather than being purely based on time. This is not only conceptually different, but also presents a number of challenges if a high precision is to be reached, such as the stability of the beam pointing within the spectrograph. As a matter of fact, the wavelength of light – contrary to its frequency – does not only depend on the refractive index of its medium, but also on its beam profile. The equation $f = c/\lambda$ is indeed exact for plane waves, but for beam bundles of limited extent, small corrections are introduced. For a Gaussian beam bundle, for instance, the wave fronts experience a gradual phase shift (the Gouy phase) while traveling through the beam waist. This changes the wavelength of light over this range – but not its frequency.

Unfortunately, astronomers generally cannot resort to direct frequency measurements. This is because beat measurements at a sensitivity and bandwidth comparable to that of an echelle spectrograph are technically still too challenging. Although it has been shown with light from Mars [10], Jupiter [11], Venus [12] and the Sun [13], that heterodyning with a laser can be used to acquire precise mid-infrared spectra [14, 15], this approach could not yet be demonstrated on fainter targets. The technique has so far also been restricted to the mid-infrared, where a large number of photons is available for heterodyning, thanks to the lower photon energy and greater spatial coherence of the sources.

Therefore, the established standard instruments for high-precision spectroscopy in astronomy are echelle spectrographs. Figure 1.3 illustrates their working principle. An echelle spectrograph disperses the light by means of an echelle grating, i.e. a ruled diffraction grating working in very high diffraction orders. The numerous diffraction orders would all spatially

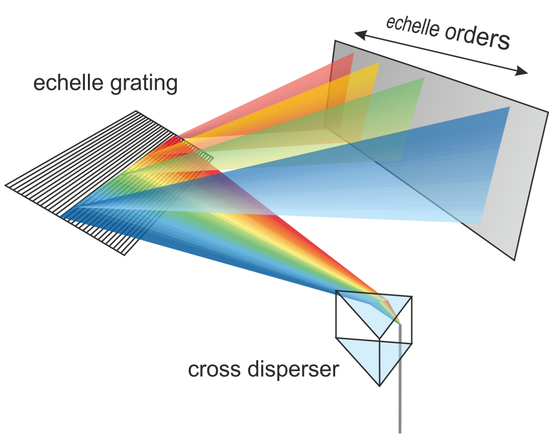

Figure 1.3 – Working principle of an echelle spectrograph (simplified). The input beam is cross-dispersed by a prism. The light is then again dispersed in perpendicular direction by an echelle grating. This is a ruled diffraction grating working in very high diffraction orders. The spatially separated diffraction orders (the echellogram) are imaged onto a CCD. Not depicted: Optics for collimation and focusing of the beam.

overlap, if the light was not dispersed in the direction perpendicular to them. This is done by a cross disperser, which is usually a prism (or grism) located after or sometimes before the echelle grating. The combination of echelle grating and cross disperser separates the spectral components in space, creating a so-called echellogram, which is imaged onto a charge-coupled device (CCD). Conceptually, the echelle spectrograph compares the wavelength of light to the length scale of its grating (the pitch of its grooves), which amounts to a wavelength measurement.

High-precision echelle spectrographs typically have a spectral resolution of $R = \lambda/\Delta\lambda \approx 100\,000$, where λ is the wavelength and $\Delta\lambda$ is the full-width at half-maximum (FWHM) of a spectral resolution element. A higher resolution usually comes at the price of a reduced wavelength coverage. For faint targets, higher resolution is also often undesirable, because the same number of photons would have to be distributed among a larger number of CCD pixels, which degrades the signal-to-noise ratio due to an increased readout noise. Most spectrographs cover the visible spectral range, where stars have the largest selection of high-quality Fraunhofer lines, and where Earth's atmosphere has its best transparency. There is however also a significant number of spectrographs operating in the near-infrared, using the transmission windows that Earth's atmosphere offers in this range. Here, the scientific interest lies in a number of objects that can best be observed in the infrared spectral region.

For measuring wavelengths with an echelle spectrograph, the spectrograph is calibrated with a source that provides narrow spectral features at known wavelengths. In this manner, a wavelength solution is constructed. This is a mathematical function that relates the position of a spectral feature on the CCD to its wavelength. The calibration can be done before and after the science observations. In this case, the beam pointing inside the spectrograph must be very stable, to avoid spectrograph drifts that distort the calibration during the measurement. This is why spectrographs are often temperature stabilized to reduce thermal drifts. Since the wavelength of light within a medium depends on its refractive index, spectrographs are also often evacuated or pressure stabilized. Additionally, the beam profile inside the spectrograph must not change. This not only because the wavelength of light depends on its beam profile, but because imaging errors and/or vignetting translate an altered shape of the beam within the spectrograph into a changed center-of-gravity of the line positions.

The requirements on stability of the beam pointing and profile can be met much more easily with a fiber-fed spectrograph. If the science light from the telescope is coupled to the spectrograph in free space, the beam is affected by guiding errors of the telescope and by varying atmospheric seeing conditions. Transporting the light to the spectrograph via an optical fiber, in contrast, decouples the beam pointing from telescope guiding. However, it is currently not possible to efficiently couple light from astronomical sources to single-mode optical fibers, for which the decoupling of the beam parameters would be perfect. Hence,

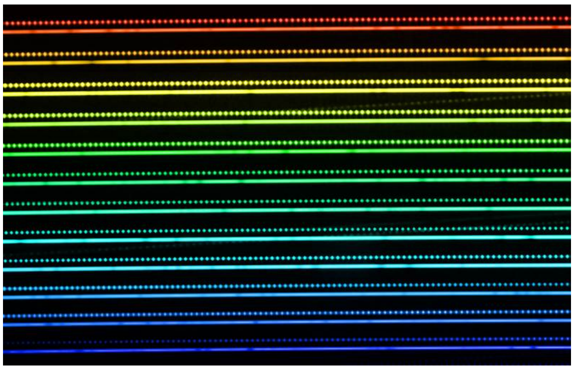

Figure 1.4 – Part of the echellogram of the two-channel fiber-fed spectrograph HARPS. The upper channel carries calibration light (here from an astro-comb), while the lower channel carries starlight from a telescope. This enables simultaneous calibration, to compensate spectrograph drifts. The two fiber channels share a rigid mechanical connection for optimum relative stability. Source of the image: ESO press release on May 30, 2012. The color is for illustrative purposes only.

multimode fibers are used for this purpose. They are very good beam homogenizers in the near-field, i.e. close to the fiber output facet, but not so in the far-field, i.e. far from the fiber output. In particular, the far-field profile can be distorted into a ring shape, if due to guiding errors the image of the object is off-center on the fiber input [16]. This effect can however be greatly reduced by the use of static fiber scramblers. Among the most successful configurations of this kind is the so-called double-scrambler [17]. It couples the beam from one fiber into another by means of two lenses. This is done such that the far-field of the first fiber is projected on the near-field of the next fiber, and vice versa. The beam at the output of this configuration exhibits good homogenization in the near-field as well as in the far-field, which effectively mitigates guiding-related uncertainties, and at the same time offers a high throughput. Besides the double scrambler, variety of other types of static scramblers exist.

Particularly high precision is provided by fiber-fed two-channel spectrographs, that permit simultaneous calibration during measurements. This configuration possesses two fiber channels at its input, that share a rigid mechanical connection. The two channels are first compared to each other, by putting calibration light simultaneously on both of them. Then, the science measurement is performed on one channel, while the second channel still carries calibration light to track spectrograph drifts. A part of the echellogram of such a two-channel fiber-fed spectrograph is shown in Fig. 1.4.

A way to provide simultaneous spectrograph calibration through only a single channel is the use of an iodine absorption cell [18,19]. The science light from the telescope passes through an iodine gas cell before entering the spectrograph, which imprints a dense forest of unresolved absorption lines on the science light. This has the advantage, that the calibration spectrum is intrinsically mode-matched to the science light, and is thus very well suited for tracking instrumental drifts, and insensitive to a changing beam profile. A drawback is the fact, that the absorption reduces the number of photons available for the science observation, which degrades the signal-to-noise ratio. The technique is also limited to the $500-630$ nm spectral range, and the superimposed iodine spectrum renders the data analysis more complicated and less robust. In most situations, the commonly preferred method is therefore to use a two-channel spectrograph, calibrated with an emission lamp.

The above-described methods have led to the construction of remarkably stable echelle spectrographs. The High-Accuracy Radial velocity Planet Searcher (HARPS) [20, 21] shall briefly be considered as an example: HARPS is a two-channel fiber-fed spectrograph. It is located at the La Silla Observatory, Chile, and operated be the European Southern Observatory (ESO). The spectrograph is installed inside of a vacuum vessel with a pressure of < 0.01 mbar inside. It is temperature-stabilized within 10 mK at 17 °C, making the spectrograph passively stable to 1 m/s over at least many hours. The remaining drifts are tracked through simultaneous calibration on the second fiber. The HARPS CCD is cooled down to −120 °C, to suppress dark current-related thermal noise, and is stabilized there within 20 mK. Its two input fibers have a 70 µm core and include a double scrambler each. The spectrograph covers the 380−690 nm spectral range with 72 echelle orders and a resolution of $R = 115\,000$.

HARPS and its peers are so stable, that their precision is not limited by their stability. Rather, the calibration sources have become the limiting factor. To quantify the calibration performance, we must distinguish between several aspects of the calibration: Its accuracy, its repeatability and its reproducibility [22].

Accuracy: The calibration is said to be accurate within certain limits, if it provides an absolute wavelength scale that – down to this level – comes close to the true wavelengths. For many applications, such as RV measurements, a very high accuracy is not required, and a systematic shift of the wavelength solution from the true wavelengths can be afforded.

Repeatability: This quantity describes, how much consecutive, identical measurements performed with the same instruments differ from each other. Often, the calibration is merely required to be repeatable (not accurate) since only relative shifts of line positions are of interest. The repeatability of the calibration can be used as a measure of its precision, which is not to be confused with its accuracy.

Reproducibility: The calibration is reproducible within certain limits, if it can be replicated on a separate, independent instrument. This is required, for instance, if results from different instruments need to be compared. Reproducibility does not necessarily imply accuracy. A systematic offset from the true wavelengths is permitted, as long as it is consistently replicated. However, the best way to ensure reproducibility is to provide accuracy.

As explained previously, spectral lamps are currently the prevailing standard sources for high-precision spectrograph calibration. The most established of these sources are thorium-argon (ThAr) lamps, which are primarily used in the visible. For the infrared spectral range, uranium-neon lamps are used, working analogously. ThAr lamps are hollow-cathode arc lamps with argon as a buffer gas for the discharge. For calibration, only the thorium lines are considered, while the neon lines are usually rejected. Thorium produces thousands of spectral features in the visible range. It is mono-isotopic with no hyperfine structure, which results in narrow and highly symmetric line profiles. The reference for the thorium wavelengths is the Los Alamos atlas of the thorium spectrum [23]. It has been obtained with an FTS at a resolution of about 600 000, and quotes the positions of approximately 11 500 lines between 300 and 1100 nm. The accuracy of the wavelengths ranges from 16 to 82 m/s at 550 nm.

A substantial problem of ThAr-lamps is the strong irregularity of line spacings and intensities. For an echelle spectrograph with a typical resolution of 100 000, line blending reduces the number of usable lines to about 4000. ThAr-lamps can also suffer from contamination. With the HARPS spectrograph it has been shown, that the calibration is repeatable within 10 m/s for a single line, and 20 cm/s globally [24]. This result could be reproduced in [25], but is only valid on short time scales. Over the full lifetime of a ThAr lamp of about 500 hours, aging causes the calibration to drift globally by several m/s. This yields a long-term repeatability comparable to the one reached with iodine cells [19]. To slow down the aging process, ThAr lamps are operated in a master-slave configuration: The slave lamp is compared to the master lamp at the beginning of every observation night. During the observations, only the slave lamp is used for calibration, while the master lamp is used as sparingly as possible.

1.3 Frequency comb-assisted astronomical spectroscopy

Due to the limitations imposed by spectrograph calibration, the currently available precision in astronomical spectroscopy fails to satisfy the demands of the scientific community. For example, this restriction prohibits the detection of Earth-sized, habitable exoplanets using the RV method. To find an exo-Earth, a repeatability of a few cm/s would be required over several years. On such time scales, however, ThAr calibration is limited to several m/s. The detection of the acceleration of the cosmic expansion would even require a repeatability of about 1 cm/s over two decades. Ultimately a calibration to 1 cm/s over arbitrary time horizons would be desirable.

Comparing these requirements to what frequency combs routinely offer in laboratory spectroscopy, the demand for a 1 cm/s repeatability appears rather modest. While a 1 cm/s uncertainty implies a fractional frequency uncertainty of 3×10^{-11} , frequency combs can reach down to the 10^{-16} level, if referenced to the best Cs clocks. Expressed in RV, this is considerably below 1 µm/s. Better yet, the frequency comb is not only repeatable, but also accurate to that level.

In 2007, Murphy et al. were the first to recognize the frequency comb as a nearly ideal calibrator for astronomical spectrographs [3]: It represents a series of evenly spaced lines of unresolved width, whose frequencies are known to absolute accuracy. Provided, that the line spacing of the comb is adapted to the spectrograph resolution, that the comb covers the full spectral range of the spectrograph, and that all comb modes supply the spectrograph CCD with the same rate of photon counts, the comb represents virtually the best conceivable calibration source. Murphy et al. show that the optimum mode spacing is about 3 times the FWHM of an optical resolution element of the spectrograph. They also derive formulas for the calibration precision that can be attained with a frequency comb in case the calibration uncertainty is dominated by photon noise. Photon noise is a fundamental limit that can only be reduced by collecting more photons on the spectrograph CCD, e.g. by increasing the observation time and by combining several CCD exposures. For the HARPS spectrograph, this formula yields an uncertainty of 0.8 cm/s in a single CCD exposure (see also [25]).

The resulting uncertainty is overwhelmingly low, considering the fact that the 15 µm wide CCD pixels of HARPS span about 1 km/s in spectral width. 1 cm/s thus corresponds to roughly 10^{-5} of the size of a pixel, or to about the size of a silicon atom of the CCD. The FWHM of a single comb line is sampled by 3.3 pixels, and its photon noise limit is of about 1 m/s. The 0.8 cm/s given above, averages down the photon noise over approximately 23 000 comb lines within the spectral range of HARPS. Although it is straightforward to locate the center of a line down to a small fraction of its FWHM, it is questionable how the derived calibration is systematically distorted, e.g. by irregularities in the pixelation or by the read-out mechanism of the CCD. A stringent search for systematics is therefore imperative to unlock the full potential of the astro-comb.

The superiority of astro-combs to ThAr-lamps can directly be seen from Fig. 1.5, where the two kinds of sources are compared. The figure is a result of the present work, and shows a small section of the HARPS CCD. Here the comb is on the upper channel of the echellogram and a ThAr lamp on the lower channel. While thorium exhibits large fluctuations in both line spacing and line intensity, the comb lines have perfectly regular spacings, and fluctuate very little in intensity. The comb also exhibits a larger number of lines, and contrary to ThAr, its line spacing can be adapted to the spectrograph. Besides, the comb has another very appealing property: While the line positions of ThAr are fixed, the line positions of the comb are tunable, such that literally every pixel within an echelle order of the CCD can be reached and calibrated. This allows characterizing and accounting for irregularities of the

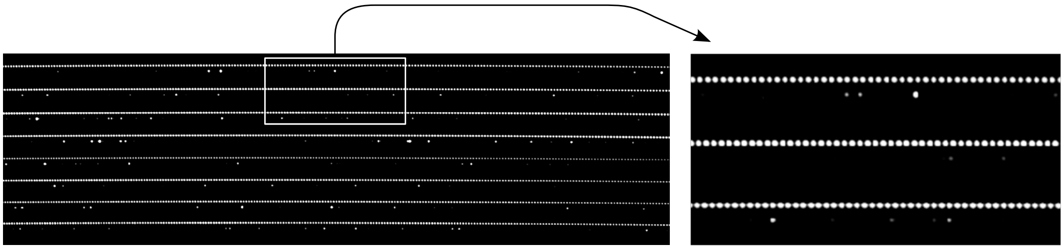

Figure 1.5 – Comparison between an astro-comb and a ThAr lamp on the HARPS spectrograph. The image shows a small section of the HARPS CCD (further magnified on the right). The comb is on the upper channel (chains of equidistant white dots), while the ThAr lamp is on the lower channel (sparsely distributed dots).

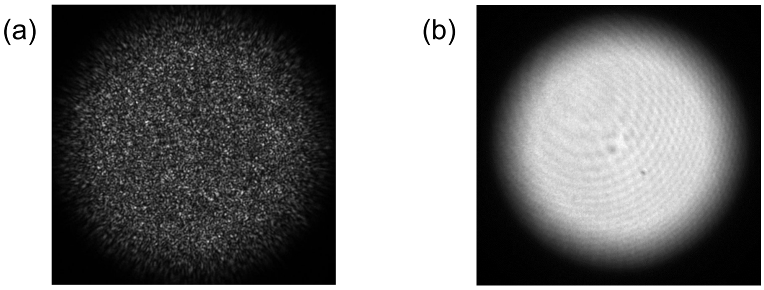

Figure 1.6 – Suppression of laser speckles through dynamic scrambling of multimode fibers. The images show the far-field of a multimode fiber with a 600 µm core, illuminated with a He-Ne laser. (a) Image of the beam profile while the fiber remains static. (b) The fiber is dynamically scrambled by a small motor with an eccentric weight, that is attached to the fiber. This makes the fiber vibrate, and the speckles move quickly. On the time scale of the exposure (100 ms), the speckle pattern is washed out. The weak fringes probably originate from the window of the employed CCD.

CCD pixelation. The astro-comb is also ideal to precisely study the instrumental line profile and its change across the echelle orders: Since the width of the comb modes is far from being resolved, each line is an image of the instrumental profile at this point.

The frequency comb however comes with a caveat: Being a laser, it exhibits nearly perfect spatial coherence. Moreover, it has a very strong temporal coherence, with a coherence length on the order of about 1 km for each comb mode. Coupling such highly coherent light through multimode fibers as they are used by spectrographs, produces laser speckles due to modal interference, as shown in Fig. 1.6(a). The speckle pattern moves at even small motions of the fiber, shifting the center of gravity of the calibration lines [25, 26]. Dynamic scrambling of the fiber is therefore crucial. This means to rapidly shake the fiber, such that the speckle pattern moves randomly. On a time scale exceeding the motion of the speckles, the light then behaves as spatially incoherent light. This is required in addition to the static scrambling explained in the previous section, which merely seeks to globally homogenize the spatial mode occupation of the fiber.

First practical implementations, demonstrating the concept of the astronomical frequency comb followed in 2008 [27–29], soon after Murphy et al.'s proposal. Also the present work reports on the development and test of an astro-comb, with the aim of making its full potential usable for astronomy. Before and during this work, three major groups have played a leading role in this field: A group from the National Institute for Standards and Technology (NIST) has been developing an astro-comb based on Er-fiber technology. Centered at 1550 nm, it aims to cover the near-infrared spectral range [30,31]. Another group from the Massachusetts Institute of Technology (MIT) aims for the visible range with a Ti:sapphire laser, based on free-space optics [28,32–37]. The present work has been made in the group at the Max-Planck-Institut für Quantenoptik (MPQ), who targets the visible spectral range using Yb-fiber laser technology [26,38–40]. This group started in 2007, about at the same time as Tobias Wilken joined to make his PhD on this project until 2010 [25]. Starting in May 2010, the present work is to be seen as the continuation of Tobias Wilken's PhD work. The research has been done in a collaboration with astronomers from the ESO and from the Kiepenheuer Institut für Sonnenphysik (KIS), and with Menlo Systems GmbH as an industrial partner. The goal of the collaboration has been the development and testing of an astro-comb that enables routine use at observatories. The system is then going to be offered by Menlo Systems as a commercial product, which has become a reality with the completion of this PhD work.

The development of astro-combs has proven to be challenging. While standard frequency combs usually have repetition rates of 80 MHz−1 GHz, for astro-combs a typical mode spacing of 10−30 GHz is required, as dictated by the resolution of astronomical spectrographs. It is extremely difficult to extract such high repetition rates directly from a mode-locked laser. Hence, the three major groups all rely on conventional frequency combs at low repetition rates, and suppress unwanted comb modes with an external Fabry-Pérot filter. Achieving a broadband wavelength coverage with these configurations has turned out to be difficult as well. Prior to the start of this work, visible spectrograph calibration could only be demonstrated over 1−3 echelle orders [25,26], each spanning about 5 nm. This narrow-band calibration already demonstrated a repeatability of 10 cm/s. A subsequent attempt for spectrograph calibration over a ~100 nm spectral range, however, failed, unexpectedly giving rise to calibration uncertainties of several 100 m/s. The present work investigates and solves this problem. Broadband spectrograph calibration is successfully demonstrated on two different spectrographs with a repeatability of 2.5 and 3 cm/s, respectively.

The ideal calibrator, as envisioned by Murphy et al., possesses a constant photon flux per comb line over its full width, as detected by the spectrograph. Only then can all calibration lines simultaneously reach their maximum signal-to-noise ratio on the CCD. In other frequency-comb applications, there is no such requirement, and the spectral envelope of broadened combs is normally strongly structured. This work thus develops spectral reshaping techniques, that provide a flat spectral envelope over a range as large as possible.

Last but not least, for being useful for astronomy, the astro-comb must be able to operate autonomously over a long time without being serviced. The system would only be controlled electronically from a remote site. This work also tries to address this aspect. It seeks to develop an alignment-free system and tries to extend the lifetimes of sensitive components.

1.4 Scientific applications

This section reviews a few science cases, where the astro-comb is expected to have a deep scientific impact. The three major examples covered in this section are far from being exhaustive. In Chapter 7 for instance, we will briefly mention further applications in solar astronomy. The following examples, however, are outstanding in the sense that they represent milestones in modern science. They make the introduction of astronomical frequency combs well worthwhile, even if associated with difficulties.

1.4.1 The hunt for Earth-like exoplanets

Extrasolar planets, or exoplanets, are planets outside of our solar system. The search for them has been a major center of interest in astronomy over the last two decades. With refinement of observational methods [41], the number of detected exoplanets has been growing at an ever accelerating pace. So far, more than 1900 planets have been found [42], and several thousand candidates are awaiting confirmation. The population of known planets is invaluable for the understanding of the formation and development of planetary systems [43]. The diversity of the observed planets is astonishing [44], and has made obvious, that the solar system does not provide a universal template for planetary system architectures. Interestingly, it has been observed, that more than 50 % of all planets are probably not orbiting a star, but are freely floating through the galaxy [45]. It is currently not clear, whether they have already formed in this state, or whether they have been ejected from planetary systems. Other remarkable findings are, that most stars harbor at least one planet, and that smaller planets are more frequent than gas giants [43, 46]. The most interesting type of planets are Earth-like planets, a category to which only a few of the currently known planets possibly belong.

An Earth-like planet is defined as a rocky planet of about the size of Earth, orbiting within the habitable zone of its host star [47]. The habitable zone is the region where a planet can have surface temperatures allowing the presence of liquid water. A major scientific question is, how common these planets are. Once found, spectroscopic examination of their atmospheres could be the next step. This might be possible while the planet is in a transit (see Fig.1.7(b)), i.e. when the light of the host star partly passes through its atmosphere. Another possibility is direct imaging of the planet. This is difficult, because the planet is very close to its overly bright host star. This obstacle could be surmounted for example by using a starshade, i.e. a disk in a precise formation flight with a space telescope [48]. The disk would be positioned such that it eclipses the star, but not the planet, enabling spectroscopy of its atmosphere. The spectroscopic measurements would allow examining the presence of water on the planet. For small rocky planets, water vapor in the atmosphere is considered a positive proxy for liquid water on their surface [47]. Another obvious question is whether such habitable planets are actually inhabited, i.e. whether they harbor any form of life. This question could be tackled by looking for biosignature gases, whose concentrations exceed the thermo-chemical equilibrium [47]. Oxygen for example is a highly reactive gas, that would soon disappear by forming compounds with other elements. A high concentration of it thus indicates, that it is continuously reproduced, e.g. through photosynthesis by living organisms.

With present instruments, direct imaging of exoplanets is successful only for giant planets in wide orbits, as in the cases of Fomalhaut b [49] and β Pictoris b [50]. Indirect methods for planet detection are thus dominating the field. Microlensing allows finding planets via their brightening effect on background stars. The method has not led to many individual detections, but allows monitoring populations of planets [46], and is not specific to any orbital period. Besides direct imaging, this is so far the only technique capable of detecting planets that are not gravitationally bound [45]. Astrometry as another method for finding exoplanets, by detecting the small elliptic (or circular) changes in position, that a planet imprints on its host star. No planet has been found with this method, but it has a long history of false detections. This may change with the European space telescope Gaia, launched in late 2013, that is conducting an extensive exoplanet search with this technique. For now, the two techniques that have enabled the most planet detections by far, are the radial-velocity (RV) method and the transit method. A big deal of information on a planet can usually only be gained, if the two techniques are combined with each other. They are thus not to be understood as being in competition with one another, but as going hand in hand.

The RV method (see Fig. 1.7(a)) detects extrasolar planets by measuring the recoil motion

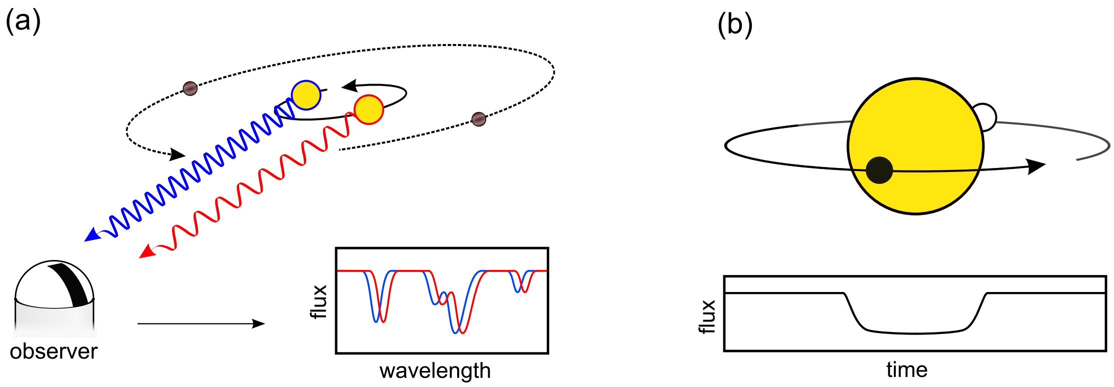

Figure 1.7 – The two primary techniques for exoplanet detection. (a) Radial-velocity (RV) method: A planet in the orbit of a star imprints a recoil motion on its host star. The illustration shows the star and its planet in two phases of the orbit: When the planet is moving away from the observer, the star moves towards the observer, and a blue shift is measured in the stellar spectrum. Likewise, a redshift is observed when the planet goes forward and the star moves away. (b) Transit method: If a planetary orbit happens to have a favorable orientation, periodic planetary transits can be observed. During such an event, the apparent brightness of the star drops because the planet passes in front of it. A second dip occurs when the star occults the planet, which is often too weak to be observed.

that a planet imprints on its host star. It works by measuring the resulting periodic RV modulations, that are manifested as Doppler shifts of the lines in the stellar spectrum. The technique thus makes use of the arsenal of instrumental tools discussed in Sec. 1.2. From the evolution of the RV over time, the period, eccentricity and the semi-major axis of the orbit can be derived. The method also yields the so-called projected mass $m \sin(i)$, with m the mass of the planet and i the inclination angle of the orbital plane versus the line of sight. Since i is not known from first principles, this yields a lower bound on the planetary mass. If a transit (see Fig. 1.7(b)) has been observed for the planet, $i \approx 90°$ is known, and the projected mass is the mass of the planet.

Using the RV method, the first planet around a Sun-like star has been found in 1995 [51], and for a long time, this was the method that had enabled the most planet discoveries. Still to this date, it is being very productive, with more than 600 detected planets so far. The first planets found with it were hot Jupiters, i.e. Jupiter-mass planets on close-in orbits. With refinement of spectroscopic instruments, and especially with the HARPS spectrograph, super-Earths have become detectable, i.e. planets of several times the size of Earth. A number of such super-Earths have been found within the habitable zone of their host stars [52–54]. The most spectacular discovery so far has been an Earth-sized planet around α Centauri B, although too close to its host star to be habitable. The planet has an orbital period of about 3 days, and an RV amplitude of 50 cm/s, which is almost at the limit of what current instruments support. An Earth-like planet around a Sun-like star would lead to a velocity amplitude of 9 cm/s over one year. As discussed in Sec. 1.2 and 1.3, this is presently out of reach because of limitations in spectrograph calibration. Using an astro-comb, on the other hand, the necessary calibration repeatability of a few cm/s should easily be attainable.

For detecting an exo-Earth, however, there are more effects to be taken into account. RV signals of stars are inherently noisy, due to stellar activity, pulsations and star spots. [55] provides a good example, on how such effects can be separated from the RV signal, but for exo-Earths, this still remains to be shown. Again, the astro-comb can make an invaluable contribution by permitting precise investigation of these effects and by helping to identify low-noise stars.

Targeting M-dwarf stars could be a shortcut for finding exo-Earths. Due to the lower mass of M-dwarfs, exo-Earths produce a stronger RV signal of about 1 m/s. Additionally, the habitable zone is closer to the star, which reduces the orbital period and thus the required measurement time. M-dwarfs have their strongest emission in the infrared. The development of infrared astro-combs is thus desirable as well, which is pursued by [30, 31]. The present work briefly presents an approach for the generation of an astro-comb, that covers both the infrared and the visible spectral regions (Sec. 3.3).

Through the Kepler space telescope, which conducted a large-scale exoplanet survey from 2009 to 2013, the transit method has become the most successful technique for exoplanet detection. It is looking for periodically recurring dips in the apparent brightness of a star, caused by repeated planetary transits (see Fig. 1.7(b)). Such periodic transits can only be observed on the small fraction of all planets whose orbits have the right orientation, and at first merely qualify a potential planet as a planetary candidate. The Kepler space telescope could detect planets down to the size of the Moon, and has delivered several thousand planetary candidates, many of which have already been confirmed. Up to 11 % of the candidates are estimated to be false positives, caused e.g. by a partly eclipsing star in a binary star system. The confirmation of the candidates as real planets usually requires follow-up observations using the RV method. Only in certain cases can planets be confirmed by other means. An example is the system Kepler-11 [56], where the planetary orbits were found to deviate from perfect periodicity. This could be shown to originate from gravitational perturbations among the planets, which confirmed their existence.

The transit method and RV method yield complementary information on a planet. With the observation of a transit, the size of the planet can be inferred, while an RV measurement provides information the planetary mass. In combination, the mean density of a planet is known, which is key for the distinction between a rocky planet and a gas planet. The Kepler space telescope has produced a decent number of Earth-like planetary candidates. The use of astro-combs would allow the confirmation of these planets through RV measurements, and to find out whether these planets are in fact rocky planets. The technical maturity of this new calibration method is thus awaited with great excitement by the astronomical community.

1.4.2 Probing the acceleration of the cosmic expansion

Albert Einstein originally modeled the universe as being static. Since Edwin Hubble discovered his law in 1929, however, it is now a well-known fact that the universe is expanding. This manifests itself in the observation, that the more distant cosmic objects such as galaxies or quasars are, the higher their redshift, i.e. the faster they are rushing away from us. Hubble's law states a proportional relationship between distance and redshift, with a present expansion rate of about 70 km s^{-1} Mpc^{-1}. This insight has led to the standard model of cosmology, according to which the universe has been born in the big bang about 13.8 billion years ago.

The measurement of the expansion rate has been greatly improved by the use of supernovae of type Ia as standard candles. Since in their rest frame, they always follow the same temporal evolution and maximum of luminosity, observing their apparent brightness provides a good way to measure intergalactic distances [57]. This brought up the discovery, that at high redshifts, there are significant deviations from Hubble's law, leading to the conclusion, that the cosmic expansion is presently accelerating. This suggests the existence of a previously unknown, energy-like component of the universe (dark energy) driving the expansion of space. The most straight-forward explanation for this is the cosmological constant of general relativity Λ, that Einstein had first assigned a non-zero value to explain his static model of the universe, which he later rejected, but is now again seriously considered.

Meanwhile, the evidence for dark energy has been backed up by measurements of the cosmic microwave background. This is the thermal radiation of the early universe, emitted at the epoch of recombination about 380 000 years after the big bang. At that time, the plasma filling the universe had just cooled down low enough to transit into a gas of neutral atoms, transparent to radiation. By now, the cosmic expansion has redshifted this radiation field so strongly, that it presently appears at a temperature of only 2.7 K. Although being extremely isotropic, the satellite COBE and later the satellites WMAP and Planck have been able to reveal tiny temperature variations at a level of 30 µK, that correspond to slight density fluctuations in the matter distribution at the time of emission. They are caused by acoustic plasma waves, the so-called baryon acoustic oscillations (BAO). From the observed temperature map, the power spectrum of the BAO can be extracted, from which cosmological parameters can be derived [58]. This again confirms the existence of dark energy, and a nearly flat geometry of space. It also provides the currently best estimates for the contributions of dark energy (68 %), dark matter[2] (27 %) and baryonic matter[3] (5 %) to the total energy density of the universe.

The large-scale structure of the universe (the cosmic web), consisting of galaxy clusters with large voids between them, is the result of early density fluctuations by BAO. The known length scale of the BAO at the time of recombination qualifies them as a standard ruler to measure cosmic distances, completely independent of the concept relying on standard candles of type Ia supernovae. Using this method to measure distance versus redshift in large galaxy surveys again confirmed the above findings [59].

The above-described observations have shaped the current understanding of this subject. According to it, there was an earlier, matter-dominated period in the development of the universe, in which the cosmic expansion was decelerated by gravitational forces. Only in its rather recent history has the expansion started to accelerate, as the matter had been sufficiently diluted to allow the dark energy to become dominant [58]. However, in spite of the convincing evidence, the conclusion of a present acceleration of the cosmic expansion is still based on certain assumptions, such as a cosmological model. It would therefore be highly desirable to monitor the cosmic expansion rate directly, in real time. That is, a survey would measure the redshifts of distant objects now and at some time in the future. From the change in redshift, the cumulative acceleration along the line of sight to each object could be deduced. Hence, for objects at high redshifts, a net deceleration caused by the matter-dominated epoch would be observed. The method is thus able to directly probe the expansion history of the universe. This would provide a direct and model-independent way to test the validity of the current conception of cosmic dynamics. In particular, it is entirely independent of a specific theory of gravitation and does not require any assumptions on the geometry of space [60].

This redshift-drift experiment was originally proposed by Allan Sandage in 1962 [61]. At that time, however, Sandage had to conclude, that the feasibility of this observation was beyond reach. In 1998 Abraham Loeb proposed to take advantage of intergalactic hydrogen gas clouds for the observation, that imprint a forest of Lyman-α absorption lines on the spectra of quasars in their background [62]. The idea is depicted in Fig. 1.8. Unlike stars or galaxies, these clouds in the intergalactic medium are not strongly affected by rotation and exhibit no activity as present in stars. Effects from proper motion are also very likely to be negligible [60, 62]. The gas clouds along the line of sight to the quasar appear at a variety of redshifts, imprinting about 100 absorption lines as a part of the Lyman-α forest on the quasar spectrum. The weaker Lyman-β forest and metal absorption lines may be added to the consideration in order to increase the sensitivity towards redshift changes [60, 62].

---

[2] A kind of matter that is currently not well understood, and that interacts with light only gravitationally.

[3] This is the normal kind of matter, that for example makes up the stars and ourselves.

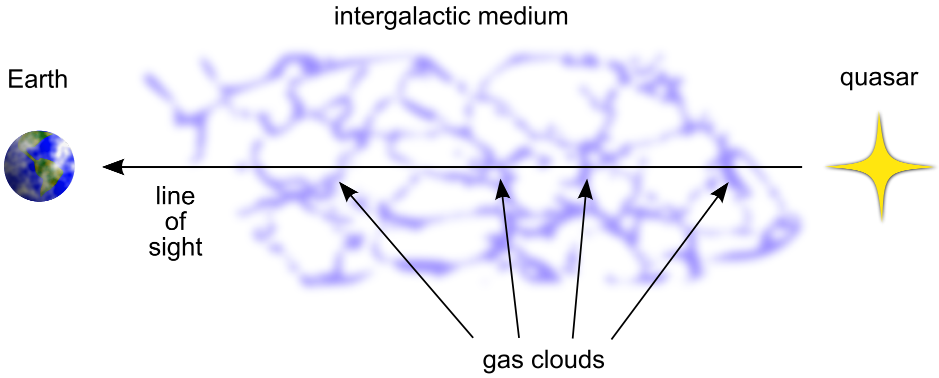

Figure 1.8 – Origin of Lyman-α forests in quasar spectra through intergalactic gas clouds. To a lesser extent, the gas clouds also contain metals, that are visible outside of the Lyman-α forest. These lines are used to search for a possible variability of the fine-structure constant (see Sec. 1.4.3).

10 years after Loeb's proposal, Liske et al. studied the feasibility of the experiment by future 40-m class telescopes [60]. One of these instruments is the planned European Extremely Large Telescope (E-ELT), ESO's current flagship project to be built in the Atacama desert in Chile [63]. The E-ELT will have a diameter of the primary mirror of 39 m, and an adaptive optics system for observations in the near-infrared. Among others, it was planned to be equipped with a fiber-fed, high-precision echelle spectrograph for visible wavelengths, named Cosmic Dynamics Experiment (CODEX). For cost reasons, however, it will probably be merged into one with the near-infrared spectrograph of the E-ELT [64].

Liske et al. came to the conclusion, that the experiment was possible and practicable with these instruments. This would require a redshift measurement of a wisely selected statistical sample of quasars, at two different epochs about two decades apart, and 4000 h of observation time. The best statistical significance would be attained at the highest redshifts, where a totaling deceleration would be observed, but the measurement would still provide the most direct evidence for an acceleration at present time. A prerequisite for this measurement, however, is that instrumental uncertainties are limited to about 1 cm/s, since the expected radial-velocity change would reach only about 6 cm/s per decade at its maximum. As discussed above, such a precise measurement would fail if the spectrograph was calibrated with traditional methods. Using a frequency comb for calibration, however, turns out to be ideal for this purpose. Not only does the frequency comb guarantee a calibration free of drifts due to its accurateness of frequency. Its absolute reference to the SI second also enables a comparison between different instruments. The results could be carried on for comparisons with future generations of instruments, in principle even over centuries.

1.4.3 Search for variability of fundamental constants

The variability of fundamental constants in time and space is an interesting theoretical possibility. At present, there is no hint why the physical constants take the numerical values they do. There is however a large variety of cosmological models that accommodate varying fundamental constants. In a model presented by John Barrow [65], for example, the fine-structure constant α changes with the cosmic expansion for a matter-dominated universe. As soon as the dark energy becomes dominant, however, and the expansion starts to accelerate, the variation of α ceases. So far, α is also the only fundamental constant with a potential observational evidence for variability. The idea of varying fundamental constants incorporates anthropic aspects, since life would not exist if they had significantly different values. α for example determines the strength of electromagnetic interaction, which e.g. dictates the behavior of atomic shells. A substantial change in α would therefore have direct impact on biochemistry and therefore on life itself [65]. Nuclear reactions would also be changed, since they depend on an interplay between nuclear forces and electrostatic repulsion among protons.

The most restrictive constraint on a linear temporal drift of α has been made by Rosenband et al. [7], by comparing two optical clocks by means of a frequency comb. They monitored the ratio of the transition frequencies of a Al^+ and a Hg^+ optical clock over one year, with a fractional uncertainty of 5×10^{-17}. The observed drift of α was consistent with zero within very tight boundaries:

$$\dot{\alpha}/\alpha = (-1.6 \pm 2.3) \times 10^{-17} \mathrm{yr}^{-1} \tag{1.4.1}$$

Another constraint on the variability of α comes from the Oklo phenomenon, a group of natural nuclear fission reactors that operated 1.8 billion years ago in Gabon, West Africa. The constraint can be deduced from the isotopic composition inside the reactor core. Especially for Samarium, the cross-section for thermal neutron capture is outstandingly sensitive to variations in α. Investigations on this matter have been carried out by a number of independent groups, usually with the result, that there is clearly no measurable variation in α [66–68]. The only exception is one case, where a statement on the constancy of α could not be given without ambiguity [69, 70]. As a representative for the Oklo results, we consider the value from [68] for the average rate of change in α over the past 1.8×10^9 years:

$$-4 \times 10^{-17} \mathrm{yr}^{-1} \leq \dot{\alpha}/\alpha \leq 3 \times 10^{-17} \mathrm{yr}^{-1} \tag{1.4.2}$$

These results do not rule out variations of α on cosmological time scales, which might not be linear as in Barrow's model. Nor do they rule out spatial variations of α. Further attempts to detect changes in α rely on abundances of elements produced in primordial nucleosythesis, or on anisotropies of the cosmic microwave background. So far, they yielded no distinct indications for an altered value of α in the early universe within a fractional uncertainty of about 0.7 % (see e.g. [71, 72]). A more accurate way to detect variations on cosmological scales is to conduct spectroscopic observations on metallic absorption lines in quasar spectra. The approach is quite similar to the one used for the detection of the accelerated cosmic expansion, depicted in Fig. 1.8. Again, the objects of consideration are intergalactic gas clouds that are in the foreground of a quasar, imprinting absorption lines on its spectrum at a variety of different redshifts. To detect a possible variation of α however, the region of interest is outside of the Lyman-α and -β forests. Initially, doublet lines from alkali metals were used, where the separation of the fine-structure components is proportional to α^2. The newer, refined version is the so-called many-multiplet method, which compares transitions of different multiplets and atoms, in order to be more sensitive to changes in α [73]. Using this technique, a group of researchers around Michael T. Murphy and John K. Webb have produced the first evidence for a variation in α, which was first understood as a temporal one [73]. They carried out further investigations [74–78] and saw their earlier finding grow in significance, finally obtaining [78]:

$$\Delta\alpha/\alpha = (-0.57 \pm 0.11) \times 10^{-5}\,, \tag{1.4.3}$$

which is the weighted mean over a look-back time between 3 and 12 billion years. Soon thereafter, comparable observations were conducted by another group [79, 80] at the VLT using the UVES spectrograph, with the result of $\Delta\alpha/\alpha = (-0.06 \pm 0.06) \times 10^{-5}$, clearly excluding Murphy et al.'s result represented by Eq. (1.4.3). This conclusion was confirmed by a separate group using the same instruments [81]. Murphy et al. published commentaries on these results [82], stating that their specified errors are impossibly low. In particular, they revealed flaws in the data analysis of Srianand et al. [79, 80], discrediting their results. Using the exact same data and line fits, Murphy et al. obtained a drastically different result, that was not in conflict with Eq. (1.4.3). Srianand published a reply [83], partly admitting some of the criticisms, but disagreeing on the conclusion, that their findings needed a revision.

Murphy et al. proceeded to extend their research, combining the Keck/HIRES (located on the northern hemisphere) with results obtained on VLT/UVES (on the southern hemisphere) [84, 85]. Because of the different locations of the two sets of instruments, they can probe different areas on the sky. Using VLT/UVES, they also found a significant change in α, but of opposite sign compared to Keck/HIRES. In their data, they could clearly identify a spatial dipole in α. The VLT/UVES data and the Keck/HIRES data independently agreed in the direction of the dipole moment. Thus, their observed variation of the fine-structure constant, that was originally seen as a temporal variation, is now interpreted as a spatial one.

Although the authors have rigorously searched for systematic errors [76], their results are still discussed critically [78], and they still do not exclude, that the results might be due to some unidentified systematic error. A potential source of error, that could not ultimately be ruled out, is the spectrograph calibration. Since the highly redshifted spectra are compared to laboratory wavelengths to infer a variation in α, an absolute calibration is required, i.e. the calibration must not only be repeatable, but also accurate. UVES and HIRES are slit spectrographs (not fiber coupled), that were calibrated with ThAr-lamps before and after each quasar observation. According to Murphy et al., the thorium wavelengths are known to sufficient accuracy to serve their purposes. As they pointed out, however, misidentification of lines could lead to high-order distortions of the wavelength calibration, emulating a non-zero $\Delta\alpha$ [76]. More recent studies have further revealed systematic distortions in the calibration of these spectrographs, that if unrecognized can have a similar effect [86]. In fact, discontinuities in the pixel-to-wavelength relation of up to 60 m/s have been identified with the astro-comb on the HARPS spectrograph (see Chapter 6 and [26]). These discontinuities were previously unknown owing to the insufficiently accurate calibration with ThAr lamps. Thus, for the astronomical search for a variability in α, the astro-comb is clearly the calibration method of choice. The absolute nature of its frequencies would greatly facilitate the comparison of lines from cosmic sources to laboratory wavelengths. It would also vastly enhance the comparability of results from different observatories, which is essential because of the assumed spatial dipole of $\Delta\alpha$. With the astro-comb, the spectrograph's instrumental line profile could also be characterized more thoroughly, which is another essential ingredient for the analysis. The astro-comb is thus expected to significantly reduce instrumental uncertainties in these measurements. It could then be used to either confirm and more closely characterize the variability of α as found by Murphy et al., or to place tighter constraints on a potential cosmological variability of α.

Chapter 2

The ytterbium fiber-based astronomical frequency comb

This chapter describes the overall setup of the astro-comb as used in this work. It must be kept in mind, however, that there are numerous alternative ways to construct an astro-comb, many of which are quite different from the one described here. Comparisons to competing astro-combs are made where appropriate, and the concluding chapter of this thesis (Chapter 8) reviews some promising concepts for future astro-combs.

It should equally be noted, that during the course of this work, a number of variations of the astro-comb have been used, differing in details of the implementation. This is partly because the setup has continuously been refined, and partly because the astro-comb needs to be adapted to the spectrograph it is designed for. The description presented here focuses on the most advanced version used in this work, but mentions details of earlier versions, wherever it is deemed to be useful. Also, this chapter concentrates on the astro-comb developed for the HARPS spectrograph. Chapter 7 will briefly describe a version for the VTT spectrograph, that was used for that chapter.

The development of the system was first carried out at the MPQ, but was later relocated to Menlo Systems. There, the scientific crew was backed up by engineers, who took care of the user friendliness and robustness of the system. The aim has been to permanently install a turn-key astro-comb on HARPS, that is available to all observers on the site, irrespective of their background or understanding of the system. This requires maintenance-free and fail-safe operation over long periods of time. It also demands well though-out automation features and software, to enable easy operation for non-experts, who control the system from a remote site. The installation is going to take place in April 2015. Soon thereafter will the astro-comb become available to the broad astronomical community within the routine observation schedule of HARPS, and support exoplanet searches.

2.1 Overview

Our approach to realizing a robust frequency comb for astronomy is to make extensive use of fiber-laser technology, and to avoid free-space optics wherever possible. Contrary to other laser systems such as Ti:sapphire frequency combs, fully alignment-free lasers and optical systems can be created from single-mode, polarization-maintaining fiber components. Such systems are also much more compact and robust than their free-space counterparts. Currently, an Er-fiber frequency comb is being prepared for a space flight on a rocket [87], which highlights the remarkable compactness and resilience of such systems. However, fiber lasers typically operate in the near-infrared, while most astronomical spectrographs are geared towards the

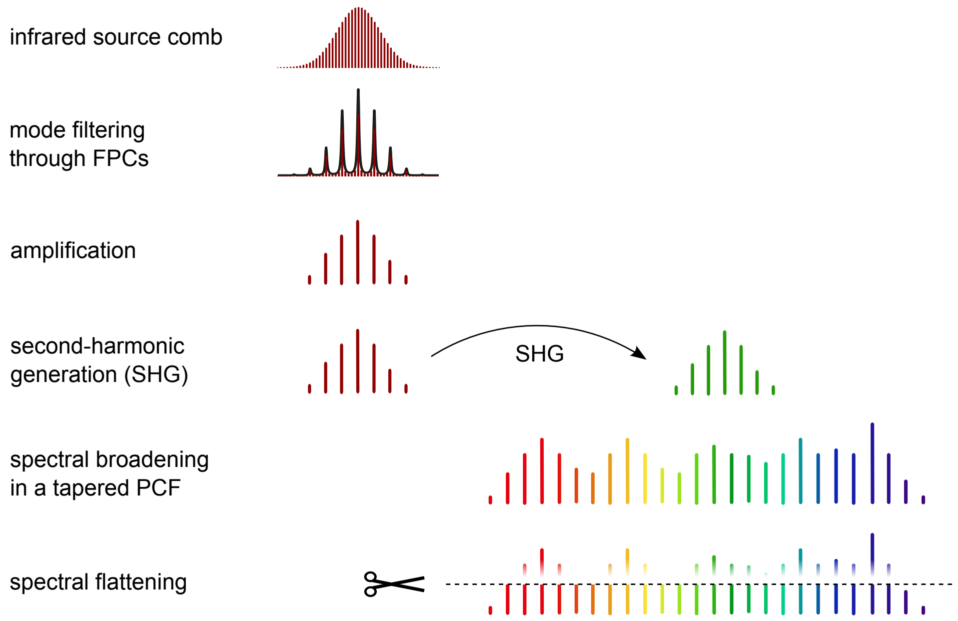

Figure 2.1 – Concept for the generation of an astro-comb as pursued in this work: An initially infrared and densely spaced frequency comb is filtered with Fabry-Pérot cavities (FPCs) to increase its mode spacing. The filtered comb is then amplified, frequency-doubled and subsequently spectrally broadened in a tapered photonic crystal fiber (PCF). The remaining structure of the spectral envelope is flattened out with a low-resolution, adaptive spectral filter.

visible spectral region. We therefore employ Yb-fiber laser technology [88], which operates at about 1040 nm, with the second harmonic near the center of the visible spectral range. The latter can be covered from there by spectral broadening.

Enabling extremely high quantum efficiencies (up to $\gtrsim 70$ %), the use of fiber laser technology also facilitates the construction of high-power amplifiers. Unlike many other lasers, the gain material of a fiber laser usually does not need to be actively cooled, because of its extremely high ratio of surface to volume that enables easy and efficient heat extraction. Particularly for Yb, the pump wavelength (around 975 nm) is extremely close to the operating wavelength (about 1040 nm), giving rise to low quantum defect heating and very efficient operation.

However, obtaining the typically required mode spacings of > 10 GHz directly from a mode-locked fiber laser is currently not practicable. Although fiber lasers with mode spacings of $10-20$ GHz have already been demonstrated [89,90], constructing a self-referenced and phase-stabilized fiber frequency comb with such large mode spacings is problematic, and remains to be shown. A self-referenceable Ti:sapphire frequency comb based on free-space optics has been demonstrated with a 10 GHz mode spacing [91]. Yet, these lasers are not in a state where they could operate autonomously for an extended period of time. Fiber lasers are thus preferred for their reliability, even if featuring lower mode spacings.

For these reasons, our system starts with a state-of-the-art 250 MHz Yb-fiber frequency comb as a source comb, and widens the mode spacing by suppressing unwanted modes, using Fabry-Pérot cavities (FPCs) as a mode filter. The comb is then transferred to the spectral region of interest by nonlinear frequency conversion. Figure 2.1 illustrates our overall concept for synthesizing the comb light for spectrograph calibration.

The unwanted comb modes are greatly reduced in power by the FPCs, but are still weakly contained in the comb spectrum after mode filtering. In literature on astro-combs, these

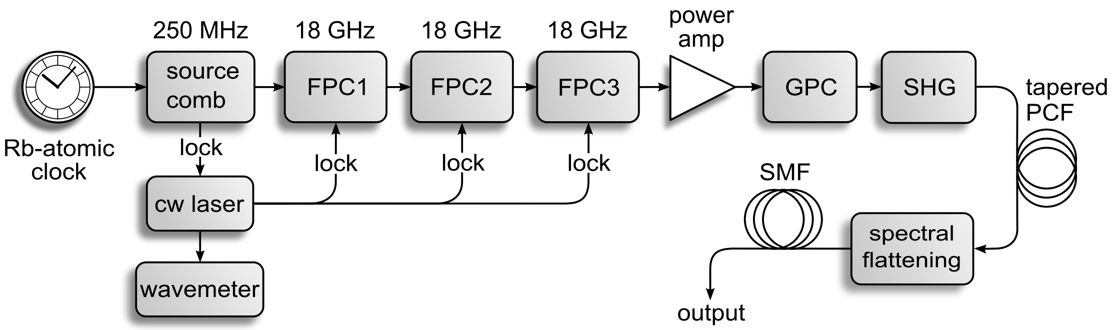

Figure 2.2 – Overview of the astro-comb system. FPC: Fabry-Pérot cavity. Cw laser: Continuous-wave fiber laser. GPC: Combined grating and prism compressor. SHG: Second-harmonic generation. PCF: Photonic crystal fiber. SMF: Single-mode fiber.

modes are commonly referred to as side-modes [29–31,33,92–94]. This expression is also used throughout this work. Conversely, the comb modes that are sought to be transmitted through the FPCs, are referred to as principal modes.

The HARPS spectrograph has a resolution of $R = 115\,000$ and a wavelength coverage of 310 nm, ranging from 380 to 690 nm [20]. The full-width at half-maximum (FWHM) of an optical resolution element is of 5 GHz at its center wavelength. The optimum mode spacing of the astro-comb is three times this value [3]. However, for HARPS an even larger spacing of 18 GHz has been chosen, such that the comb lines are completely separated on the CCD with virtually no residual overlap. This facilitates analysis of comb-calibrated HARPS data, and makes no substantial sacrifice on calibration accuracy. Figure 2.2 shows the configuration of the HARPS astro-comb. The 250 MHz source comb is referenced to a Rb-atomic clock[1]. The mode spacing is increased to 18 GHz by three identical FPCs, all with a finesse of about 2000, to provide excellent suppression of side-modes. The free spectral range (FSR) of the FPCs is stabilized by a continuous-wave (cw) fiber laser, that itself is locked to coincide with a principal comb mode. The frequency of the cw laser is measured by a wavemeter (WS/7, HighFinesse GmbH). This measurement reveals which subset of modes of the source comb is transmitted through the FPCs as principal modes.

The filtered comb is amplified to up to 15 W of optical power in a high-power fiber amplifier. The optical pulses at the output of the amplifier are compressed to a duration of about 130 fs, and are then frequency-doubled. The resulting spectrum, which is centered in the green, is then broadened in a tapered photonic crystal fiber (PCF). The broadened spectrum covers up to more than 230 nm, but its spectral envelope is strongly structured. The final step is therefore to flatten out the spectral structure by a programmable, low resolution spectral filter. The final output of the system is delivered in a single-mode fiber, providing the best possible beam quality.

The fiber-based parts of the astro-comb rely almost exclusively on polarization-maintaining single-mode fibers. The whole system is remotely controlled via a sophisticated software interface, that has been carefully designed to meet the needs of astronomers. The most remarkable feature of the software is an automation function that upon a single mouse click automatically starts up the complete system from any initial state. This goes from mode-locking and phase-stabilizing the source comb, to locking the cw laser and the FPCs to the correct resonances, and optimizing the coupling into the tapered PCF. Figure 2.3 shows photos of the finished astro-comb system.

---

[1] Model: PRS10, Stanford Research Systems, Inc.. Other RF-references can readily be connected.

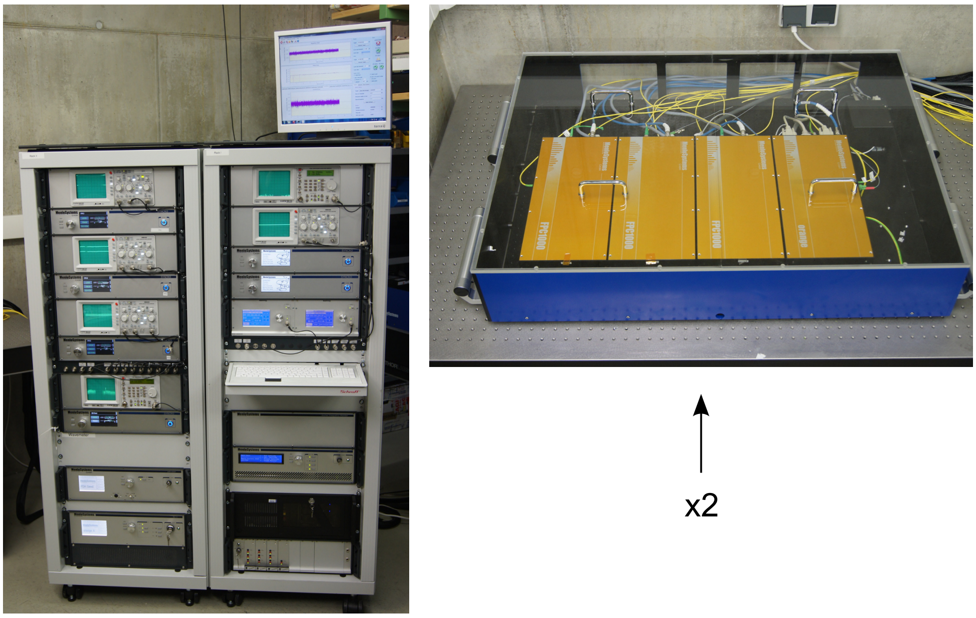

Figure 2.3 – Photographs of the astro-comb for the HARPS spectrograph (photos taken by T. Steinmetz). The two racks in the image on the left contain the electronics, pump diode lasers for the power amplifier, and the cw laser. The image on the right shows an enclosure of the optical system. The complete optics of the astro-comb are located inside of two enclosures of identical format (only one of them is shown), connected via optical fiber. The optical subunits are located in the orange, about shoe box-sized boxes.

It should be noted, that the astro-comb has to fulfill conflicting requirements: It needs to operate at an extremely high repetition rate of 18 GHz, and still be able to drive the two nonlinear steps of SHG and spectral broadening. At such high repetition rates, however, the average optical power is distributed among a large number of optical pulses per unit of time, leaving very little energy to each pulse for driving the nonlinearities. We solve this problem by employing a high-power fiber amplifier to obtain an average power as high as possible, and by using specially developed tapered PCFs, that are able to provide good spectral broadening even at very modest peak powers.

A competing group at the MIT has circumvented this conflict in their Ti:sapphire-based astro-comb by placing the increase of the repetition rate by the mode filter after the spectral broadening [36, 95]. This however introduces another conflict: For obtaining a good side-mode suppression, FPCs with a high finesse are are required. As explained later in this chapter, intra-cavity dispersion limits the spectral bandwidth that can be transmitted through the FPC, particularly for high finesse. The requirement of a good side-mode suppression is thus in conflict with a broadband astro-comb output. The MIT group has thus resorted to low-finesse cavities ($F \approx 100$), of which two are concatenated. Intra-cavity dispersion is minimized by employing complementary pairs of chirped cavity mirrors [96]. This results in a >40 dB side-mode suppression, enabling a calibration to better than 10 cm/s [36, 95].

A group from the NIST has developed an astro-comb that is quite similar to ours. It functions analogously, but employs Er-fiber technology at 1550 nm. SHG is omitted in that system, and the filtered IR comb is directly broadened in a highly nonlinear fiber to provide a broadband astro-comb for applications in the IR [30, 31].

In our astro-comb, the SHG is already driven quite inefficiently (conversion efficiency $\sim 4\,\%$) because of the high repetition rate, leaving little power for spectral broadening. Placing the

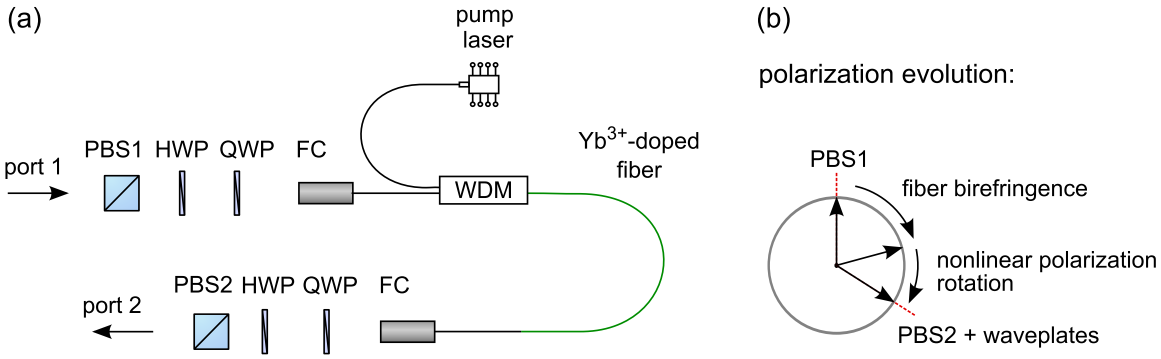

Figure 2.4 – Mode-locking by nonlinear polarization evolution. (a) Part of the laser beam path that favors ultrashort pulses. The laser as a whole uses a ring resonator, so a part of the light from port 2 is fed back to port 1. PBS: Polarizing beam splitter. HWP: Half-wave plate. QWP: Quater-wave plate. FC: Fiber collimator. WDM: Wavelength division multiplexer. (b) Polarization evolution. The gain fiber modifies the polarization through its weakly birefringent core. Ultrashort pulses alter this birefringence through the nonlinear response of the refractive index tensor. The waveplates are adjusted such that the light is only fully transmitted through PBS2 with this nonlinearity.

mode filter, that increases the repetition rate, after the SHG would however hardly be an option. This is because the mode filtering introduces substantial power losses due to rejection of modes and insertion losses on a number of components. Being outside of the Yb-gain spectrum after SHG, the losses could not be compensated anymore by the employed Yb-fiber technology, leaving even less power for spectral broadening.

The rest of this chapter describes in detail the subsystems of the astro-comb. Research on physical mechanisms inside the tapered PCF is presented in later chapters (Chapters 3 and 4). The spectral flattening unit is only covered in Chapter 5, since it has first been developed and demonstrated within the course of this work, and is hence worth being considered separately.

2.2 The source comb

The source comb, as the initial near-IR frequency comb from which the astro-comb is synthesized, is a 250 MHz Yb-fiber frequency comb. It consists of two major parts: The oscillator and the f:$2f$-interferometer. The oscillator is a mode-locked fiber laser, that emits the femtosecond pulse train that in the frequency domain forms the source comb. A part of this pulse train is sent into the f:$2f$-interferometer, that measures the offset frequency and repetition rate of the comb. The other part is passed on to the FPC filter chain.

For the right choice of the oscillator design, stability and low maintenance are the highest priorities. The HARPS astro-comb has long relied on nonlinear polarization evolution (NPE) as a mode-locking mechanism. The principle of this mode-locking scheme is illustrated and explained in Fig. 2.4. An in-depth description of this type of oscillator is given in [25]. Most of the results in this work have been obtained with an NPE oscillator. Even though this provided a robust mode-lock over many months, it could not be guaranteed that the mode-lock would be kept up for years without readjusting the polarization optics inside the laser. Similarly, as detailed below, the f:$2f$-interferometer could generate signals of sufficient quality to enable a stable phase-lock of the offset frequency, but the lock could occasionally fail, requiring manual intervention.

The solution for us was to switch to figure-9 oscillators, that had been newly developed

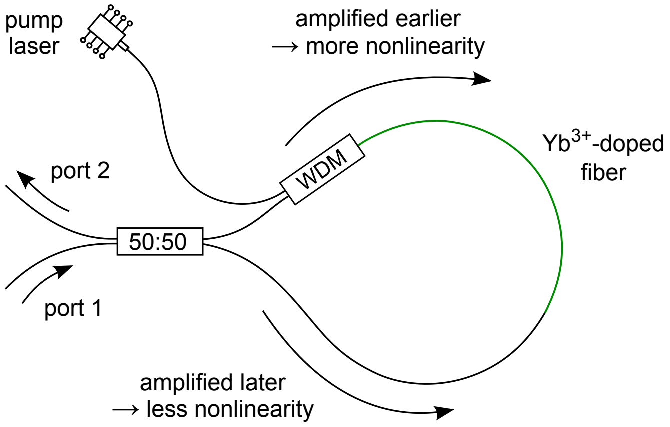

Figure 2.5 – Nonlinear amplifying loop mirror. The input beam is split by a 50:50 fused fiber coupler. The two parts traverse the loop in opposite directions. One part is amplified earlier than the other one, and can thus accumulate a greater nonlinear phase shift along the fiber loop. When interfering on the fiber coupler after traversing the loop, the light from port 1 is fully transferred to port 2 only for certain nonlinear phase shifts. Cw light would be directed backward to port 1, where it is blocked by an optical isolator (not shown). In a figure-9 oscillator, the fiber-loop design is more complex than shown here, but shares the same basic principle.

by Menlo Systems. This is a modified figure-8 laser that employs polarization-maintaining fibers. It mode-locks by virtue of a nonlinear amplifying loop mirror [97], whose principle is illustrated and explained in Fig. 2.5. As an interferometric mode-locking mechanism, this imposes a much more well-defined oscillation regime, resulting in a considerably more stable and noise-free operation. In fact, we have never seen one of these oscillators spontaneously lose its mode-lock.

Figures 2.4 and 2.5 are reduced to the parts of the oscillator that enable mode-locking. Additionally, the oscillators also incorporate an intra-cavity grating compressor for dispersion compensation. A polarizing beam splitter (PBS) functions as an output coupler that splits off the oscillator output from the intra-cavity beam. An optical isolator is placed after the output, to protect the oscillator from external back-reflections. To permit phase stabilization of the generated comb, the oscillators incorporate a piezo-mounted mirror that adjusts the cavity length for control of the repetition rate. The offset frequency is adjusted via the pump current, for fast control. Slow drifts of the offset frequency are compensated with a motorized intra-cavity glass wedge.

The offset frequency of the oscillator is monitored by means of a Mach-Zehnder-type f:$2f$-interferometer as shown in Fig 2.6. It amplifies the light from the oscillator in a core-pumped fiber amplifier, and then compresses it to pulse durations of about 100 fs with a grating compressor. It then generates an octave-spanning spectrum in a PCF. The beam paths of the longer and shorter wavelengths are separated by a dichroic mirror in a Mach-Zehnder-like configuration. The longer wavelengths are frequency-doubled in a $KNbO_3$ crystal. The shorter wavelengths are retarded by a pair of glass wedges, to match their group delay to that of the second harmonic, before the two beams are recombined. A combination of a grating and an iris selects a spectral region of the overlapped beam, that is directed onto a photodiode. The photodiode detects a beat note, the so-called offset beat, whose frequency is equal in magnitude to the offset frequency.

The f:$2f$-interferometer as described above has been used to obtain many of the results presented in later chapters. Finally, however, it has been replaced by a commercial XPS 800

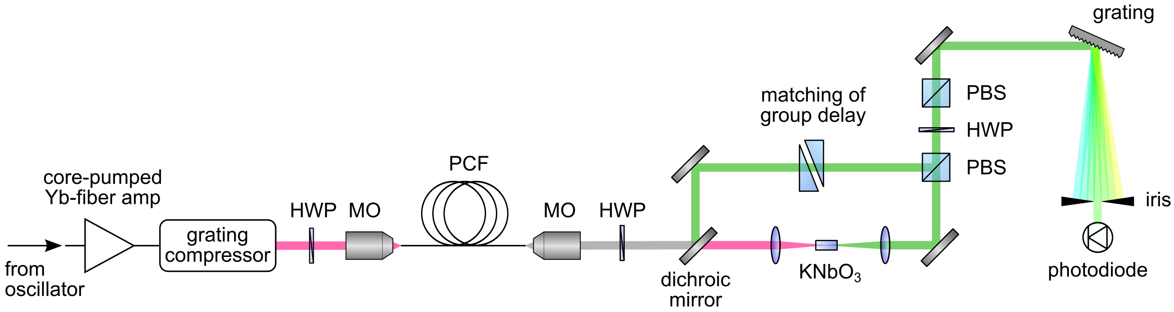

Figure 2.6 – f:$2f$-interferometer. After amplification and pulse compression in a grating compressor, the light from the oscillator is coupled into a photonic crystal fiber (PCF) through a microscope objective (MO), for generation of an octave-spanning spectrum. The longer wavelengths are frequency-doubled in a $KNbO_3$ crystal. The shorter wavelengths are retarded in a separate path to give them the same group delay as the frequency-doubled part, with which they interfere on the photodiode. A half-wave plate (HWP) between two polarizing beam splitters (PBS) projects the separate polarizations onto a common axis.

from Menlo Systems. It is conceptually very similar to the one in Fig. 2.6, but uses a somewhat different design. It is considerably more compact, but most importantly its beam path never needs to be realigned. It thus fulfills our need for autonomous long-term operation.

Figure 2.7 shows some results obtained with an NPE oscillator. The spectrum of the oscillator output is remarkably broad (Fig. 2.7(a)). Further down the beam path of the astro-comb, the spectral bandwidth is reduced considerably by gain narrowing of the power amplifier. This reduces the transform limit to about 100 fs, and also shifts the center wavelength to about 1060 nm. Figure 2.7(b) shows the offset beat that was obtained from this oscillator. The 32 dB signal-to-noise (S/N) ratio and 530 kHz FWHM of the offset beat, both measured at a resolution bandwidth (RBW) of 10 kHz, is about typical for this type of oscillator. However, S/N ratios of >35 dB have already been obtained with this type of oscillator at a 20 kHz RBW. NPE mode-locking thus offers S/N ratios of >30 dB as required for a stable phase lock, and the resulting comb has been shown to lock reliably over at least many hours [25]. Uninterrupted phase locking for weeks or months, however, can so far not be guaranteed.

An NPE oscillator with a fundamental repetition rate of 500 MHz has been built at Menlo Systems, modeled after [25]. The higher initial mode spacing facilitates mode filtering in the astro-comb setup. During tests, both its spectrum and its offset beat were found to resemble that of the 250 MHz version, and the comb could be phase-locked just as easily. It was however never used in the astro-comb. Instead, a 250 MHz figure-9 oscillator was integrated into the astro-comb. The figure-9 oscillator has so far not been produced in a 500 MHz version, but the slightly more tedious mode filtering is accepted in exchange for the long-term reliability of the figure-9 oscillator. Figure 2.8(a) shows its spectrum. Compared to the NPE oscillator, the spectrum is narrower, and centered at shorter wavelength. The power amplifier of the astro-comb reduces the bandwidth of this spectrum to a transform limit of about 120 fs, and shifts its center to about 1037 nm. Figure 2.8(b) shows the offset beat of this oscillator. Its extremely narrow-band and noise-free signal enables a very stable and reliable phase lock. Even better offset-beat signals with a >50 dB S/N ratio (at 20 kHz RBW) have already been observed with this type of oscillator.

The electronic configuration of the RF-phase lock is the same for both oscillators. The lock of the offset frequency and repetition rate is supported by two RF synthesizers, that convert the 10 MHz signal of the RF reference phase-coherently into a signal of arbitrary frequency.

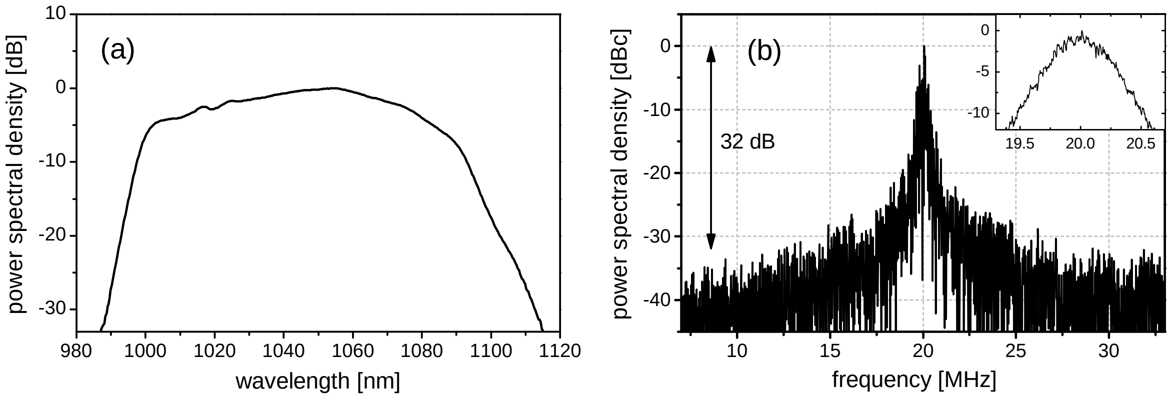

Figure 2.7 – Spectrum and offset beat of a nonlinear-polarization evolution (NPE) oscillator with a 250 MHz repetition rate. (a) Spectrum, measured at a resolution of 0.2 nm. Center wavelength: 1046 nm. Full-width at half-maximum (FWHM): 62 nm. Transform limit of pulse duration: 35 fs. (b) Offset beat obtained with this oscillator, locked at 20 MHz, and measured with an RF spectrum analyzer. Resolution bandwidth: 10 kHz. Signal-to-noise ratio: 32 dB. Inset: Close-up towards peak of the signal, averaged over 100 acquisitions. FWHM: 530 kHz.

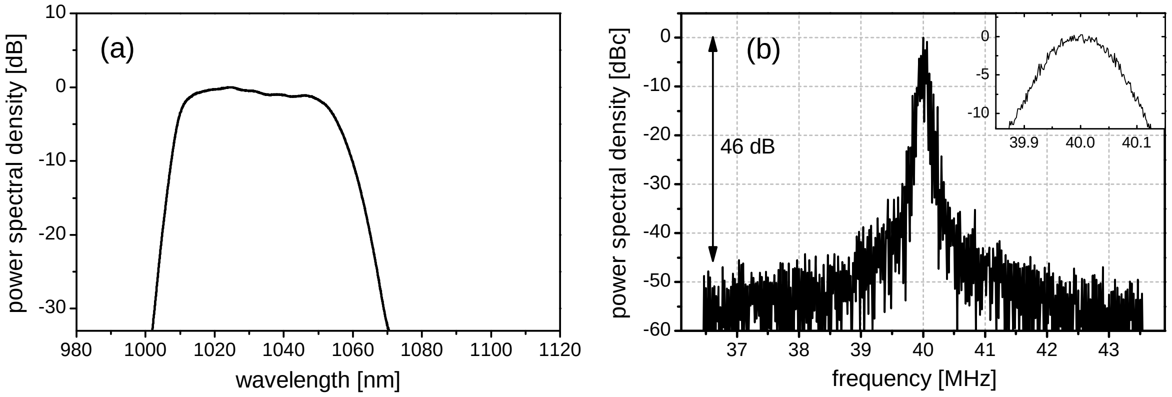

Figure 2.8 – Spectrum and offset beat of a 250 MHz figure-9 oscillator. (a) Spectrum, measured at a resolution of 0.1 nm. Center wavelength: 1032 nm. Full-width at half-maximum (FWHM): 43 nm. Transform limit of pulse duration: 60 fs. (b) Offset beat, locked at 40 MHz, and measured with an RF spectrum analyzer. Resolution bandwidth: 10 kHz. Signal-to-noise ratio: 46 dB. Inset: Close-up towards peak of the signal, averaged over 100 acquisitions. FWHM: 120 kHz.

The offset beat is locked directly to the signal of one of the two synthesizers using a digital phase detector and a proportional-integral (PI) controller, keeping the offset beat in phase with the signal of the synthesizer. This scheme allows direct and easy control of the offset frequency, by adjusting the frequency of the synthesizer as desired. It should be kept in mind, however, that the SHG within the astro-comb system (see Fig. 2.2) doubles the offset frequency of the mode-filtered comb. A change in the offset frequency of the source comb therefore comes out twice as large in the output of the astro-comb.

The lock of the repetition rate is a bit more intricate. The repetition rate is picked up with a photodiode, and the 4$^{\text{th}}$ harmonic of the repetition rate at 1 GHz and is converted down to 20 MHz by mixing it with a 980 MHz signal. This is then phase-locked to the 20 MHz signal of the corresponding synthesizer. This locking scheme implicates, that if the frequency of the synthesizer is changed by a certain amount, the change of the repetition rate of the source comb is only a fourth of this value. The mode filter of the HARPS astro-comb multiplies the repetition rate by a factor of 72. The change in the repetition rate of the astro-comb is thus 18 times the frequency change of the synthesizer.

While the repetition rate is always positive, the offset frequency of the source comb as phase-locked to the RF synthesizer can take both positive and negative values. The offset beat is usually monitored on an RF spectrum analyzer as in Figs. 2.7(b) and 2.8(b), but its center frequency only indicates the absolute value the offset frequency, as the RF spectrum analyzer cannot distinguish between positive and negative frequencies. The sign must therefore be determined in a dedicated procedure.

How to determine the sign of the offset frequency: The sign of the offset frequency is determined by regarding the beat note between the comb and the cw laser (cw beat) used for locking the FPCs. For this purpose, the cw laser is released from the lock to its nearby comb mode. The repetition rate of the source comb is then slightly increased, and the change of the cw beat frequency is observed on an RF spectrum analyzer. Next, the absolute value of the offset frequency is increased, and the change of the cw beat is again observed. If the cw beat moves into the same direction in both cases, then the offset beat is positive, otherwise it is negative. Afterwards, all locks are restored at their usual frequencies. An alternative method could make use of the wavemeter in Fig. 2.2 measuring the optical frequency of the cw laser, which coincides with one of the comb modes. This however requires the wavemeter to be sufficiently accurate.

2.3 Mode filtering

The initial frequency comb with a 250 MHz repetition rate is far too densely spaced to be resolved by common astronomical echelle spectrographs. Mode filtering through FPCs to widen the mode spacing is thus an essential part of the astro-comb. Before their technical implementation is treated, the following subsections give an overview of their working principle and some related difficulties (see also [25, 38]).

2.3.1 Theoretical description

An FPC is made of a pair of two opposed mirrors with radii of curvature r_1 and r_2 at a distance L (Fig. 2.9) . The condition for the formation of a stable optical cavity mode is $0 \leq g_1 g_2 \leq 1$, with $g_i = 1 - L/r_i$. A combination of two plane mirrors is hence at the border of the stability criterion, compromising the attainable cavity finesse. Therefore, at least one of the cavity mirrors is usually curved. For two mirrors of identical reflectivity R, the transmitted power P_T as a function of optical frequency f is given by [98]:

$$\frac{P_T}{P_0} = \frac{(1-R)^2}{(1-R)^2 + 4R\sin^2\left(\frac{\Delta\varphi}{2}\right)}\,, \qquad \Delta\varphi = \frac{4\pi L f}{c} n(f) + 2\varphi_m(f) + 2\varphi_{Gouy} \tag{2.3.1}$$

Here, P_0 is the optical power at the cavity input, and $\Delta\varphi$ is the total phase lag that the light experiences during a cavity round-trip. It consists of several components, with the first one describing the phase lag from propagation through the cavity filled with a medium (usually air) of refractive index $n(f)$. The second contribution arises from the dispersion of the mirror coatings as described by the wavelength dependent phase shift $\varphi_m(f)$. The last contribution is due to the Gouy phase shift φ_{Gouy}, that the beam experiences when passing through the beam waist between the two mirrors. It depends on the radius of curvature of the mirrors, and also differs for different spatial cavity modes. The cavity has a peak in transmission, when

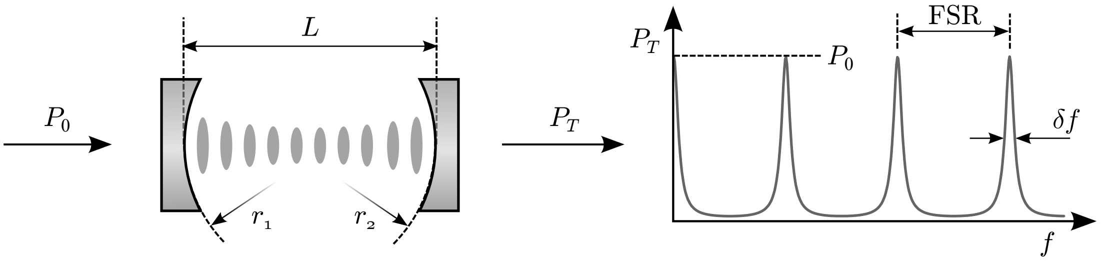

Figure 2.9 – Principle of a Fabry-Pérot filter cavity. Left-hand side: Two opposed mirrors with radii of curvature $r_1$and r_2 at a distance L form a spectral filter for the input light of optical power P_0. Right-hand side: Transmitted optical power P_T as a function of frequency f. The distance between two adjacent transmission peaks is the free spectral range (FSR). The full-width at half-maximum of a transmission peak is δf.

the resonance condition $\Delta\varphi = 2\pi q$ is fulfilled, where $q \geq 0$ is an integer number quoting the longitudinal cavity mode number. This occurs at frequencies $f_{q\,i\,j}$, where the integers $i, j \geq 0$ are the transverse mode numbers of the respective cavity mode [98]:

$$f_{q\,i\,j} = \frac{c}{2\,L\,n\,(f)} \left\{ q + \frac{\varphi_m\,(f)}{\pi} + \left[\frac{1+i+j}{\pi} \arccos\left(\pm\sqrt{g_1 g_2}\right) \right] \right\}, \tag{2.3.2}$$

with "+" applying for $g_1, g_2 \geq 0$, and "−" for $g_1, g_2 \leq 0$. The term in square brackets accounts for the Gouy phase. Unless stated differently, we assume that only the fundamental spatial cavity mode (TEM$_{00}$) is excited, i.e. $i = j = 0$. The frequency distance of adjacent resonances is the free spectral range (FSR) with FSR $\approx c/\left(2\,L\,n\right)$, neglecting the frequency dependence of n and φ_m over this range. The FWHM of a cavity transmission is denoted by δf. The ratio of the two is specified by the cavity finesse $F = \text{FSR}/\delta f$. It depends only on the mirror reflectivity R, foreseen that there are no other intra-cavity losses. For $R > 0.5$, the finesse is well approximated as $F \approx \pi\sqrt{R}/\left(1 - R\right)$.

For using an FPC as a mode filter to increase the mode spacing of a frequency comb, the FSR is chosen to be an integer multiple $m\,f_r$ of the initial mode spacing f_r. As a result, only every m^{th} mode is transmitted through the FPC, while the other ones are rejected. This multiplies the mode spacing by an integer factor m, which is referred to as the filter ratio. The situation is represented in the upper part of Fig. 2.10. After filtering, the suppressed modes are still weakly present in the comb structure as side-modes. Using Eq. (2.3.1), it can easily be shown, that the suppression factor ϱ of the strongest side-mode relative to its adjacent principal mode is approximately given by:

$$\varrho \approx \left(2F/m\right)^2 \tag{2.3.3}$$

Not only does the mode filtering suppress unwanted comb modes, but it also induces a shift of the spectral phase on either side of the FPC resonance. Consequently, the side-modes receive a different phase shift upon mode filtering than the principal modes (see lower part of Fig. 2.10). The shift of the spectral phase upon transmission through an FPC is given by:

$$\varphi\,(f) = \arctan\left(\frac{\sin\left(\Delta\varphi\right)}{\frac{1}{R} - \cos\left(\Delta\varphi\right)}\right) \tag{2.3.4}$$

In the application to spectrograph calibration, the side-modes are a source of uncertainty. The spectrograph generally has insufficient spectral resolution to resolve the side-modes from

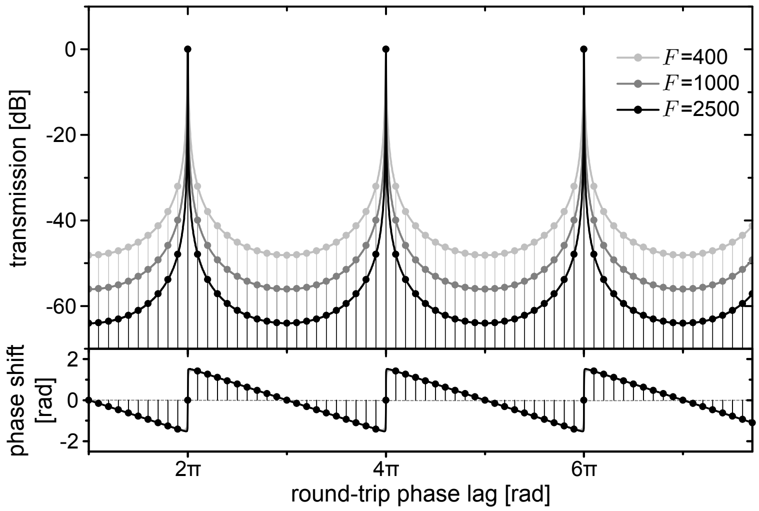

Figure 2.10 – Theoretical effect of a mode filter formed by a Fabry-Pérot cavity (FPC) on a transmitted frequency comb. The filter ratio is chosen to be $m = 20$. Results for three different values of the finesse F are shown. The filled circles with drop lines indicate the comb modes. Top: FPC transmission. Bottom: Phase shift upon FPC transmission (nearly identical for the three values of F).

the principal modes. Hence, the frequencies of the calibration lines as measured by the spectrograph approximately represent the center-of-gravity of groups of lines, each consisting of a principal mode and its surrounding side-modes. Asymmetric and insufficient suppression of side-modes can shift the line centroids by Δf in frequency. Usually, this shift is dominated by the strongest side-mode, separated by the initial mode spacing f_r from its adjacent principal mode. The worst-case centroid shift can then be estimated by assuming maximum side-mode asymmetry, i.e. inferring that this side-mode is only present on one side of the principal mode:

$$\Delta f \lesssim f_r/\varrho \tag{2.3.5}$$

As an example, we consider a frequency comb with an initial repetition rate of 250 MHz, filtered to 18 GHz ($m = 72$). Assuming a cavity finesse of $F = 2000$, a suppression factor ϱ of 3086 (or 35 dB) is obtained from Eq. (2.3.3). Equation (2.3.5) then indicates a calibration uncertainty of 81 kHz. However, as detailed in Chapter 4, the side-modes are massively amplified by the nonlinear processes of SHG and spectral broadening. Several concatenated FPCs are thus necessary to ensure sufficient side-mode suppression after side-mode amplification. The side-modes are generally not amplified symmetrically, due to the different phases of the side-modes on either side of a principal mode [92]. As in practice the total asymmetry is not precisely known, Eq. (2.3.5) assumes maximum asymmetry for the side-modes.

2.3.2 Potential pitfalls of mode filtering

Widening of the mode spacing through mode filtering is among the most intricate parts of the astro-comb system. For proper practical implementation, a number of aspects have to be considered, that are discussed in the following.

Cavity dispersion and offset

Both the mirror coatings and the intra-cavity air are dispersive. As a result, the optical path length of an FPC – and thus the FSR – is wavelength dependent. This limits the bandwidth

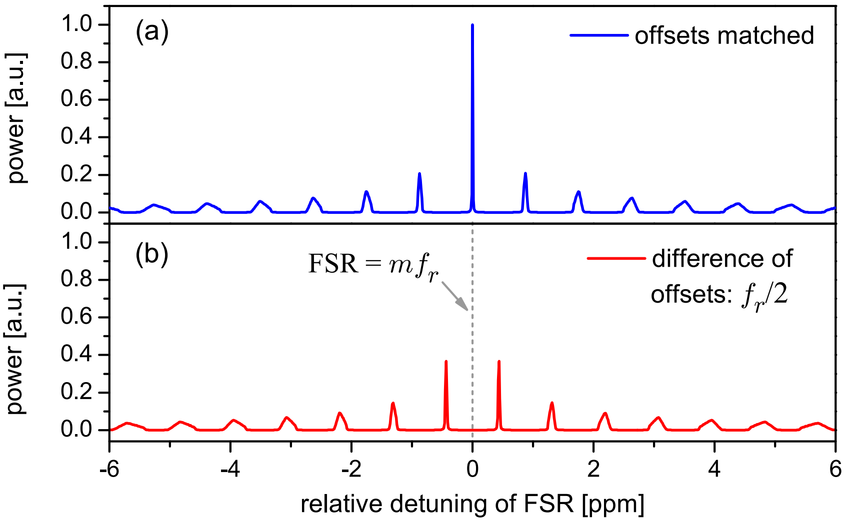

Figure 2.11 – Simulated scans of the length of a dispersion-free Fabry-Pérot cavity (FPC), for a finesse of 2500, a filter ratio of $m = 20$, and the input spectrum of Fig. 2.7. The vertical axis shows the optical power that is transmitted through the FPC. The horizontal axis shows the fractional detuning of the free spectral range (FSR) of the FPC from the condition FSR $= m\, f_r$ in parts per million. f_r refers to the repetition rate of the comb before filtering. (a) Cavity scan with the comb offset frequency matched to the FPC offset. (b) Cavity scan for a difference of $f_r/2$ of the two offsets.

over which the FPC resonances can coincide with comb modes. Ultimately, this means that cavity dispersion limits the possible transmission bandwidth of the comb spectrum through the FPC.

Both FPC dispersion, and the Gouy-phase shift within the FPC, cause the FPC transmissions to be shifted by a certain amount, as can be seen from Eq. (2.3.2) for $q = 0$. In analogy to the offset frequency of a frequency comb, we call this the FPC offset. This offset can be understood as the effect of a carrier-envelope phase shift of the optical pulses within the cavity that occurs on each round trip. This is analogous to the case of the offset frequency of a frequency comb, see Eq. (1.1.5).

The offset frequency of the comb needs to be matched to the FPC offset, in order to enable the transmission of a maximum bandwidth through the FPC. If this is not the case, the comb can only be transmitted over a limited bandwidth, by detuning the FSR of the FPC from the condition FSR $= m\, f_r$. This can be seen in Fig 2.11, where simulated scans of the FPC length are shown for matched and for mismatched offsets. In this simulation, the transmitted power can be used as a measure of the bandwidth transmitted through the FPC. Full transmission is only seen for matched offsets (Fig 2.11(a)) at FSR $= m\, f_r$. On either side of this central peak, we can see a lower peak that corresponds to transmission of a different subset of comb modes. The severity of the effects from a mismatched offset increase with the FPC finesse, and with the desired bandwidth of the filtered comb, and decrease with increasing filter ratio m. Due to intra-cavity dispersion, the FPC offset is also subject to a wavelength dependence, further limiting the attainable bandwidth.

The fixed FPC offset is the main reason, why the offset frequency of the astro-comb in this work cannot easily be tuned over a very wide range. If the astro-comb lines need to be tuned to reach different pixels on a spectrograph CCD, it is thus preferable to tune the repetition rate, which allows shifting the comb lines by a much larger amount.

Due to the contribution of the intra-cavity air, the FPC offset depends on air pressure.

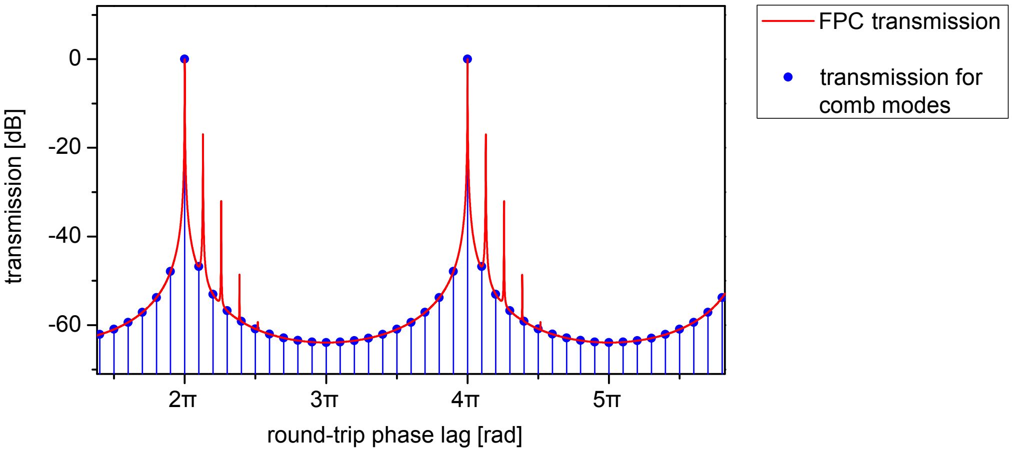

Figure 2.12 – Simulated effect of higher-order spatial modes (HOMs) on Fabry-Pérot cavity (FPC) transmission. The overlap of the optical mode at the FPC input with the HOMs is assumed to decline exponentially with the sum of the transverse mode numbers i and j, and to have a 2.5 % overlap for $i+j=1$ relative to $i+j=0$. The mirror curvature was assumed to be chosen such that the transmission peaks of the HOMs are located between the side-modes, minimizing the effect on side-mode suppression.

This is an important aspect, because astro-combs are usually assembled in laboratories not very far above sea level, and are then transported to observatories located on mountain tops. The changed altitude may require a different locking point of the comb offset frequency to keep it matched to the FPC offset.

The FPC offset depends on the mirror coatings, intra-cavity dispersion, and the radii of curvature of the cavity mirrors. Due to the prefactor outside of the curly brackets in Eq. (2.3.2), which approximately equals the FSR, the contributions of the Gouy-phase and mirror coatings to the FPC offset scale with the FSR. This can also be understood through the analogy to the offset frequency of a frequency comb, see Eq. (1.1.5). As a consequence, FPCs with different FSRs can have different offsets, even if constructed from the same mirrors. This can be compensated by choosing different mirror curvatures for different FSRs, which however is difficult since the contribution of the mirror coatings is uncertain due to manufacturing tolerances.

Earlier versions of the astro-comb have used a chain of FPCs with different FSRs for mode filtering. This has the benefit of enabling a lower filter ratio on each FPC, but has the downside of a possible mismatch of the different FPC offsets. Newer versions of the astro-comb therefore employ a chain of identical FPCs.

Higher order spatial modes

According to Eq. (2.3.2), the resonance frequencies of an FPC are usually different for different spatial modes. The FPC injection is normally optimized towards $i=j=0$, but higher-order spatial modes (HOMs), i.e. $i+j>0$, are generally also excited to some degree. Depending on how strongly the HOMs are excited, they add to the spectral transmission of the FPC. The red line in Fig. 2.12 shows an example of how the transmission function of an FPC might look like, if altered by HOMs. It can clearly be seen, that their effect is asymmetric about the fundamental transmission, because the resonances of the HOMs are always shifted towards higher frequencies for the same transverse mode number q. The frequency shift depends on the radii of curvature of the FPC mirrors. This can be exploited to position their frequencies in

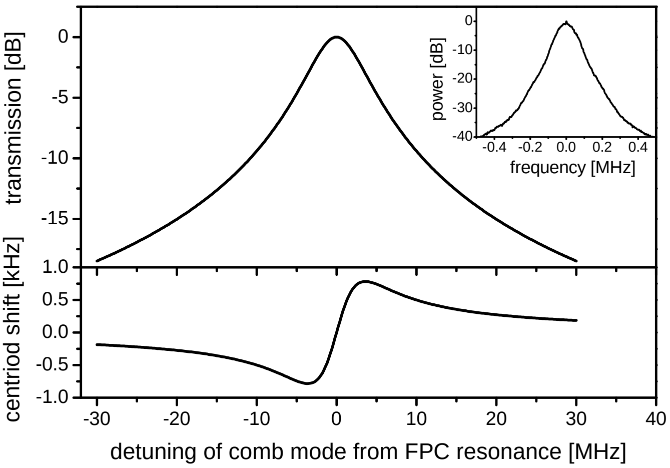

Figure 2.13 – Effects of Fabry-Pérot cavity (FPC) transmission on a comb mode, computed for a finesse of 2500 and free spectral range of 18 GHz. Top: Total transmission of the mode. Bottom: Centroid shift of the mode caused by skewing of its shape. The inset shows the mode profile that was assumed for the simulation (full-width at half-maximum: 79 kHz). It has been obtained from a beat between a 250 MHz figure-9 frequency comb and a single-frequency cw fiber laser.

between the side-modes as in Fig. 2.12, in order to mitigate the negative effects on side-mode suppression. This becomes increasingly difficult with higher filter ratio m. But still, a direct coincidence of a low-order HOM with a side-mode should be avoided at all cost.

Another way to mitigate the effect of the HOMs is to maximize the mode-matching of the cavity injection to the fundamental cavity mode. This automatically reduces the matching to the HOMs, since the cavity modes are mathematically orthogonal. The output of the FPC is normally coupled into a single-mode fiber. If the fiber coupling is properly matched to the fundamental cavity mode, it should act as a spatial mode filter, having a low coupling efficiently for HOMs. Excellent optical alignment of the FPC subunits is therefore a vital factor for the astro-comb as a whole.

Off-resonant cavity transmission

In the center of the IR comb spectrum, the stabilization of the FSR of the FPCs should keep the principal comb modes accurately centered at the FPC resonances. On short time scales, however, the FPC lock can be disturbed, e.g. by acoustic noise. Inaccurate locking can also occur permanently due to maladjusted lock electronics. At the borders of the spectrum, principal comb modes can also be off-resonant due intra-cavity dispersion.

If a principal comb mode is located on the slope of the FPC filter function rather than on its center, this has a twofold effect: Firstly, the transmission of the principal mode is reduced, and secondly, its shape is distorted, which shifts its centroid [25,29]. To quantify the wost-case centroid shift, the initial profile of the comb modes must be known. This can be obtained from the beat between the source comb and the cw laser that is integrated in the astro-comb. Beating a figure-9 oscillator with a Koheras single-frequency fiber laser (line width < 35 kHz), we measure a beat note with a 79 kHz FWHM, which we use as a conservative estimate for the profile of the comb modes. The simulation in Fig. 2.13 shows, that an FPC at an 18 GHz FSR and a finesse of 2500 can shift the centroid of this line by up to 0.8 kHz. The shift is approximately proportional to the derivative of the filter function with respect to the optical frequency, with the maximum shift occurring for an attenuation of 3 dB. Further

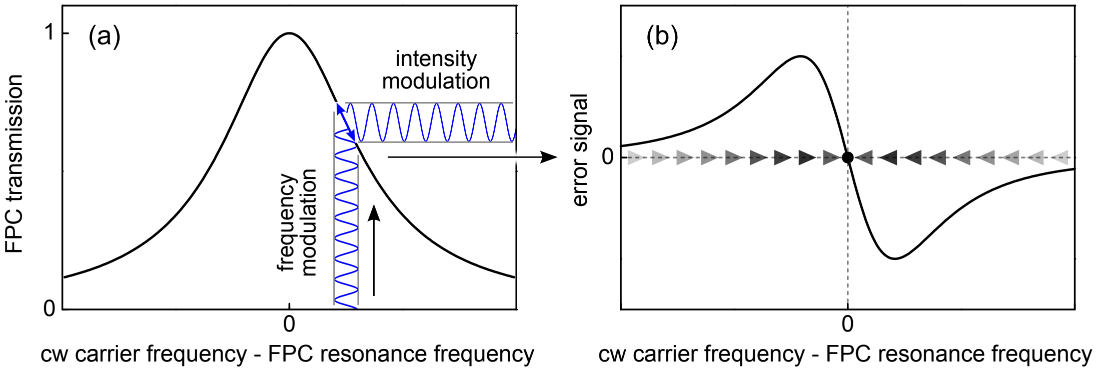

Figure 2.14 – Principle of the Pound-Drever-Hall lock. (a) The black line indicates the transmission function of a Fabry-Pérot cavity (FPC). The resonance frequency of the FPC is to be locked to the frequency of a continuous-wave (cw) laser. The cw laser is modulated in frequency (blue). This causes an intensity modulation after transmission through the FPC, that is proportional to the slope of the FPC filter function. (b) The amplitude of the intensity modulation is used as an error signal, that drives the difference between the cw carrier frequency and the FPC resonance frequency towards zero, as indicated by the triangles.

simulations reveal that the centroid shifts by concatenated FPCs are additive in very good approximation, and that subsequent SHG doubles the centroid shift. A chain of three such FPCs with subsequent SHG can thus shift the centroid by up to 4.8 kHz (about 0.3 cm/s).

The effect is more pronounced with an NPE oscillator, owing to its broader lines. The beat note with the cw laser had a 160 kHz FWHM, resulting in a 15 kHz (0.8 cm/s) maximum shift for 3 FPCs and subsequent SHG. Generally, the effect increases with increasing width of the comb modes, increasing finesse, and decreasing FSR.

A shift of the principal modes from resonance also reduces the suppression of the side-modes relative to the principal modes. The main reason for this is the reduction of the power of the principal modes: If for a finesse of 2500 and a filter ratio of $m = 72$, the principal mode is off resonance by 0.02 % of the FSR (or 3.6 MHz for FSR = 18 GHz), the power of the principal modes declines by 3 dB, but the side-modes only change by less than 0.13 dB. The worst-case effect can be limited by adjusting the trigger level of the interlock circuit of the astro-comb (see Sec. 2.4), which shuts down the astro-comb output almost immediately, if the FPC transmission drops too far. Additionally, intra-cavity dispersion of the FPCs should be minimized, and the offset frequency of the source comb should be well matched to the FPC offsets.

2.3.3 Technical implementation

For stabilization of the FSRs of the FPCs to the source comb, different locking schemes have been studied prior to this work [25]. The Pound-Drever-Hall lock has stood the test of time as the preferred scheme for FPC locking in the astro-comb. It uses an auxiliary cw laser, that itself is locked to a comb mode. The cw laser is given a sinusoidal phase modulation, which implies a frequency modulation with a 90° phase shift relative to the phase modulation. The frequency modulation results in an amplitude modulation upon transmission of the cw laser through the FPC (see Fig. 2.14(a)), that is detected with a photodiode. The difference frequency of this signal with the RF signal of the original phase modulation is generated in an RF mixer. This yields a DC voltage proportional to the amplitude of the intensity modulation. For a sufficiently low modulation amplitude, this demodulated signal is also proportional to

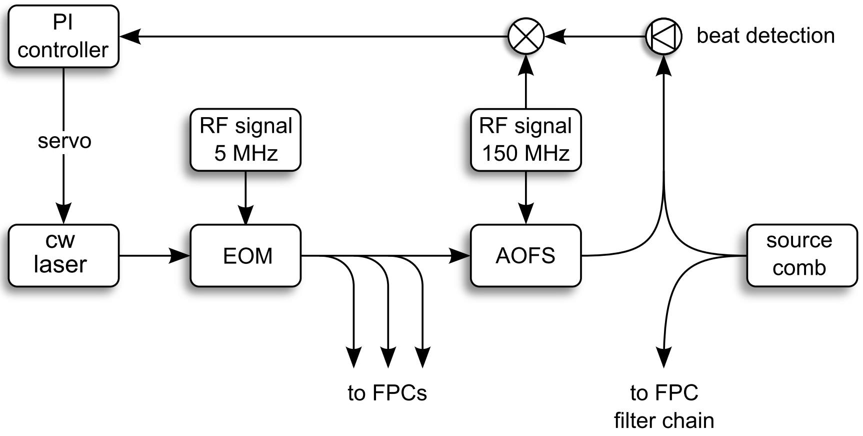

Figure 2.15 – Locking scheme of the continuous-wave (cw) laser to a comb mode. The cw laser (single-frequency fiber laser) receives a 5 MHz phase modulation by an electro-optic modulator (EOM) to support the stabilization of the Fabry-Pérot cavities (FPCs). Since locking at a frequency of zero is challenging, the cw laser experiences a 150 MHz frequency shift by an acousto-optic frequency shifter (AOFS) before detection of the beat with the comb. The beat is then phase-locked to the frequency by which the cw laser has been shifted. Optical signals are split off or combined using fused fiber couplers.

the slope of the FPC transmission function at the optical carrier frequency of the cw laser. It is of opposite sign on the two sides of the FPC resonance, and vanishes at its center. It can thus be used as an error signal for a feedback loop that controls the cavity length (see Fig. 2.14(b)).

A part of the spectrum that is sent through the FPCs is later absorbed in the gain fiber of the power amplifier of the astro-comb. The mode filter thus needs to be adapted to the spectrum as it is after the power amplifier, not as it is at the FPC input. This implies a center wavelength of about 1060 nm if an NPE oscillator is used (see Sec. 2.2), and a center wavelength of about 1040 nm if a figure-9 oscillator is used. The cw laser in our setup is a Koheras single-frequency fiber laser from NKT Photonics. To optimize the lock of the FPCs at the center of the amplified spectrum, a cw laser with a 1064 nm wavelength is chosen for use with an NPE oscillator, and a 1040 nm wavelength is chosen for a figure-9 oscillator. A 5 MHz phase modulation is imprinted on the cw laser by an electro-optic modulator (EOM), as indicated in Fig. 2.15. For locking of the cw laser to a comb mode, the frequency of the cw laser is shifted by 150 MHz using an acousto-optic frequency shifter (AOFS), before beating it with the source comb. The beat is then stabilized at 150 MHz by phase-locking it to the 150 MHz RF signal that drives the AOFS. This means that the cw laser itself has no shift relative to comb mode it is locked to. It is necessary to introduce the frequency shift before the beat detection, because a phase-lock at 0 Hz is technically challenging.

Figure 2.16 illustrates the design and stabilization of the FPCs. The optical cavity has a plano-concave geometry, with a small flat mirror glued on a piezo tube. Two lenses on either side of the cavity establish mode matching between the fundamental cavity mode and the in and outgoing fiber channels. The cavity mirrors are mounted inside of a mechanical structure that consists of two thick brass tubes. This construction ensures maximum mechanical stability. Additionally, the whole assembly of the FPC is enclosed in a box with very good vibration isolation from below. The cw light is spatially overlapped with the comb light in crossed polarization with a fiber-optic polarization beam splitter. This ensures perfect spatial mode matching between the two beams. After being transmitted through the FPC, the two beams

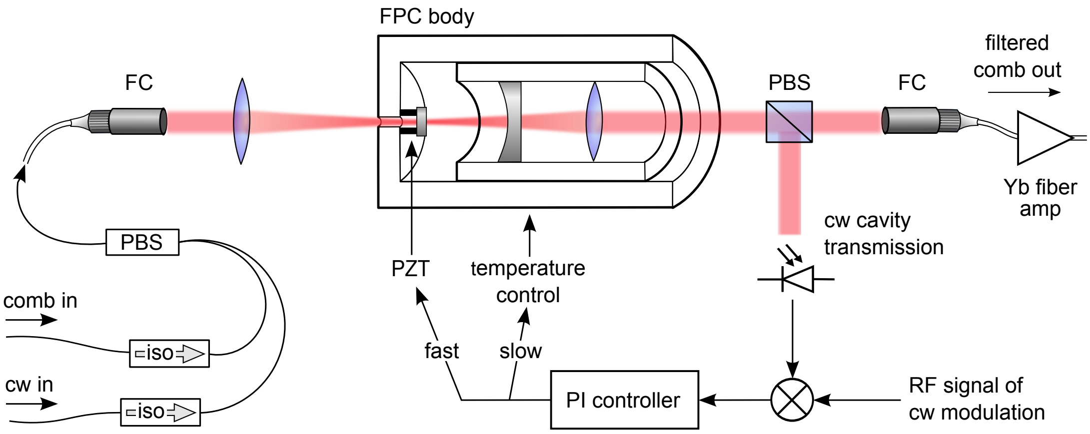

Figure 2.16 – Design and stabilization of a single Fabry-Pérot cavity (FPC). The body of the FPC is made of two thick brass tubes. The smaller mirror of the plano-concave cavity is glued on a PZT piezo tube. The FPC is stabilized to the cw laser, whose polarization is perpendicular to that of the comb, putting into practice a Pound-Drever-Hall locking scheme. The triangle at the filtered comb output represents a core-pumped Yb-fiber amplifier that compensates losses. PBS: Polarizing beam splitter. FC: Fiber collimator. Iso: Optical isolator.

are separated by a polarization beam splitter cube. The beam of the cw laser is then picked up by a photodiode, monitoring the amplitude modulation of the transmitted cw laser. Mixing this signal with the RF signal of the original phase modulation of the cw laser yields an error signal, that vanishes if the frequency of the cw laser is in the center of the FPC resonance. The length of the FPC is locked to this by a PI servo loop, controlling the voltage on the piezo tube of the flat mirror for fast control, and a Peltier element regulating the temperature of the FPC body to compensate slow drifts. After each FPC, the comb light is amplified in a core-pumped, Yb-doped fiber amplifier to compensate the losses at the FPC. The first FPC is also preceded by an amplifier, as it suffers greater power losses than the others, since it rejects previously unsuppressed modes.

The design of the FPC unit in Fig. 2.16 does not depict elements that merely support alignment: On either side of the FPC body, there is a pair of plane mirrors that help aligning the beam to match the fundamental cavity mode as well as possible. Half-wave plates at the fiber collimators help aligning the polarization along the axes of the fibers, which are polarization-maintaining. The FPC body incorporates a fine-adjustment screw, that shifts the inner tube relative to the outer tube, controlling the cavity length. Moreover, the FPC body has a flexure hinge on the side of the piezo actuator, that allows adjusting the angle of the piezo-mounted mirror.

There have been attempts to replace the PBS cube in Fig. 2.16 by a fiber PBS, like the one at the FPC input. This results in a more compact and alignment-free design. Most of these fiber components have however insufficient polarization extinction ratio (PER), and thus do not fully separate the cw light from the comb light after the FPC. The spurious cw light is then amplified in the subsequent fiber amplifier. In a cascade of FPCs, this light can then interfere with the cw light fed into the next FPC by another PBS with poor PER, and distort the error signal of the cavity lock. Replacing the PBS cube by a fiber PBS therefore only works with fiber components that feature excellent PER. In a cascade of several FPCs, it is also important to place optical isolators between the individual FPCs. Otherwise, parasitic cavities are formed between the mirror surfaces of the output mirror of one FPC and the input

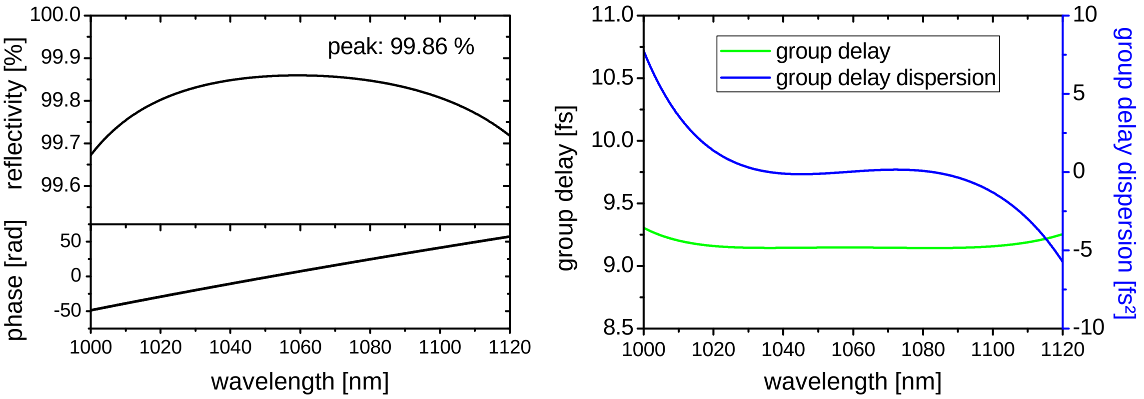

Figure 2.17 – Properties of the mirror coatings calculated from the design by the manufacturer (UltraFast Innovations GmbH). The maximum reflectivity of 99.86 % at 1060 nm, corresponds to a finesse of 2242. The absolute value of the group delay dispersion stays below 0.2 fs^2 for a 55 nm wide range.

mirror of the next FPC.

As discussed earlier in this chapter, it is of vital importance to keep intra-cavity dispersion as low as possible. For this reason, our FPC mirrors use specially designed mirror coatings with minimized dispersion, manufactured by UltraFast Innovations GmbH. Figure 2.17 shows their dispersion and reflectivity properties. The mirrors employ a conventional Bragg-stack design of the dielectric layers. A chirped mirror design as in [96] is not required to minimize the dispersion over this limited range. The coatings described here are optimized for an NPE oscillator (~1060 nm center wavelength after power amplification), but a version for the figure-9 oscillator has recently also been fabricated (~1040 nm center wavelength). According to the mirror design, the absolute value of the group-delay dispersion (GDD) is < 0.2 fs^2 over > 50 nm, centered at 1060 nm. Although this indicates an extremely low dispersion, the actual absolute value of the GDD over this range is limited by manufacturing tolerances to < 2 fs^2, which is still very low. Using this value, and the dispersion of the intra-cavity air as obtained from [99, 100], it is calculated that intra-cavity dispersion is not an issue in our system.

The finesse of an FPC can be characterized by scanning its length while monitoring the transmission signal of the cw laser on an oscilloscope. For this measurement, the FPC resonance is not locked to the cw laser. Instead, the FPC length is dithered to repeatedly scan the resonance across the cw laser's frequency. The scan is kept slow enough to ensure that the cavity photon lifetime or limited electronic bandwidth have no influence on the transmission curve measured during the scan. The finesse is calculated from the FPC transmission curve as the ratio of the known FSR of 18 GHz divided by to the FWHM of the transmission peak. In order to add a frequency scale to the scan of the FPC length, we exploit the side bands that are created by the phase modulation of the cw laser. Exclusively for this purpose, we set the frequency of the modulation to 60 MHz for better separation of the side bands. The three strong transmissions in a single scan of the cavity length are fitted with a sum of three Lorentzian functions, as demonstrated in Fig. 2.18 at a wavelength of 1040 nm. Approximating the FPC transmission function by a Lorentzian implies linearization of the sine term in Eq. (2.3.1), which works well in the proximity of a resonance. Knowing, that the separation of the two outer Lorentzians in Fig. 2.18 corresponds to 120 MHz, the FWHM of the central Lorentzian is determined to be 9.42 MHz, leading to a cavity finesse of 1911. The measurement has also been carried out at 1064 nm on the same mirror coatings, yielding a finesse of > 3000. This value is considerably above the design value (see Fig. 2.17), but has been confirmed by

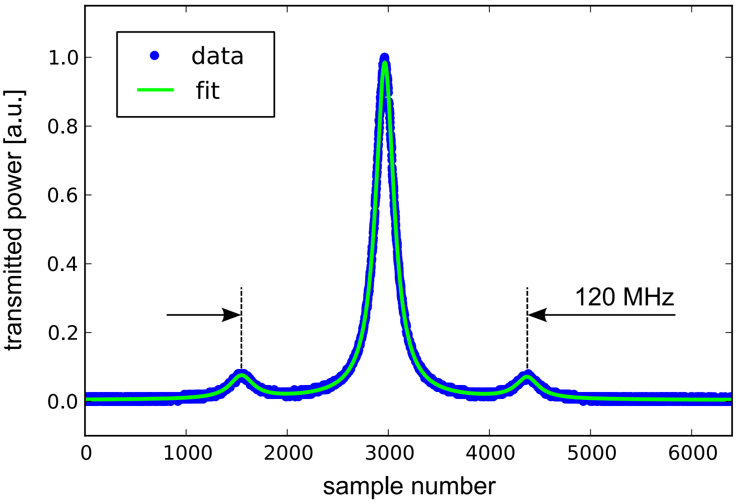

Figure 2.18 – Measurement of the finesse of a Fabry-Pérot cavity. The data points show a time trace of the cavity transmission during a scan of the cavity length, sampled in equidistant time steps by an oscilloscope. The transmitted light stems from a 1040 nm cw fiber laser, modulated at 60 MHz, which creates two main modulation side bands with a separation of 120 MHz to each other. The three major lines are fitted with a sum of three Lorentzian functions (green line), from which the cavity finesse of 1911 can be deduced.

cavity ring-down measurements carried out by the manufacturer.

Assuming a finesse of the FPCs of 1911, the expected side-mode suppression is 103 dB after the full chain of 3 FPCs at an FSR of 18 GHz. The subsequent SHG and spectral broadening re-amplify side-modes (see Chapter 4). It is estimated, that in a worst-case scenario, the side-modes still remain suppressed to better than 51 dB. Consequently, these modes cannot shift the center-of-gravity of a calibration line, as seen by the spectrograph, by more than 2 kHz, or 1 mm/s in terms of radial velocity. Line shifts due to skewing of the mode profile through the FPC filter function should be limited to below 1 cm/s, for both a figure-9 or an NPE oscillator. For the concept presented in this chapter, we thus expect an accuracy of better than 1 cm/s.

2.4 Nonlinear frequency conversion

After mode filtering, the comb spectrum is frequency-doubled and then broadened to cover a large portion of the visible spectral range. In order to drive these nonlinear optical effects, high peak intensities are required, which are hard to achieve at a pulse repetition rate of 18 GHz. We therefore employ a high-power fiber amplifier (see Fig. 2.19(a)) to amplify the pulse train to up to 15 W of average power. This is possible by pumping the core of the Yb-doped gain fiber from the surrounding cladding, which allows the use of powerful multimode diode lasers for pumping [101]. The unabsorbed part of the pump light is dumped at a heat sink at the end of the gain fiber.

In this pumping scheme, the pump light is absorbed less efficiently by the doped fiber core than in a core-pumped amplifier. This can give rise to a lower population inversion, and usually requires an about 10 times longer gain fiber of several meters in length. The cladding-pumped amplifier therefore has an extremely high gain, but also a strong reabsorption of the signal to be amplified. The latter mechanism is caused by the overlap of the pump-absorption spectrum and the gain spectrum of Yb^{3+}. The effect of signal reabsorption is more pronounced at shorter wavelengths, which is why the amplifier shifts the center wavelength of a broadband input signal. The center wavelength of an NPE oscillator is shifted to about 1060 nm. The spectrum of a figure-9 oscillator is shifted by much less, to about 1040 nm, due to its lower bandwidth. Because of the shorter wavelength of the amplified signal, the gain fiber needs to be shorter for the figure-9 oscillator to provide an efficient gain (about 3 m, as opposed to about 5 m for the NPE oscillator). The signal reabsorption can be saturated, since it pumps the gain medium [102]. For this reason, and for its extremely high gain, the amplifier has the tendency to produce giant pulses through Q-switching, destroying parts of the optical system. Therefore, even though the amplifier is protected by an optical isolator, back-reflections represent a potential threat. The high-power fiber amplifier must also not be pumped without being seeded. This is why the amplifier incorporates a fiber coupler that allows the monitoring of both the seed at the amplifier input and the signal traveling in back direction. If either of them reaches a critical value, the pump lasers are shut down by an interlock circuit within less than 10 µs, in order to prevent damage.

After the power amplifier, the optical pulse train enters a free-space region (Fig. 2.19(b)). Being heavily chirped by about 30 m of optical fiber along the complete beam path to this point, the optical pulses need to be re-compressed. We introduce the necessary amount of anomalous group-velocity dispersion by sending the beam through a combined grating and prism compressor, that allows controlling the linear and quadratic chirp independently. Specially optimized transmission gratings and Brewster-angled prisms give it an insertion loss as low as 20 %. More details about the compressor are found in [25]. The resulting 130 fs pulse duration in case of a figure-9 oscillator, and 100 fs in case of an NPE oscillator are close to the transform limit. The pulses are then frequency-doubled in a 3 mm long lithium triborate (LBO) crystal. A half-wave plate (HWP) is used to align the polarization along the direction required for SHG. LBO has been found to provide the best trade-off between SHG efficiency, SHG bandwidth, and a low walk-off angle between the second harmonic and the fundamental light [25]. The latter effect makes the beam profile elliptic, making it hard to efficiently couple it into the subsequent PCF. Employing high-quality LBO crystals has been found to be important, because crystals of low quality can degrade at this high optical power. The SHG yields up to more than 500 mW of green average power, but less than half of this amount is usually sufficient.

For spectral broadening, the green light is coupled into a tapered PCF, that is discussed in more detail in Chapter 3. The fiber has a 2 µm core diameter at both ends. In between, it is tapered down to a core diameter of about 540 nm, which is maintained over 20 to 30 cm. A HWP is used to align the input polarization along one of the two polarization eigenaxes of the PCF. This is necessary because of the PCF birefringence, owing to the small but finite ellipticity of the core caused the fabrication process [103]. The broadened spectrum strongly depends on the amount of light coupled through the PCF. In the past, drifting alignment of the PCF coupling was an issue, requiring frequent readjustments. This problem has been solved by actively stabilizing the fiber coupling with a piezo-driven mirror before the fiber (FiberLock, TEM Messtechnik GmbH). It works by slightly displacing the beam in circular fashion around the direction of maximum coupling efficiency at a rate of 169 Hz. If this circle is not precisely centered around the maximum, this causes a slight amplitude modulation on the light transmitted through the PCF, whose phase reveals the direction into which to adjust the mirror. Any resulting modulation side-bands are irrelevant for astronomical spectrograph calibration, as they cannot induce calibration errors exceeding the sub-mm/s scale, because of the low frequency of the modulations. Additionally, we have improved the passive stability of the fiber coupling by connectorizing the fiber ends with FC/APC connectors. This involves processing the ends of the PCF by collapsing the air-holes around fiber core and polishing the end facets. This has the additional benefit of greatly facilitating the handling of the PCF,

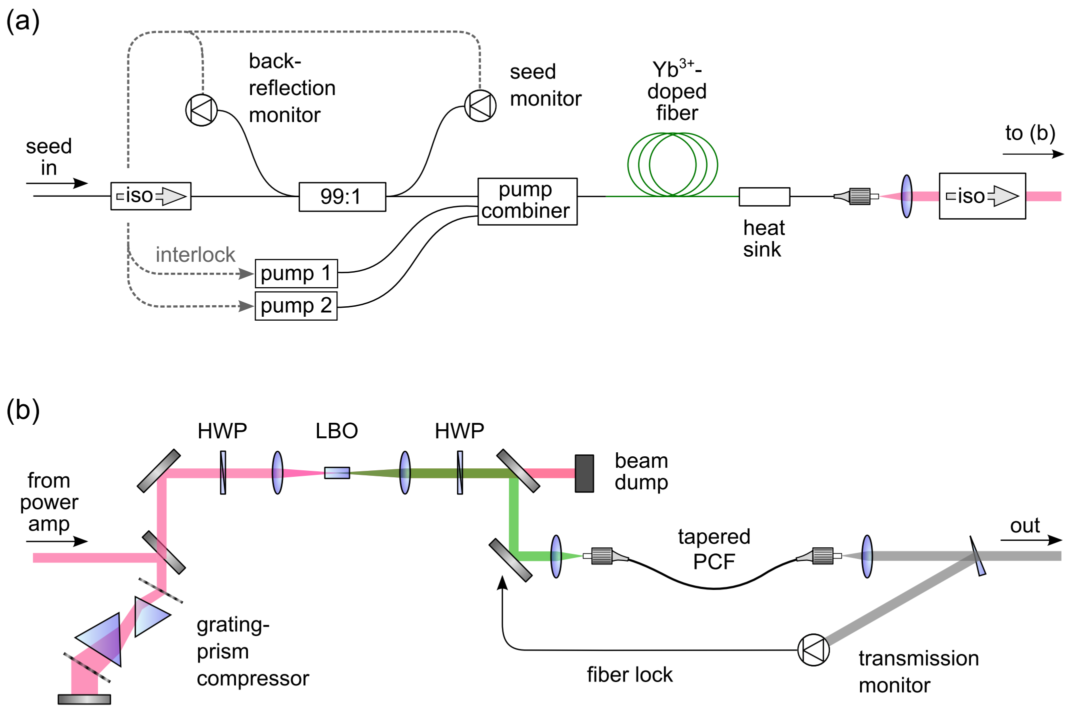

Figure 2.19 – Nonlinear frequency conversion. (a) Cladding-pumped power amplifier that provides the power to drive the nonlinearities for frequency conversion. The interlock shuts down the pump diode lasers if the amplifier seed or feedback fall or rise to critical values. This amplifier is represented by a triangle in Fig. 2.2. (b) Pulse compression, followed by second-harmonic generation and spectral broadening. An active feedback loop stabilizes the PCF coupling. HWP: Half-wave plate. LBO: Lithium triborate crystal. PCF: Photonic crystal fiber.

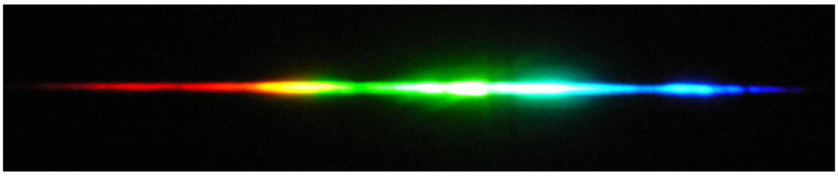

Figure 2.20 – Broadened spectrum of the 18 GHz astro-comb (no spectral flattening applied). The image represents a photograph of the astro-comb output, that was dispersed by a grating and projected on a wall (photo by R. Holzwarth).

that can now easily be exchanged as a simple patch cable. For experimentation however, it is still preferred to work with bare, cleaved fiber ends, which minimizes time spent on fiber preparation. Figure 2.20 shows a photograph of the broadened 18 GHz spectrum of the astro-comb, with about 90 mW of optical power coupled through. A bandwidth of up to >230 nm at -20 dB below the peak of the spectrum is obtained, which covers more than 74 % of the spectral range of the HARPS spectrograph.

Chapter 3

Photonic crystal fibers for spectral broadening

Photonic crystal fibers (PCFs) [104,105] are fibers whose core is surrounded by a hole structure that runs along the fiber length, giving rise to guidance of light within the core. Different kinds of PCFs are used for a variety of applications. A main center of interest is the engineering of the nonlinear interaction between light and matter. PCFs can either be designed to enhance optical nonlinearities in the core medium (e.g. [106]), or to avoid them as much as possible (see e.g. [101]). For the former case, the hole structure can be tailored to support very small mode areas over very long fiber lengths, which greatly helps enforcing optical nonlinearities. A careful design of the hole structure also allows engineering the dispersion profile of the fiber, which is critical for ultrashort pulse propagation and soliton formation. This offers great flexibility to give rise to various kinds of nonlinear optical effects, such as soliton fission, soliton self-frequency shift, or dispersive wave generation [103, 107].

PCFs have played a key role for the development of frequency combs, as they first permitted the generation of an octave-spanning spectrum for self-referencing to stabilize the offset frequency [1, 2]. A spectrum that has been broadened by optical nonlinearities is generally referred to as a supercontinuum. In the case of a broadened frequency comb, this term is a bit of a misnomer, because the broadened spectrum is normally not continuous, but still consists of discrete comb modes. Nevertheless, the term is also used in this context.

For astro-combs, PCFs play a critical role in broadening the spectrum to cover the spectral range of astronomical spectrographs, which is mostly in the visible. The unique possibilities of PCFs can be extended by tapering them [108]. We make use of this technique to efficiently broaden spectra at repetition rates as high as 18 GHz, where only very limited pulse energies in the pJ range are available. Tapered PCFs of a similar kind have been demonstrated beforehand to provide very efficient spectral broadening of visible ultrashort pulses [25, 109]. We build upon these results to broaden the spectrum of a green astro-comb, as described in the following section, working in close collaboration with the group of Prof. Philip Russell at the Max-Planck-Institut für die Physik des Lichts (MPL).

It was found, however, that these tapered PCFs are limited in lifetime, as detailed in the later Sec. 3.2. We demonstrate, that the lifetime of the tapered PCFs can be greatly extended, but not yet sufficiently for a long-term maintenance-free operation. An alternative concept is thus developed, aiming at broadening IR astro-combs strongly enough to cover the visible spectral range, as presented in the last section of this chapter. Since this is the newer approach, and associated with its own challenges, the rest of this work uses the former concept of broadening green astro-combs. This means, that the tapered PCFs had to be exchanged regularly while conducting the astronomical measurement campaigns in the Chapters 6 and 7.

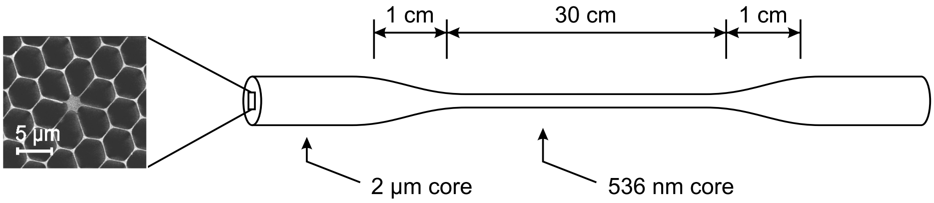

Figure 3.1 – Photonic crystal fiber (PCF) taper design. Image on the left: Scanning-electron micrograph of an untapered fiber end, zoomed towards the core. Right-hand side: The original PCF with a 2 µm core diameter is tapered down to a 536 nm core within a 1 cm long taper transition. The core diameter is then kept at this value over a 30 cm long taper waist. Outer diameter of the fiber: 120 µm (untapered), 32 µm (taper waist).

3.1 Spectral broadening of green astro-combs

For efficient spectral broadening of the 18 GHz train of green fs pulses (see Sec. 2.4), anomalous group velocity dispersion (GVD) is required in this spectral range to allow the formation of optical solitons. This represents a challenge, because the GVD of fused silica – the most common base material for PCFs – turns anomalous only for wavelengths above 1.27 µm [110]. The strong material dispersion in the green has to be balanced with the waveguide dispersion given by the geometrical structure of the PCF. This is facilitated by a high air-filling fraction in air-hole region, and by tapering the PCF down to very small core diameters. The small core also helps achieving high peak intensities to efficiently drive optical nonlinearities. This is especially important considering the extremely low pulse energies in the low pJ regime available from the green astro-comb. This section shows how tapered PCFs can be tailored to provide optimal conditions for spectral broadening of these pulses.

Figure 3.1 depicts the design of the tapered PCFs used for the studies presented here. The PCF has a solid core that is made of high-purity fused silica (Heraeus F300). The fiber sections outside of the tapered region have a core diameter of 2.0 µm. The core is surrounded by a cobweb structure with an air-filling fraction of > 95 %, suspending the core at 6 silica membranes each ~100 nm thick. The diameter of the PCF core is reduced to 536 nm within a 30 cm long taper waist. The untapered fiber ends are connected to the taper waist by transitions of 1 cm in length, with an approximately conical shape. The untapered ends and transitions enable efficient coupling of light into the extremely small core of the tapered region. The length of the untapered fiber piece at the input side is kept at about 2 cm, in order to prevent the incoming pulses from being stretched by too much material dispersion. The length of the untapered region at the output side is uncritical. As detailed below, a series of tapers with different waist diameters has been drawn, showing that the 536 nm core diameter is close to optimal for the intended purpose.

The tapers are fabricated from untapered PCFs using the flame-brush technique [108,111]. A small heat zone, over which the glass has a reduced viscosity, is moved to and fro along the fiber, while the fiber ends are pulled apart. The motion of the heat zone as a function of the fiber elongation determines the taper geometry [112,113], and is programmed to produce the taper design as outlined above. The tapers studied in this section have been manufactured by Sebastian Stark at the MPL, using a small butane-oxygen flame to form the heat zone. An analysis of the tapered fiber section was conducted at the MPL using a scanning electron microscope. This confirmed, that the tapering reduced the PCF structure in size as expected, while well preserving its geometry.

The taper fabrication was later moved to Menlo Systems, where most of the tapers used for the following section were produced. In this setup, the heat zone was created by a ther-

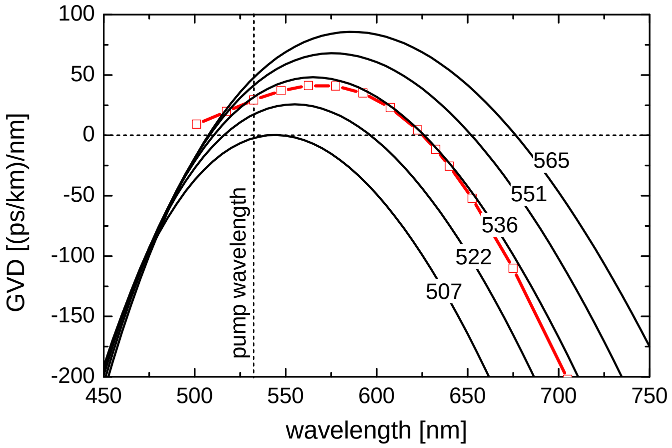

Figure 3.2 – Group-velocity dispersion (GVD) of tapered photonic crystal fibers (PCFs) for different core diameters at their taper waist. In the given units, positive values indicate anomalous GVD, whereas negative values indicate normal GVD. Black lines: Calculated GVD. The core diameter in nm is annotated to each curve. Red squares: GVD of a tapered PCF with a 536 nm core diameter at the taper waist, measured with a white-light interferometer. The calculations and measurements have been made by Sebastian Stark at the MPL.

moelectric oven with a $MoSi_2$ heater, comparable to [114] although slightly differing in its implementation. This provided very accurate control over the temperature of the heat zone, which is one of the most critical parameters of the taper drawing process. The temperature must be adjusted to the point where plastic deformation is possible without breaking the fiber, but must also remain low enough to prevent a reduction of the air-filling fraction of the PCF through contraction of the air-holes.

For numerical modeling, the PCF core is well approximated by a suspended silica strand, thanks to the very high air-filling fraction of the surrounding hole structure. This model is used to calculate the fiber GVD as shown in Fig. 3.2. The GVD within the taper waist is dominated by waveguide dispersion rather than by material dispersion. Even relatively small changes in the core diameter lead to substantial changes of the anomalous GVD region, which disappears completely for core diameters < 507 nm. A wide anomalous GVD region comprising the pump wavelength[1] can be established in the visible. This enables soliton formation and thus an extremely efficient excitation of optical nonlinearity. Only a rather low amount of anomalous GVD is desired at the pump wavelength, in order to achieve a high soliton order [110] already at modest pulse energies. Additionally, the positions of the two zero-dispersion wavelengths relative to the pump wavelength are of critical importance for the possibility to generate dispersive waves extending the broadened spectrum into the normal GVD regions [103]. This suggests that there must be an optimum waist diameter, considering the theoretical GVD curves in Fig. 3.2. For a 536 nm core, the fiber GVD has also been measured with a white-light interferometer (red squares in Fig. 3.2), with the results being in very good agreement with the numerical calculations.

The astro-comb used to test the tapered PCFs was similar to the one described in the previous chapter, but had a slightly lower repetition rate of 14 GHz. It was generated from a nonlinear polarization evolution (NPE) oscillator filtered by three cascaded Fabry-Pérot cavities with a finesse of 400 and a free spectral range of 2 GHz, 14 GHz and 14 GHz, respectively.

---

[1] In this context, the pump wave is understood as the light injected into the PCF, i.e. the green multi-GHz train of ultrashort pulses.

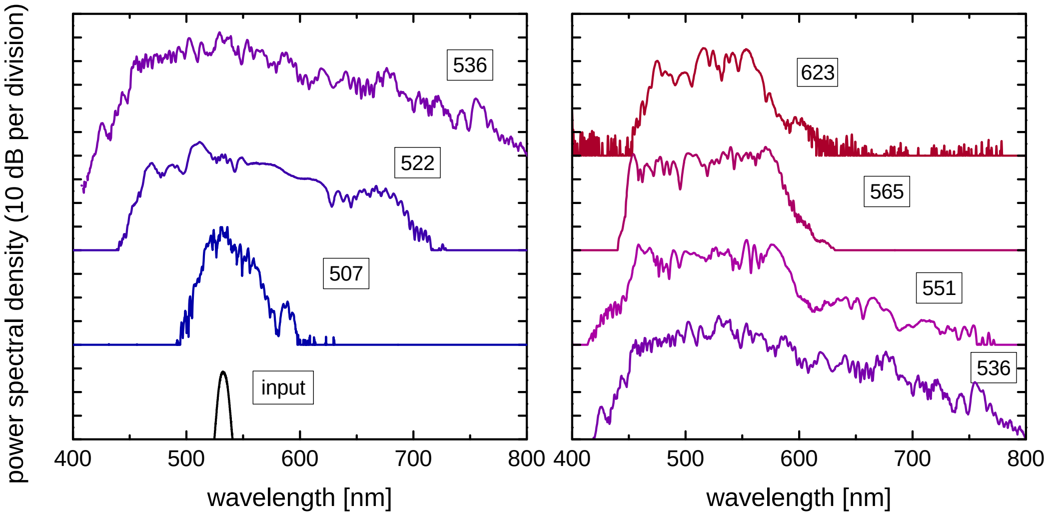

Figure 3.3 – Broadened spectra from tapered photonic crystal fibers (PCFs) with different core diameters at their waist. The core diameters in nm are annotated to the curves. The spectra have been measured with an optical spectrum analyzer at a resolution of 1 nm. The spectrum at the PCF input is shown by the black line on the lower left. Coupled power: 60 mW. Repetition rate: 14 GHz.

After amplification to 6 W of average power, the filtered pulse train was compressed to a pulse duration of 100 fs, and subsequently frequency-doubled in a 3 mm long LBO crystal. The resulting green comb spectrum was centered at 532 nm with a full-width at half-maximum of 5.3 nm. It had an average power of 120 mW, of which 60 mW were coupled through the tapered PCF, yielding a coupling efficiency of 50 %.

Figure 3.3 shows the output spectra obtained with tapers of different waist diameters, as well as the input spectrum. An approximately box-shaped spectrum is observed over the anomalous GVD region with a dispersive wave at the blue edge. For core diameters of 507 nm and below, the anomalous GVD region vanishes, and the bandwidth of the broadened spectrum shrinks drastically. This regime is purely governed by self-phase modulation of pulses that are being stretched in time by dispersion. For certain waist diameters, an additional red radiation band formed by a dispersive wave greatly extends the spectral bandwidth. It reaches further towards the IR for larger taper widths, but also declines in power. An optimum is reached for a 536 nm core, resulting in a total −20 dB-bandwidth of the broadened spectrum of 235 nm ranging from 450 to 685 nm, which covers 76 % of the spectral bandwidth of the HARPS spectrograph [20].

The evolution of the spectrum and pulse shape during propagation along the tapered fiber has been simulated by numerically solving the generalized nonlinear Schrödinger equation using the split-step Fourier method [110, 111]. The simulation was made for a 536 nm core with 2 cm long untapered pieces and 1 cm long transitions at both ends. The input pulse was assumed to be a 100 fs transform limited pulse with 10 pJ pulse energy. The results are shown in Fig. 3.4. The increase in pulse duration through dispersion in the untapered piece and transition at the fiber input turns out to be close to negligible. After the first 10 cm the spectrum broadens extensively, and dispersive waves are emitted towards the blue and red spectral regions. The fiber length necessary for this to occur is occasionally referred to as the activation length [115]. As seen in Fig. 3.4, spectral broadening is essentially completed after the activation length, and the process of soliton fission takes over, initiating the breakup of the higher-order soliton into fundamental solitons. The first ejected soliton has the shortest

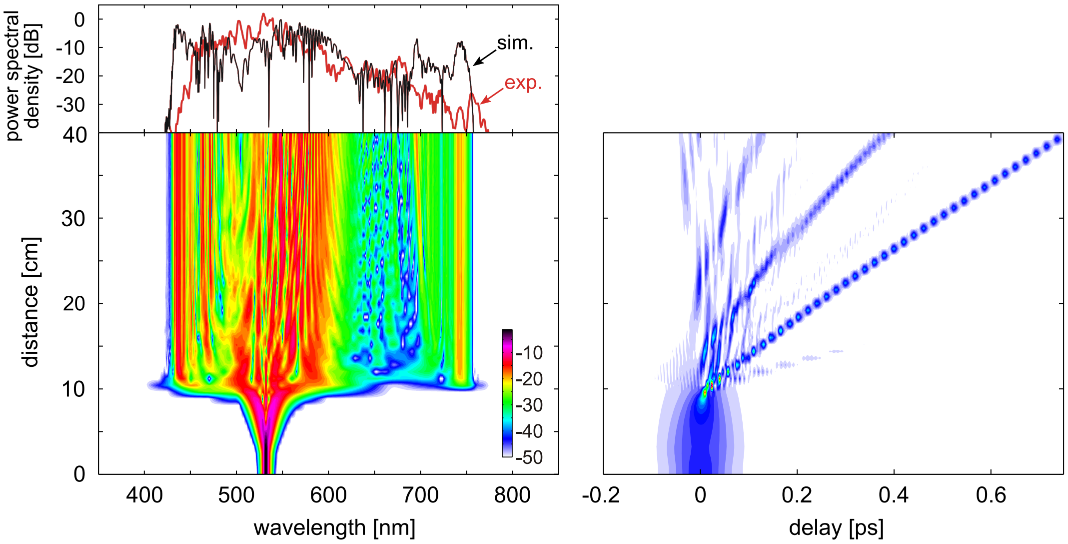

Figure 3.4 – Simulated evolution of a 10 pJ pulse in spectrum (left) and pulse shape (right) during propagation along a 40 cm long tapered photonic crystal fiber. 2 cm long untapered pieces and 1 cm transitions are included at both ends. Core diameter at taper waist: 536 nm. The top figure shows a comparison between the simulated and a measured output spectrum. The simulation has been made by Sebastian Stark at the MPL.

duration (~13 fs), and is most strongly subject to stimulated Raman scattering, which is responsible for the emission of the red dispersive wave. The upper part of Fig. 3.4 shows a comparison between the measured and the simulated output spectrum. The two are in good agreement, and particularly the radiation band in red is well reproduced. It should be noted, however, that the pulse energy of 4.3 pJ used in the experiment is less than half of that in the simulation, which explains the differences. The activation length depends critically on pulse energy, which means that in the experiment, full spectral broadening is only reached towards the end of the taper waist. This can easily be seen by eye, as the point at which the light scattered out of the bare fiber turns from green to white.

3.2 Photoinduced damage of tapered photonic crystal fibers

The above-described tapered PCFs have been found to be subject to photoinduced damage during use. After a certain time, the spectral bandwidth is observed to decrease, and the spectrum starts to change rapidly with time. The red part of the spectrum is usually observed to disappear first. Useful lifetimes for tapers drawn with a butane-oxygen flame were found to be up to several hours. It was also observed, that after a few months of storage the fibers returned to their initial behavior, yielding a broad and stable output spectrum until damaged again.

3.2.1 Understanding the nature of the degradation

Understanding a problem is usually the first step towards solving it. In the search for the cause of the limited lifetime of the PCFs, the setup depicted in Fig. 3.5 has proven to be very helpful. It consists of an 18 GHz green astro-comb, which is coupled through a tapered PCF for spectral broadening. As usual, the polarization at the PCF input is aligned along one of the two polarization eigenaxes of the PCF core by a half-wave plate (HWP), to obtain optimum spectral broadening. At the PCF output, the two eigenaxes of the PCF are projected upon

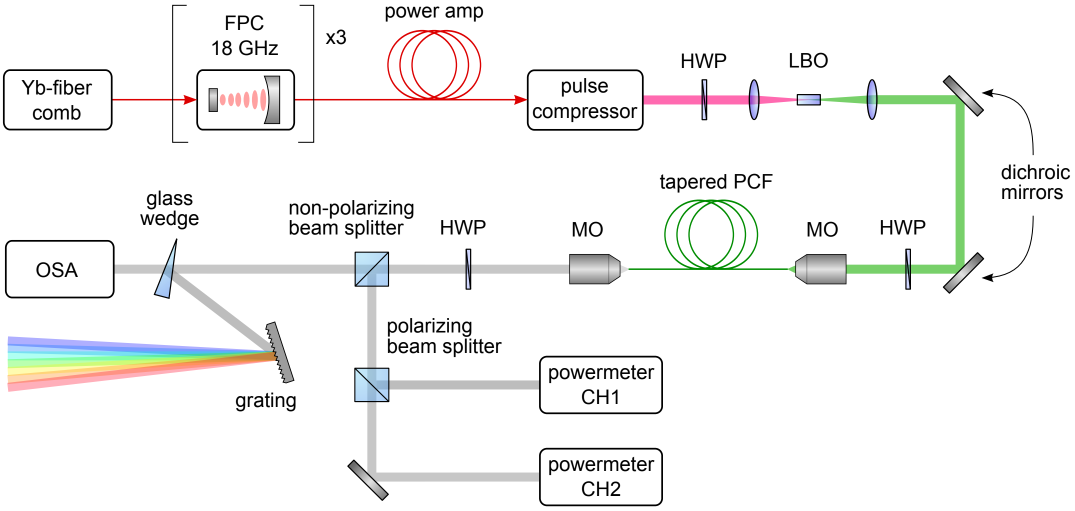

Figure 3.5 – Setup for examining photoinduced damage of tapered photonic crystal fibers (PCFs), using a green 18 GHz astro-comb (upper part). A half-wave plate (HWP) aligns the input polarization along an eigenaxis of the PCF core. Another HWP at the output matches both of the PCF eigenaxes to those of a polarizing beam splitter, to separately monitor their optical power with two powermeters (CH1, CH2). The PCF output spectrum is monitored by an optical spectrum analyzer (OSA).

the axes of a polarizing beam splitter by an achromatic HWP, where the optical power on each polarization axis is monitored by a powermeter. The PCF output spectrum is monitored by an optical spectrum analyzer (OSA), consisting of a scanning monochromator. The spectrum is also monitored by eye with the aid of a grating that projects the spectrum on a laboratory wall. Usually in these experiments, a somewhat higher optical power is coupled through the tapered PCFs than needed for spectral broadening. This accelerates the photoinduced damage, and thus allows conducting the experiments in less time.

Figure 3.6 shows a measurement obtained with this setup. The examined tapered PCF was drawn with a butane-oxygen flame, closely reproducing the design from Fig. 3.1. A lower spectral bandwidth is obtained with this fiber, due to the lack of the dispersive wave in the red. This is presumably the result of the lower air-filling fraction of the hole structure of this PCF of about 83 %. Aligning the input polarization along a polarization eigenaxis of the PCF core yielded a polarization-extinction ratio (PER) of the broadened output of 8 dB. 151 mW of optical power were coupled through the PCF, resulting in a -20 dB-bandwidth of 156 nm. Both the spectrum and the PER initially remained stable for more than 10 min. Then however, the PER declined rapidly, and subsequently indicated wild changes of polarization of the PCF output. This is accompanied by changes of the output spectrum, and a correlation between the PER and the spectrum is found. This correlation is not surprising, since spectral broadening in PCFs depends on polarization also under normal circumstances. After 42 min of total measurement time, the transmission through the PCF had dropped by about 8 % at the pump wavelength. The decline in transmission was found to be reproducible in further tests, and is neither due to a drift of the fiber alignment, nor due to a degradation of the fiber end facets. Cleaving both fiber ends after photoinduced damage, to ensure clean and intact fiber facets, did not reverse any of the observed effects.

In order to provide a quantitative measure of the time span that it takes for photoinduced damage to occur, we define the PCF lifetime as the time between the start of the measurement and the decline of the PER to zero, i.e. the time until the two powermeter curves cross. This

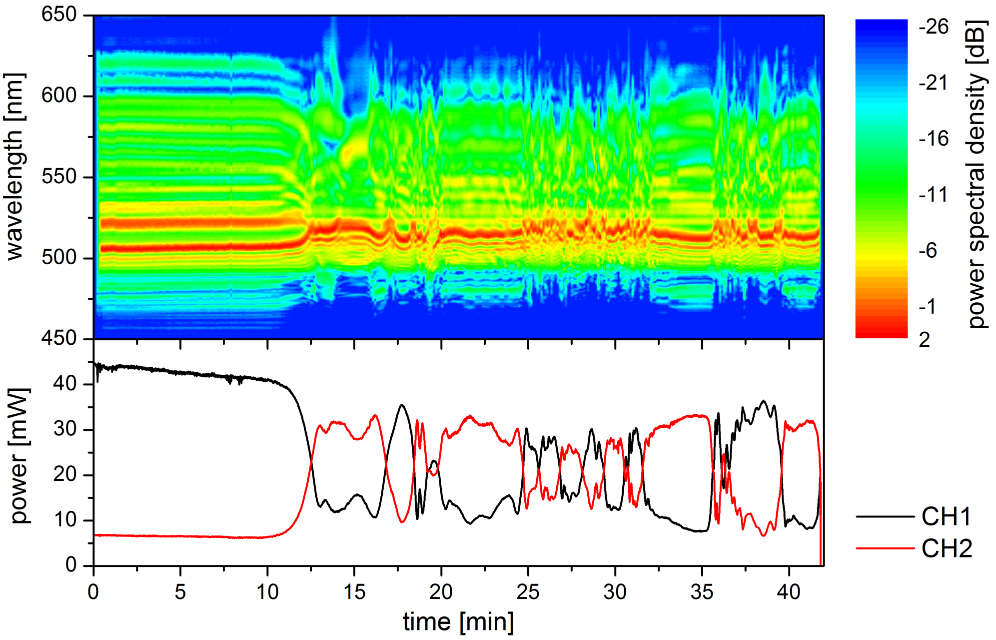

Figure 3.6 – Photoinduced damage of a tapered photonic crystal fiber (PCF). The taper was drawn with a butane-oxygen flame. Top: Evolution of the spectrum over time. Bottom: Evolution of the power on the two polarization eigenaxes of the PCF core. The PCF lifetime, defined as the time after which the two power curves cross, is 12.5 min. Coupled power: 151 mW.

definition yields a lifetime of 12.5 min for the measurement shown in Fig. 3.6.

The above-described phenomenon in supercontinuum generation has – to our knowledge – never been reported before in literature. This is not too surprising, considering the extremely exotic parameters of our spectral broadening, e.g. in terms of repetition rate, center wavelength or core size of the tapered PCF. Our investigations therefore partly explore unknown scientific territory. However, certain elements of the observed phenomenon have been reported previously, most of them in a seemingly different context. Taken together, these reports give a picture of what is happening, and reveal that known mechanisms underlie our astonishing findings.

Our observed polarization evolution is very unexpected, and has never been reported before to occur in PCFs. A similar effect on polarization has however been observed when transmitting visible cw lasers through germanosilicate fibers [116]. There, the polarization conversion is caused by a birefringent refractive index change, induced by color-center formation. This modifies an already birefringent fiber to form a rocking filter [117] that acts as a very efficient polarization converter: Light is injected into the fiber with a 45° polarization angle relative to the fiber birefringence axis. The +45° linear polarization is periodically transformed to −45° and back. The induced birefringence lines up with the polarization directions, and thus modifies the intrinsic birefringence of the fiber to rock from side to side along the fiber length with the polarization beat period of the fiber. This holographic, birefringent index grating structure can resonantly transfer light from one polarization axis of the fiber to the other.

In the case of tapered PCFs, formation of rocking filters may occur spontaneously, which can plausibly explain the observed phenomenon. The tapered PCFs are however made of fused silica, which is much more resistant against color-center formation than germanosilicate. In fused silica, only two sorts of color centers prevail, that can be created by splitting covalent Si-O bonds [118]: An unpaired electron that forms a dangling bond on a Si atom ($\equiv \mathrm{Si}\bullet$) is known

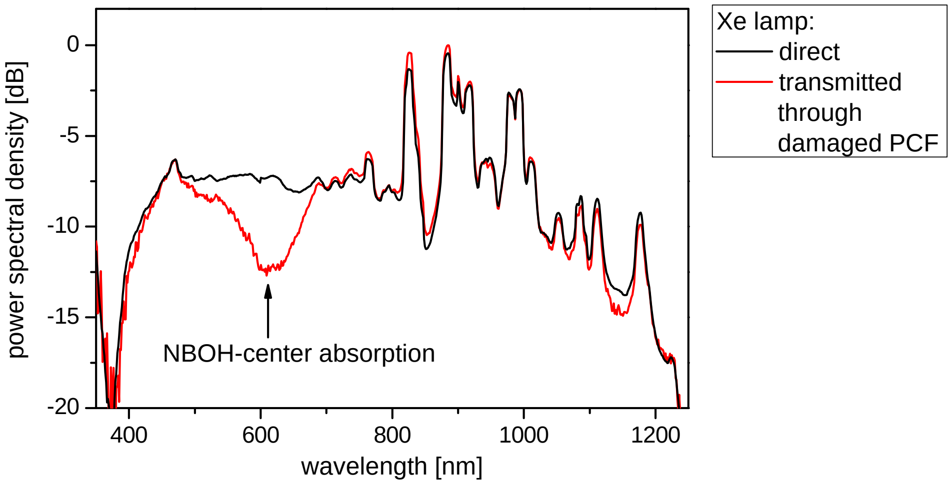

Figure 3.7 – Spectroscopic evidence for non-bridging oxygen-hole (NBOH) centers in a tapered photonic crystal fiber (PCF) after photoinduced damage. The light of a Xe lamp was transmitted through a damaged PCF. Black line: Spectrum of the Xe lamp before PCF. Red line: Spectrum at PCF output. Resolution of the measurement: 10 nm.

as an oxygen deficiency center, or E' center. Here, $\equiv$ denotes single bonds to three O atoms of the surrounding glass network. A dangling bond on an O atom ($\equiv \mathrm{Si} - \mathrm{O}\bullet$) is a non-bridging oxygen-hole (NBOH) center. Color centers can disappear over time (annealing), which can be drastically sped up by the application of heat (thermal annealing). With the electronic band gap of silica of about 8 eV, color-center formation can occur through multiphoton absorption from NIR ultrashort pulses [119], two-photon absorption of UV excimer lasers (e.g. ArF, KrF) [120–122], absorption of γ or x-rays, or through massive energetic particles. The color centers have strong and broad absorption bands in the UV, centered at 210 nm for E' centers, and (apart from a relatively weak visible absorption) at 265 nm for NBOH centers [119]. Therefore, color centers have been studied extensively in the context of photodarkening of fused silica during excimer laser irradiation (solarization) [118,120–124]. The formation of the UV absorption is accompanied by a volume compactification of the glass matrix [120,125,126], and by an increase in refractive index. The latter effect is exploited for laser inscription of waveguides to bulk glass [119,126,127], and for the fabrication of fiber Bragg-gratings [128].

The current scientific understanding of laser-induced refractive index changes in glass is incomplete. A Kramers-Kronig mechanism has been proposed, that explains the isotropic increase in refractive index through the absorption bands of the color centers and trapped photoelectrons. Measurements on germanosilicate indicate that this is the dominant contribution for this material [129]. The birefringent contribution has been explained as the preferential breaking of chemical bonds that are aligned in the direction of incident linearly polarized light [130]. This reduces the polarizability, and thus the refractive index, in this direction [130]. The large isotropic increase of the refractive index may originate from electrons released during color-center formation, that are afterwards trapped at a host of randomly oriented sites [130]. Volume compaction however also contributes to the isotropic increase of refractive index, and in many cases is seen as the dominant mechanism [121,126]. This effect can persist even after bleaching of the color-center absorption. Structural changes in the glass matrix caused by linearly polarized light can also induce [121] or reduce [116] stress birefringence. Furthermore, formation of self-organized nanolayers along the polarization of the incident light can also be a source of birefringence [126].

Table 3.1 – Lifetimes of tapered photonic crystal fibers (PCFs) before and after tempering to anneal the induced color centers. Lifetime 1: Initial lifetimes of previously unused PCFs at 200 mW transmitted optical power. Light transmission continued for another 40 min after elapse of this time span. The PCFs were then heated to different temperatures (leftmost column) and kept there for 30 min. Lifetime 2: Lifetimes of the PCFs after the heat treatment, tested at 150 mW transmitted power.

annealing temp.	lifetime 1 @ 200 mW	lifetime 2 @ 150 mW
900 °C	10.8 min	49 min
700 °C	7.3 min	1.7 min
500 °C	6.3 min	7.7 s
300 °C	8.8 min	12 s

Color-center formation during supercontinuum generation in a PCF made of fused silica has been reported in [131]. This was however not associated with an instability of the broadened spectrum comparable to what observed with the astro-comb. An influence on the polarization has also not been reported. Instead, the color centers became noticeable solely by their absorption. NBOH centers have a broad absorption band in the visible, with a maximum at 630 nm [131–133]. This absorption is often ignored, because its strength is less than 3 % of the UV absorption of NBOH centers, but can become significant in the presence of a massive amount of NBOH centers.

We look for the characteristic absorption of NBOH centers by transmitting the light of a Xe-arc lamp through a tapered PCF upon which photoinduced damage has previously been inflicted. The transmitted spectrum as measured on an optical spectrum analyzer very clearly reveals the presence of the visible absorption profile of NBOH centers, as shown in Fig. 3.7. No evidence for the presence of this absorption was found in tapered PCFs that had not been used for spectral broadening prior to the measurement. Control experiments using a visible supercontinuum source instead of a Xe lamp confirmed these results. The development of this absorption can well explain the reduced fiber transmission after photoinduced damage, and the often observed suppression of the red part of the broadened spectrum.

Another characteristic of color centers is their annealing dynamics. The refractive index modification that accompanies color-center formation in fused silica rapidly disappears when the material is heated to 900 °C [126]. In order to test the possibility of thermal annealing, four tapered PCFs were treated with 200 mW of transmitted optical power, resulting in lifetimes between 6 and 11 min. After elapse of the lifetime, the transmission of optical power continued for another 40 min, in order to induce a fair amount of color centers. The PCFs were then heated in an oven to 300 °C, 500 °C, 700 °C, and 900 °C, respectively, and kept there for 30 min. Remarkable changes were found on the PCF that was tempered at 900 °C: Letting it hang down vertically, it was not straight anymore, but tended towards the bend that it had in the oven. 900 °C is known to be temperature at which fused silica becomes soft enough for stress to relax. When putting it to the astro-comb setup, it was found to be extremely fragile. Presumably this is because the heat treatment initiated crack formation due to local crystallization of the glass at the fiber surface [134], and/or due to crack growth caused by stress corrosion [123, 135]. While trying to cleave the PCF to ensure clean and intact end facets, the untapered parts and large portions of the taper transitions broke away on both sides. As this led to a poor coupling efficiency, the PCF could not be tested at a transmitted power of 200 mW as before, but instead was tested at 150 mW. Although no such anomalies were found with the other PCFs, they too were tested at 150 mW, to ensure comparability among the four PCFs. The PCF heated to 900 °C lived more than a factor of 4 longer than in the first run, showing that the annealing was successful (see Tab. 3.1). The longer lifetime may be due to the lower transmitted power. All the other PCFs lived much shorter than previously, despite the lower power, and the polarization at their output started to change immediately. This shows that at 700 °C and below, the photoinduced damage persisted.

From the above results and comparisons to literature, it is concluded, that the limitation of the PCF lifetime is due to formation of color centers in a multiphoton process, which in turn induces absorption and birefringence, disturbing supercontinuum generation. The process strongly depends on the transmitted optical power, but the supercontinuum generation itself also strongly depends on this parameter. However, with tapers that have inappropriate parameters for good spectral broadening, the photoinduced damage is still observed unabatedly, indicating that the pump light itself is the major driver of the process, which is in unison with [131]. The speed of the process is observed to increase with the repetition rate, as the fiber transmits more pulses over time. It is however also possible that beyond this, color-center generation is more efficient at higher repetition rates, due to the finite lifetimes of the intermediate photochemical reaction products of 400 to 800 ps [136].

3.2.2 Increasing PCF lifetime

The gained understanding of the cause of the fiber degradation enables testing specific strategies to increase the PCF lifetime to a useful time span. If the lifetime can be increased to surpass the annealing time the induced defects at room temperature (or half this time span assuming that the astro-comb is only going to be used 12 h per day), the PCF lifetime will no longer be limited by this problem. The estimated lifetime necessary for this is between roughly 1 and 3 months. Considering the great success with which color center-induced problems have been managed in other applications (e.g. [137]), this goal does not appear unrealistic.

Using a polarization-maintaining core

As we have seen, the instability of the broadened spectrum is mainly caused by induced birefringence that disturbs the polarization of light propagating inside the fiber core. An obvious solution to this problem is the use of a polarization-maintaining PCF, i.e. a PCF with a core whose intrinsic birefringence is so strong, that it cannot easily be overcome be some induced birefringence. For this we use a PCF with a strongly elliptic core (Fig. 3.8(a)), with a width of 2.0 µm / 4.6 µm. The outer diameter of the fiber is 130 µm, tapered down to 42 µm with a butane-oxygen flame. The taper geometry (and the choice of material) is otherwise the same as before, i.e. the PCF has a 30 cm long taper waist with 1 cm transitions on both sides.

The PCF was tested over 48.5 h (see Fig. 3.8 (b) and (c)), with a transmitted power of 200 mW (coupling efficiency 53 %), a spectral broadening to a −20 dB-bandwidth of 129 nm, and a PER of 9 dB at the start of the measurement. A decline in transmission, supposedly due to the absorption of forming NBOH centers, is obvious at the beginning of test period. The PER also declined, but stabilized at 3 to 5 dB. The spectral bandwidth was stable over a large time span, but shrank drastically after approximately 24 h. Although this PCF did not exceed its lifetime according to our formal definition (PER dropping to zero), it must be stated, that this PCF usefully fulfilled its purpose only for roughly 24 h. In spite of the higher coupled power, this constitutes an improvement by more than 2 orders of magnitude relative to the measurement shown in Fig. 3.6. It must however also be noted, that the area of the tapered core is larger by a factor of 3.4, which implies a lower intensity in the core. It is not precisely known by how much the intensity lowered, because of the evanescent light field outside of the core, which should become quite noticeable at such small core diameters.

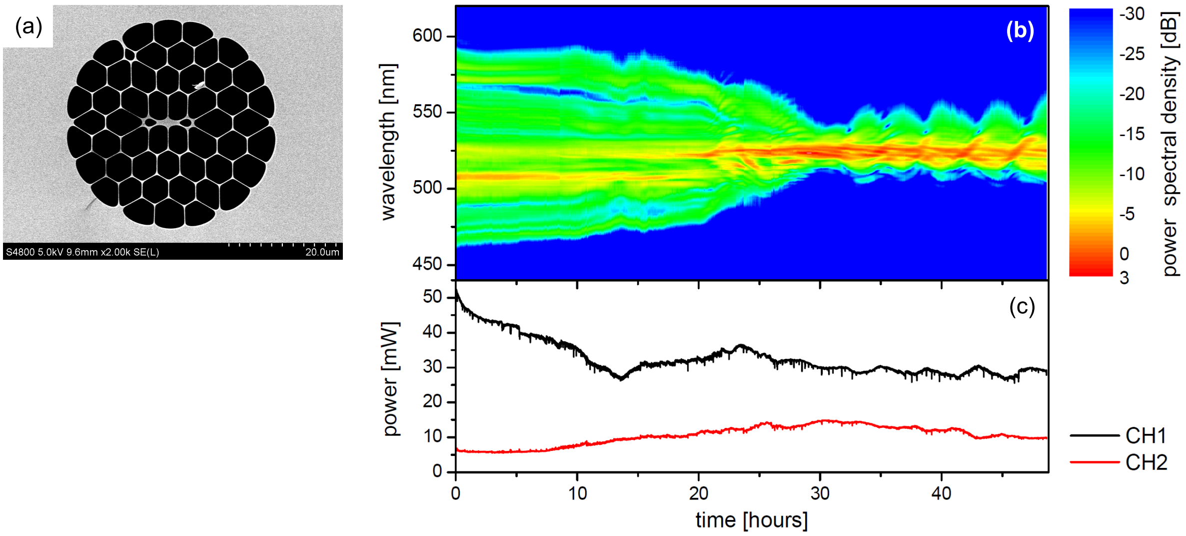

Figure 3.8 – Photoinduced damage of a highly birefringent tapered photonic crystal fiber (PCF). (a) Scanning-electron micrograph of the hole structure of the untapered PCF. The core is approximately elliptic with a width of 2.0 µm / 4.6 µm, tapered down to 0.66 µm / 1.5 µm. (b) Evolution of the spectrum over 48.5 h. (c) Evolution of the optical power on the two polarization eigenaxes of the PCF. Total transmitted power in the beginning: 200 mW.

After the measurement, the transmission through the fiber had dropped by 20 % at the pump wavelength, which was clearly not due to a degradation of the fiber ends, and must therefore be ascribed to color-center absorption. During the measurement, the transmitted power declined by an additional 20 % owing to a slight degradation of the SHG crystal, which was later replaced by a higher-quality one. The degradation of the spectral bandwidth can however by no means be attributed to the reduced transmitted power: Prior to this measurement, the PCF had shortly been tested at a transmitted power of 106 mW, yielding a −20 dB-bandwidth of 115 nm. After the long-term test, only 52 nm were yielded at 114 mW, and after the first 31 h of the test, only 26 nm were obtained at about 150 mW. The declining spectral bandwidth is therefore suspected to stem from altered properties of the fiber core, possibly affecting its density, extent, geometry, dispersion, or nonlinearity.

OH-doping

Previous studies have reported an enhanced resistance against color-center formation in OH-doped (or “wet”) fused silica as opposed to OH-free (“dry”) fused silica [121, 122]. OH doping also enables a fast recovery of the material at room temperature, because of the finite mobility of the hydrogen in the glass [122]. Hydrogen atoms can attach themselves to the dangling bonds of color centers, which suppresses their absorption. Furthermore, the OH groups function as network modifiers, helping to reduce the number of strained Si-O bonds, that are known to be particularly inclined to form color centers [123]. The helpfulness of OH is however controversial. In [122] it was found that the suppressed color-center absorption can rapidly reappear upon continued laser irradiation, probably due to dissociation of the OH groups. In [121], the OH doping could not suppress the induced birefringence, and in [137] wet fused silica even turned out to be less resilient against color-center formation than dry fused silica.

In order to test the helpfulness of employing OH-doped glass, tapers were drawn from PCFs with a core doped with 1000 ppm OH (Heraeus Spectrosil) using a butane-oxygen flame, replicating the design from Fig. 3.1. One such taper was tested at a transmitted power of 180 mW, yielding a lifetime of 7 min. The test was stopped in a moment in which the PER was close to zero (0.22 dB). Five days later, the PER was still almost unchanged (0.31 dB), and the fiber output immediately continued to be in an unstable regime upon continuation of the test. A reference fiber of Heraeus F300 glass (≤ 1 ppm OH, standard used for all other samples) yielded a lifetime of 11 min at the same transmitted power. Although it is unclear how well a high OH-content is preserved during the fiber and taper drawing processes, it is concluded, that an increased OH content of the core does not lead to a measurable increase in lifetime. A substantial acceleration of the annealing process was also not found.

Cooling during irradiation

In [121], color-center formation is reported to have a very strong temperature dependence between 0 °C and 100 °C, with a drastically lower solarization rate at lower temperatures. Similarly, in [122] color-center formation could be slowed down by a factor of three, just by blowing cold nitrogen gas at 0 °C against the sample. This is explained by the fact, that the first transient reaction step is the formation of an exciton, that can either recombine radiatively without any further consequences, or decay non-radiatively forming a color center. The relative likelihood of the two alternative reaction paths is temperature dependent.

For a test, the ambient temperature of a tapered PCF was reduced by putting its taper waist and transitions between two pads filled with cooling gel. A Pt-temperature sensor between the two pads indicated 0 °C over the full time span. The 3 cm long fiber end at the input had to be connectorized, with collapsing of the air-holes, in order to prevent water from being condensed on the fiber surface, and soaked into the air-holes. The connector provided good thermal contact to the mount, keeping the fiber end at close to room temperature. The fiber was tested at a transmitted power of 156 mW with a lifetime of 22 min. An identical fiber was tested without cooling at 24.5 °C, at the same transmitted power, yielding an identical lifetime of 22 min. The lower temperature obviously did not enable a measurably longer lifetime. The reason for this could be, that the fiber core is heated by the transmitted light to a temperature significantly above ambient, where the temperature dependence of the color-center formation rate is less pronounced [121].

The influence of tapering parameters

It is a known fact, that the drawing conditions of optical fibers have an influence on their inclination to form color centers [138, 139]. The reason is, that strained Si-O bonds act as precursors of color centers, as they can be split more easily, which can be understood as a local reduction of the band-gap. The number of these strained bonds depends on the conditions from which the glass has been cooled down [118].

We test the dependence of the taper lifetime on taper drawing conditions by using a thermoelectric oven for fiber tapering. The temperature of the heater inside the oven was measured with a pyrometer, and adjusted with its electric current. In the following we specify the temperature inside a 1 mm wide groove in the heater, within which the fiber is guided during taper drawing. The temperature of the fiber itself at this position is not known, but should be close to this value. The tapers drawn with this setup had a waist length of 20 cm. The other parameters closely follow the design in Fig. 3.1.

Lifetimes of tapers drawn at different temperatures are listed in Tab. 3.2. It can clearly be seen, that the lifetimes increase with drawing temperature. The only exception is a taper drawn at 1510 °C, which was drawn at 4-fold speed relative to the other tapers. As a consequence, the glass was exposed to the heat for a shorter time, and the fiber was exposed to a higher strain during the drawing process, as measurable with a force sensor integrated in the setup.

Table 3.2 – Influence of taper drawing parameters (two leftmost columns) on the measured lifetimes at the indicated transmitted optical powers.

Temp. [°C]	speed	opt. power[mW]	lifetime [min]
1467	×1	115	12
1483	×1	115	50
1486	×1	115	72
1497	×1	115	100
1510	×4	115	61
1529	×1	127	>1050

The taper drawn at the highest temperature (1529 °C), was tested at a transmitted power of 127 mW, yielding a -20 dB-bandwidth of the broadened output of 146 nm. It exhibited stable behavior over 17.5 h, after which the test was aborted without having exceeded the PCF lifetime.

Tapering at even much higher temperature is not straight-forward, because the air-holes of the PCF tend to collapse when the glass becomes too soft. It is possible to prevent this collapse by controlling the gas pressure inside the air holes [140], but with higher temperatures it becomes increasingly difficult to find the right pressure to keep the hole size stable. With this technique, tapers with lifetimes exceeding 24 h at good spectral broadening could be demonstrated, which was the best we could achieve. This shows, that the right choice of drawing conditions can increase the taper lifetime by up to 2 orders of magnitude.

Heat treatment before tapering

The results from optimization of taper drawing parameters are in very good agreement with the common theory, that strained chemical bonds act as precursors of photoinduced damage. Drawing the tapers slowly and at high temperatures seems to result in a lower concentration of precursors. This however leaves the open question, whether these precursors are induced by the drawing process (e.g. by the exerted strain), or whether the precursors are already contained in the glass before the tapering process. In the latter case, the taper drawing is thought to reduce the precursor concentration by permitting a structural relaxation of the glass.

In order to clarify the above question, the lifetimes of two tapers are compared. The first taper undergoes a heat treatment before tapering, which consists of sweeping the oven at 1540 °C over the region to be tapered for 60 min. The temperature of the oven is then reduced to 1480 °C for drawing of the taper. The second taper is drawn at the same temperature, but without previous heat treatment. Both tapers were tested at a transmitted power of 160 mW, with a lifetime of 258 min for the first taper and 38 min for the second one, as shown in Fig. 3.9. If the precursors were only produced in the tapering process, the heat treatment prior to tapering should have had no effect. However, it increased the lifetime by a factor of 6.7. The experiment was repeated, with an increase in lifetime of 7.6 in the second experiment. This shows, that a substantial portion of the precursors originates from the production of the PCF or even from the production of the glass for its preform. A more extended heat treatment than described here was found to make the fiber very fragile, similar to what described on page 51, which leads to breaking of the fiber during the tapering process.

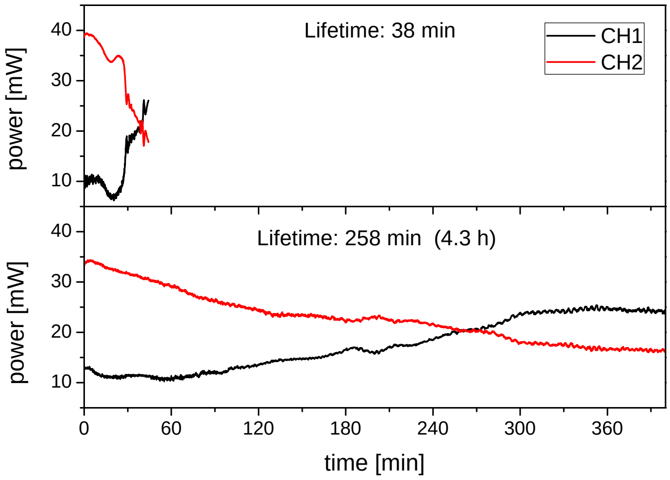

Figure 3.9 – Influence of a heat treatment prior to fiber tapering on PCF lifetime. Top: No heat treatment. Bottom: 60 min heat treatment at 1540 °C. The tapers were drawn at 1480 °C and tested at a transmitted power of 160 mW.

H_2-impregnation / F-doping

A technique that has been very successful in suppressing solarization in UV applications of fused silica bulk glass and fibers is the impregnation of the glass with H_2 [123, 137]. This is accomplished by exposing it to a H_2 atmosphere at high pressure and temperature over an extended period of time. This results in interstitial H_2 molecules within the glass matrix, that have a high degree of mobility, and terminate the dangling bonds of color centers by forming OH groups on them. For samples as thin as a tapered fiber, it is however of particular importance to store the H_2-loaded sample at very low temperatures (e.g. -90 °C) before using it for laser transmission, to prevent the H_2 from diffusing out in the meantime [137]. Even though it could be shown in many studies, that H_2-impregnation very effectively suppresses the build-up of color-center absorption, it is unclear, whether it also suppresses the associated birefringence, which in our case is a major source of problems.

Another very successful technique for suppressing color-center formation in fused silica is fluorine-doping [124, 133]. Fluorine, similar to OH, modifies the glass network by forming terminated O-F and Si-F bonds. Contrary to OH, the fluorine bonds are stronger than even Si-O bonds and cannot easily be dissociated. The modification of the glass network lowers the viscosity of the glass and allows relaxation of local stress. Fluorine also preferentially attaches itself to strained bonds. This reduces the concentration of color-center precursors. It has been shown, that F-doping of 1 mol% is very efficient in reducing color-center formation [124]. Preliminary tests of tapered PCFs with an F-doped core appear to yield promising results. Using F-doped glass also for the surrounding hole-structure might further enhance the durability by prohibiting the light from reaching the undoped regions, and by avoiding stress at material interfaces.

Combining several approaches

It might be possible to overcome the lifetime issue by combining several approaches. In [138, 139] for example, long-lived multimode fibers for excimer-laser transmission could be implemented by a combination of optimized drawing conditions, H_2 impregnation, and F-doping. In our case, optimized drawing conditions might increase the lifetime of a strongly birefringent

PCF by 2 orders of magnitude, as it was the case for the lowly birefringent PCFs. This could result in lifetimes that exceed the annealing time of the induced defects at room temperature. This however adds complexity, as several parameters have to be controlled successfully at the same time. The highly birefringent PCF in Fig. 3.8 for example, cannot easily be drawn at high temperatures, because the two smaller air-holes next to the core tend to collapse very easily. Further, the effects of several combined strategies might not be additive. If, for example, F-doping already leads to a good structural relaxation of the glass, then optimized drawing conditions might not add very much upon this. So far, a breaking success from a combination of several concepts has eluded us.

3.3 Spectral broadening of infrared astro-combs

Another strategy to prevent photoinduced damage consists of broadening the infrared, amplified 18 GHz astro-comb directly, without the intermediate step of SHG. In this case, the comb spectrum has to be broadened so strongly, that its short-wavelength side covers a wide portion of the visible spectral range. The photon energies of the pump pulses in this scenario are much lower than in broadening of green ultrashort pulses, making the formation of color centers an even higher-order multiphoton process. The generated visible light consists of dispersive waves in the normal GVD regime, that rapidly spread in time, and are thus not likely to provide high enough peak powers for color-center formation.

The main challenge in driving such massive spectral broadening with an 18 GHz pulse train is the handling of thermal power, resulting from the fairly high average optical powers that need to be transmitted through a small PCF core. PCFs made of SF6 glass provide about 10 times higher nonlinearity than those made of fused silica, and can therefore provide very broad output spectra at extremely low pulse energies [141]. SF6 however softens at significantly lower temperature than fused silica, and can therefore melt down very easily when confronted with the high average powers required for astro-comb generation. Fused silica is therefore still the material of choice. In the tests presented here, the nonlinearity of fused silica PCFs is enhanced by adding germanium as a dopant to the core material.

The fact that the visible part of the broadened spectrum is made of dispersive waves comes with a minor obstacle. As the fiber-optic analog to Cherenkov radiation, dispersive wave generation is bound to a phase-matching condition, which is why most of its power is usually concentrated around a narrow spectral peak. It has been shown, that with very short pulses (~ 10 fs) the spectra of dispersive waves can be broader than usual [142,143], but phase matching is still a factor that restricts the bandwidth. We solve this problem by using a tapered PCF. Along the taper transition, the core width and therefore the fiber dispersion changes, and with it the wavelength at which phase matching occurs. This distributes the generated dispersive waves over a wide spectral range. This concept had already been applied in [36,95], to extend a Ti:sapphire frequency comb with a < 10 fs pulse duration and a 1 GHz repetition rate into the visible. This was followed by an increase of the mode spacing to 20 GHz by two Fabry-Pérot filter cavities. In our case, all parameters of the spectral broadening are much more extreme: The repetition rate is higher (18 GHz), pulse duration is longer (100 fs), and the pump wavelength lies further in the IR (~ 1055 nm).

It can be very difficult to achieve stable fiber coupling when injecting several W of average power into a bare small-core PCF. Therefore, the input side is connectorized for the tests presented here, as shown in Fig. 3.10(a). This involves collapsing of the air holes over the first ~ 125 µm. This has the additional advantage of reducing the intensity on the air-glass interface of the fiber facet, which protects it from attracting and combusting dust particles by optical tweezing. This is otherwise considered a common damage mechanism [36]. Figure 3.10(b)

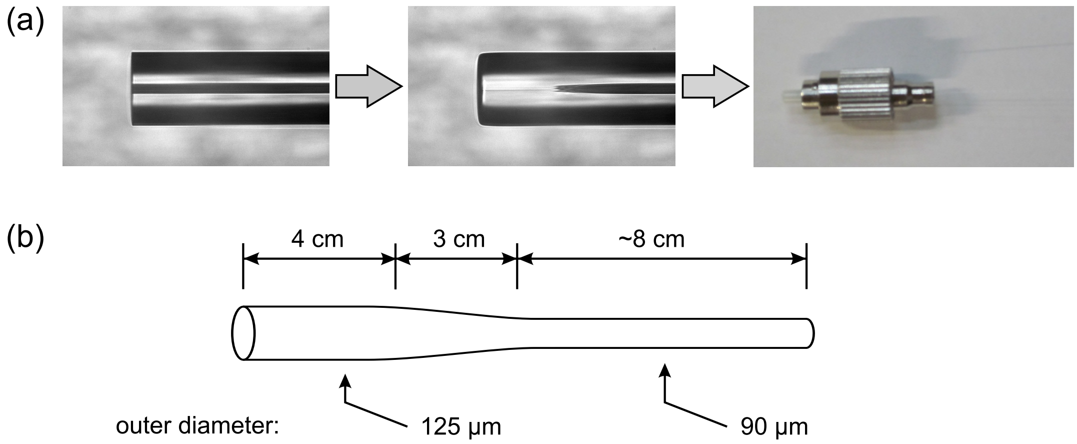

Figure 3.10 – Tapered photonic crystal fiber (PCF) for broadening of infrared astro-combs into the visible range. (a) Steps in processing the PCF input facet: Sealing of air holes and polished integration into an FC/APC connector. (b) Design of the fiber taper.

depicts the design of the fiber taper. The outer fiber diameter is reduced only slightly, from 125 µm to 90 µm, over a length of 3 cm. Before and after this transition, there are pieces with constant fiber diameter of 4 cm and ~8 cm in length. These pieces could have been kept shorter, but a decent length was chosen for convenience.

The untapered fiber is available with different core diameters (around 2 µm), and thus with different zero-dispersion wavelengths. Figure 3.11(a) shows the dispersive waves generated from some of these PCFs, and how the characteristic peak in the normal GVD regime depends on the zero-dispersion wavelength. For a tapered fiber, it is expected that the dispersive wave gets distributed over this range. Figure 3.11(b) shows the full bandwidth generated with an untapered PCF. The broadened spectrum covers a large range in the infrared region, and may also be useful for astronomical spectrograph calibration in the IR. For these PCFs, coupling efficiencies of up to 80 % were reached. The higher coupling efficiencies as compared to the case of broadening of green ultrashort pulses is due to the fact, that here beam profile is not distorted into an elliptical shape by SHG.

When using tapered PCFs for broadening of infrared pulses, as outlined above, an unexpected behavior is observed: Already at relatively modest transmitted powers of around 1 W, a strong green output starts to appear. This green light does not appear immediately, but builds up slowly over a time of about 10 s. The green spectrum is about 50 nm broad and exhibits rapid fluctuations, as shown in Fig. 3.12(b). Its polarization was however found to be approximately linear and stable. When turning down the power amplifier, leaving 10 mW transmitted through the PCF, a narrowband green output persists, that exhibits features of SHG (Fig. 3.12(a)). In order to clarify, whether SHG is in fact present within these fibers, a beat measurement with a cw laser was carried out. The cw laser was locked at $f_l = 20\,\mathrm{MHz}$ from a comb mode of the infrared astro-comb. It was then frequency-doubled, and a beat note with the visible output of the tapered PCF was recorded. If the visible PCF output is generated by SHG, the resulting beat note is expected at $2\,f_l$. If on the other hand it is created by dispersive wave generation, the beat is expected at $2\,f_l + f_0$, where f_0 is the offset frequency of the infrared astro-comb. As shown by the inset in Fig. 3.12(a), a clear beat at 40 MHz was observed, with all the signatures of the fast analog phase-lock used to control the frequency of the cw laser. A second beat note was not found.

It is thus concluded, that the PCF generates the green spectrum through SHG of the

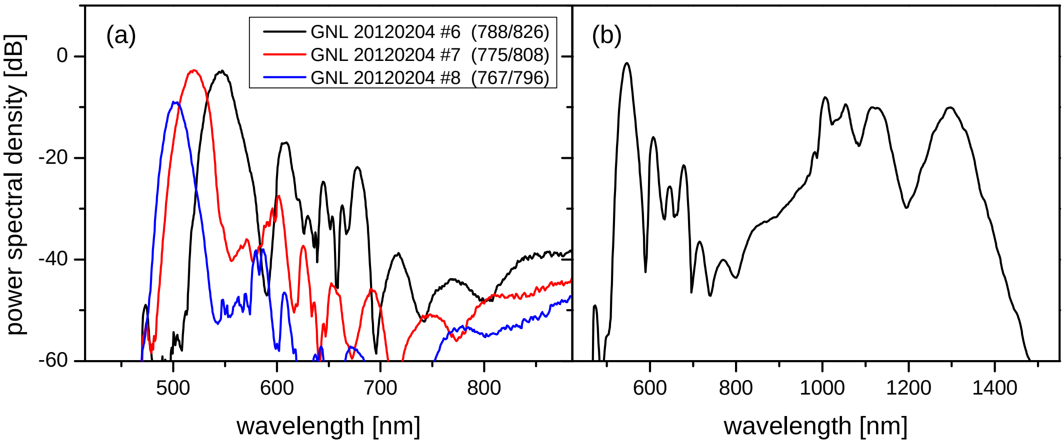

Figure 3.11 – Broadened spectra from untapered photonic crystal fibers (PCFs) with Ge-doped cores of different sizes. The spectra were broadened from an astro-comb at 1055 nm and a repetition rate of 18 GHz. Transmitted power: 5 W. (a) Dispersive-wave region for different core diameters, and hence different zero-dispersion wavelengths. The legend shows the PCF identification number (Menlo Systems) and the zero-dispersion wavelengths of the two polarization axes in brackets (the first value was used). (b) Full broadened spectrum with a zero-dispersion wavelength of 788 nm. The infrared part has been slightly attenuated.

infrared part. SHG in optical fibers has been observed before [144, 145], through inscription of a periodic poling that phase-matches SHG. In these experiments, an infrared laser was injected into the fiber together with its second harmonic. Through the interaction of the two wavelengths, optical rectification becomes a $\chi^{(3)}$-process. This writes a periodic poling into the material, with precisely the right period to phase-match SHG. The second harmonic at the fiber input can then be removed, and the second harmonic at the output persists. In our case, this process may occur spontaneously, in a self-organized fashion, seeded from noise or from a very weak dispersive wave at about the right wavelength. The fluctuations in the output spectrum at higher powers may reflect the self-organized nature of the periodic poling. The broad bandwidth may at least partly be due to cross-phase modulation between the second harmonic and fundamental waves as in [144].

Using this mechanism to generate a broadband visible astro-comb is undesirable, not only because of the fluctuations of the visible spectrum. The process of SHG doubles the offset frequency. So, if there is a weak dispersive wave at about the same wavelength, this constitutes an interleaved second frequency comb that might disturb astronomical spectrograph calibration. Further, with the infrared and the visible parts having different offset frequencies, it is currently not clear, how cross-phase modulation between the two might disturb the overall comb structure.

It is striking, that SHG in fibers has so far only been observed in doped fiber cores, notably in Ge-doped fibers [144, 145]. Ge-doped fused silica (germanosilicate) is much more photosensitive than pure fused silica, with green cw light already enabling the inscription of refractive index gratings. It must therefore be assumed that in our case, the periodic poling was enabled by Ge-related defect formation.

The formation of a second harmonic was found to be absolutely reproducible with all tapers drawn with a butane-oxygen flame. It is however also remarkable, that SHG is not observed with any of the untapered Ge-doped PCFs. This suggests, that the photosensitivity is enhanced by tapering the PCFs. Using a hydrogen flame for taper drawing, which entails a higher

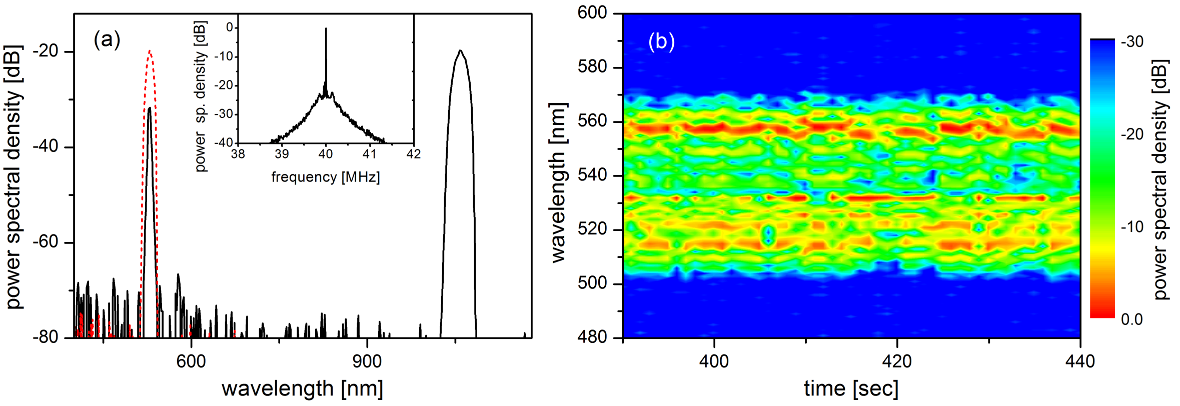

Figure 3.12 – Second-harmonic generation inside a tapered PCF with a Ge-doped core. Repetition rate: 18 GHz. (a) Output spectrum at 10 mW transmitted power. The infrared part is attenuated relative to the visible part. The red dashed line is the theoretical SHG of the infrared part. Inset: Beat note between the visible PCF output and the second harmonic of a cw laser, whose fundamental frequency is locked at a distance of 20 MHz from a comb mode of the infrared comb. (b) Time evolution of the visible PCF output at a transmitted 1.3 W. Temporal resolution: 1 s.

temperature of the heat zone as compared to a butane-oxygen flame, resulted in tapered PCFs that obviously did not generate a second harmonic, which reinforces this conclusion. Similarly to the case of photoinduced damage laid out in the previous section, stressed chemical bonds might be the precursors of the Ge-related defects. As with many topics related to defect formation in glass, the understanding of this subject currently remains incomplete.

Figure 3.13 shows the visible part of the spectrum generated with a PCF taper that was drawn with a hydrogen flame. Two distinct spectral maxima can be seen on both sides. They are supposed to stem from the fiber sections with constant diameter before and after the taper transition. The spectral portions between those maxima, generated inside the transition, should depend on the shape of the taper. Therefore, with further optimization of the taper geometry, it should be possible to make this spectrum more homogeneous. Work on this matter is in presently in progress, and Fig. 3.13 is only to be seen as a first, intermediate result.

The results presented here demonstrate, that a big part of the visible range can in fact be covered through dispersive-wave generation from an initially infrared astro-comb. Although damage on the entrance facets was found to be a common problem with the PCFs used, despite connectorization, very promising work on this matter is currently in progress. The results also show, that Ge-doping to enhance dispersive-wave generation should be used with great caution. To be sure that no unwanted second harmonic is generated within the fiber, which might disturb astronomical spectrograph calibration, it appears recommendable to use pure fused silica as a core material.

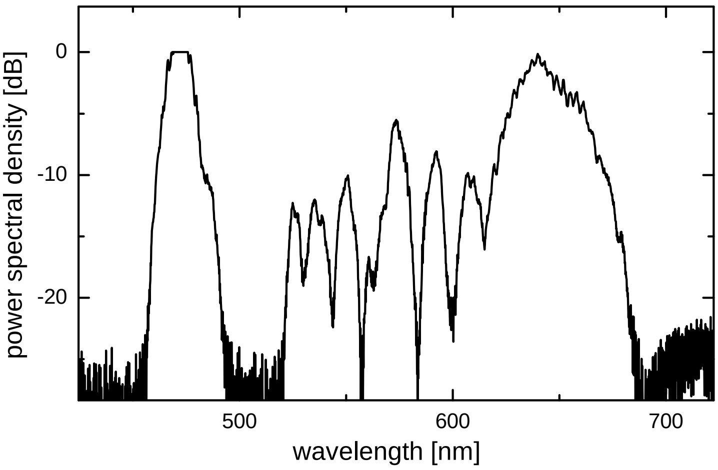

Figure 3.13 – Visible part of a 18 GHz frequency comb, broadened from 1055 nm in a tapered PCF with a Ge-doped core, and measured with a Thorlabs CCD spectrometer. The taper has been drawn with a hydrogen flame. Coupled power: 5 W.

Chapter 4

Amplification of side-modes through nonlinear processes

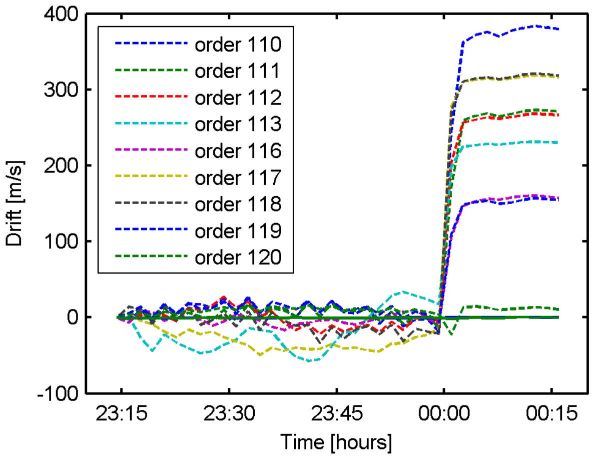

Figure 4.1 – Calibration drift measured on the HARPS spectrograph in March 2010. One channel carries a broadened green astro-comb (dashed lines) while the other one carries its unbroadened green output (solid lines). At 23:58, the average line positions of the broadened comb were shifted abruptly, probably due to realignment of the tapered photonic crystal fiber that broadens the spectrum. The measurement was carried out by Wilken and coworkers [25,146], just before the start of the present work. They used an earlier version of the astro-comb with lower side-mode suppression.

As already pointed out in previous chapters, astronomical spectrographs require astro-combs to provide multi-GHz mode spacings, due to their spectral resolution. In our approach, this comb structure is synthesized from a source comb with initially more densely spaced modes, by filtering it through a series of Fabry-Pérot cavities (FPCs) that resonantly transmit only every m^{th} mode (see Chapter 2). In this scheme however, the unwanted modes, or side-modes, are not suppressed perfectly, and are still weakly contained in the filtered comb. Astronomical spectrographs normally do not resolve the side-modes from their adjacent principal modes (the comb modes that are sought to be transmitted through the FPCs). Therefore, the frequency of a calibration line as it appears on the spectrograph CCD is approximately given by the centroid of a group of modes, consisting of a principal mode and its surrounding side-modes. If the side-modes are suppressed insufficiently and asymmetrically around a principal mode, they can shift the line centroid, which results in calibration errors [29,33,92].

An important caveat is that nonlinear optical processes can reduce side-mode suppression. The side-modes are thus amplified relative to their adjacent principal modes, which we define as side-mode amplification. The importance and potential severity of this issue is exemplified by the results of an astro-comb test campaign at the HARPS spectrograph in March 2010. At that time, just before the start of the present work, Wilken and coworkers tested an astro-comb very similar to the one described in Chapter 2, but with lower side-mode suppression [25]. While this astro-comb provided a stable calibration within the expected 0.1 m/s without spectral broadening, the calibration of the broadened comb was subject to tremendous drifts of up to 400 m/s (see Fig. 4.1). Shortly after these results, it was shown both experimentally [30, 31, 39, 146] and in numerical simulations [92, 93], that spectral broadening in nonlinear fibers can dramatically re-amplify side-modes. Prior to this, it had already pointed out by [25], using a few theoretical arguments, that second-harmonic generation (SHG) re-amplifies side-modes. All of these nonlinear frequency conversion processes are however most conveniently performed after mode filtering, because power losses from the mode filter can otherwise not easily be compensated by a subsequent amplifier, and because filtering a very broad spectrum is technically difficult due to intra-cavity dispersion of FPCs.

Therefore, side-mode amplification through nonlinear optical processes deserves careful consideration. This chapter is devoted to an in-depth study of this aspect, both theoretically with a simplified model, and experimentally using highly sensitive heterodyne measurements on different astro-combs. The model predicts a 6 dB side-mode amplification for SHG, which is confirmed experimentally. The growth due to spectral broadening, in contrast, can be much stronger, asymmetric around the principal modes, and generally increases with nonlinear propagation length. An upper limit for this effect is derived in this chapter, which is confirmed by heterodyne measurements. This upper limit is of particular interest for spectrograph calibration, where it guarantees a certain calibration precision, regardless of any asymmetry in side-mode suppression. The model developed here can also be used for other purposes, e.g. to describe noise amplification in frequency combs, which is a related problem as explained in [92], or to describe side-mode amplification through self-phase modulation (SPM) in fiber amplifiers, which has been done in a similar way in [93].

4.1 Theoretical model

Side-mode amplification through spectral broadening in nonlinear fibers can be modeled very comprehensively by numerically solving the generalized nonlinear Schrödinger equation, as done by Chang et al. [92, 93]. These simulations are quite realistic and contain effects such as fiber dispersion, SPM, self-steepening and stimulated Raman scattering. However, such complex computer models can often obscure the underlying physics, and at times a more simplistic model can enable a better understanding. We also believe that the exact parameters of a real system are hard to grasp in a computer simulation.

Therefore, our model takes into account SPM and SHG only, and in particular neglects effects that generate side-mode asymmetries. Since in practice it would be difficult to control asymmetry with sufficient accuracy, we assume maximum asymmetric side-modes to estimate the calibration errors (see Eq. (2.3.5)). Our approximation yields compact expressions for side-mode amplification and spectral broadening, that are valid in the regimes of interest. These regimes assume sufficient initial side-mode suppression and a nonlinear optical fiber limited in length to where spectral broadening comes to a halt (to avoid solitonic effects). An upper limit on side-mode amplification is derived, that allows estimating the required side-mode suppression after mode filtering. We verify that our approximations are useful by comparing the results with experimental data and with full-fetched split-step Fourier method,

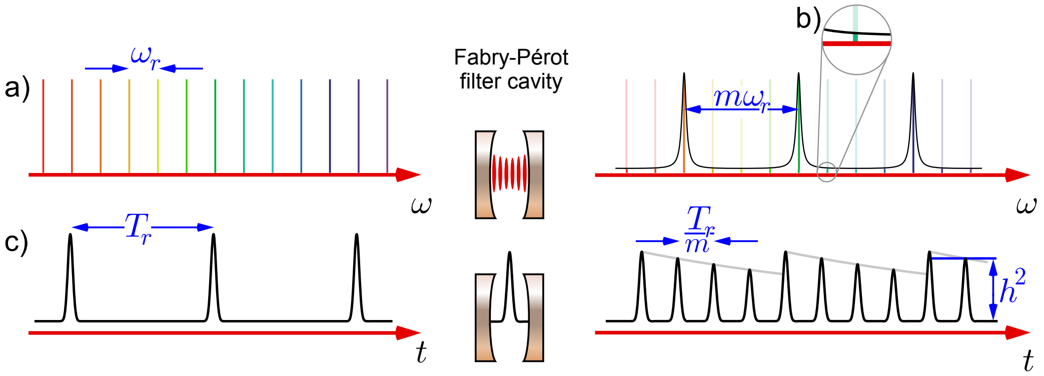

Figure 4.2 – (a) Frequency domain: A Fabry-Pérot cavity is used as a spectral filter. Its free spectral range is an integer multiple (here $m = 4$) of the initial mode spacing $\omega_r = 2\pi/T_r$. (b) The finite finesse of the cavity leads to unwanted side-modes to each principal mode. (c) In the time domain the pulse stored inside the cavity gets replenished by the next pulse from the initial pulse train only every m^{th} round trip. The finite finesse leads to an exponential decay of the pulse energy between these events with a normalized electric field reduction h. The resulting amplitude modulation causes the side bands to appear.

which takes dispersion into account, as well as testing higher filter ratios $m > 2$, for which the cavity transmission phase causes asymmetries. We also explain, why effects such as stimulated Raman scattering, self-steepening, and guided acoustic-wave Brillouin scattering (GAWBS) can be neglected in our description.

As a starting point, we consider the time-domain and frequency-domain descriptions of a frequency comb with side-modes. A source comb is filtered by the almost periodic transmission function of an FPC, with its free spectral range (FSR) set to an integer multiple m of the mode spacing of the source comb. This suppresses all but every m^{th} mode of the initial frequency comb, multiplying the repetition rate accordingly (see Fig. 4.2). For a perfectly mode-matched, dispersion-compensated cavity with finesse F, the suppression factor of the strongest side-mode is approximated by Eq. (2.3.3).

In the time domain, the finite side-mode suppression is expressed by a decline in field amplitude from one pulse to the next, until the pulse circulating within the FPC is replenished by the next input pulse (see Fig. 4.2). From this time domain image, the comb structure can be inferred by Fourier transformation as in Sec. 1.1. To keep our treatment as simple as possible, we assume a zero offset frequency, and consider a filter ratio of $m = 2$, which corresponds to a train of alternating strong and weak pulses. The weak pulses are weaker in field amplitude by a factor of $h \leq 1$. The associated comb structure has only one side-mode between two principal modes. Under these conditions the side-modes are essentially symmetric by construction. The initial side-mode suppression[1] $\varrho_i\,(h)$ in this scenario is derived by dividing the alternating pulse train into double pulses. The electric field of such a double pulse is inserted as E_1 into Eq. (1.1.2). The calculation then proceeds in analogy to Eqs. (1.1.3) and (1.1.4), yielding:

$$\varrho_i(h) \equiv \frac{(1+h)^2}{(1-h)^2} \tag{4.1.1}$$

This result can intuitively be understood as a spectral interference: The term $(1+h)^2$ is the constructive interference of the spectra of the two subpulses, while $(1-h)^2$ is their destructive interference. A train of identical subpulses with $h = 1$ corresponds to infinite side-mode

---

[1] Throughout this work, the suppression is always measured in terms of optical power, not field amplitude.

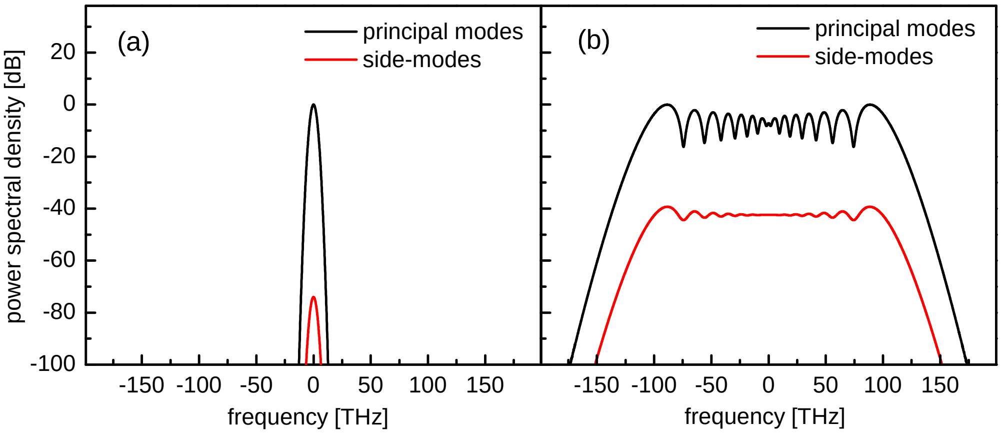

Figure 4.3 – Spectral envelope of the principal modes (black line) and interleaved side-modes (red line), for a filter ratio of $m = 2$ and an initial suppression of 74 dB. The optical pulses are initially transform-limited with 100 fs FWHM pulse duration and Gaussian shape. (a) Before nonlinear propagation. (b) After nonlinear propagation over a distance of 44 times the nonlinear length.

suppression $\varrho_i(h = 1) = \infty$, whereas a finite suppression is obtained for $h < 1$. Our model for side-mode amplification incorporates the main physical mechanism for spectral broadening in nonlinear fibers, which is SPM. To derive the resulting side-mode gain, we consider Gaussian pulses with a normalized electric field amplitude before nonlinear propagation ($z = 0$) given by [110]:

$$U(z=0,T) = \exp\left[-\left(1+i\,C\right)\frac{T^2}{2T_0^2}\right] \tag{4.1.2}$$

where $T = t - z/v_g$ is the time in a retarded reference frame, with the time t, the propagation length z, and the group velocity v_g. C is the temporal frequency-chirp, and $T_0 = T_{\mathrm{FWHM}}/\left[2\sqrt{\ln(2)}\right]$, with the full-width at half-maximum (FWHM) pulse duration T_{FWHM} of the optical power of the pulse. The propagation length z determines the intensity-dependent nonlinear phase ϕ_{NL}:

$$U(z,T) = U(0,T)\exp\left(i\,\phi_{\mathrm{NL}}\right), \qquad \phi_{\mathrm{NL}} = \left|U(0,T)\right|^2\frac{z}{L_{\mathrm{NL}}} \tag{4.1.3}$$

with the nonlinear length $L_{\mathrm{NL}} = (\gamma P_0)^{-1}$, the peak power of the pulse P_0, and $\gamma = n_2\omega_c/cA_{\mathrm{eff}}$ as defined in [110] with the nonlinear refractive index n_2, the optical carrier frequency ω_c and the effective beam cross section A_{eff}. A typical value of γ for the experimental conditions described in Sec. 4.2 is 1 W^{-1} m^{-1} [147], such that for 50 W peak power pulses the nonlinear length is 2 cm. The spectral envelope of such an alternating pulse train after SPM is obtained by Fourier transformation, where the time shift of the weaker pulse of half the repetition period T_r can be taken into account via the shift theorem. Its nonlinear phase shift is smaller by h^2, which can be included in the effective propagation distance. To calculate the power spectral density $S(\omega)$ at frequency ω after SPM, it is sufficient to consider a single repetition of the optical pulse sequence, here a double pulse:

$$S(\omega) = \left|\int\limits_{-\infty}^{+\infty}\left[U\left(z,T\right) + hU\left(h^2 z,T\right)\exp\left(i\omega\frac{T_r}{2}\right)\right]\exp\left[i\left(\omega-\omega_c\right)T\right]dT\right|^2 \tag{4.1.4}$$

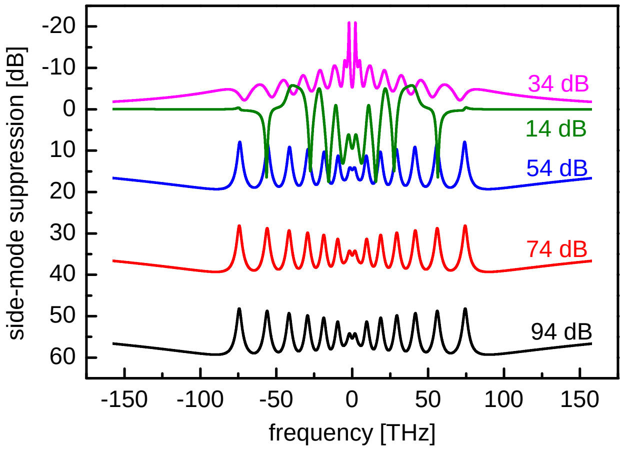

Figure 4.4 – Side-mode suppression versus optical frequency after propagation over 44 times the nonlinear length for different values of the initial side-mode suppression. The initial suppression is written at each curve, and the filter ratio is $m = 2$. The optical pulses have a 100 fs FWHM pulse duration with a Gaussian envelope and no initial chirp.

To compute this integral with a strongly oscillatory integrand numerically, we found the Runge-Kutta-method with adaptive step-size control [148] or fast Fourier transformation [148] to be effective. The latter proved to be faster and more precise. For the principal modes, $S(\omega)$ is evaluated at frequencies $\omega = 2n\omega_r$, and for the side-modes at frequencies $\omega = (2n + 1)\omega_r$, with the repetition rate $\omega_r = 2\pi/T_r$ and integer mode number n. For the modeling we set the carrier frequency ω_c to zero as it only shifts the resulting spectrum.

To facilitate comparison with our experimental results presented in Sec. 4.3, we demonstrate the behavior for the following parameters: The initial suppression $\varrho_i(h)$ is set to 74 dB ($\Rightarrow 1 - h = 4 \times 10^{-4}$), the pulse duration to 100 fs FWHM with a repetition rate of $\omega_r = 2\pi \times 9$ GHz. The pulse duration is assumed to be initially transform-limited ($C = 0$), and the propagation length z is chosen to be $44\,L_{\mathrm{NL}}$. The resulting spectra before and after nonlinear propagation are shown in Fig. 4.3. Besides the obvious degradation of side-mode suppression, it can be seen, that SPM imprints a structure on the spectra, which is more pronounced for the principal mode spectrum than for the side-mode spectrum. Figure 4.4 shows the resulting side-mode suppression for different values of the initial suppression under otherwise identical conditions. For the interesting case of well-suppressed initial side-modes, we find that the amount and spectral structure of the side-mode amplification is independent of the initial suppression. Under these conditions the side-mode gain due to SPM is between 35 and 46 dB. For poorly suppressed initial side-modes the gain spectrum changes considerably, and we can observe the optical power to be transferred back to the principal modes.

The calculations were repeated for the filter ratios $m = 6$ and $m = 20$. For $m > 2$ the side-modes acquire asymmetric phase shifts upon transmission through the FPC which turn into asymmetric powers after SPM [92]. It was found that as long as the side-modes stay considerably weaker than the principal modes, the final powers of all side-modes can be very well approximated by the case $m = 2$, i.e. Eq. (4.1.4) with equal initial suppression. The approximation through $m = 2$ improves with larger initial side-mode suppression as the asymmetry of the side-mode gain decreases.

The investigation of the (usually unwanted) side-mode gain has to be complemented by the (usually wanted) spectral broadening, because both effects appear simultaneously. We quantify the width of the rather structured spectra by their root-mean-square-bandwidth (RMS-bandwidth), which is computed as the standard deviation of the power spectrum, see

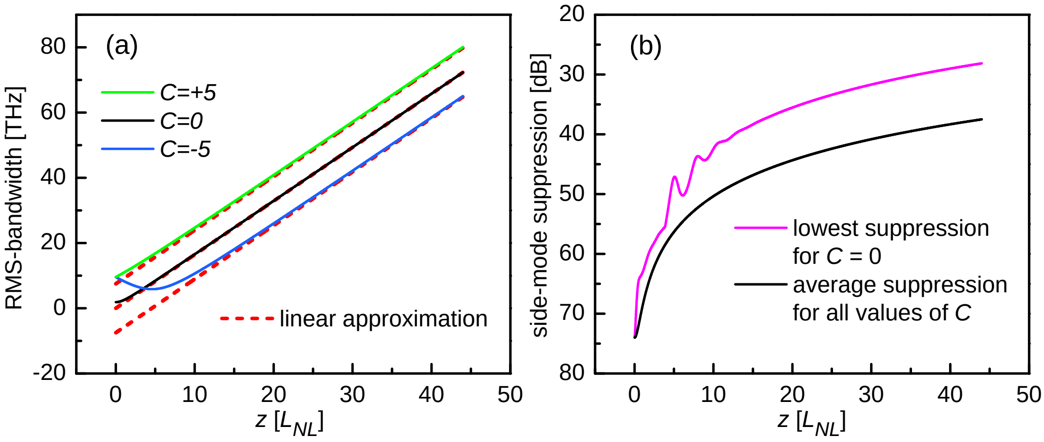

Figure 4.5 – (a) Evolution of the RMS-bandwidth as a function of the propagation length z for Gaussian pulses with 100 fs FWHM pulse duration, 74 dB initial side-mode suppression and different initial chirps C. Red dashed line: Approximation given by Eq. (4.1.6). (b) Evolution of the average side-mode suppression (independent of chirp and pulse duration) and the lowest side-mode suppression within the −20 dB-bandwidth for initially unchirped pulses.

Eq. (A.1.2) in the appendix. For the side-mode amplification, we average the power ratios of all side-modes relative to their adjacent principal modes, weighted by the power of each principal mode. The increase of this value measures the average side-mode amplification, and the inverse of this value is used to quantify the average side-mode suppression. Additionally, we identify the single side-mode with lowest side-mode suppression within the −20 dB-bandwidth of the overall spectral envelope. This can serve as an estimate for the worst-case side-mode suppression.

As demonstrated in the Appendix A.1, the evolution of the RMS-bandwidth with propagation length can be calculated analytically in the limit of high side-mode suppression. The evolution of the RMS-bandwidth Δf_{RMS} then is given by:

$$2\pi\,\Delta f_{\mathrm{RMS}} = \frac{2\sqrt{\ln(2)}}{T_{\mathrm{FWHM}}}\sqrt{\frac{1}{2}+\frac{C^2}{2}+\frac{C}{\sqrt{2}}\frac{z}{L_{\mathrm{NL}}}+\frac{2}{3\sqrt{3}}\left(\frac{z}{L_{\mathrm{NL}}}\right)^2} \tag{4.1.5}$$

For large propagation lengths z and small initial chirps C, Δf_{RMS} becomes linear in both z/L_{NL} and C:

$$2\pi\,\Delta f_{\mathrm{RMS}} \approx \frac{1}{T_{\mathrm{FWHM}}}\frac{2\sqrt{2\ln(2)}}{\sqrt{3\sqrt{3}}}\left(\frac{3}{4}\sqrt{\frac{3}{2}}C+\frac{z}{L_{\mathrm{NL}}}\right) \tag{4.1.6}$$

The last two equations are compared in Fig. 4.5(a) for $C = +5$, $C = 0$ and $C = -5$. Notice that in Fig. 4.5, the pulses have identical pulse durations $T_{\mathrm{FWHM}} = 100$ fs but different transform limits, depending on the value of the initial chirp C. $C = \pm 5$ corresponds to 5 times the transform-limited time-bandwidth product, or in this case to a transform limit of 20 fs FWHM. We see, that the linear approximation given by Eq. (4.1.6) is quite good except for the first few nonlinear lengths.

The average side-mode amplification is quantified by the amplification factor A_{avg}. Similarly to Δf_{RMS}, its evolution with z/L_{NL} can be obtained analytically (see Appendix A.1), and is found to be given by:

$$A_{\mathrm{avg}} = 1+\frac{4}{\sqrt{3}}\left(\frac{z}{L_{\mathrm{NL}}}\right)^2 \tag{4.1.7}$$

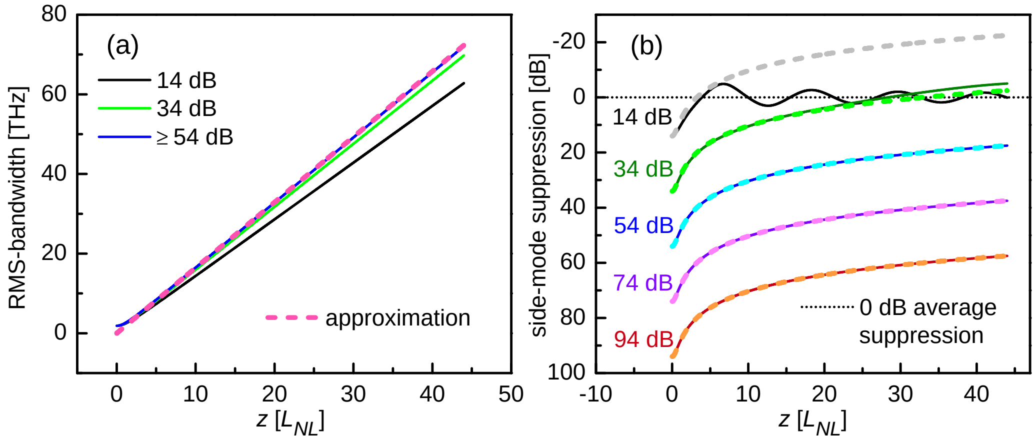

Figure 4.6 – (a) RMS-bandwidth versus propagation length for different initial suppressions. For initial suppressions ≥ 54 dB the curves are virtually identical. The dashed line is the linear approximation given by Eq. (4.1.6). (b) Average side-mode suppression versus propagation length for different initial suppressions. Here, the dashed lines represent the approximation for high side-mode suppression given by Eq. (4.1.7). In all cases, the pulses are assumed to have a 100 fs FWHM duration, Gaussian shape, and no initial chirp.

This relation is an important conclusion of this chapter. Remarkably, it is found to be valid independently of pulse duration and chirp. As explained below, it is also independent of the initial side-mode suppression and fiber dispersion within reasonable limits. The average side-mode amplification can thus be obtained by solely determining the propagation length z in terms of L_{NL}. Later in this section, we show how to estimate z in terms of L_{NL} experimentally from the observed spectral broadening via Eq. (4.1.6). In contrast to the average side-mode suppression, the lowest side-mode suppression within the -20 dB-bandwidth depends on the initial chirp. For initially transform-limited pulses it is never more than 10 dB below the average suppression, see Fig. 4.5(b).

Equations (4.1.5)–(4.1.7) hold as long as the side-modes do not exceed the principal modes in power. This can be seen from Fig. 4.6, where the Eqs. (4.1.6) and (4.1.7) are compared with results from Eq. (4.1.4) for different initial suppressions. Significant deviations are observed in Fig. 4.6 as soon as the side-mode suppression approaches the 0 dB-level. As only the case of well-suppressed side-modes is suitable for practical applications, this is not a substantial limitation to the usefulness of Eqs. (4.1.5)–(4.1.7).

We now show how dispersion, which has been neglected so far, can be included in the above considerations. The main effect of dispersion is to alter the pulse duration and chirp. The resulting modulation of the peak power merely changes the nonlinear length L_{NL}. As A_{avg} is independent of pulse duration and chirp, the evolution of A_{avg} with z in terms of L_{NL} is expected to be unaffected by dispersion. The RMS-bandwidth, however, will no longer increase linearly while the pulse duration changes, as its slope scales with the inverse of T_{FWHM}, see Eq. (4.1.6). So, if dispersion monotonically stretches the pulses, the broadening will be smaller than the one given by Eq. (4.1.6), if T_{FWHM} is the initial FWHM pulse duration. On the other hand, if the pulses are compressed during propagation, the broadening will be larger. Spectral broadening usually only takes place in the latter scenario, as only then can nonlinearities be driven efficiently at moderate pulse energies. Pulse compression during propagation usually takes place in the anomalous group-velocity dispersion (GVD) regime, where the interplay of nonlinearity and dispersion can compress even initially transform-limited pulses.

In order to verify these simplifying arguments about the influence of dispersion, we use the

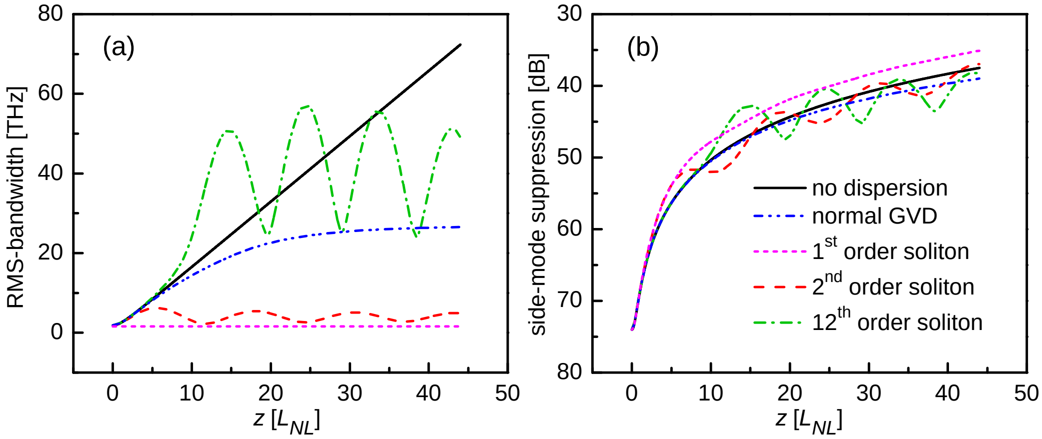

Figure 4.7 – Evolution of (a) the RMS-bandwidth and (b) the average side-mode suppression during nonlinear propagation for initially unchirped 100 fs-pulses in different dispersion regimes. The curve for normal group-velocity dispersion (GVD) assumes +25 fs^2 per initial L_{NL}. In the case of anomalous GVD, solitons of various orders are formed depending on the amount of GVD. The pulses are launched with a Gaussian shape except for the first-order soliton, which starts out as a sech^2 pulse.

split-step Fourier method [110], which can precisely describe nonlinear pulse propagation under dispersion. In this case, the value of L_{NL} changes during propagation due to changing peak power. Therefore, the propagation length in terms of L_{NL} is now given by $\int_0^z [1/L_{\mathrm{NL}}(z')]\, dz'$, which replaces z/L_{NL} in Eqs. (4.1.6) and (4.1.7). The fiber dispersion is quantified with respect to the initial nonlinear length. We assume a GVD of +25 fs^2 per initial L_{NL} for the case of normal GVD, and −25 fs^2 for anomalous GVD. In the latter case, the pulses evolve into 12$^{\mathrm{th}}$ order solitons. The evolution into a second-order soliton is obtained by assuming −1000 fs^2 per initial L_{NL}. We also simulated the propagation of an initial first-order soliton assuming −3220 fs^2 per initial L_{NL} and an initial 100 fs sech^2-pulse shape. Figure 4.7 shows the evolution of the RMS-bandwidth and average suppression for these regimes. We find, that the side-mode amplification follows the curve for non-dispersive propagation within ±5 dB in all cases. The deviation is probably due to the deformed pulse shape. The evolution of the RMS-bandwidth can generally be well understood by the above discussion, as long as soliton formation has not yet occurred. However, as soon as a soliton has formed, spectral broadening essentially stops, but side-mode amplification continues. In the case of higher-order solitons, we also observe oscillations of the RMS-bandwidth. These oscillations are not likely to occur in experiments, as higher-order solitons usually decay into fundamental solitons in more realistic scenarios [110].

The nonlinear fiber length and optical power should therefore be dimensioned in a way, that soliton formation, marked by a fast increase of optical bandwidth followed by a stagnation of spectral broadening, occurs just at the end of the nonlinear fiber. Furthermore, the input pulses should be transform-limited, as shorter pulses are expected to have a more favorable ratio of obtained optical bandwidth to side-mode amplification. Under these conditions, an upper limit on the propagation length in terms of L_{NL} is obtained from the observed spectral broadening via Eq. (4.1.6). In combination with Eq. (4.1.7) this gives an upper limit on the average side-mode amplification. Based on the results for the non-dispersive scenario, the lowest side-mode suppression is less than a factor of 10 below the average suppression. A worst-case estimation for the side-mode amplification A as a function of initial pulse duration T_{FWHM} and final RMS-bandwidth Δf_{RMS} can then be given as:

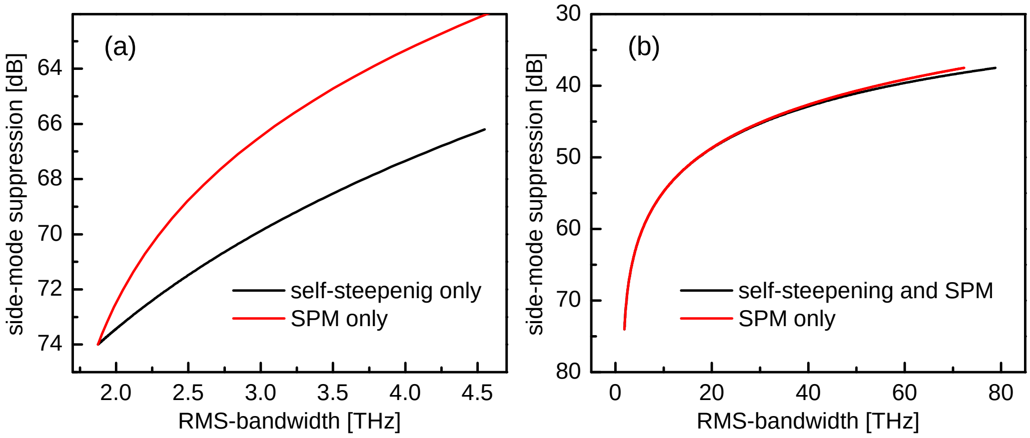

Figure 4.8 – Average side-mode suppression versus spectral bandwidth, with and without self-steepening and self-phase modulation (SPM). All other parameters are the same as in Fig. 4.3. (a) Comparison of pure self-steepening with pure SPM. (b) Comparison of a mixture of self-steepening and SPM with pure SPM. In all cases, the curve that includes self-steepening is below the one for pure SPM. This means, that for a given amount of spectral broadening, self-steepening amplifies the side-modes less than SPM.

$$A < 10 \left[1 + \frac{6\pi^2}{\ln(2)} \left(T_{\mathrm{FWHM}}\, \Delta f_{\mathrm{RMS}} \right)^2 \right] \tag{4.1.8}$$

The factor of 10 in Eq. (4.1.8) takes into account the spectral structure of the side-mode gain. This structure results from the fact, that during spectral broadening the spectrum develops modulations, that are more pronounced for the principal modes than for the side-modes, see Figs. (4.3) and (4.4). The largest peak-to-valley modulation in Fig. (4.3) is 16 dB, which leads to the factor of 10 in Eq. (4.1.8). For the broadened spectra reported in the experimental part of this work, this was about equal to the deepest modulations that have been observed. For spectra with significantly deeper modulations, the prefactor should be adapted accordingly. For example, a conservative estimation would be to replace the factor of 10 by the depth of the deepest dip in the measured spectrum.

Self-steepening, which has been neglected so far, is a higher-order nonlinear effect than SPM[2]. The bulk of the spectral broadening and side-mode amplification will therefore be caused by SPM. The split-step method makes it easy to incorporate self-steepening into our numerical model. Its main effect is to make the final pulse shape and spectral envelope asymmetric. We find, that the side-mode amplification through self-steepening is consistently lower than the one caused by SPM at equal spectral broadening, see Fig. 4.8. So, if we neglect self-steepening, and attribute the spectral broadening fully to SPM as done in Eq. (4.1.8), we overestimate the side-mode amplification, and the upper limit represented by Eq. (4.1.8) still holds.

The effect of stimulated Raman scattering (SRS) on side-mode amplification has been studied in [92]. It was found, that concerning side-mode amplification, SPM is the dominant mechanism over SRS. Similarly to what we find for self-steepening it can thus be concluded, that even if SRS is strong enough to contribute substantially to the spectral broadening, attributing the complete broadening to SPM overestimates the side-mode amplification, and Eq. (4.1.8) still holds.

---

[2] Self-phase modulation (SPM) refers to an intensity-dependence of the phase velocity, while self-steepening is an intensity-dependence of the group velocity [110].

Guided acoustic-wave Brillouin scattering (GAWBS) has been shown to be a very efficient gain mechanism in photonic crystal fibers (PCFs), transferring optical power from one spectral mode to another, if their relative optical frequency difference is in resonance with an acoustic mode of the PCF core [149]. The bandwidth of the acoustic resonances, and thus of the optical gain profile, however, is in the range of some MHz only. So, even in the situation, that a side-mode is inside the gain profile of a principal mode, the side-mode amplification can only be driven by one principal mode at a time. For our experimental conditions described in the next section, we estimate, that even under resonant conditions the gain provided for the side-modes is more than seven orders of magnitude lower than the gain provided by SPM, assuming the same gain coefficient as in [149].

As detailed in Sec. 2.4, SHG can be used to convert a filtered frequency comb into the visible spectral range. The second harmonic polarization $P^{2\omega}(t) = 2\epsilon_0\chi^{(2)}E^2(t)$, which mostly generates sum frequencies in this context, produces a frequency comb with the same mode spacing but doubles the offset frequency. To examine what happens to the side-mode suppression in this case, we again assume an alternating pulse sequence with $m = 2$. Assuming an undepleted pump wave, SHG scales with the square of the fundamental power such that the side-mode amplification is given by $\varrho_i(h)/\varrho_i(h^2) = 4 - \mathcal{O}\left[(1-h)^2\right]$. The side-modes are therefore amplified by 6 dB in power upon SHG, provided that the side-modes are sufficiently suppressed ($h \to 1$). The same is true for any other value of m.

4.2 Experimental setup

As shown in Fig. 4.9, our experimental setup consists of two parts: A filtered frequency comb for astronomical applications (astro-comb) and a heterodyne system used for side-mode characterization. The source of the astro-comb is a mode-locked ytterbium-fiber laser with a repetition rate of 250 MHz and a center wavelength of around 1030 nm. The mode spacing of the comb is increased in two steps using concatenated Fabry-Pérot cavities (FPCs) with a finesse of about 400. In order to stabilize the FPCs, an Nd:YAG continuous wave (cw) laser is phase-locked without an offset to a mode of the source comb. The FPCs are stabilized to the cw laser, using an orthogonal polarization, with the Pound-Drever-Hall scheme (see Sec. 2.3.3). Between the FPCs, an ytterbium-doped single-clad fiber amplifier compensates the losses in optical power due to the filtering. The filtered frequency comb is amplified to up to 8 W of average power by an ytterbium-doped double-clad fiber amplifier, that also shifts the center of the spectral envelope to about 1060 nm. The optical pulses are compressed to 100 fs FWHM pulse duration by a combined grating and prism compressor, and frequency-doubled in a 3 mm long LBO crystal with a conversion efficiency of up to 3 %. The frequency-doubled light is coupled into a tapered PCF with a 30 cm long uniform taper waist and a core diameter of around 540 nm in the tapered section (see Sec. 3.1). The coupling efficiency is about 50 %, resulting in up to 80 mW of spectrally broadened light with a −20 dB-bandwidth of 120 to 240 nm. A half-wave plate is used to control the polarization at the input of the PCF.

In the heterodyne system, an external cavity diode laser (ECDL) is used as a tunable cw source, which is locked with a +20 MHz offset to one of the comb modes. For this purpose, a fast analog phase-locked loop is employed, enabling a tight lock with a line width of the locked beat signal below 1 Hz [150, 151]. This extremely low line width enables an excellent signal-to-noise ratio in the heterodyne measurements, allowing the detection of even extremely weak side-modes.

The cw laser is amplified to 3 W of power in a two-stage ytterbium-doped fiber amplifier, and then frequency-doubled in a single pass through a 5 mm long $KNbO_3$-crystal. The resulting 1.5 mW of green light has a strongly astigmatic beam profile, which is compensated by a tilted

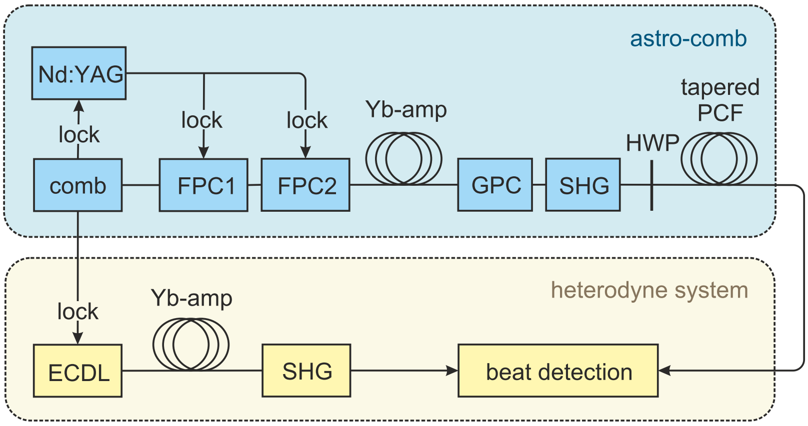

Figure 4.9 – Basic experimental setup of which several variations have been used in the experiments described here. Comb: 250 MHz mode-locked ytterbium-doped fiber frequency comb. Nd:YAG: Neodymium-doped continuous-wave laser. ECDL: External-cavity diode laser. Yb-amp: Ytterbium-doped fiber power amplifier. GPC: Combined grating and prism compressor. SHG: Second-harmonic generation stage. HWP: Half-wave plate. PCF: Photonic crystal fiber.

curved mirror and a lens. Finally, both the astro-comb and the green cw light are coupled through the same single-mode fiber for mode-matching with strong damping in the infrared (IR) and then focused onto a fast photodiode.

This setup was modified in several ways to characterize the effects of the individual nonlinear steps separately, and to adapt the system to the intended applications: First, the PCF and both SHG stages were removed, to measure the side-mode suppression in the IR. The effect of the SHG on the side-mode suppression was then investigated by reinstalling the SHG stages. Next, the PCF was added to see the effect of SPM. Finally, a third FPC was added to further suppress the side-modes. Moreover, different FPC filter ratios were used to characterize the system under the conditions intended for applications.

4.3 Experimental results

The measured heterodyne signal was analyzed with an RF spectrum analyzer. We compensated for the slightly frequency-dependent sensitivity and the noise level of our detection system, i.e. photodetectors and amplifiers. We observed a small random frequency shift in the range of ±25 Hz on the signal when using the amplifier of the astro-comb at high power[3], probably caused by insufficient stabilization of the pump diodes. Consequently we limited the resolution bandwidth of our measurements to 91 Hz when working with frequency-doubled light. This limited our capability to detect side-modes in the green to a maximum suppression of about 60 to 70 dB, as opposed to 80 to 100 dB in the IR.

We first used the heterodyne system to test the performance of the two FPCs, which were set to an FSR of 2.25 GHz and 18 GHz, respectively. The filter scheme employs an intermediate 2.25 GHz, to keep the filter ratio in each filter step low enough to provide sufficient seed power for the optical amplifiers between the FPCs. The filter ratio of the first FPC has been chosen such that the higher-order spatial modes of the subsequent FPCs are not resonant with any transmitted modes of the first FPC. The measured side-mode suppression in the IR is shown in Fig. 4.10. Comparing with the computed TEM_{00} transmission curve of the FPCs, we find

---

[3] These frequency shifts correspond to radial-velocity shifts on the µm/s scale only, and are therefore of no concern for astronomical spectrograph calibration.

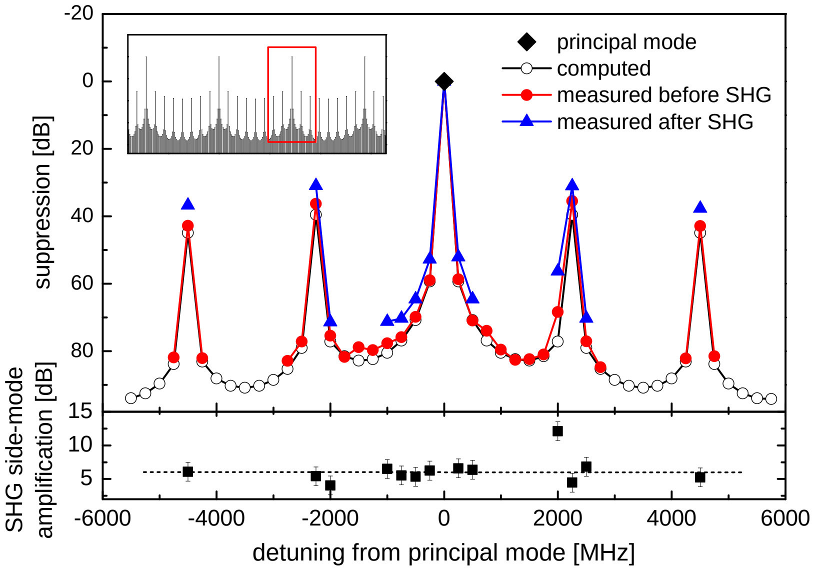

Figure 4.10 – Mode suppression at 1064 (532) nm with two filter cavities of 2.25 GHz and 18 GHz free spectral range: Beat measurement before second-harmonic generation (SHG) (red circles, resolution bandwidth: 1 Hz), theoretically expected values before SHG (hollow circles) and beat measurement after SHG (blue triangles, resolution bandwidth: 91 Hz). Inset: Larger section of the comb structure with principal modes and side-modes. The red square shows the modes under investigation. Bottom: Difference of side-mode suppression before and after SHG. The dashed line marks the 6 dB-level.

very good agreement except for the side-modes in the vicinity of the $\mathrm{TEM}_{01}/\mathrm{TEM}_{10}$ spatial modes of the cavities. This is the case at an offset from the principal mode of +750 MHz and −1.5 GHz for FPC1, and most significantly, at +2 GHz with an excursion of 9 dB for FPC2. All other deviations are probably due to the fact, that the finesse of FPC2 is slightly lower than derived from the mirror specifications.

Adding the SHG stages shown in the setup of Fig. 4.9 resulted in a configuration similar to the one that was used for calibration of an astronomical spectrograph in 2009 [26]. To characterize the effect of SHG on side-mode suppression, the heterodyne signals before SHG and after SHG were compared. As shown in Fig. 4.10, we find the expected increase by 6 dB in power within the estimated accuracy of the heterodyne measurement of ±1 dB. The only exception is the mode at +2 GHz affected by the higher-order spatial transmission of FPC2.

For the characterization of SPM, the two FPCs were tuned to 2 GHz and 14 GHz respectively, leading to a measured suppression in the IR of the strongest side-mode of 38 dB, which is 2 dB less than expected from the mirror specifications. Adding the tapered PCF as shown in Fig. 4.9 generates a broad spectral envelope. Its width can be adjusted with the pump current of the power amplifier of the astro-comb. At the maximum current of 4 A we obtained an average power of 60 mW coupled through the PCF and measured a spectral width of 122 nm at the −20 dB point. From the corresponding RMS-bandwidth of 23.5 THz we estimate the worst-case side-mode amplification to be 37 dB using Eq. (4.1.8) with T_{FWHM} =100 fs plus 6 dB resulting from the SHG. Given the initial side-mode suppression of 38 dB this actually means, that some of the approximations of Eq. (4.1.8) break down, and the side-modes can become stronger than the principal modes (see Fig. 4.6).

In fact this is what was observed with only two FPCs. The principal modes lost a significant amount of power to the side-modes and were depleted. In addition we observed the powers

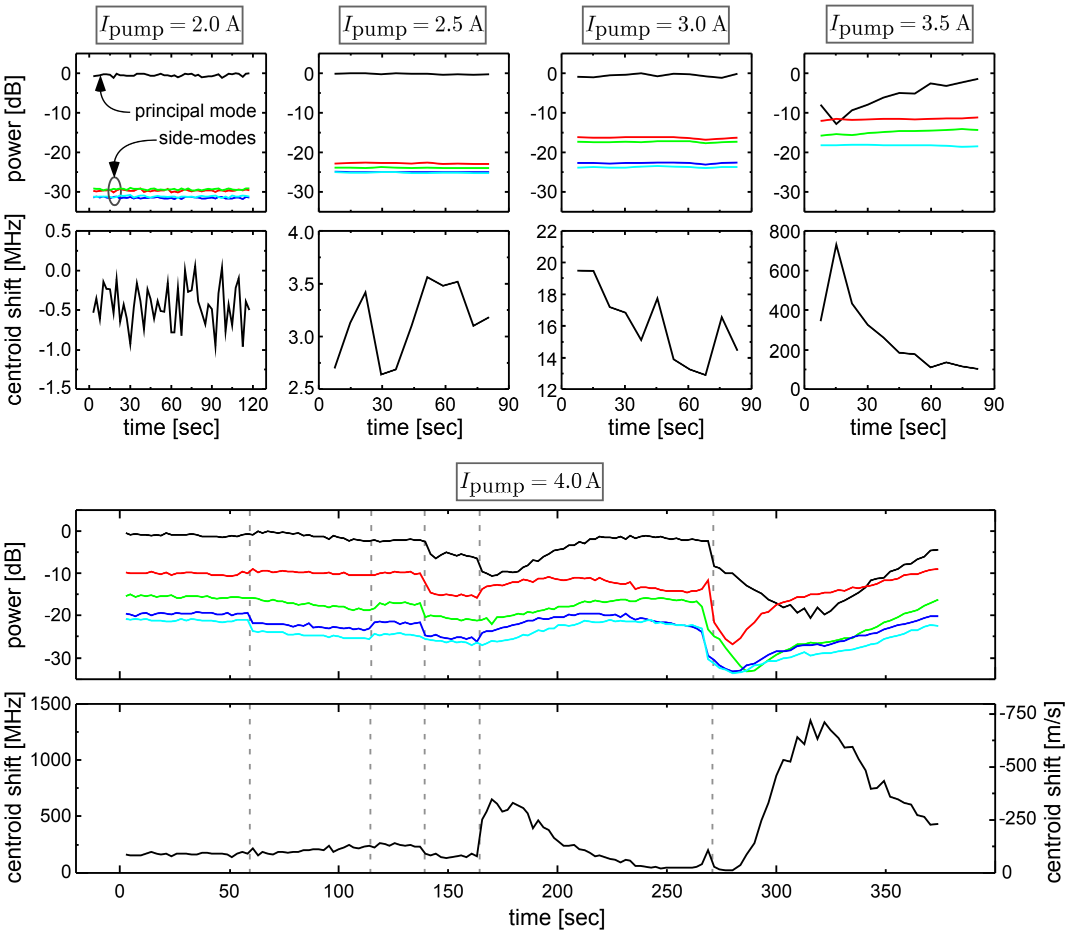

Figure 4.11 – Heterodyne measurement of the principal (black) and side-mode powers (colored) around 532 nm of the broadened frequency comb. The optical power for SPM was varied by changing the pump current of the Yb-fiber amplifier of the astro-comb (see Fig. 4.9). The corresponding shift of the center of gravity of the group of lines is shown below each plot. For large currents some of the side-modes are amplified to powers exceeding the principal mode. In this situation we also observe strong polarization dependence of the side-mode amplification as shown in the lower graph. The dashed vertical lines indicate when the half-wave plate in front of the PCF was rotated by about 20°. Side-mode color code: +2 GHz, −2 GHz, +4 GHz and −4 GHz. The side-mode suppression before spectral broadening was 32 dB.

of the side-modes and principal modes after SPM to fluctuate in time, which is probably associated with the spectral structure of the side-mode suppression (see Fig. 4.4): Fluctuating coupled optical power or rotation of the waveplate results in changing nonlinear phase shifts and therefore in a changing spectral structure of the suppression. This shifts regions with good or bad suppression in and out of the position of the investigated modes. We therefore recorded time traces of the powers of the dominant side-modes at ±2 GHz and ±4 GHz as shown in Fig. 4.11.

In the application of the broadened frequency comb for spectrograph calibration, such a behavior can be problematic for calibration accuracy. This is because the side-modes are usually too close to the principal modes to be resolved by the spectrograph as individual lines. To estimate the impact on calibration accuracy, we calculated the center of gravity of the measured ensemble of lines. This allows us to determine the expected calibration errors as shown in Fig. 4.11. These errors are for most applications not acceptable and defy the idea of

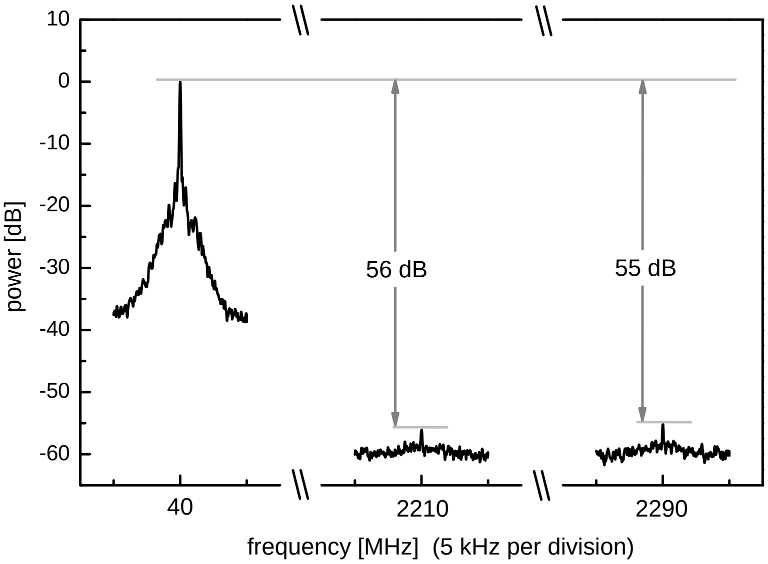

Figure 4.12 – Heterodyne beat note measurement at 532 nm of the principal and two strongest side-modes of a frequency-doubled and spectrally broadened astro-comb. The signal of the principal mode appears at 40 MHz, while the signal of the side-modes at +2250 MHz (−2250 MHz) appear at 2290 MHz (2210 MHz). The indicated values for the side-mode suppression include corrections for the RF-electronics. Resolution bandwidth: 91 Hz.

precise comb calibration.

To improve the side-mode suppression, we added further FPCs to the astro-comb setup. This configuration was used in a campaign for calibration of the HARPS spectrograph in November 2010 [39] (Sec. 6.2). For the test presented here, the first FPC was tuned to 2.25 GHz and two others were operated at 18 GHz. Before SHG the suppression of the two strongest side-modes at ±2.25 GHz was measured to be 78 dB and 76 dB respectively. We assume a 6 dB side-mode amplification caused by the subsequent SHG. After inserting the tapered PCF we could generate a spectral envelope with a −20 dB-bandwidth of 242 nm or 44.2 THz RMS. The side-modes were now observed to be short-term stable and symmetric within ±1 dB with a suppression of significantly better than 50 dB (see Fig. 4.12). This is in agreement with Eq. (4.1.8) with T_{FWHM} =100 fs, which predicts a suppression of at least 28 dB. Since this suppression would be insufficient for the most challenging future applications of the astro-comb, we added a fourth FPC for the HARPS campaign in January 2011 [39] (Sec. 6.2).

As the side-mode suppression is expected to have a spectral structure, it is desirable to measure the suppression for several wavelengths across the spectrum. This has been done on an astro-comb system that was subsequently installed at the Vacuum Tower Telescope (VTT) in Tenerife [152] (see Chapter 7). It uses two FPCs with an FSR of 6 GHz. Heterodyne measurements at 1060 nm / 530 nm of the dominant side-modes at ±250 MHz showed a suppression of 62 dB and 63 dB before SHG. After SHG a suppression of 57 dB was measured on both sides of the principal mode, again confirming the 6 dB amplification by SHG within the estimated accuracy of the measurement of ±1 dB. Under the same conditions the suppression was identical at 1064 nm / 532 nm and at 1054 nm / 527 nm, which supports the assumption of a uniform initial suppression.

Using a tapered PCF, we obtained a −20 dB-bandwidth of 151 nm, or 40.6 THz RMS. Applying Eq. (4.1.8) with T_{FWHM} =100 fs we expect a side-mode suppression of at least 16 dB. The suppression was measured at 532 nm, 521 nm and 515 nm, as shown in Fig. 4.13. Again, we observed spontaneous changes of the side-mode suppression, but in this case on a time scale

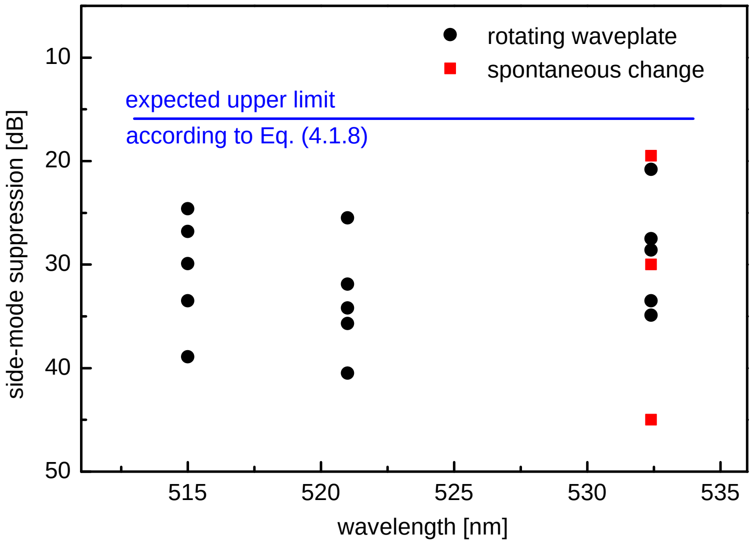

Figure 4.13 – Suppression of the strongest side-mode measured at 3 different wavelengths at the Tenerife VTT astro-comb system. The three red squares indicate subsequent measurements without any action taken in between. The black circles are measurements with different polarization directions before the PCF.

of hours, as seen on the data points at 532 nm. A significant polarization dependence was also observed. By rotating the half-wave plate in front of the PCF we could collect a number of different data points within a short time. As can be seen from Fig. 4.13, none of the data points exceeded the expected upper limit.

To improve the side-mode suppression on the VTT system, the FPCs have later been equipped with new mirrors [153]. The finesse of the two FPCs was hereby increased to 3096 and 2143, respectively, as measured with the method described in Sec. 2.3.3. Consequently we now expect a side-mode suppression of the broadened VTT astro-comb of at least 47 dB. This should permit a calibration accuracy of at least 4.7 kHz.

Chapter 5

Spectral flattening of broadened frequency combs

Astronomical spectrographs typically cover a spectral range of several 100 nm, mostly in the visible, to collect a large number of high-quality spectral features. To cover this region with calibration lines, the spectrum of a narrow-band frequency comb is commonly broadened in a photonic crystal fiber (PCF) (see Chapter 3), or in a highly nonlinear single-mode fiber [30,31]. The resulting supercontinuum is fully coherent and covers a wide spectral range, but its spectral envelope exhibits a pronounced structure. As the calibration repeatability with broadened astro-combs has reached the photon-noise limit (see Chapter 6), the spectral structure is now constraining the obtained precision. This is because the number of collected photoelectrons in each measured spectrum is limited by the most intense line in the comb spectrum, which must be kept below the saturation level of the CCD of the spectrograph. The highest number of photoelectrons, and therefore the lowest photon noise, is thus achieved with a completely flat envelope, having a uniform count rate for all comb lines over the entire spectral range of the spectrograph. To this aim, a-posteriori flattening of the broadened frequency comb spectrum has been proposed [3]. This is accomplished by truncating the broadened spectra at a constant level, which equalizes the signals of the calibration lines and thereby maximizes each line's signal-to-noise ratio.

Designed mirrors have been suggested for this purpose [29], but their reflectivity curves are fixed, and cannot be adapted to a changing spectral structure of the supercontinuum. Acousto-optic tunable filters [154] could be used instead, but their diffracted output is frequency-shifted, compromising the precision of the frequency comb calibration. The zero-order diffraction is not shifted, but does not offer sufficient dynamic range to flatten a structured, broadband supercontinuum. Spectral drainage from unwanted diffraction orders might also be a problem.

In this chapter, we demonstrate spectral flattening by use of liquid crystal-based spatial light modulators, yielding >200 nm wide flat-top spectra in the visible range. We also investigate the usability of micromirror-based spatial light modulators for this purpose. Similar shaping setups have already been used extensively, e.g. to control the temporal shape of ultrashort pulses [155,156] for applications like coherent control of chemical reactions [157] or two-dimensional spectroscopy [158]. Such shaping devices have also been utilized at telecom wavelengths, to modify the temporal pulse shape prior to spectral broadening such that the resulting supercontinuum is flattened [159]. Our approach of shaping the spectrum after spectral broadening is far more promising in terms of obtained optical bandwidth, flatness and ease of applicability. This comes at the expense of a much lower final intensity, since here the shaping can only be accomplished by reducing the power of selected spectral components. For applications in astronomy, however, high optical power is usually not a requirement.

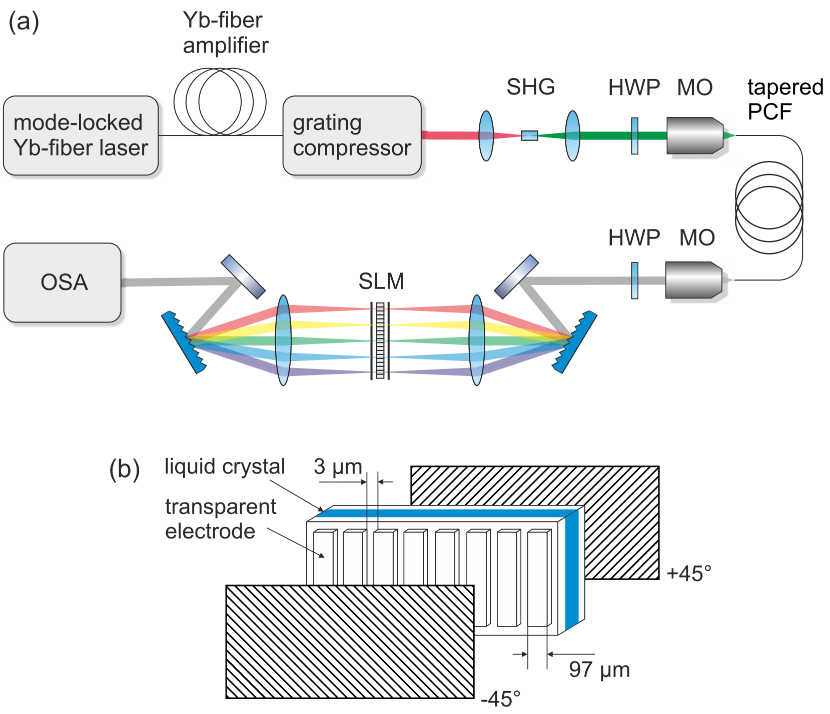

Figure 5.1 – (a) Experimental Setup. SHG: Second-harmonic generation; HWP: Half-wave plate; MO: Microscope objective; PCF: Photonic crystal fiber; SLM: Spatial light modulator. (b) Schematic of the SLM. The two hatched areas represent two foil polarizers aligned at a ±45° angle versus the electrodes of the SLM.

5.1 Using a liquid crystal device in transmission

Our approach to provide spectral reshaping of light is to spatially separate its spectral components with a grating and a lens, and to adaptively attenuate the individual spectral components by means of a spatial light modulator (SLM). In this section, the SLM used for this purpose is a pixelated liquid crystal (LC) device operated in transmission.

For convenience, the spectral flattening is tested at a relatively low repetition rate of 210 MHz. The results can however directly be scaled to the repetition rates in the 10 GHz range, that are typical for astronomical frequency combs. In fact, the flattening setup described here has successfully been deployed during a campaign at the HARPS spectrograph in February 2012, where it was used to flatten an astro-comb at a 18 GHz repetition rate for spectrograph calibration (see Sec. 6.3).

Our setup is shown in Fig. 5.1(a). The light source is a mode-locked ytterbium-doped fiber laser with a 210 MHz repetition rate and a center wavelength of about 1030 nm. It is amplified in an ytterbium-doped double-clad fiber amplifier, which shifts the center wavelength to about 1060 nm. The optical pulses are then compressed to 100 fs full-width at half-maximum (FWHM) pulse duration by a grating compressor, and then frequency-doubled in a 3 mm long LBO crystal. The second harmonic is separated from the infrared light by two dichroic mirrors (not depicted in Fig. 5.1), and coupled into a tapered PCF with a coupling efficiency of 45 %. A half-wave plate is used to align the polarization at the PCF input along the direction of maximum spectral broadening. The tapered PCF uses a design similar to the ones presented in Sec. 3.1. The PCF was manufactured with a 5 μm core, and tapered down to a core diameter of 570 nm over a 30 cm long taper waist (credit to Gordon Wong, MPL). The PCF has a 5 cm long taper transition and a 5 cm long untapered section on each side of the taper waist.

The air-filling fraction of the hole pattern surrounding the PCF core is estimated to be 83 %. The broadened output of the tapered PCF is collimated and sent into the spectral shaping section. Here, the individual spectral components are dispersed by a grating with 1800 grooves per mm, and then parallelized by an achromatic lens with a focal length of $f = 12$ cm. At the same time, each spectral component is focused on the LC layer of an SLM modulating the transmitted intensity. The spectral components are then collimated and recombined to a single beam by another lens and a grating. The distance of each of these components to the next is f, making up the typical $4f$-configuration [155, 156] with the SLM in the focal plane. The spectrum at the output of the shaping setup is monitored by an optical spectrum analyzer (OSA), which consists of a fiber-coupled scanning monochromator.

The SLM that we use is a Jenoptik SLM-S640, which is schematically shown in Fig. 5.1(b). It has a continuous layer of a nematic LC between two glass substrates with 640 transparent electrodes (hereafter also referred to as pixels or px) on their surface. The electrodes are 1 cm high and 97 µm broad with 3 µm wide gaps between them, resulting in an active area of the SLM of 1 cm × 6.4 cm. This arrangement is placed between a pair of crossed polarizers with a ±45° angle relative to the electrodes of the SLM. We use foil polarizers with a polarization extinction ratio of 30 dB at 532 nm. Voltages between 0 and 5 V (AC) can be applied to the pixels with a 12 bit resolution.

Due to the 2 inch diameter of the lenses, only 470 of the 640 pixels of the SLM are illuminated. The whole shaping setup has a maximum transmission of about 10 %, with the largest losses occurring at the gratings and on the first polarizer. Since the polarizers are aligned in a 45° angle versus the grooves of the gratings, the polarization of the incoming light cannot be aligned to minimize the losses on the gratings and polarizers at the same time. The polarization is adjusted with an achromatic half-wave plate at the PCF output to achieve a compromise.

5.1.1 Calibration and algorithm

The algorithm that we use for flattening of the supercontinuum requires precise calibration of the shaping device. We distinguish between two separate calibration steps that we term transmission calibration and wavelength calibration.

The transmission calibration relates the voltage on the SLM pixels to the obtained transmission for a given wavelength. This information is first retrieved for a single wavelength only, and then scaled to other wavelengths. For this purpose, we restrict the PCF output to the center wavelength of our supercontinuum, by reducing the pump current of the amplifier until the optical power does not allow spectral broadening anymore. The FWHM of the resulting spectrum is 2.77 nm and its center of gravity is at $\lambda_c = 535.16$ nm. The OSA in Fig. 5.1(a) is replaced by a photodiode measuring the transmitted intensity as a function of voltage, which is uniformly applied to all pixels. The result is shown in Fig 5.2(a), which also reveals, that the 12 bit voltage resolution allows adjusting the transmission at the −20 dB point with a precision of ±0.09 dB. The transmission $T(U, \lambda)$ as a function of voltage U and wavelength λ is related to the phase delay $\Delta\Phi(U, \lambda)$ between the ordinary and the extraordinary axis of the LC by:

$$T(U, \lambda) = \sin^2\left(\frac{\Delta\Phi(U, \lambda)}{2}\right) \tag{5.1.1}$$

Knowing, that $\Delta\Phi(U, \lambda)$ decreases monotonically with increasing U, and that the last maximum has a phase delay of π, $\Delta\Phi(U, \lambda_c)$ can be obtained from Eq. (5.1.1). Normalizing the transmission curve, measured at the wavelength λ_c, between each maximum and minimum

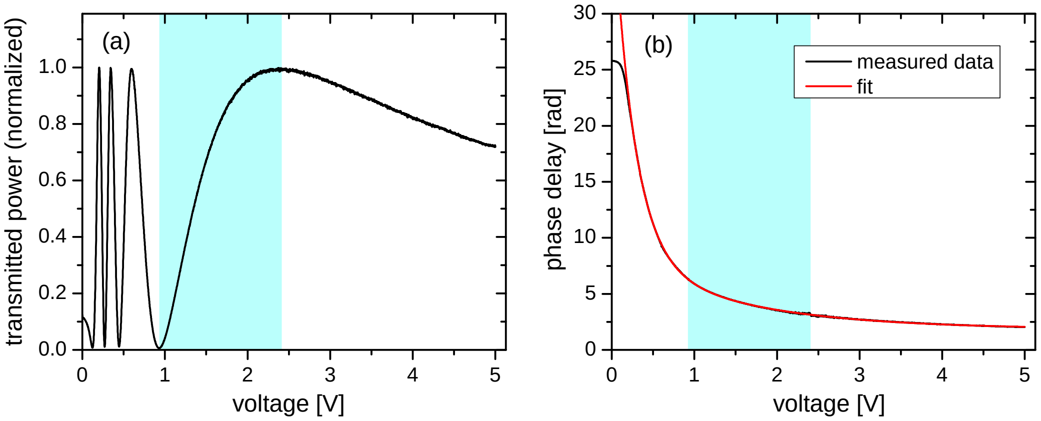

Figure 5.2 – Transmission calibration for a single wavelength of 535.16 nm. (a) Measured transmission as a function of voltage, (b) corresponding phase delay between the ordinary and extraordinary axis of the liquid crystal as a function of voltage. The blue shaded area is the region in which the device is operated at this wavelength.

to the interval $[0,1]$, $\Delta\Phi\,(U,\,\lambda_c)$ is obtained as shown in Fig. 5.2(b). A sum of two exponential functions can be fitted to these data excluding the first 0.25 V. This yields an analytical expression for $\Delta\Phi\,(U,\,\lambda_c)$ and has the benefit of removing noise from the measurement. Alternatively, the measured values for $\Delta\Phi\,(U,\,\lambda_c)$ can directly be used as a look-up table. To obtain $\Delta\Phi\,(U,\,\lambda)$ for an arbitrary wavelength λ, we use the known wavelength dependence of the refractive index difference Δn between the two axes of the LC, which (without a voltage) is approximately given by:

$$\Delta n\,(U=0,\lambda) = \frac{\Delta n_\infty \lambda}{\sqrt{\lambda^2-\lambda_0^2}} \qquad n_\infty = 0.2002,\ \lambda_0 = 327.44\,\mathrm{nm} \tag{5.1.2}$$

With $\Delta\Phi\,(U,\,\lambda) = 2\pi\,\Delta n\,(U,\,\lambda)\;d/\lambda$, where d is the thickness of the LC, this determines how $\Delta\Phi\,(U,\,\lambda_c)$ scales with wavelength. Consequently, the phase delay $\Delta\Phi\,(U,\,\lambda)$ for arbitrary wavelengths λ can be derived from the measurement performed at the wavelength λ_c:

$$\Delta\Phi\,(U,\,\lambda) = \frac{\sqrt{\lambda_c^2-\lambda_0^2}}{\sqrt{\lambda^2-\lambda_0^2}}\Delta\Phi\,(U,\,\lambda_c) \tag{5.1.3}$$

This relationship was roughly checked with three single-frequency lasers at 633 nm, 532 nm and 408 nm, and was confirmed within ±6 % over the full voltage range. We choose to operate the SLM at a $\Delta\Phi\,(U,\,\lambda)$ between π and 2π for all wavelengths λ (see Fig. 5.2).

As a next step, we execute the wavelength calibration, which specifies the center wavelength of the transmission profile of each pixel. In this procedure, we sequentially change one pixel at a time to be fully transparent while the others are opaque. After each step, the transmitted spectrum is fitted with a Gaussian function, and the center wavelength is attributed to this pixel. The whole active area of the SLM is mapped in this manner in steps of 10 px. The resulting relationship between the center wavelength λ of each pixel and its pixel number p is fitted with a 4^{th} order polynomial $\lambda\,(p)$, as shown in Fig. 5.3. The deviation of the measured center wavelengths from the fitted curve is within 0.25 px. As explained below, this value must stay lower than 0.5 px for the flattening algorithm to work. From Fig. 5.3 it can also be seen, that on average the width of a single pixel corresponds to a wavelength range of 0.43 nm.

When the flattening algorithm is started, the SLM is first switched to full transmission for all wavelengths in order to measure the shape of the supercontinuum without any spectral

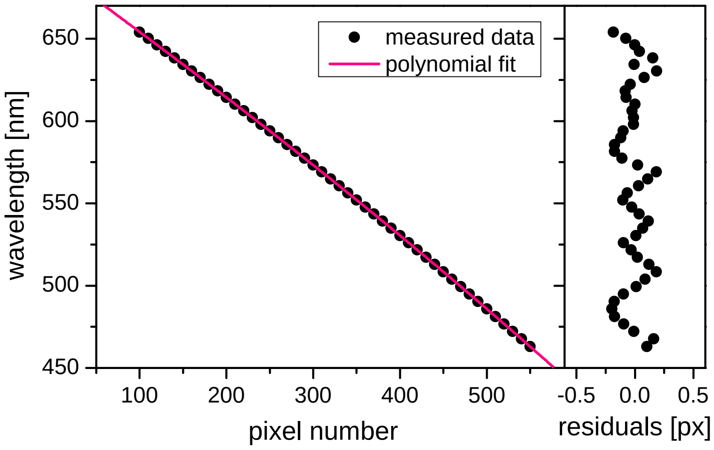

Figure 5.3 – Wavelength calibration. Left: The center wavelengths of the transmission profiles of the SLM-pixels are measured in steps of 10 pixels (black dots), and then approximated by a fourth-order polynomial. Right: Difference between the measured values and the polynomial in pixels (px). The absolute value of this difference must always stay below 0.5 px (see Sec. 5.1.2).

shaping applied to it. From this, we compute and store the target value for the transmitted spectrum at each wavelength, which is 20 dB below the peak of the spectrum. We then compute the required voltages $U\,(p)$ for all pixels at positions p in order to truncate the spectrum at the target value and thus form a flat-top spectral envelope. For this we use Eqs. (5.1.1) and (5.1.3), as well as $\Delta\Phi\,(U,\,\lambda_c)$ and $\lambda\,(p)$ from the calibration procedure. The spectral flattening is now re-iterated in the following way: Without changing the voltages on the SLM pixels, a new spectrum is measured by the OSA. Using the transmission function of the SLM known from the voltages $U\,(p)$, the spectrum without spectral shaping is computed. Based on this new hypothetical spectrum, the required voltages $U\,(p)$ are again computed as earlier, and applied. This process is repeated continuously, adapting itself to time-varying input spectra. The targeted spectral flatness is normally not reached within a single iteration because of imperfections of the transmission calibration. Rather than updating the calibration after each iteration, this feedback loop works by updating the hypothetical spectra instead.

It shall be mentioned, that other algorithms for spectral flattening are conceivable. For example, the downhill simplex-method [148] could be tailored to fulfill this task. This algorithm would not require any calibration at all, but at the cost of a substantially slower convergence.

5.1.2 Results

Before the flattening algorithm described above was put into practice, the effect of the gaps between the electrodes of the SLM (depicted in Fig. 5.1(b)) was characterized and prevented from being a potential limitation to the achieved spectral flatness. Pixel gaps are known to be a potential source of problems in pulse shaping devices [160]. Using a ×20 microscope objective for the collimation of the PCF output, the collimated beam had a FWHM of 1.2 mm. The FWHM of the focal spot for a single wavelength at 535 nm is then 24 µm, which is almost an order of magnitude larger than the width the pixel gaps. Nevertheless, we observe a pronounced effect resulting from these gaps: If we gradually decrease the transmission through the SLM, an increasing modulation in the transmission spectrum is observed, with a peak-to-valley modulation-depth of up to 7 dB, as shown in Fig. 5.4(a). We believe, that this is because the gaps create an inhomogeneous distribution of the electric field that extends into the LC layer, and thereby expands to a size that can be optically resolved. The resulting modulations can

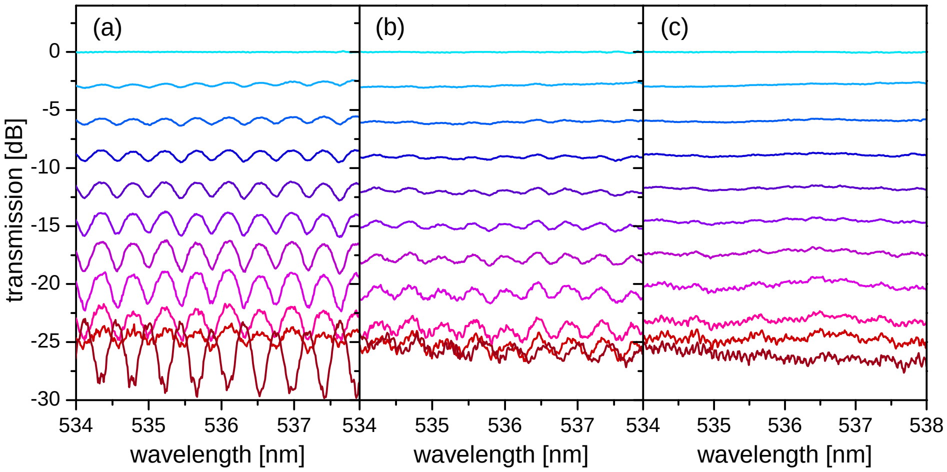

Figure 5.4 – Spectral transmission versus wavelength for different attenuation levels on the spatial light modulator (SLM). The spectral transmission was measured with the optical spectrum analyzer in Fig. 5.1 at a resolution of 0.05 nm. Distance of the SLM to the focal plane of the shaping setup: (a) 0 mm, (b) 7 mm, (c) 9 mm.

be reduced significantly, by moving the SLM out of the focal plane (see Fig. 5.4(b) and (c)). A similar improvement could be achieved by reducing the beam diameter at the PCF output using a ×60 microscope objective for collimation while leaving the SLM in the focal plane. For the following investigations, we chose to place the SLM at a distance of 9 mm from the focal plane as in Fig. 5.4(c), where there are no significant modulations arising from the gaps anymore. Here, the FWHM of an optical resolution element is 93 µm, which was measured to increase the FWHM of the transmission profile of a single pixel at 535 nm from 0.39 nm for the position at focus to 0.52 nm. Figure 5.4(c) also shows the dynamic range of the transmission control of 27 dB.

After the calibration procedure described in Sec. 5.1.1, the pump current of the fiber amplifier was increased until 5.2 mW of optical power were transmitted through the tapered PCF. The resulting output spectrum had a bandwidth of 248 nm at −20 dB below the peak, completely filling the 201 nm wide transmission window of the shaping setup. Applying the spectral flattening algorithm described in Sec. 5.1.1, we obtained a 201 nm flat-top ranging from 447 nm to 648 nm. After the first iteration, the spectrum was already flat within ±1.6 dB, which improved until a steady-state was reached after 4 iterations. The degree of flatness upon the first iteration and the speed of convergence can vary upon the quality of the calibration. Figure 5.5 shows the spectrum before the start and after the convergence of the flattening algorithm. Between 447 and 648 nm, the measured spectrum converges within ±0.37 dB (or ±8.5 %) of the target value, with a root-mean square scatter of 0.11 dB (2.5 %), limited by the noise of the OSA. This degree of flatness is kept up over arbitrary periods of time, as long as the input spectrum does not change too much during a single iteration of the flattening algorithm. With our setup, a single iteration takes 5.3 seconds, limited by the OSA. This compares to the time scale on which the spectral shape of the supercontinuum changes: Typically, it remains identical within ±0.5 dB over at least 16 seconds, and within ±1 dB over at least 32 seconds. The optical power of the flattened supercontinuum amounts to 17 µW, which must still be attenuated by several orders of magnitude for most astronomical spectrographs. Beyond that, the optical power of a frequency comb system usually scales with its repetition rate.

Please note that we are characterizing the spectrum in terms power spectral density in mW per nm. Considering the photon flux per comb line, the top of the flattened spectrum

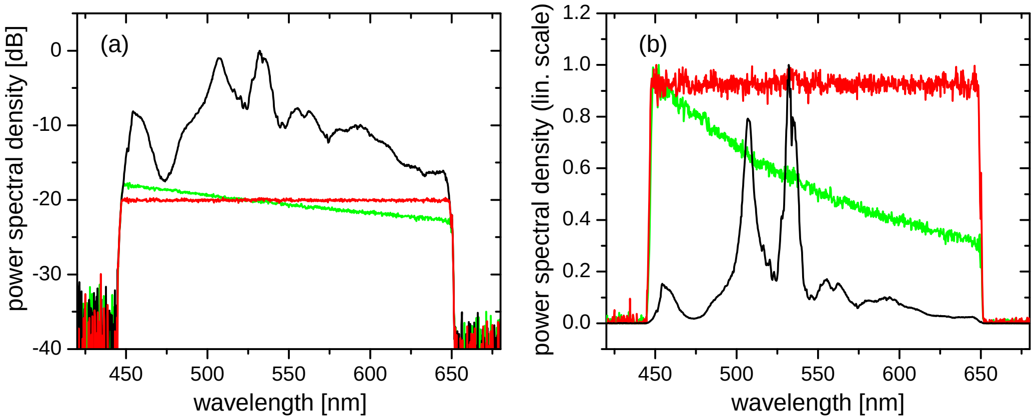

Figure 5.5 – Demonstration of spectral flattening. Black line: Before flattening. Red line: After 4 iterations. Light green line: Spectral flattening algorithm executed in photons per comb line. (a) Representation in a logarithmic scale (b) in a linear scale (normalized). Resolution of the optical spectrum analyzer: 0.5 nm.

as shown by the red line in Fig. 5.5 has a non-zero slope. This is because the photon energy scales with the optical frequency f, and because the number of comb lines per nm scales with f^2. Furthermore, a given astronomical spectrograph has a distinct wavelength-dependent response. Such effects can readily be included and compensated as a part of the flattening algorithm. This is demonstrated by the light green line in Fig. 5.5, which has been flattened in terms of photon flux per comb line. Assuming a constant quantum efficiency, this increases the number of photoelectrons that a spectrograph can collect in a single exposure by a factor of 5.7, indicating a 2.4 times lower photon noise.

In order to keep the spectrum flat over longer periods of time, precise wavelength calibration is required. This is demonstrated in Fig. 5.6, where a linear function was added to the polynomial $\lambda(p)$, which approximates the center wavelength of each pixel, see Fig. 5.3. This changed the wavelength calibration by up to 1.8 px. While the flattening algorithm is running, the spectrum progressively develops modulations, as shown in Fig. 5.6. This can be understood in the following way: If the wavelength calibration is off by $m \geq 1$ pixels, and if the optical power transmitted through pixel number n must be reduced, the algorithm will in fact reduce the transmission through pixel number $n + m$. Since this has virtually no effect on pixel number n, the algorithm reduces the transmission through pixel number $n + m$ even further. As this eventually leads to a dip in the transmission at pixel number $n + m$, the transmission at that point must be increased. However, the algorithm will not do this on pixel number $n + m$, but on pixel number $n + 2m$. This process continues and produces a periodic modulation pattern. The resulting modulations have a period of a least two pixels, while the modulations that can potentially arise from the gaps between the pixels have a period of exactly one pixel. From Fig. 5.6 we can see, that no modulations of the first kind are produced as long as the wavelength calibration is accurate within ±0.5 px. In setups in which the pixels are much smaller than one optical resolution element, we suppose that the calibration must only be accurate within half the FWHM of an optical resolution element.

While changing the phase delay on the LC, the SLM imprints a Doppler shift on the transmitted comb. This is however negligible for astronomical spectrograph calibration even for exposure times as short as 1 s: If the SLM ramps across its maximum phase shift of 7 π over 1 s, this adds or removes 3.5 optical cycles in 5×10^{14} for visible light of 500 THz (600 nm). The resulting calibration error is of 7×10^{-15} (~2 µm/s).

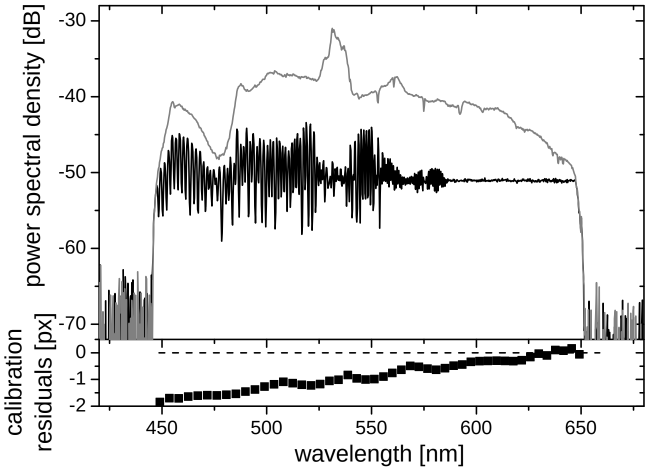

Figure 5.6 – Example of an attempt to apply the spectral flattening algorithm with a distorted wavelength calibration. Top: Initial spectrum (gray line) and spectrum after 50 iterations (black line). Bottom: Deviation of the measured center wavelength of each pixel from the one assumed from the modified calibration data. At the level of the dashed line, the disagreement between these two would be zero. Resolution of the optical spectrum analyzer: 0.5 nm.

5.2 Advanced configurations

Although the spectral flattening setup presented in the previous section has successfully been used during a campaign on the HARPS spectrograph, it leaves considerable room for improvement. For example, by using a fast CCD spectrometer instead of a scanning monochromator to measure the spectrum, the duration of a single iteration of the flattening algorithm can be shortened drastically. This is specifically important when the envelope of the input spectrum changes quickly. A CCD spectrometer has the additional benefits of not having any moving parts, and lower cost and size. Furthermore, a reflective SLM can be used, which reduces the number of optical components and the size of the shaping setup, and facilitates its alignment by having fewer degrees of freedom. Such SLMs usually also have smaller active areas, which permits the use of smaller optics, again reducing the size of the setup.

In the rest of this chapter, these improvements are put into practice. Two types of reflective SLMs are tested for their applicability to spectral shaping. The first one is a liquid crystal on silicon (LCOS) device, and the second one is a micromirror array. Both types of SLMs are commonly used in projectors, and are thus readily available. While the LCOS SLM is shown to be very well suited for our purposes, it is found that common micromirror arrays have quite undesirable properties.

5.2.1 Using a liquid crystal on silicon device

The LCOS SLM that is used to implement a reflective, LC-based spectral shaping setup is a Holoeye PLUTO. A similar device had already been tested in [161] for pulse-shaping applications. The SLM consists of an LC layer with transparent electrodes on one side, and reflective silver electrodes on the other side. Each pair of opposed electrodes represents a pixel. The active area of the SLM has a format of 1920 px × 1080 px, with a pixel pitch of 8 µm × 8 µm. The device is connected to a computer as a second screen (owing to its common application in projectors), for which we use an external USB graphics card. The patterns to be displayed on the SLM are converted into 8 bit gray-scale images, and then displayed there in full-screen mode, and always on top of all other windows. The mouse cursor is set to disappear

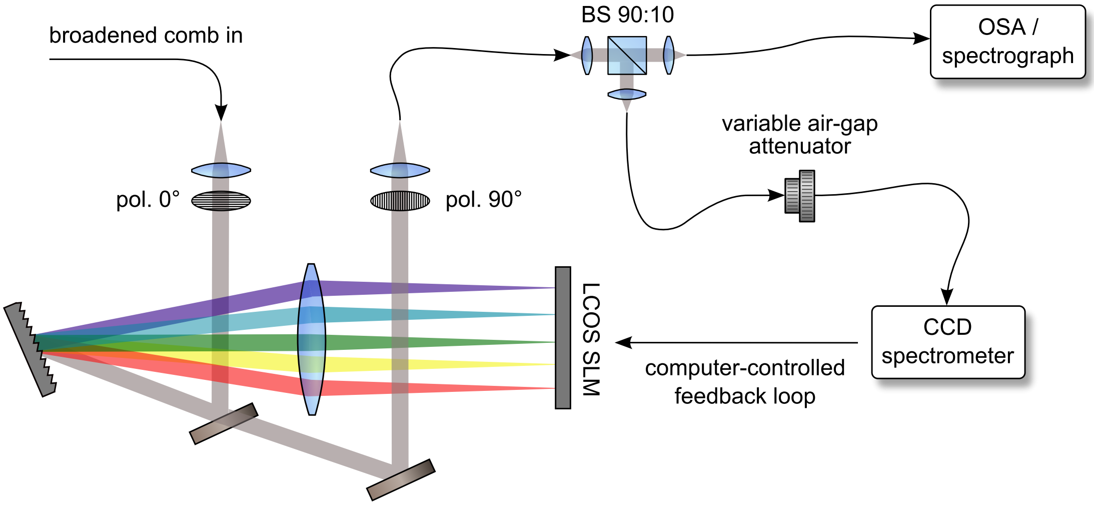

Figure 5.7 – Spectral flattening setup with the LCOS SLM. The spectral transmission is controlled by adjusting the voltages on the liquid crystal pixels of the SLM, altering the polarization between a pair of two crossed foil polarizers. Pol.: Polarizer. BS: Non-polarizing beam splitter. LCOS: Liquid crystal on silicon. SLM: Spatial light modulator. OSA: Optical spectrum analyzer (here taking the place of the astronomical spectrograph).

when it enters this area, to ensure undisturbed operation.

The spectral flattening setup with the LCOS SLM is depicted in Fig. 5.7. The spectral components of the input beam are spatially separated with a grating and an achromatic cylindrical lens. The spectral components are imaged along the columns of the SLM that rotates their polarization depending on the pixel voltages. The spectral components are then recombined to a single beam by passing again through the same beam path in opposite direction. The whole arrangement has single-mode fibers at its input and output, where a pair of crossed polarizers translates the altered polarization of the spectrum into a spectrally resolved intensity change. The spectrally reshaped output is distributed among a small CCD spectrometer (Thorlabs CCS125) and the astronomical spectrograph to be calibrated. The CCD spectrometer is in a computer-controlled feedback loop with the SLM, designed to adaptively keep the spectrum flat (see Sec. 5.1.1).

The grating in this setup has 600 grooves/mm, and the cylindrical lens has a focal length of 75 mm, yielding a transmission window of >300 nm for this setup, centered at about 575 nm. The input beam has an FWHM of about 1 mm, giving the setup a spectral resolution of 0.4 nm at 532 nm, which is about equal to the resolution of the CCD spectrometer. With a single pixel corresponding to a spectral width of less than 0.2 nm, individual pixels are not optically resolved.

The voltages on the SLM pixels can be set with an 8 bit resolution (256 gray values). With a line-shaped focus along the SLM columns, the spatial resolution of the SLM along the focus can be used to interpolate between different gray values. This was however not found to be necessary to achieve our goals in terms of spectral flatness. Should the focus not be perfectly parallel to the pixel columns, this can be compensated by rotating the pattern displayed on the 2D pixel array by the corresponding angle.

The algorithm used for spectral flattening is largely identical to the one described in the previous section. The transmission calibration was however found to be less critical with the LCOS SLM. Figure 5.8 shows the power transmitted through the flattening setup as a function of gray value on the SLM for three different wavelengths. The maximum attenuation

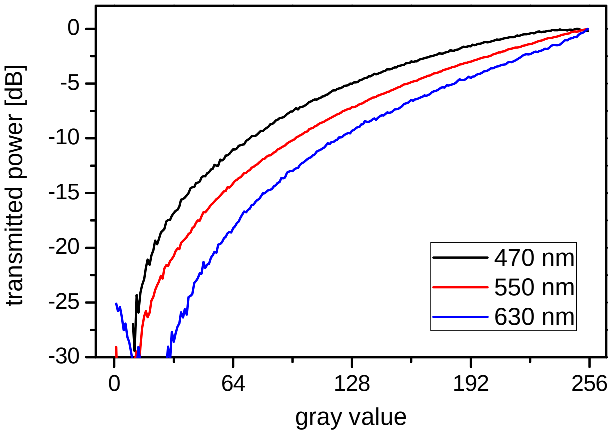

Figure 5.8 – Transmission calibration with the Holoeye Pluto SLM for three different wavelengths, over the full range of the 8 bit gray values (0−5 V, AC).

exceeds 27 dB. For all wavelengths, the transmission curve is observed to be strictly monotonic down to an attenuation of 24 dB, probably because the device acts as a low-order waveplate. For this reason, the flattening algorithm still converged rapidly and reliably, even if the same transmission curve (measured at 532 nm) was assumed for all wavelengths.

For test purposes the astro-comb is replaced by a standard 250 MHz Yb-fiber frequency comb, that is frequency-doubled and spectrally broadened in a tapered PCF. An OSA consisting of a scanning monochromator takes the place of the astronomical spectrograph. The OSA measures the power spectral density in mW/nm, and thus has a spectral response that is quite different from that of the CCD spectrometer. Additionally, the split ratio of the beam splitter has a wavelength dependence. A spectrum is therefore not flat as measured by the OSA, when it appears flat on the CCD spectrometer. Recording a spectrum simultaneously with the OSA and the CCD spectrometer allows generating a look-up table that quantifies this effect. The software of the SLM control uses the look-up table to compensate the different response of

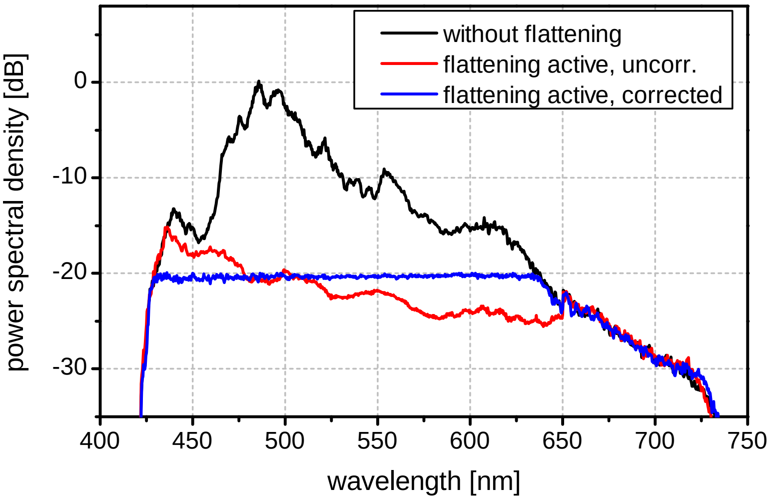

Figure 5.9 – Flattening of a 250 MHz broadened comb spectrum, using the spectral flattening setup with the LCOS SLM in Fig. 5.7. All spectra have been recorded with the OSA at a resolution of 0.5 nm. Black Line: Spectrum with the SLM at full transmission for all wavelengths. Red line: Spectral flattening active, truncating the spectrum at 20 dB below the previous maximum, without correction for instrumental spectral responses and parasitic spectral filters. Blue line: Flattened spectrum with correction for these effects.

the OSA. Much in the same way, the algorithm can also be adapted to the spectral response of any astronomical spectrograph. The test result with the OSA is shown in Fig. 5.9. During the recording time of these spectra of about 5 min (very slow, high-sensitivity scan of the monochromator), the spectral flattening algorithm was running continuously with one iteration every 400 ms. The flattened spectrum that includes the correction by the look-up table is flat within ±0.58 dB (±13 %) over a 211 nm wide spectral range. The residual unevenness of the flat-top amounts to an RMS of 0.18 dB (4.1 %). This result shows the excellent suitability of this setup for assisting in astronomical spectrograph calibration with astro-combs.

5.2.2 Using a micromirror array

Micromirror arrays have become standard SLMs in projectors for the consumer market. They consist of a two-dimensional array of mircometer-sized metal mirrors on a silicon chip, each representing a pixel. By application of a voltage, the mirrors can be steered into one of two stable tilt angles. In one angle, the incident light is reflected to follow an imaging beam path, while in the other position, the light is deflected out of the beam path and gets blocked. Each mirror is rapidly switched back and forth between these two positions. The ratio of the time spans that a pixel spends in the two positions (the duty cycle) determines its gray value.

Micromirror arrays have a number of advantages over LC-based SLMs: Since their operation is independent of polarization, the incident light does not need to be polarized. Since the attenuation is given by the duty cycle, and is not wavelength dependent, a transmission calibration as with LC-based SLMs in unnecessary. Micromirror arrays are also available over a very wide wavelength range. For example, Texas Instruments offers its DMD chips for 350−2500 nm. The Jenoptik SLM-S is specified to be functional between 430 and 1600 nm. In our tests, we have also obtained an extremely high contrast of >40 dB, which is hard to reach with LC-based SLMs.

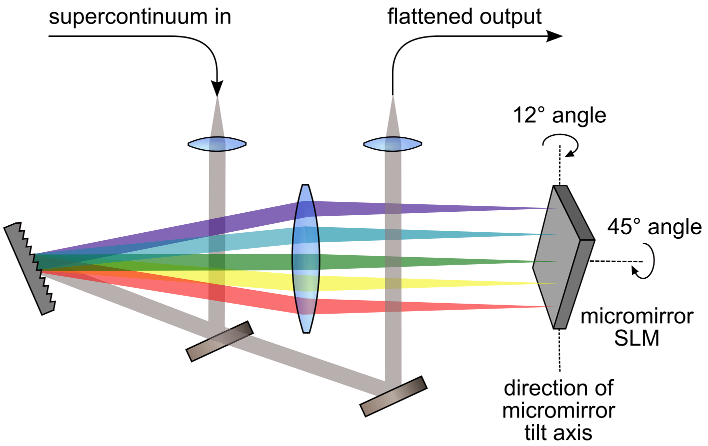

Figure 5.10 – Spectral flattening setup with a micromirror spatial light modulator (SLM). The micromirrors that represent the SLM pixels can have a +12° or −12° tilt along their diagonal. The SLM is positioned (see annotated angles) such that the beam is back-reflected for one of the two stable positions of the micromirrors.

The micromirror array used for our tests is a Texas Instruments DMD chip (0.7” XGA 2x LVDS) for visible wavelengths. It possesses 1024 × 768 aluminum mirrors with a 13.6 µm pitch. The micromirrors can be tilted along their diagonal by +12° and by −12° relative to the plane in which the mirrors are arranged. The chip is mounted on a V4100 board from Vialux, that offers convenient programming interfaces to control the micromirrors. The complete setup is shown in Fig. 5.10. As earlier, the spectral components of the incoming beam are spatially separated by a grating and an achromatic cylindrical lens and projected onto the SLM in a folded $4f$-configuration. The active area of the SLM is positioned versus the incident light such that the micromirrors reflect the light back when they are in their −12° tilt angle. This

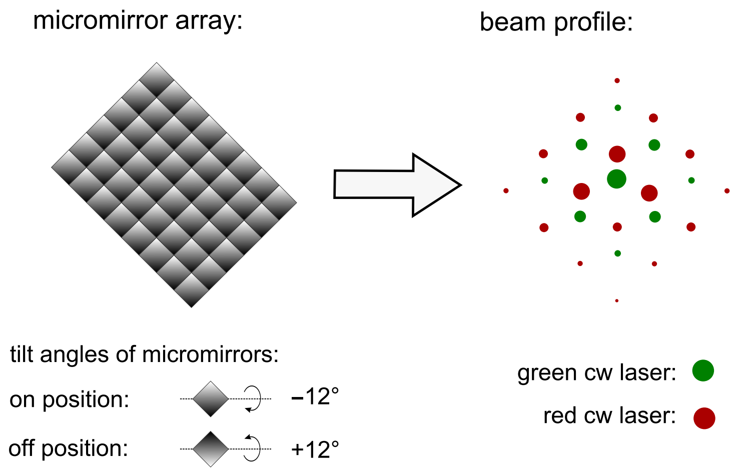

Figure 5.11 – Schematic depiction of the diffraction pattern that arises on a micromirror SLM with tilted mirrors, for two different wavelengths. Left-hand side: The micromirrors are all assumed to have a $-12°$ tilt relative to the plane in which they are arranged. Right-hand side: Profile of two collinear beams of different wavelength, after being reflected on the SLM. Note that the direction of maximum diffraction efficiency does not correspond to the zero-order diffraction, but roughly to the 10^{th} to 5^{th} order, depending on the wavelength.

means, that the SLM itself needs a 12° tilt in the opposite direction. Additionally, since the micromirrors are titled along their diagonal, the pixel columns of the SLM need to be in a 45° angle relative to the dispersion direction of the grating (see Fig. 5.10). Consequently, the patterns displayed on the SLM need to be rotated by 45° in the opposite direction, to account for the positioning of the SLM. The part of the light that is back-reflected by the SLM is recombined into a single beam, and coupled into a single-mode fiber representing the output of the setup.

In tests conducted with this configuration, it was found that diffraction on the SLM had a severe impact on the beam profile and its spatial chirp, making a subsequent fiber coupling impractical. The problem is illustrated in Fig. 5.11 for the case of a uniform $-12°$ tilt of all mirrors. The resulting surface is similar to that of a blazed grating. Light that is reflected off this surface is directed into several diffraction orders. The strongest order, considered as the "back-reflected" beam, is of about 10^{th} to 5^{th} diffraction order between 400 and 800 nm. As a result, the reflected beam has a strong wavelength dependence. LC-based SLMs also generate diffraction patterns due to their pixelation, but their maximum diffraction efficiency is reached at the 0^{th} order, whose direction is wavelength-independent.

To avoid these problems, it would be necessary to be able to keep the mirrors at 0° as one of the two stable positions. Such SLMs are available for example from the Fraunhofer Institute for Photonic Microsystems (IPMS), and used e.g. in microlithography. These devices are however more costly, and are usually only produced on demand. They are also expected to feature a lower contrast than the DMD chip tested in this section. For these reasons, LC-based SLMs are currently the preferred option. However, if for future astro-combs, the spectrum is extended into the UV, or towards the mid-infrared, custom-made micromirror SLMs might be worth a consideration. Possible Doppler shifts of the comb modes due to the motions of the mirrors need to be investigated when settled for a specific solution.

Chapter 6

Testing the astronomical frequency comb on the HARPS spectrograph

The HARPS spectrograph [20,21], located at ESO's La Silla Observatory in the Atacama desert in Chile, is one of the leading instruments in high-precision astronomical spectroscopy to date. For this reason, HARPS has been selected for in-field testing of a major line of experimental astro-combs, in a collaboration comprising the ESO, the MPQ, and Menlo Systems GmbH. A total of five measurement campaigns have been conducted between 2009 and 2012. The project is concluded in April 2015, with the installation of an astro-comb that will permanently assist exoplanet searches with HARPS.

Two of the test campaigns on HARPS had been carried out before the present work, and are documented in [25, 26]. These campaigns have demonstrated calibration of HARPS with an unbroadened, green astro-comb over $1-3$ echelle orders in January 2009. This yielded a calibration repeatability of 10 cm/s. Another test in March 2010 used a broadened astro-comb covering > 100 nm. The calibration with this system was however unstable even on the 100 m/s-level, due to the effect of side-mode amplification through spectral broadening (see Chapter 4).

The campaigns reported on in this work have been conducted in November 2010, January 2011, and February 2012. Calibration of HARPS over up to more than 200 nm, and a calibration repeatability down to 2.5 cm/s on a time scale of hours were achieved. Observations of the exoplanet-host star HD 75289 yielded the first comb-calibrated measurement of a planetary orbit documented in literature, and a comb-calibrated atlas of the solar lines was derived from observations of moonlight. The 2.5 cm/s repeatability suggests sufficient precision for the detection of exo-Earths, but the time base of only a few hours is still insufficient. Systematic calibration shifts due to the CCD readout mechanism and data extraction software were therefore thoroughly characterized, to lay the foundation for a demonstration over a sufficiently long time horizon.

6.1 Instruments & data processing techniques

The astro-combs used in this chapter all follow the basic architecture described in Chapter 2. However, representing earlier development stages of that system, their configurations slightly differ. The configurations and properties of the astro-combs used in the campaigns are listed in Tab. 6.1. All astro-combs used an Yb-based nonlinear polarization evolution (NPE) oscillator as a source comb. This was followed by a sequence of 3 to 4 Fabry-Pérot cavities (FPCs) that increased the mode spacing to 18 GHz. The FPCs did not have identical free spectral ranges (FSRs), but the first FPC in the sequence increased the mode spacing to an intermediate

Table 6.1 – Configurations and properties of the astro-combs used in this chapter, such as the number of Fabry-Pérot cavities (FPCs), and their finesse and free spectral ranges (FSRs). In all these astro-combs, the series of FPCs is followed by second-harmonic generation and spectral broadening. The given mode spacing and offset frequency represent the standard setting unless detuned deliberately. The error by mode skewing assumes a line shape as obtained by a beat measurement (as in Sec. 2.3.2) with an NPE oscillator (full-width at half-maximum: 160 kHz).

	Nov. 2010	Jan. 2011	Feb. 2012
mode spacing [GHz]	18	18	18
offset frequency [GHz]	7.04	7.04	12.96
number of FPCs	3	4	3
FSRs [GHz]	2, 18, 18	2, 18, 18, 18	4.5, 18, 18
finesse	400	400	3000
max. error through side-modes [cm/s]	130	<0.1	<0.1
max. error through mode skewing [cm/s]	0.6	0.6	2
spectral flattening	no	no	yes

2 GHz, or 4.5 GHz respectively. Further, the FPCs used in two of the campaigns employed the mirror coatings described in [25] instead of the ones from Chapter 2, featuring a finesse of 400. Table 6.1 lists the computed worst-case centroid shifts of the comb modes caused by skewing of their shape (see Sec. 2.3.2) and the maximum line shift through side-modes estimated from Eq. (4.1.8).

The series of FPCs was followed by second-harmonic generation (SHG), to transfer the filtered comb spectrum into the green, and by a subsequent tapered photonic crystal fiber (PCF) for spectral broadening, see Secs. 3.1 and 3.2. Being usable for one day at best, the tapered PCFs had to be exchanged regularly. Under optimal conditions, a spectral bandwidth of ≥ 200 nm could be obtained. The astro-comb of February 2012 was additionally equipped with a spatial light modulator for flattening of the broadened spectrum (Sec. 5.1). The RF reference of the astro-comb was the same in all campaigns, namely a PRS10 Rb-atomic clock from Stanford Research Instruments, stable within 10^{-11} (0.3 cm/s) for integration times exceeding 10 s. It is accurate only within a few 5×10^{-10} (a few 15 cm/s), which can however be improved to better than 10^{-11} (0.3 cm/s) by locking it to GPS.

The HARPS spectrograph is a fiber-fed, cross-dispersed echelle spectrograph (see Sec. 1.2), with a spectral range of 380−690 nm. Its 72 echelle orders are separated by a grism and imaged upon two CCDs consisting of 4096 × 2048 px with a pixel pitch of 15 µm. The CCDs are kept at a temperature of −120 °C to minimize their dark current, and stabilized there within 20 mK. HARPS has a resolution of $\lambda/\Delta\lambda = 115\,000$. An optical resolution element spans about 3.3 px, which at the center wavelength corresponds to 5 GHz in optical frequency. Figure 6.1 shows the open vacuum vessel of HARPS, giving a clear view on its two echelle gratings. Thanks to its temperature stabilization (10 mK) and evacuation (0.01 mbar), HARPS is passively stable within 1 m/s over at least many hours [20].

To track the residual spectrograph drifts, HARPS disposes of a second input fiber. During the observations, one of the two fibers carries science light from the telescope, while the other one is used for simultaneous calibration. In the measurements reported here, the calibration is performed with the astro-comb, taking the place of the thorium-argon (ThAr) lamps which presently remain the standard calibration sources for HARPS. The science light for HARPS is supplied by the 3.6 m-Telescope, a Cassegrain telescope in an equatorial horseshoe mount (see photograph in Fig. 6.1), named after the diameter of its primary mirror of 3.6 m. It incorporates a tip-tilt guiding system ensuring fast and accurate centering of the object image

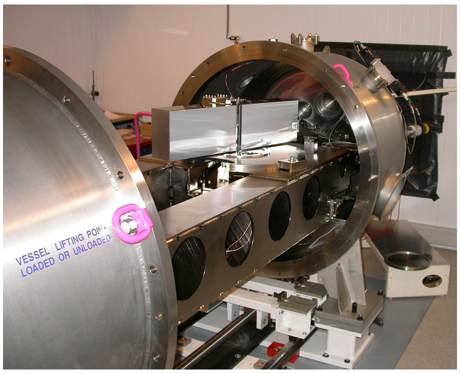

Figure 6.1 – Upper left: HARPS spectrograph with open vacuum vessel (photo: ESO) Right: 3.6 m -Telescope (photo by Th. Udem). HARPS is connected to this telescope via two optical fibers.

on the fiber tip. Residual telescope guiding uncertainties still lead to a varying spatial mode occupation in the multimode fibers feeding HARPS (70 µm core diameter), which translate into radial-velocity (RV) uncertainties. To homogenize the mode distribution, HARPS has a double scrambler [17] at each input fiber, limiting RV uncertainties from telescope guiding to 10 cm/s [162].

As already discussed in Chapter 1, the use of multimode fibers represents an obstacle especially for the astro-comb. Owing to the very high spatial and temporal coherence of the comb modes, the beam profile of each comb mode acquires laser speckles upon transmission through multimode fibers due to modal interference. The speckle pattern changes with the slightest motion of the fiber, resulting in large calibration uncertainties, which for HARPS are found to be around 1 m/s [25]. Static scramblers such as double scramblers do not solve this problem. As demonstrated in [25, 26], the solution is to employ dynamic scramblers that shake the fiber to make the speckle pattern change rapidly. This washes out the speckles and establishes a behavior equivalent to that of spatially incoherent light.

Figure 6.2 shows the coupling scheme of the multimode fibers that deliver the comb light to the spectrograph. The first fiber in this scheme is exchangeable, and scrambled by a combination of dynamic and static fiber scramblers. As a standard choice, we employed a static, periodic bend structure as a static scrambler [163]. For dynamic scrambling, an electric motor imprinted a temporally changing bend on the fiber. Additionally, a small electric motor with a spinning eccentric weight was attached to the fiber, to make the fiber vibrate. In 2010 and 2011, the scrambled fiber was a plastic fiber with a 980 µm core. Its very high numerical aperture and large core diameter provides a large number of guided modes, and thus a large number of very small speckles, which makes dynamic scrambling very efficient. In 2012, a silica fiber with a 200 µm octagonal core was used instead. It supports a lower number of spatial modes, but its lack of cylindrical symmetry provides excellent static scrambling properties.

For experimentation, even more scramblers were occasionally used. For example, the lens at the input of the first fiber in Fig. 6.2 could be replaced by an integrating sphere for fiber coupling. This provided a very homogeneous and isotropic fiber illumination, which however came at the expense of a very low coupling efficiency (compare e.g. to [164]). Instead, a static diffuser (sanded glass plate) could be placed before the fiber input to provide a similar effect.

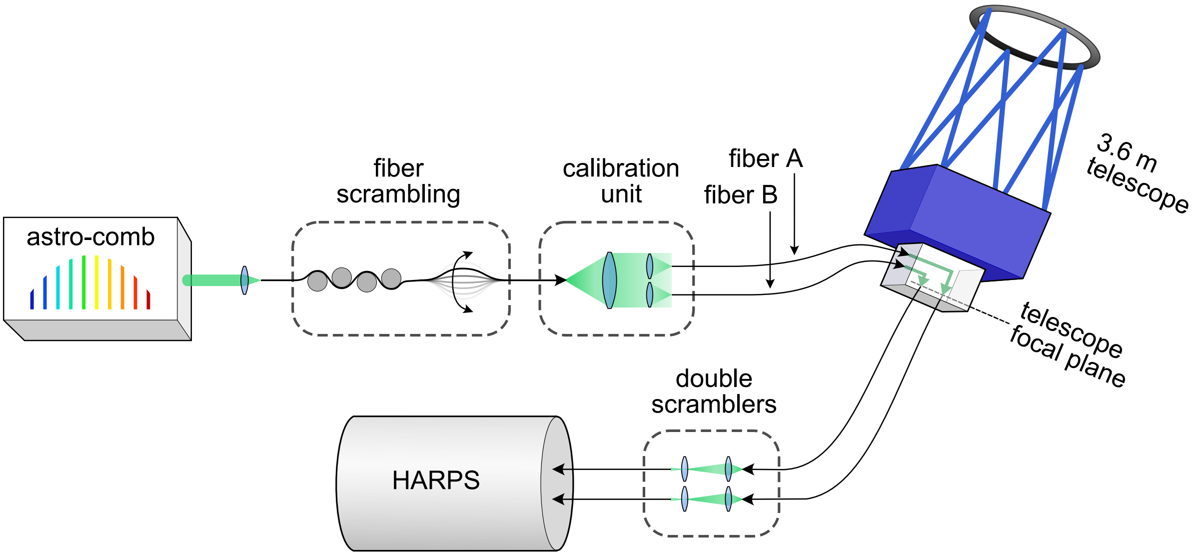

Figure 6.2 – Coupling of the astro-comb output to the HARPS spectrograph in a sequence of multimode fibers. The comb light is fed into a fiber that is scrambled by combination of static and dynamic mode scramblers, to homogenize the spatial mode distribution. The light is then distributed among two fibers (A and B) and passes from there through the focal plane of the telescope, for coupling to the fibers leading to HARPS. HARPS has a double scrambler at each fiber input, further enhancing the homogeneity of the mode distribution.

The diffuser could also be rotated to add some dynamic scrambling.

The output of the scrambled fiber is distributed among two fiber channels (A and B) by an arrangement of three lenses as indicated in Fig. 6.2 (calibration unit). From the output of these fibers, the light is projected through the focal plane of the telescope onto the fibers leading to the HARPS spectrograph. The double scrambler at each input fiber of HARPS again provides static mode scrambling for the comb light.

Figure 6.3 shows a HARPS CCD image with the astro-comb on both input channels, obtained on February 7, 2012. Each echelle order spans about 5 to 10 nm, with a spectral overlap of approximately 30 % from one order to the next. The 115th echelle order (center wavelength: 530 nm) is lost inside the gap between the two CCDs, and for channel B, order 116 is partly clipped at the gap. The bandwidth of the comb spectrum is 190 nm, with more than 10 000 comb lines in each channel. Due to the spectral overlap of the orders, many of the comb lines appear twice.

From the two-dimensional image as shown in Fig. 6.3, the spectrum is extracted as a one-dimensional data string by the HARPS pipeline. This piece of software uses an optimal extraction algorithm [165] to project the pixels in each echelle order onto the spectral axis. Order 97 of channel A, as extracted by the pipeline, is shown in Fig. 6.4. To attribute absolute frequencies to the comb lines, their mode numbers must be known, which requires a coarse calibration. Standard ThAr calibration is employed for this purpose, which we also use to resolve the 500 MHz ambiguity (250 MHz before SHG) of the offset frequency of the astro-comb. As mentioned in Chapter 2, this can also be done by using the wavemeter in the astro-comb system to clarify which set of comb modes is transmitted through the FPCs, but a ThAr-calibrated measurement with HARPS is accurate enough for this task, and serves as a cross-check.

As shown in Fig. 6.4, the comb lines in the extracted spectra are fitted with Gaussian functions to determine their line centers. The fit is carried out with least-squares optimization

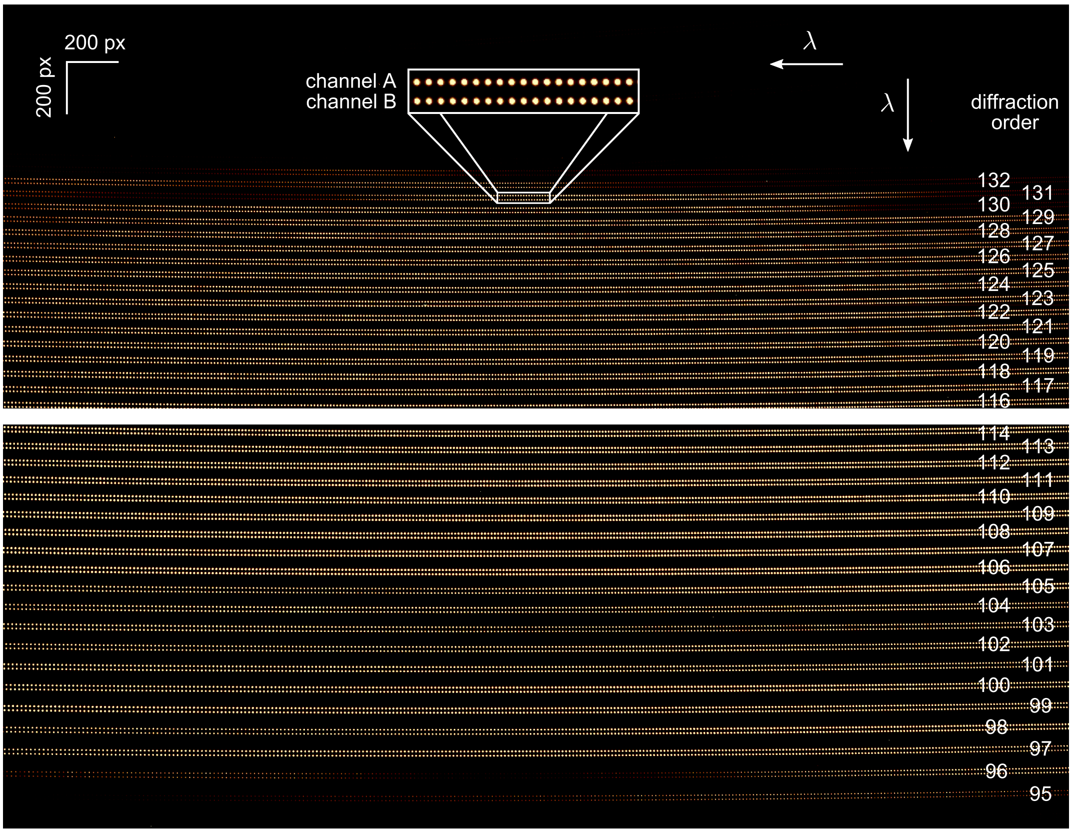

Figure 6.3 – Image recorded by the two HARPS CCDs with the astro-comb on both fiber channels. A 4096 × 1550 px section of each CCD is shown. The full range of each CCD amounts to 4096 × 2048 px. The inset shows 200 × 50 px around the diffraction order 131. Order 115 is completely lost within the gap between the two CCDs, and order 116 of channel B is clipped at the gap. About 37 illuminated orders are fully contained in the acquisition.

using the Levenberg-Marquardt algorithm [148]. In the square-sum of the fit residuals (χ^2) minimized by the algorithm, each data point is weighted by its squared inverse standard deviation given by photon noise. The photon-noise of the data points is calculated as $\sqrt{|N| + R^2}$, which includes the CCD readout noise R. N is the number of detected photoelectrons in each data point, which includes subtraction of dark and bias current of the CCD, and correction of different sensitivity of adjacent pixels (flat fielding). The absolute value of N is used to avoid negative values after subtraction of the CCD dark and bias current. The photon-noise limit of the uncertainty of the fitted line centers is calculated after the formula given in [3].

The positions of the comb lines and their uncertainties are the basis for further analysis. In combination with the known frequencies of the corresponding comb modes, the pixel-to-frequency relationship can be mapped across each echelle order. As detailed below, this relationship can be approximated by polynomial functions, which represent an absolute spectrograph calibration in optical frequency. The calibration repeatability – the most interesting quantity for most applications such as planet hunting – is determined from a series of spectrograph exposures with comb light on both channels. The line shifts are measured relative to a reference exposure, usually the first one in a series of spectrograph exposures. The total calibration shift of each channel is the average over all line shifts in the channel. In this average, each comb line of the analyzed exposure is weighted by the inverse variance of its line center given by photon noise (see also [25]). The difference of the calibration shifts in the channels A and B characterizes the ability to precisely track spectrograph drifts, and is thus a measure

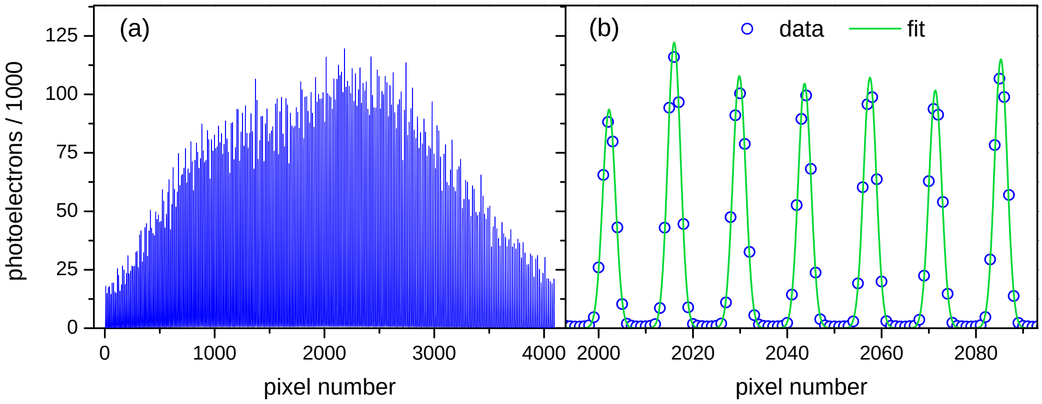

Figure 6.4 – Processing of astro-comb data acquired with HARPS. (a) Diffraction order 97 of channel A (center wavelength: 631 nm; 295 comb lines contained), extracted from the acquisition shown in Fig. 6.3. The 1D data string plotted in this figure has been obtained from the 2D image by the HARPS pipeline, a software provided to HARPS users by ESO. (b) Central portion of the data shown in part (a), with a Gaussian function fitted to each comb line.

of the calibration repeatability. Ideally, the standard deviation of the differential shifts of the channels A and B in a series of calibration exposures should be consistent with photon noise.

6.2 Campaigns of November 2010 & January 2011

The campaigns of November 2010 and January 2011 can be considered as one. Between the two campaigns, the astro-comb was left at the observatory, and was given an upgrade just before the start of the second campaign, by installing a fourth FPC as indicated in Tab. 6.1. The astro-comb was operated both night and day. The night-time was mainly used for comb-calibrated astronomical observations, and daytime was reserved for calibration tests. The following subsections present the most important scientific results.

6.2.1 Calibration repeatability

The calibration repeatability was examined in more than 60 series of spectrograph exposures with the astro-comb on both input channels of HARPS. Each series was given a length of about 10−100 exposures with exposure times of 10−40 s followed by a 30 s delay for CCD readout. During each series, all experimental conditions were kept as constant as possible. These conditions were however deliberately changed between the series in order to clarify their potential influence on calibration repeatability. This includes variations of properties of the astro-comb such as its optical power, offset frequency, side-mode suppression, and polarization of its output. The injection of the astro-comb into the multimode fibers and the mode scrambling were also varied, as well as parameters of HARPS such as the cooling of its CCDs and vibrations from its vacuum pump. It must be stressed that these parameters were changed far beyond normal operating conditions. The spectrum of the astro-comb was also subject to changes, owing to slightly different properties of the PCFs used, changing coupling efficiencies into the PCFs, and due to PCF degradation towards the end of their lifetimes.

This section presents an independent data analysis by the author of this dissertation, which is generally in good agreement with the results published in [39]. Slight differences are likely to be caused by cuts that exclude comb lines from the analysis, based on their properties such

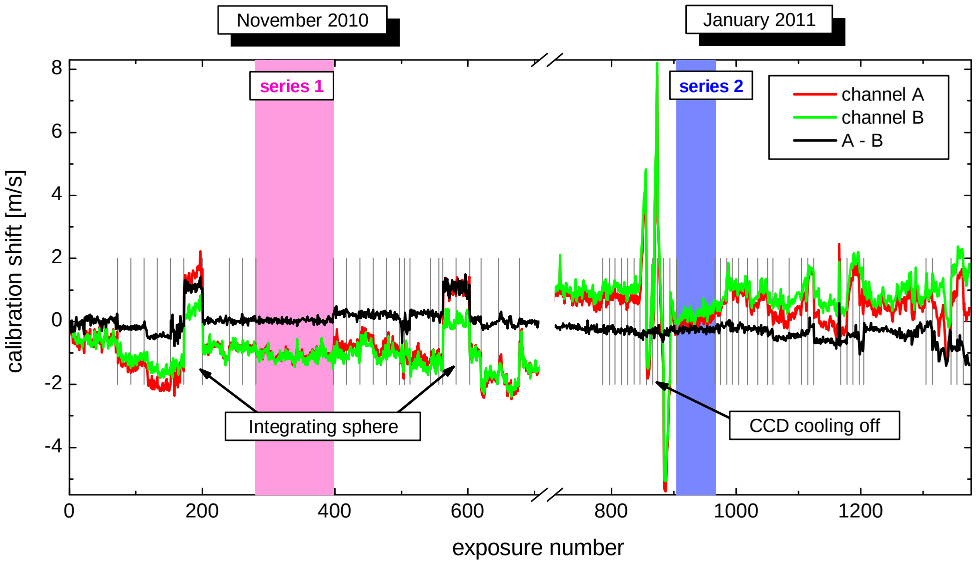

Figure 6.5 – Full range of calibration tests in November 2010 and January 2011, with the astrocomb on both input channels of HARPS. The plot shows the calibration shifts of the channels A (red line) and B (green line) and the difference between them (black line) for each spectrograph exposure. The reference is the first exposure of the November data. The vertical lines separate individual series of exposures during which experimental conditions were kept constant. Two series of particular interest are highlighted by the shaded areas, and tests in which an integrating sphere was used, or in which the CCD cooling was turned off, are labeled.

as width, amplitude and position. These cuts are needed to sort out lines that suffer from effects such as cosmic ray hits, hot pixels, grating ghosts, or malconvergence of the line fit, but their threshold levels are known to influence the result. Some differences also arise from a slightly different range of analyzed spectrograph exposures and series.

Figure 6.5 shows the calibration shifts of channel A, B, and their difference over the full range of data of November 2010 and January 2011. The shifts have been computed relative to the first exposure of November 2010. While the shifts of the channels A and B by themselves mainly reflect the instrumental drifts of HARPS and do not limit the performance, the differential shifts (A−B) determine the traceability of these instrumental drifts and thus the calibration repeatability. A noticeable spectrograph drift in the channels A and B of > 2 m/s occurred between November 2010 and January 2011, while A−B remained nearly unchanged. It is also remarkable, that while switching off the CCD cooling, the channels A and B drifted by about ±6 m/s, while A−B was nearly unaffected.

The calibration repeatability determined for each individual series is close to the photon noise limit of 6−10 cm/s. Significant shifts in A−B are however often observed between the series, supposedly due to systematic effects caused by the variations in experimental conditions. The instances in which an integrating sphere was inserted into the beam path lead to particularly noteworthy differential shifts of about 1 m/s. The effect of the integrating sphere is twofold: It equalizes the occupation of spatial modes within the subsequent multimode fiber, and it strongly reduces the optical power of the comb. The shift might therefore either be due to the altered spatial mode distribution, or due to signal level-dependent effects (see Sec. 6.3.1). However, despite such systematic effects and the fact that the spectrograph's parameters were changed far beyond regular operating conditions, the standard deviation of the differential calibration shifts is of 40 cm/s over the complete two test periods.

The series 1 and 2 as marked in Fig. 6.5, are among the longest consecutive measurements

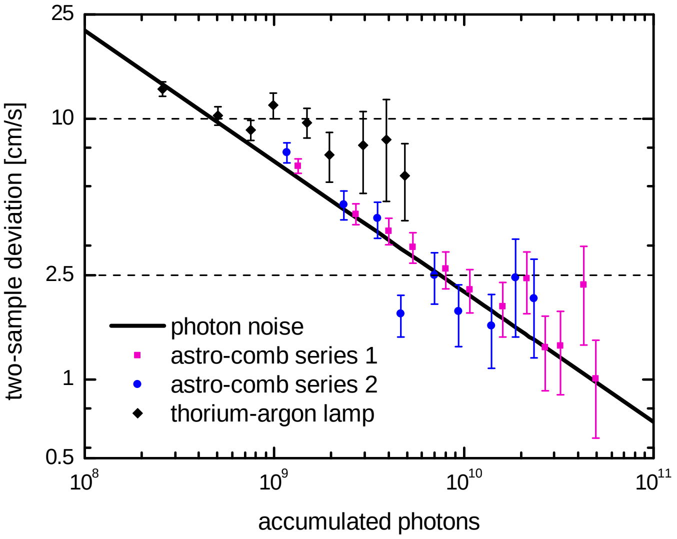

Figure 6.6 – Improvement of the calibration repeatability, characterized by the two-sample deviation, with increasing number of detected photons. The number of photons is increased by adding up subsequent exposures into bins, with the minimum number of photons corresponding to just one exposure per bin. The error bars represent the uncertainty of the two-sample deviation, estimated from the number of bins. The analysis is displayed for the series 1 and 2 from Fig. 6.5, and for comparison for a series of 116 thorium-argon calibrations. The black line represents the two-sample deviation expected from photon noise-limited statistics.

under constant conditions. Series 1, with an exposure time of 20 s, exhibits a standard deviation (photon noise given in brackets) of 6.4 cm/s (5.8 cm/s) in A—B. The standard deviation of series 2 (exposure time: 30 s) is of 7.0 cm/s (6.4 cm/s). The calibration repeatability can be further enhanced by reducing the photon noise, i.e. by accumulating more photons in each data point of the series. We do this by adding up a given number of consecutive exposures into bins. We characterize the series of binned exposures by their two-sample deviations σ_y in A—B:

$$\sigma_y = \sqrt{\frac{1}{2}\left\langle (y_k - y_{k+1})^2 \right\rangle} \tag{6.2.1}$$

Here, the angle brackets denote the average over the shifts of the binned exposures y_k. The two-sample deviation is commonly used to characterize the uncertainty of continuously drifting quantities, e.g. to quantify the stability of oscillators such as atomic clocks. Contrary to the Allan deviation, it allows for a dead time between the measurements, which in our series is given by the CCD readout time. Figure 6.6 shows the two-sample deviation as a function of accumulated photons per bin for series 1 and 2. It follows the photon noise limit, in proportion to the square root of the number of accumulated photons down to 2.5 cm/s. After accumulating more than about 5×10^9 photons per bin, which is reached after 4 min with the present spectral shape of the astro-comb, no further improvement is evident, and effects other than photon noise seem to become dominant. The uncertainty of the two-sample deviation of the two series (error bars in Fig. 6.6) is estimated from the number of bins by comparing it to a Monte-Carlo simulation. For comparison, Fig. 6.6 also shows the two-sample deviation for a series of ThAr calibrations of 116 exposures, analyzed by G. Lo Curto, ESO. Here, the two-sample deviation drops below 10 cm/s before effects other than photon noise dominate. Since the thorium lines are less regular and less densely spaced than the comb lines, accumulating 5×10^9 photons requires 30 min of continuous data acquisition with the ThAr lamp.

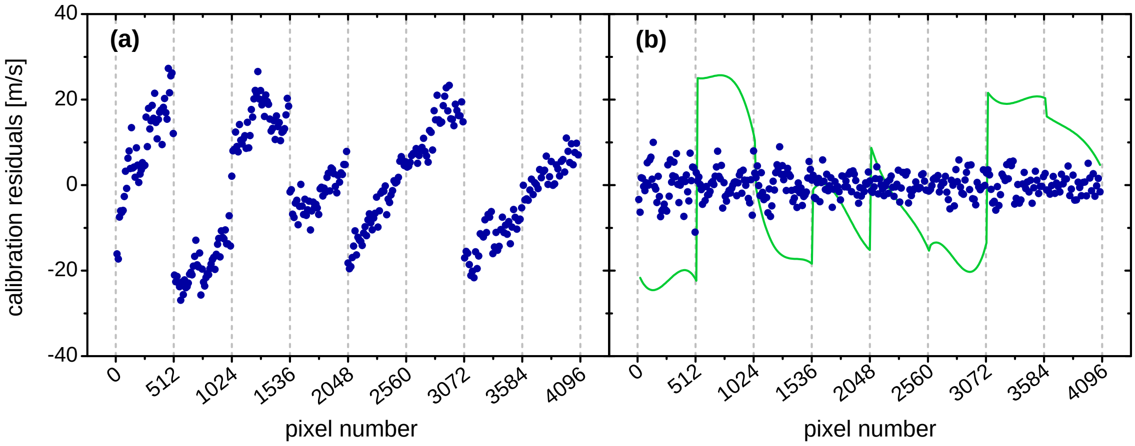

Figure 6.7 – Residuals from the frequency solution derived from the astro-comb, expressed in m/s, for echelle order 108 (center wavelength: 566.8 nm), channel A. The frequency solution represents an absolute frequency calibration, obtained by fitting a 3$^{\text{rd}}$ order polynomial to the known optical frequencies of the comb lines versus their observed positions on the CCD. The blue dots are the fit residuals. (a) Global fit across the full width of the CCD. The residuals change abruptly every 512 px. Root-mean-square (RMS) scatter of the residuals: 13 m/s. Photon-noise limit: 1.8 m/s. (b) CCD width divided into chunks of 512 px with a separate fit for each chunk. RMS scatter of residuals: 3.1 m/s. Photon-noise limit: 1.8 m/s. The green line indicates the difference between the comb calibration and the regular thorium-argon frequency solution.

6.2.2 Absolute calibration

A great advantage of the astro-comb over other astronomical calibration sources is its extreme accuracy, resulting from the accuracy of its RF reference. This can be taken advantage of for an absolute calibration, that accurately attributes an optical frequency to any measured line as a function of its position on the CCD. The absolute calibration also profits from the very dense and uniform sampling of the echelle orders provided by the astro-comb. While planet-hunting applications benefit from the astro-comb mainly for its high repeatability, the accuracy of its absolute calibration can be beneficial e.g. to compare spectra from different instruments. In Sec. 6.2.3 this property is exploited to create an improved atlas of the solar lines in the visible. The cosmological search for variability of fundamental constants from quasar observations is another application that demands accuracy instead of mere repeatability.

In order to demonstrate absolute calibration of the HARPS spectrograph using the astro-comb, we use a single spectrograph exposure dating from November 28, 2010. Knowing the optical frequencies of the comb modes, the observed line positions sample the pixel-to-frequency relation across each echelle order of HARPS. A 3$^{\text{rd}}$ order polynomial function – referred to as the frequency solution – is fitted to approximate this relation, which represents an absolute calibration. In this fit, the comb lines are weighted by their inverse variance given by photon noise. The goodness of this fit can be judged from the fit residuals, i.e. from the deviation of the comb lines from the frequency solution, as represented in Fig. 6.7 for echelle order 108 in channel A.

If the fit is carried out globally across the echelle order (Fig. 6.7(a)), abrupt changes in the fit residuals are observed every 512 px, indicating discontinuities in the pixel-to-frequency relation at these points. This had already been observed in earlier measurements with the astro-comb on HARPS in 2009 [25, 26], and was attributed to imperfections of the CCD pixelation caused by its manufacturing process: The HARPS CCDs have been fabricated with a 1024 × 512 px wide mask, stitching the full CCD together from smaller lithographic blocks of

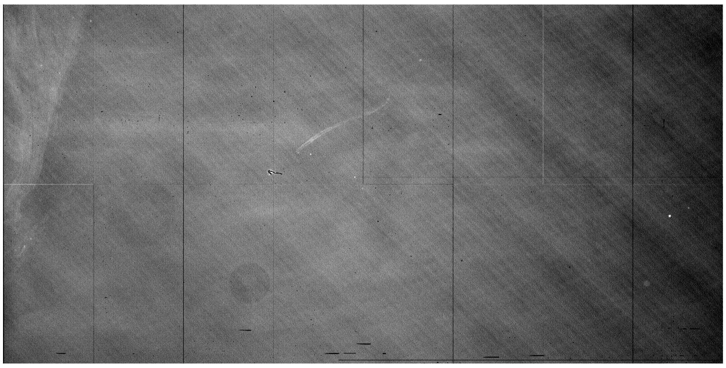

Figure 6.8 – Technical flat-field of one of the two HARPS CCDs. An altered sensitivity can be seen near the junctions between the 1024 × 512 px wide master blocks that make up the CCD pixel array. The diagonal stripes arise from uneven device thinning during fabrication of the (back-illuminated) CCD chip.

pixels. Figure 6.8 shows a flat-field exposure of one of the CCDs, where an altered sensitivity of the pixels close to the junctions is evident. The manifestation as discontinuities in the calibration had not been found before the use of astro-combs, owing to the lower accuracy and line density of ThAr lamps.

The discontinuities in the pixel-to-frequency relation can be handled by dividing the CCD width into chunks of 512 px, and by deriving a separate frequency solution for each of these chunks [25, 26]. This is done in Fig. 6.7(b) by a piecewise 3rd order polynomial fit. This implies 32 fitted parameters for the 328 comb lines contained in the echelle order. The root-mean-square (RMS) scatter of the residuals around the frequency solution of 3.1 m/s is more than 70 % above its photon-noise limit of 1.8 m/s. Summing up a large number of exposures considerably reduces the photon noise, but leaves the calibration residuals at about the same level [25]. It is therefore concluded, that these residuals mainly arise from irregularities of the CCD pixelation within the master blocks.

The difference between the frequency solutions derived from the astro-comb and from regular ThAr calibration is within ±26 m/s for echelle order 108 (green line in Fig. 6.7(b)). However, in other echelle orders this difference can reach up to >60 m/s (see [25, 26]), and order 108 is among those where the discrepancy is least pronounced. The large deviation is partly due to the relative inaccuracy of the known wavelengths of the thorium lines, but mainly the ThAr calibration suffers from distortions because it does not take into account the discontinuities at the junctions between the master blocks of the CCD.

6.2.3 Astronomical observations

The astro-comb in November 2010 has been used for nocturnal astronomical observations. This was the first time that an astro-comb had been used to trace the orbit of an extrasolar planet. Furthermore, an accurate atlas of solar lines was derived from observations of moonlight, which can serve as a secondary standard for calibration of other spectrographs. This demonstrates the integration of the astro-comb into standard observations, and proves its great value and potential for astronomical applications.

A comb-calibrated solar atlas

The absolute calibration provided by the astro-comb is exploited to create a new and more accurate atlas of the solar lines in the visible spectral range. HARPS had already been used

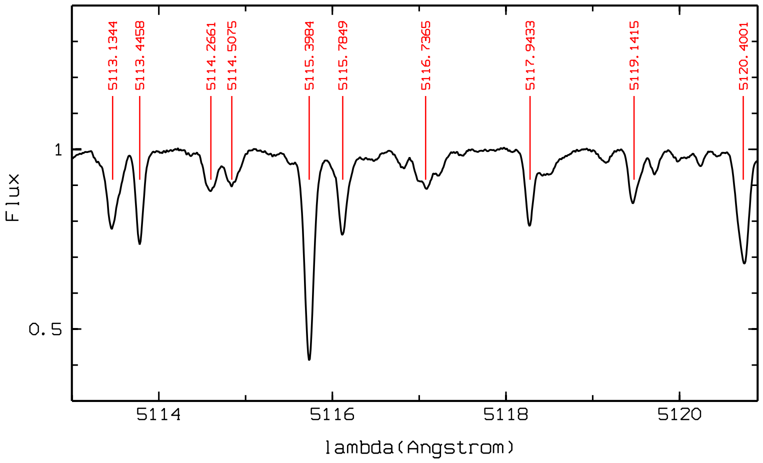

Figure 6.9 – Small portion of the atlas of solar lines, calibrated with the astro-comb as an absolute reference. The atlas has been created from five comb-calibrated observations of moonlight with HARPS in November 2010. The marked lines are labeled with their attributed center wavelengths in Å. Analysis of the data has been made by P. Molaro and coworkers. The full atlas of solar lines covers 476−585 nm, with a 4 nm gap around 532 nm.

earlier to generate a solar atlas with ThAr calibration, using the sunlight reflected from an asteroid [166]. However, with the above-described results for absolute calibration with the astro-comb, it must be concluded, that this earlier solar atlas is affected by distortions of the wavelength calibration of several tens of m/s, and that with the astro-comb, the accuracy of this atlas can be significantly improved.

To acquire solar spectra averaged over the full solar disk, the 3.6 m-Telescope was pointed at the Moon on November 25, 2010. Five spectra with exposure times between 60 s and 150 s were recorded with HARPS between 05:47:20 and 05:59:54 coordinated universal time (UTC). The spectral bandwidth of the astro-comb on that night provided sufficient optical power to calibrate the measurement over 476−585 nm. The moonlight was put on channel A of HARPS, while the astro-comb remained on channel B to track overnight instrumental drifts.

From these data, a comb-calibrated solar atlas was created by P. Molaro and coworkers at the Osservatorio Astronomico di Trieste, Italy. DAOSPEC was used to automatically find absorption lines and fit them with Gaussian functions to locate the line centers. Defining the line center through a Gaussian fit is an approximation, and the real line profiles are generally asymmetric. The Gaussian approximation has however the advantage of being easily measured and reproduced. The observed center wavelengths of the lines were corrected by the Doppler shifts from the motion of the Moon with respect to the Sun and of the Moon with respect to the observer. This yielded a list of 575 lines at 476−530 nm and 534−585 nm, with a 4 nm gap at 532 nm due to the gap between the two HARPS CCDs. Figure 6.9 shows a small portion of the atlas. The full line list is available under `cdsarc.u-strasbg.fr`(`130.79.128.5`) or `http://cdsarc.u-strasbg.fr/viz-bin/qcat?J/A+A/560/A61`.

The average accuracy of the lines is of 12 ± 6 m/s, and is free of instrumental effects, and for many lines the accuracy is as good as ≤ 5 m/s. This constitutes an improvement of a factor of 2−3 over the previously most accurate line list. The line atlas can be used to calibrate any ground or space spectrograph to that accuracy. It can also serve as a reference to track line shifts during solar activity cycles and as a benchmark for models of the solar photosphere. More on the comb-calibrated solar atlas can be read in [167].

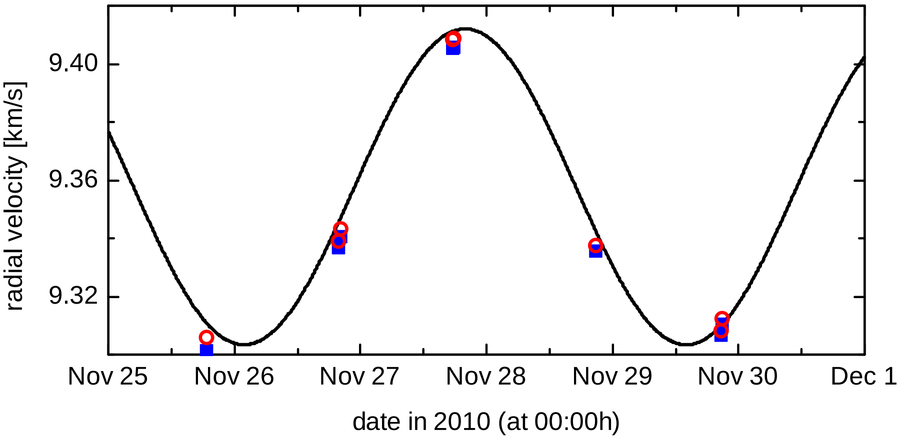

Figure 6.10 – Observation of the radial velocity of the exoplanet-host star HD 75289, using the astro-comb. This solar-type star is orbited by a Jupiter-mass planet with a period of 3.5 days. The planetary orbit is indicated by the black line that has been fitted to eleven radial-velocity measurements with HARPS. Three of the measurements were made in 2009 with thorium-argon (ThAr) calibration only, and eight were made in 2010 both with ThAr (blue squares) and comb calibration (red circles). Some of the data points lie very close to each other, and are hard to recognize as separate measurements. The uncertainty of the data points is smaller than the size of the data markers. The analysis has been made by G. Lo Curto, ESO.

Exoplanet HD 75289 b

The star HD 75289 is a 6 Gyr old, non-active main-sequence star of spectral type G0. It is located in the southern Vela constellation, at a distance of 29 pc (95 ly) from the Sun. It is more rich in metal than the Sun, and with a mass of 1.15 $\mathrm{M}_\odot$ and an effective temperature of 6000 K, it is slightly more massive and hotter. In the year 2000, a planetary companion (HD 75289 b) was found in its orbit using the CORALIE spectrograph at the 1.2 m Euler Swiss telescope at the La Silla Observatory (Chile) [168]. The planet has a minimum (or projected) mass of $m \sin(i) = 0.42\, M_{\mathrm{Jupiter}}$ and an estimated maximum mass of 0.51 $\mathrm{M}_{\mathrm{Jupiter}}$. It is in a circular orbit at 0.046 AU from its parent star, with a period of 3.5 d. It thus belongs to the class of “hot Jupiters” – Jupiter-mass planets in close-in orbits around their host stars.

The star has been observed eight times with HARPS from November 25 to November 29, 2010. Each observation was made twice, once calibrated with the astro-comb and once with a state-of-the-art ThAr lamp. Three more observations from the HARPS archive, dating from 2009, were added to the data set. The data have been analyzed by G. Lo Curto, ESO. The radial velocity (RV) was determined for each observation by cross-correlation of the measured spectra with a spectral mask in the solar system barycenter, with correction for instrumental drifts using the calibration. The uncertainties of the obtained RV changes are between 0.5 and 0.8 m/s with both types of calibration, dominated by the photon noise of the stellar spectrum. The difference between both absolute calibrations is of ~2.5 m/s, limited by the accuracy of the ThAr lamp. A Keplerian-model orbit was fitted to these data points. Figure 6.10 shows the data and the fit over a 6 d range.

The results are consistent with earlier observations. The mean RV is 9.36 km/s relative to the solar system barycenter. The root mean square of the fit residuals is 6 m/s. The deviation from the fit could either be due to stellar activity, pulsations, or due to another yet unidentified companion. HD 75289 is in fact known to have a low-mass stellar companion (0.135 $\mathrm{M}_\odot$) in a wide orbit (621 AU) [169], but this is estimated to cause an annual RV change of 7 cm/s only, and is thus excluded as the source of the observed deviations.

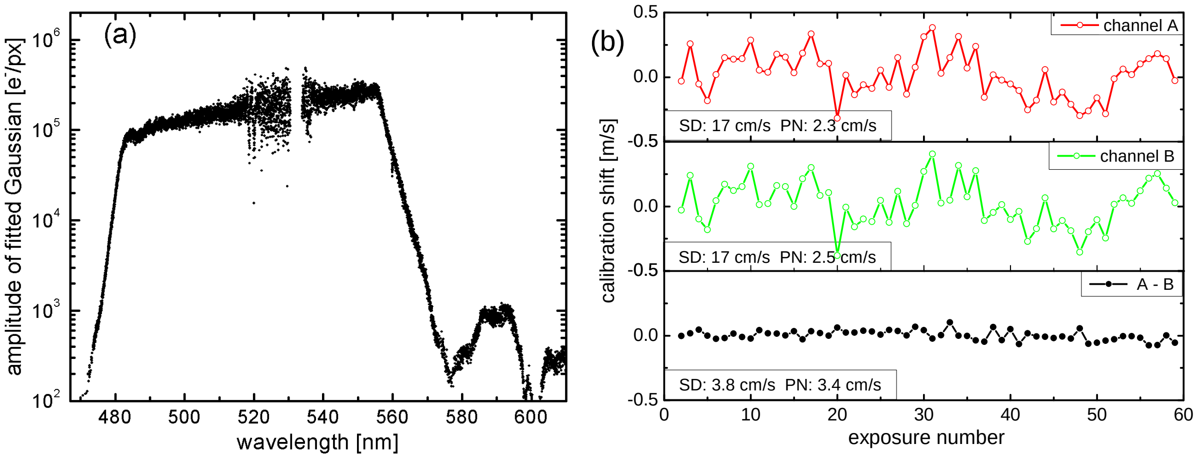

Figure 6.11 – Flattened 18 GHz astro-comb spectrum on the HARPS spectrograph in February 13, 2012. (a) Amplitude spectrum of the Gaussian functions fitted to the comb lines in channel A of the first exposure. The blaze function in each echelle order has been corrected with a flat-field exposure. (b) Series of 59 spectrograph exposures with the astro-comb on both channels A and B, with the first exposure serving as a reference. The standard deviation (SD) of the differential calibration shifts (A−B) is of 3.8 cm/s, with a photon noise (PN) of 3.4 cm/s.

6.3 Campaign of February 2012

The campaigns of November 2010 and January 2011 left the open question for the systematic effects that prevented the 2.5 cm/s repeatability from being reached over time scales of days and more. For searching Earth-like exoplanets, the ability to maintain this precision over time scales of up to several years is critical. The identification and characterization of the involved systematic effects is therefore indispensable. With its unparalleled photon noise and density of uniform and unblended lines, the astro-comb is an ideal tool for probing these effects, which was the main focus of the campaign of February 2012.

The previous results indicated a particularly remarkable shift upon the use of an integrating sphere as a mode scrambler. The reason for this shift could either lie in the reduction of the transmitted optical power, or in the altered spatial mode occupation in the subsequent multimode fibers. A systematic search for signal level-dependent line shifts is thus reported in Sec. 6.3.1. To tackle the aspect of the spatial mode distribution in the multimode fibers, a variety of different kinds and combinations of static and dynamic mode scramblers were tested. However, no major new insights could be gained from this, and this matter deserves further investigation.

The astro-comb of February 2012 was the first to incorporate a spatial light modulator for spectral flattening of the broadened comb spectrum (see Sec. 5.1). Figure 6.11(a) shows a flattened spectrum measured with HARPS. Because the coupling of the astro-comb to the spectrograph was extremely lossy (attenuation about 70 dB), the spectrum was truncated at 12 dB below its maximum, instead of the usual 20 dB. The resulting flat top is 74 nm wide, which however contains a 3 nm wide gap resulting from the gap between the two HARPS CCDs. The obtained spectral bandwidth was restricted by the available tapered PCFs for spectral broadening. The flattened region mainly suffers from strong line-to-line intensity fluctuations, especially near the spectral portions that overlap with the unbroadened spectrum. Such strong line-by-line fluctuations are not always present to this extent, and were not nearly as strong in many astro-comb exposures of 2010/11. An investigation of the circumstances under which this occurs might disclose ways to avoid this issue. For example, the polarization selection made by the flattening setup (compare to [25]) or interference effects in the multimode fiber coupling and scrambling system might possibly be important influences. The flat-top of the spectrum is slightly inclined, because the spectral response of HARPS was not factored in by the flattening algorithm. With the setup being in its earliest development stage, the flat-top also exhibits slight modulations from optically resolved pixels of the SLM. With more sophistication, an improved flatness should be attainable.

Figure 6.11(b) shows a series of spectrograph exposures with comb light on both channels, obtained with the spectrum of Fig. 6.11(a). Despite all shortcomings, the SLM was able to reduce the photon noise of the differential calibration shifts (A−B) from the 6 cm/s typical for earlier campaigns to 3.4 cm/s. The standard deviation of A−B of 3.8 cm/s is close to the photon noise limit.

6.3.1 Signal level-dependent systematics

Systematic line shifts that depend on the signal level on the spectrograph CCD are known to arise from charge transfer inefficiency (CTI) during CCD readout [170, 171]. Figure 6.12 illustrates the effect. During the readout of a CCD, charges are progressively transferred from one pixel to the next towards the readout amplifier. This transfer is generally incomplete, and a certain fraction of the charge carriers remain in the previous pixel, which is referred to as CTI. This distorts the shape of the detected lines, and shifts their centroid. With a decreasing number of charge carriers to be transferred, the fraction of the charge carriers that elude the transfer becomes larger, i.e. the effect of CTI grows stronger. As a result, the measured position of a spectral line on the CCD depends on its signal level. The readout is carried out in two directions, both of which suffer from CTI: The charges are first transferred to a shift register (parallel readout), and then displaced along the shift register leading to the readout amplifier (serial readout), see Fig. 6.12(b). The echelle orders of HARPS are oriented along the parallel readout direction, in which CTI is less pronounced [172], thus minimizing the effect of CTI on the measured spectra.

In order to characterize signal level-dependent line shifts on HARPS, its channel B was attenuated while using channel A to track instrumental drifts. The differential calibration shift between the two channels as a function of the attenuation is used to measure signal-level dependent effects. The attenuation of channel B was implemented by inserting gray filters of various optical densities into the beam path at the location where the two channels are separated. The optical density (OD) of a gray filter is defined as $\log_{10}(I_0/I)$, where I_0 and I are the light intensities directly before and after the gray filter, respectively. The OD was varied from 0.0 (corresponding to no inserted gray filter at all) to 2.0 (attenuation by a factor of 100), in steps of 0.2. A series of 10 spectrograph exposures was made for every OD. As the CTI depends on the speed of the CCD readout [172], it should be noted that the readout time was 22.6 s, as usual for all exposures in this chapter. The exposure time was kept constant at 40 s. The result is shown in Fig 6.13, revealing systematic calibration shifts of up to $\sim$4 m/s.

This result does however not explain differential calibration shifts that occur when both channels are attenuated by the same amount. This was the case for example when using an integrating sphere for coupling the astro-comb to HARPS in earlier campaigns. In order to address this problem, identical gray filters were inserted into both channels A and B at the entrance to the HARPS spectrograph. A series of 10 exposures was made with every filter, tracking the induced shift in the channels A, B and A−B as a function of the filter OD (see Fig. 6.14). It can clearly be seen, that channel A experiences a significantly greater calibration shift than channel B of up to almost 6 m/s, which causes a shift in A−B of up to 3 m/s. To a small extent this difference could be due to the fact, that the optical power delivered to HARPS is not quite the same for the two channels. In fact, channel A was about 8 %

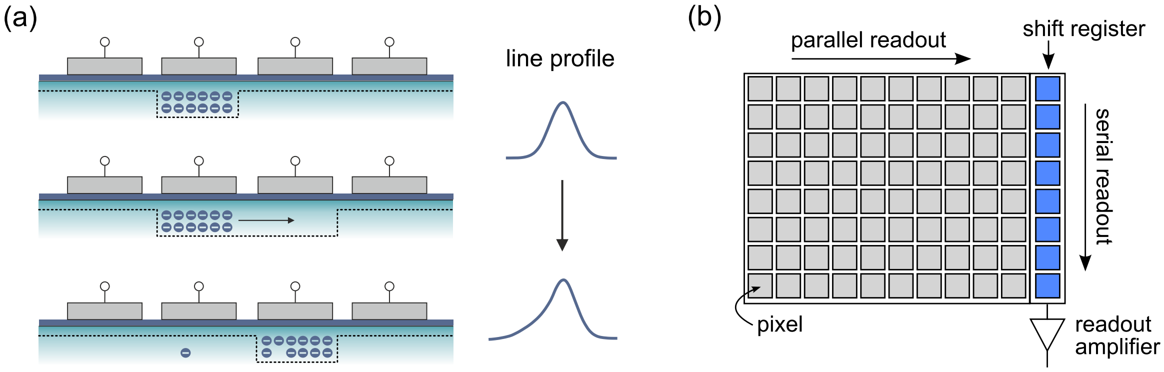

Figure 6.12 – Illustrations of the CCD readout. (a) Photoelectrons (blue dots) are transferred from one pixel to the next by adjusting the electrostatic potential (dotted line) through the electrodes on top. The fact that not all electrons are transferred is known as charge transfer inefficiency (CTI). As a consequence, the profiles and positions of spectral lines detected by the CCD are distorted. (b) Setup of a full-frame CCD. The charges from the pixels in the photosensitive area of the CCD are transferred to a shift register (parallel readout), in which the charges are then transferred towards the readout amplifier (serial readout). Both readout directions are affected by CTI.

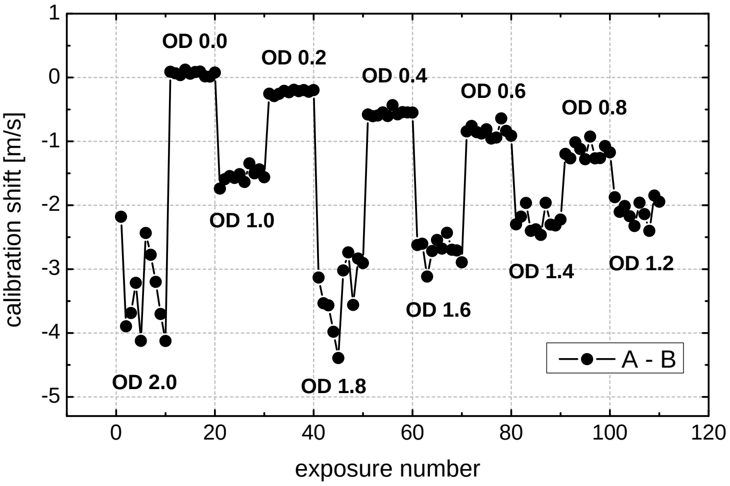

Figure 6.13 – Differential calibration shifts for different signal levels in channel B of HARPS, across eleven series of ten spectrograph exposures each, with comb light on both channels. While the signal level of channel A was kept constant to track instrumental drifts, gray filters of different optical density (OD) were inserted into channel B to reduce its signal level on the spectrograph CCD. The OD is annotated to each series, and is given by the decadic logarithm of the damping factor of the filter. Obvious shifts in A−B are observed as a function of the OD.

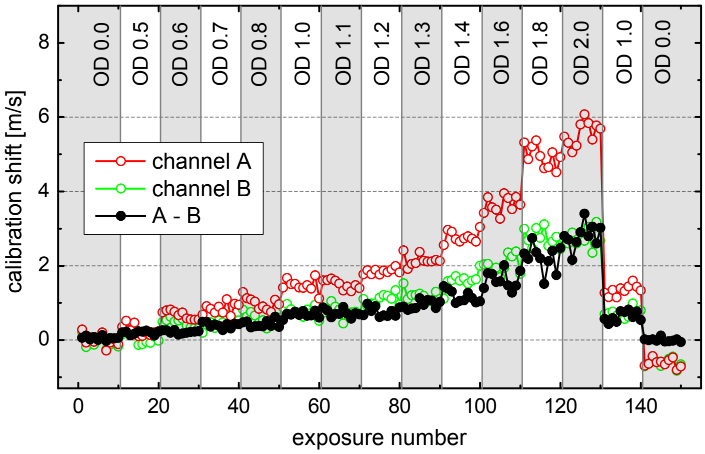

Figure 6.14 – Calibration shifts for different signal levels in both input channels of HARPS, across fifteen series of ten spectrograph exposures each, with comb light on both channels. Gray filters of identical optical density (OD) have been inserted into both channels, as indicated by the shaded areas. The OD is given by the decadic logarithm of the damping factor of the filter. Even though the OD is identical in both channels, the induced calibration shift is not.

dimmer than channel B. However, this cannot nearly explain the vastly different calibration shifts upon gray filter insertion.

As it turned out, CTI is not the only mechanism that causes signal level-dependent line shifts in our measurements. Another source of systematic errors is the HARPS pipeline, which projects the two-dimensional CCD image of each echelle order onto a spectral axis, creating one-dimensional spectra that are the basis of our analysis. The pipeline uses an optimal extraction algorithm after Horne [165]. It computes each data point of the spectrum as a weighted sum of several CCD pixels, so as to obtain optimum signal-to-noise ratio and spectrophotometric accuracy. In order to test the influence of the pipeline, raw CCD images were dimmed numerically by dividing the signal by a constant factor before having them processed by the pipeline. This analysis was done by G. Lo Curto, ESO. The bias and dark current were subtracted before the division and re-added afterwards, to simulate realistic conditions. After processing by the pipeline, the comb lines were fitted with Gaussian functions as usual to determine the calibration shifts relative to the result obtained without the numerical signal attenuation. Figure 6.15 shows the results for an attenuation of up to a factor of 100 averaged over 30 different comb exposures of HARPS. Channel A reacts more strongly with a shift of up to 8 m/s as opposed to up to 4−5 m/s for channel B, leaving differential shifts of up to nearly 4 m/s. This is in very good qualitative agreement with the above-described measurements, but yields a slightly larger shift. The difference could be due to CTI, indicating that both CTI and effects from the pipeline are relevant, with the pipeline contributing more to the systematic error budget. It should be stressed, however, that the effect of the pipeline is purely software-related, and has no physical basis. It is therefore not a fundamental limitation, since it can be circumvented by using a different software.

In order to separate CTI-related line shifts from effects caused by the pipeline, Zhao et al. [173] have analyzed the raw CCD images of the measurements in Fig. 6.14. This involved analyzing the 2D comb-line images on the HARPS CCD and characterizing their line shapes, which avoids data extraction by the pipeline. They found a noticeable effect of the optical attenuation on the asymmetry of the lines, which is interpreted as being a result of CTI.

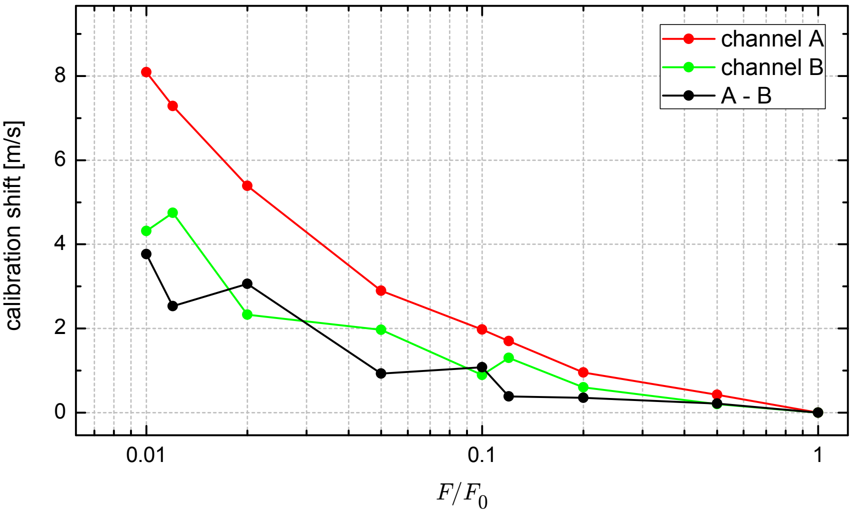

Figure 6.15 – Signal level-dependent calibration shifts caused by the HARPS pipeline – a software that extracts one-dimensional spectra from the two-dimensional CCD images. The plot shows the calibration shifts caused by numerically reducing the signal level of a CCD image from its original value F_0 to F, before having it processed by the pipeline. The bias and dark current of the CCD is subtracted before the reduction of the signal level, and added afterwards. Each data point is an average over 30 different measured spectrograph exposures with the astro-comb on both channels A and B. The analysis has been done by G. Lo Curto, ESO.

6.3.2 Offset frequency and repetition rate tuning

A great strength of the astro-comb over other calibration sources is its ability to provide tunable line positions, which can be used to map the pixel-to-frequency relation with very high resolution. The campaign of 2012 therefore also included tests with different comb structures, whose calibration results were checked for their compatibility. This addresses the question of calibration reproducibility rather than repeatability, i.e. whether different astro-combs yield consistent results. For most applications such as planet hunting, only the repeatability, which was characterized in the previous sections, is relevant. Reproducibility is vital to compare results obtained with different spectrographs and/or astro-combs. As an application, we rely on this property to compare results from different campaigns at HARPS with different astro-combs having different offset frequencies and repetition rates (Sec. 6.4).

In order to test the influence of the repetition rate f_r and offset frequency f_0 on calibration reproducibility, several series of exposures, each with a different setting of f_r or f_0, are recorded. Similar to what done when determining the calibration repeatability, all exposures are compared to a common reference to determine the calibration shift. However, this now involves comparing exposures with detuned line positions. Therefore, the shift of the comb lines is computed by subtracting their position from the one expected from a linear interpolation of the comb lines in the reference, taking into account the altered mode frequencies. The total calibration shift is then again averaged over all lines, with each line weighted by the inverse variance of its position given by photon noise.

Figure 6.16 shows two series of exposures with $f_0 = 12.90\,\mathrm{GHz}$ and $f_0 = 12.96\,\mathrm{GHz}$. The reference is the first exposure of the first series. The standard deviation of the differential calibration shifts (A−B) is of 6.3 cm/s, with a photon noise of 5.1 cm/s. The deviation from photon noise is about the same as within each individual series, indicating that the calibrations remain consistent upon detuning f_0. Unfortunately, f_0 has a very limited tuning range, and cannot be detuned by much more than shown here with this astro-comb, due mainly to the

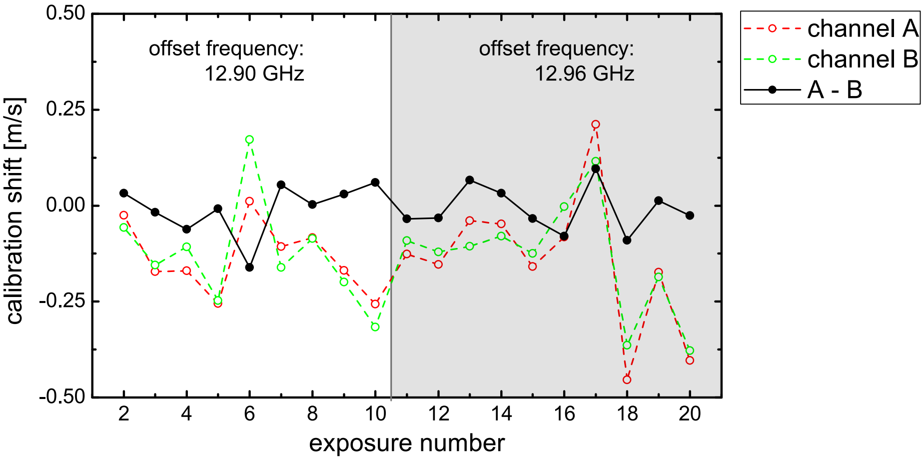

Figure 6.16 – Effect of changing the offset frequency f_0 of the astro-comb on spectrograph calibration. The plot shows the calibration shifts for two series of HARPS exposures with different f_0 and the astro-comb on both channels. The first exposure of the first series is used as the reference for both series. The altered offset frequency is taken into account by linear interpolation between the comb lines of the reference. The standard deviation (and corresponding photon noise) in A−B is of 6.9 (5.2) cm/s for the first series, 6.0 (5.0) cm/s for the second series, and 6.3 (5.1) cm/s across both series.

fixed offset frequency of the FPCs. Tuning f_r has the downside of giving a different frequency shift to each comb mode, but the benefit of allowing to detune their frequencies by a much larger amount.

In Fig. 6.17, f_r was increased from 18 GHz in 8 steps of +72 kHz. In the center of the spectrum, each step changes the frequency of the comb modes by 2.3 GHz, corresponding to 1.4 px. The full frequency range over which the comb modes are detuned is about equal to the mode spacing. With the line FWHM of about 3.3 px, every pixel within an echelle order is reached by the comb light during the scan. 10 exposures with comb light on both channels were made for every step. The measurement was concluded with a series 20 exposures with a repetition rate of exactly 18 GHz, whose last exposure serves as a reference for all other exposures. It should be noted, that this last series was made 7 hours after the previous series due to technical problems. A noticeable shift in the channels A and B is therefore caused by instrumental drifts before the last series.

The standard deviation of the differential calibration shifts over the full scan is of 7.4 cm/s, which is considerably above the photon noise of 3.9 cm/s, while for each individual series, this figure is only about 13 % above photon noise. This might be an indication, that f_r could have some small systematic influence. When passing from 18.000 432 GHz to 18.000 504 GHz, the center of gravity of the series in A−B is shifted by 14 cm/s, corresponding to more than 6 times the estimated uncertainty of the series centroid. The reason for this could be, that the linear interpolation between the comb modes does not sufficiently take into account irregularities of the CCD pixelation as treated in Sec. 6.2.2.

The scan of f_r can be used to sample the pixel-to-frequency relation in each echelle order more densely than in Sec. 6.2.2. In fact, such a densely sampled calibration map has been created from this series. A detailed presentation of this map is however omitted here, because there is little additional insight to be gained relative to Sec. 6.2.2. Ideally, such a map should be created with two independent astro-combs on the two channels, with one of them operating at constant f_r to track instrumental drifts during the scan. Otherwise, the measurement has

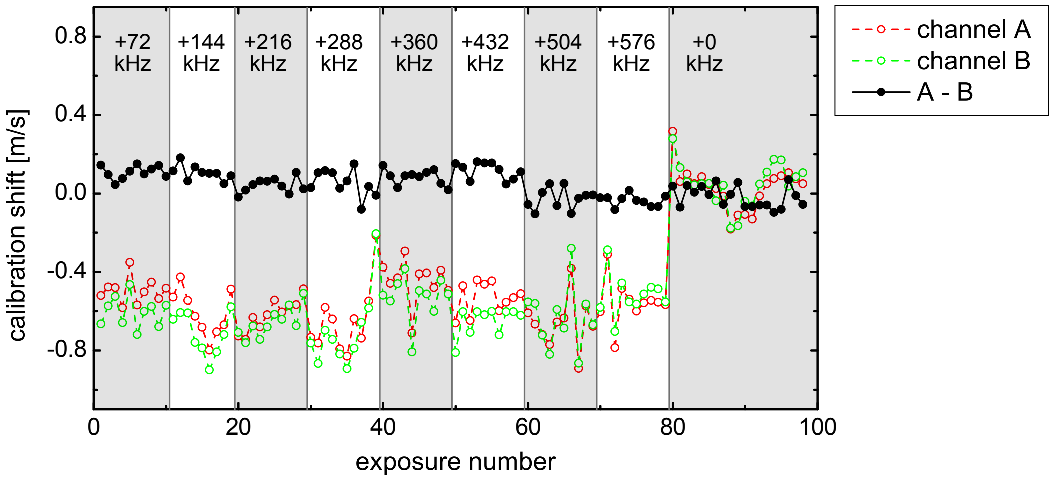

Figure 6.17 – Effect of changing the repetition rate of the astro-comb on spectrograph calibration. The plot shows nine series of HARPS exposures with the astro-comb on both channels A and B, at different repetition rates. The repetition rate of the astro-comb is 18 GHz plus the values indicated in the shaded areas. The last exposure of the last series serves as a reference to compute the calibration shifts. The different repetition rates are taken into account by linear interpolation between the comb modes of the reference. Standard deviation over all plotted data points in A−B: 7.4 cm/s. Photon noise: 3.9 cm/s. Average standard deviation for the individual series: 4.4 cm/s. Average photon noise: 3.9 cm/s.

to rely on the passive stability of the spectrograph (limiting the precision to ~1 m/s), or on detecting global spectrograph drifts via interpolation between comb modes as demonstrated above (estimated precision: ~7 cm/s).

6.4 All campaigns: Monitoring long-term drifts

Applications such as the hunt for exo-Earths or a real-time measurement of the cosmic acceleration require maintaining a cm/s-precision over several years, or decades, respectively. Long-term measurements of the calibration repeatability are therefore of great interest. The data available from all five astro-comb campaigns on HARPS, from January 2009 to February 2012, span more than 3 years, and thus constitute such a measurement. We compare these data to a common reference exposure from 2012, where the astro-comb covered a large bandwidth with good signal-to-noise ratio. As the astro-combs of the different campaigns differed in offset frequency and repetition rate, we interpolate linearly between the comb modes of the reference. From the results in Sec. 6.3.2, we expect this interpolation to work within a precision of approximately 7 cm/s.

Figure 6.18 shows the calibration shifts for all 3287 exposures with the astro-comb on both channels. This also comprises two additional series made with a 14 GHz astro-comb at the beginning of the November 2010 data, which are not included in Sec. 6.2. Data from the campaign of March 2010 are not included, because the astro-comb in this campaign suffered severely from excessively strong side-modes (see [25, 146] or Fig. 4.1). As evident from the time series in the channels A and B, HARPS has drifted by approximately 22 m/s during the 3 years. The differential calibration shifts (A−B) show how accurately this drift could be tracked. Here, a number of different systematic effects interfere, and are partly hard to separate from each other.

Regarding the full range of data in A−B, signal level-dependent effects (see Sec. 6.3.1)

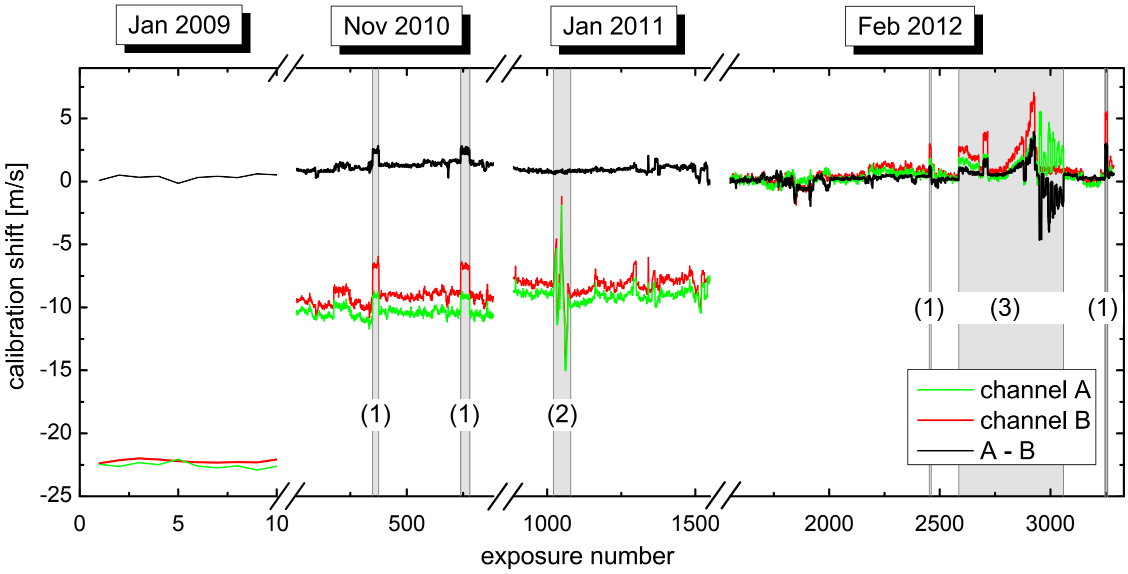

Figure 6.18 – Calibration shifts over all available spectrograph exposures with the astro-comb on both input channels of HARPS, including earlier campaigns. Data from the campaign in March 2010 are not shown, because the calibration was affected by excessively strong side-modes. Only a single series of ten exposures is included from January 2009. (1) With integrating sphere. (2) CCD cooling switched off. (3) Signal attenuation (gray filters).

seem to generate the largest variations in A−B, and appear to be the dominant source of error. Excluding all measurements in which the signal level has deliberately been reduced by insertion of a gray filter or an integrating sphere reduces the standard deviation in A−B over all exposures from 76 cm/s to 56 cm/s. Strikingly, global shifts in A−B seem to be present between the campaigns. The data of November 2010 and January 2011 are offset by +0.8 m/s in A−B relative to the two other campaigns. This might be explained by an altered spatial mode occupation in the multimode fibers at the HARPS input, due to altered fiber injection and scrambling. It could also be a result of instrumental drifts in A−B. At least partly, signal level-dependent calibration shifts also merge into this, as the optical power was often not quite equally distributed among the channels A and B.

Should there be a small instrumental drift in A−B over time horizons of years, this is not necessarily a limitation. The drift could be calibrated at the beginning of each observation night by putting the astro-comb on both channels to measure the shift in A−B, and then leaving the comb on one channel as a reference for the observations. A−B is then only required to be stable over the course of one night. The relatively small overall differential drifts in Fig. 6.18 give an optimistic outlook on this possibility. Systematic uncertainties however can generally not be handled this way. The spatial mode occupation of science light (e.g. starlight) in the multimode fibers might be different from that of the comb light, and may vary with time due to guiding errors. It is also questionable, whether the signal levels of comb and science light can be sufficiently well equalized or stabilized. The above-described results show that these systematic uncertainties require further investigation and strategies for their elimination.

Chapter 7

Comb-calibrated solar spectroscopy through single-mode fibers at the VTT spectrograph

In this chapter, the use of single-mode fibers for comb calibration of astronomical spectrographs is explored. The tests presented here have been performed at the Vacuum Tower Telescope (VTT) – a solar telescope operated by the Kiepenheuer Institut für Sonnenphysik, that is located at the Observatorio del Teide in Tenerife, Canary Islands. During the course of this work, two separate campaigns have been carried out, one in October 2011 and one in May 2012, to permanently install and test an astro-comb at the VTT echelle spectrograph, making this the first permanent installation of an astro-comb worldwide. In these campaigns, different calibration schemes have been investigated to optimize the obtained calibration precision.

The very high optical powers available from the Sun allow the use of single-mode fibers (SMFs) to feed the spectrograph both with sunlight and comb light, tolerating low coupling efficiencies on the part of the Sun. However, advances in adaptive optics are anticipated to enable efficient SMF coupling of distant stars [174], making this approach interesting for night-time astronomy as well. As an alternative to adaptive optics, photonic lanterns have recently been developed as efficient multimode to single-mode converters for astronomical applications [175, 176]. They split up the light of a multimode fiber into an array of SMF channels. The use of SMFs fully decouples the spatial beam parameters in the spectrograph from telescope guiding, which potentially limits the precision of other fiber-fed spectrographs. SMFs also eliminate the degradation of the beam profile through formation of laser speckles upon fiber coupling of coherent light. For multimode fibers, this occurs due to modal interference. This point is particularly critical for the astro-comb, owing to its high degree of coherence.

Another concept that we introduce for spectrograph calibration with an astro-comb is multiplexing of the fiber channel, which involves coupling both comb and sunlight into one single fiber. We investigate both temporally separated and simultaneous fiber injection of the two sources. Especially the latter concept is shown to enable very accurate tracking of spectrograph drifts during measurements. This eliminates the need for an extra fiber for calibration, that can potentially drift versus the other one and thereby cause calibration errors. In combination with the use of SMFs, we obtain nearly perfect spatial mode-matching between comb and sunlight, and thus an extremely robust calibration. This is similar to the mode in which iodine absorption cells are operated, which however absorb a part of the science light, and are surpassed by astro-combs in a number of calibration characteristics such as accuracy, repeatability, and spectral coverage.

The methodology is demonstrated by observing the 5-minute oscillations in the integrated solar spectrum, i.e. in the spectrum averaged over the full solar disk. These oscillations are well understood [177] and have been extensively characterized [178–180]. They hence represent a suitable test-bed for our method. The observation of integrated sunlight, considering the "Sun-as-a-star", is of great interest for night-time astronomy, as it allows investigating effects like stellar activity on radial-velocity (RV) measurements. These studies could not be carried out in such detail on other stars, but are needed for a more accurate search for extrasolar planets. Of course, our method is not limited to integrated sunlight, and the VTT telescope allows placing the SMF tip in the image of the Sun. This results in spatially resolved, comb-calibrated measurements, supported by the adaptive optics of the VTT. Currently, this approach is being used to study the center-to-limb variation of the solar convective blue shift, and is proposed for characterization of the solar meridional motion [152].

The calibration obtained with this method is also applied to assess the stability of absorption lines from Earth's atmosphere. Our novel concept for spectrograph calibration is believed to be important for future high-precision astronomy, and shows how future astro-combs could be utilized. Other observatories might consider a multiplexed fiber delivery, although employing multimode fibers. With further evolving fiber-injection techniques, future instruments might use multiplexed SMFs even on faint astronomical targets, e.g. for exoplanet searches.

7.1 Instruments and observations

The observations described and analyzed in this chapter were made at the VTT in Tenerife [181], where an infrared astro-comb had already been tested in 2008 [27]. For our tests, we fed the VTT echelle spectrograph with integrated sunlight from the auxiliary full-disk telescope ChroTel [182, 183], located in the same building as the VTT telescope. Within the beam path of the ChroTel, we installed a lens that produced an about 4 mm wide image of the pupil of the telescope, in which we placed the tip of an SMF with a 2.5 µm core diameter. The lens roughly matched the numerical aperture (NA) of the sunlight to the fiber NA of 0.13. This resulted in 800 nW of visible sunlight coupled into the SMF, which corresponds to a coupling efficiency of 0.1 ppm with respect to the total solar radiation power collected by the telescope. The fairly low coupling efficiency is mainly due to the fact, that to an earthbound observer the Sun – unlike other stars – appears as an extended source with poor spatial coherence properties. Its light thus consists of a multitude of spatial modes without a well-defined relative phase. Only one of these modes can be fully matched, and thereby efficiently coupled, to the single spatial mode of an SMF at a time. The sunlight collected by the ChroTel consists of several million spatial modes, as can be deduced from its optical resolution. This necessarily entails a poor spatial mode overlap of the guided mode of the SMF with the incident light field at the pupil image. The problem could be circumvented by coupling each spatial mode to a different SMF, e.g. with a photonic lantern, but in our case this is impractical because of the great number of spatial modes. This is different for distant stars, where photonic lanterns should represent a viable solution. Further, a diffraction limited image of a distant star, e.g. obtained by employing adaptive optics, could enable coupling into an SMF with efficiencies of > 70 % [174].

The SMF in this setup collects light from every point of the solar disk, but not with equal efficiency, owing to the approximately Gaussian-shaped acceptance profile of the SMF. This is because in the pupil image, light from different locations on the Sun is incident from different angles. As a result, the observed solar spectrum represents a weighted average over the solar disk. The rotation of the Sun imprints a ± 2 km/s RV variation across the solar disk. Inaccurate telescope guiding can consequently distort the RV measurement, by shifting the centroid of the weighted spatial average towards the blue or red-shifted region. The specified guiding accuracy

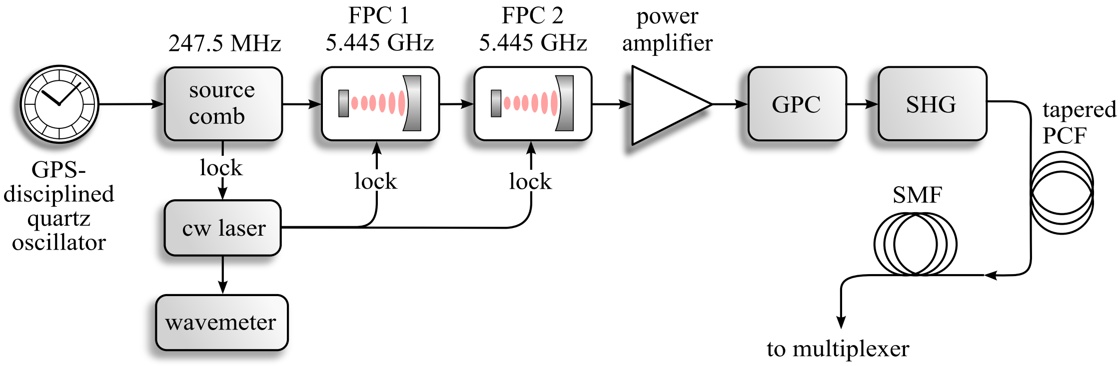

Figure 7.1 – Schematic of the astro-comb at the VTT after the upgrade in 2012. The source comb uses an Yb-based nonlinear polarization evolution oscillator (see Chapter 2). GPS: Global positioning system. FPC: Fabry-Pérot cavity. Cw: Continuous wave. GPC: Combined grating and prism pulse compressor. SHG: Second-harmonic generation. PCF: Photonic crystal fiber. SMF: Single-mode fiber.

of 0.5 arcsec of the ChroTel should keep the resulting RV errors below approximately 1 m/s. This guiding accuracy can however only be guaranteed under sufficiently good observation conditions. It is also important to note, that this sort of RV error from telescope guiding would not exist, if the technique was used in stellar night-time astronomy, since distant stars are normally not spatially resolved.

The astro-comb as installed at the VTT in October 2011, is described in Sec. 4.3 and [152], and has been characterized by heterodyning as shown in Fig. 4.13. In May 2012, just before making the tests reported here, the system was upgraded to enable higher calibration accuracy and more reliable operation. The configuration of the astro-comb after the upgrade is depicted in Fig. 7.1. The upgrade involved the integration of a new source comb with 247.5 MHz repetition rate and 50 MHz offset frequency. Both quantities are referenced to a GPS-disciplined quartz oscillator, accurate within a fractional uncertainty of $< 10^{-12}$ for integration times exceeding 1 s. During the upgrade of the comb system, the cavity mirrors of the two Fabry-Pérot cavities (FPCs) were exchanged to enable higher side-mode suppression. The finesse of both FPCs was characterized using the technique described in Sec. 2.3.3, and determined to be 3096 and 2143, respectively. The origin of the difference is not known, but could either be due to manufacturing tolerances or due to a slight contamination of the mirror surfaces in the second FPC. The radius of curvature of 50 mm of the curved mirrors in the plano-concave cavities forced us to revise the filter ratio, to obtain optimal suppression of higher-order spatial cavity modes. Both FPCs were set to a filter ratio of 22 (from originally 24 as in Sec. 4.3), resulting in a repetition rate of 5.445 GHz of the filtered comb. After frequency-doubling of the filtered comb, the spectrum is broadened in a tapered photonic crystal fiber and is coupled into an SMF representing the output of the comb system. The structure of the spectral envelope of the broadened comb could have been flattened out using a spatial light modulator (see Chapter 5). However, this was not necessary, because with the VTT spectrograph only a very narrow spectral window of less than 1 nm is observed at a time. Over a bandwidth of 460−680 nm, a power spectral density sufficient for spectrograph calibration could reliably be achieved. Based on the results in Chapter 4 it is estimated, that the side-modes in this astro-comb are suppressed to better than 47 dB, and thus cannot shift the calibration by more than 5 kHz. At a center wavelength of 630 nm, as used in this chapter, this corresponds to 3 mm/s. Furthermore, owing to the finite width of the comb modes, the mode filtering can shift their center of gravity by skewing their shape, in case the filter transmission peaks are not

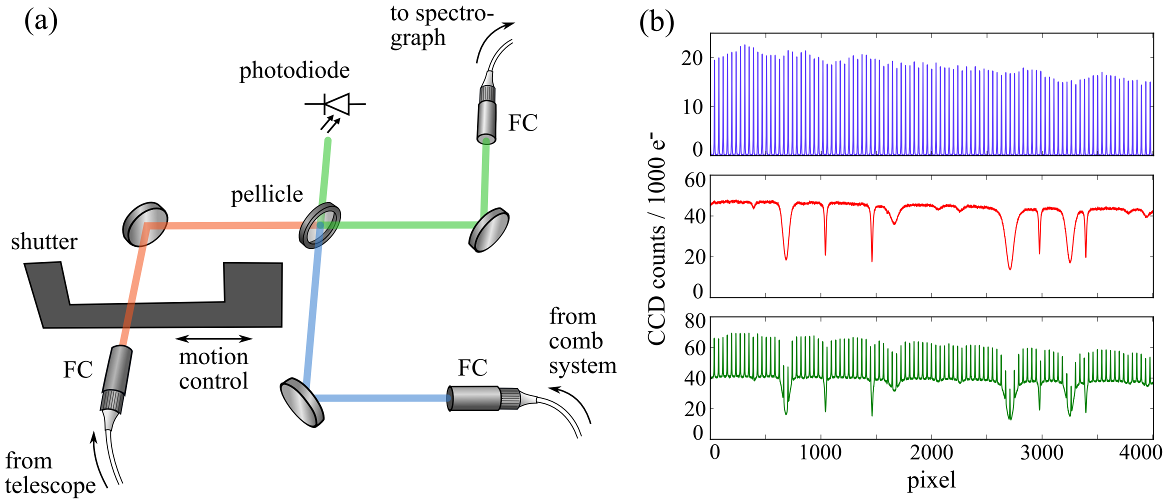

Figure 7.2 – (a) Setup of the optical multiplexer: The sunlight (red) from the telescope and the comb light (blue) enter the free-space section through fiber collimators (FC). They are combined (green) on a pellicle beam splitter, and then coupled into the output fiber leading to the spectrograph. The shutter can be positioned to block either the sunlight, the comb light, neither, or both. Three silver mirrors inside the beam path support optical alignment. (b) Spectra as measured using the VTT spectrograph at different positions of the shutter, with the multiplexer transmitting only comb light (top), sunlight (center), or both (bottom).

perfectly centered at their position [29]. In analogy to the discussion in Sec. 2.3.2 we estimate, that this effect can cause line shifts of up to 2.1 cm/s for this astro-comb.

The sunlight from the telescope and the calibration light from the astro-comb are combined into one SMF by an optical multiplexer that is shown in Fig. 7.2(a). The fiber-coupled comb and sunlight enter the free-space section of the multiplexer through fiber collimators using achromatic triplet lenses. The two beams are overlapped on a 2 µm thick uncoated pellicle, that on average reflects 8 % of the comb light and transmits 92 % of the sunlight. The reflectivity (and transmittance) is modulated by interferences on the two surfaces of the pellicle. Its very low thickness stretches the period of the modulation to much larger than the observed spectral range of 0.7 nm (see below). Another solution would be to replace the pellicle by a wedged glass plate, to suppress the modulation. The combined beam of comb and sunlight is coupled into an SMF leading to the spectrograph. All fibers are identical, feature single-mode guidance from 450 to 680 nm, and use connectors with angled end facets. The pellicle produces a second overlapped output, which for alignment purposes is monitored on a photodiode. Within the free-space section, there is a beam shutter in form of a U-shaped black metal panel, whose position is controlled with a motorized linear translation stage. Four positions for the shutter are defined, in which it blocks either the beam from the Sun, that of the comb, neither, or both.

The output fiber of the multiplexer leads to the VTT echelle spectrograph. From there, the light is focused through the entrance slit of the spectrograph by an aspheric lens, that matches the NA of the beam to that of the spectrograph. The VTT spectrograph has a very high resolution of $R = 10^6$, but usually only observes a single echelle order at a time, and hence only a rather narrow spectral range. The center wavelength of the observation can be tuned over a wide range by adjusting the angles of the echelle grating and predisperser. The image plane of the spectrograph can be accessed freely, allowing to place and exchange CCD cameras as desired by the user. With the PCO 4000 camera that we used to record our spectra, we could observe a 0.7 nm wide spectral range that we centered at 630.0 nm. The CCD chip of the camera was cooled down to −18 °C, had a root-mean-square (RMS) readout-noise of 11 photoelectrons, and counted 3.3 photoelectrons for every step of the 14 bit readout amplifier. The CCD had a 9 µm × 9 µm pixel pitch with 4008 pixels in the dispersion direction of the echelle order and 2672 pixels perpendicular to it. We employed an 8-to-1 hardware binning of the pixels in the latter direction. Along the illuminated pixels, we summed up 5 of the binned pixels in every column perpendicular to the dispersion direction, in order to gain a 1-dimensional data string from the CCD image.

For all exposures, we chose an exposure time of 1000 ms. The position of the shutter within the multiplexer was changed periodically for the observations, to first record a spectrum with comb light only, then with sunlight only, and finally with both, after which the cycle was repeated (see Fig. 7.2(b)). Between the exposures, we left a 1000 ms pause for the shutter to move. With this choice of the exposure cycle, two different multiplexed calibration schemes can be put into practice: If only the frames with pure sunlight or pure comb light are considered, the solar spectrum can be calibrated by interpolating the calibrations obtained from the comb exposures directly before and directly after each Sun exposure. This temporally separated signal transmission is known as time-division multiplexing. We refer to this calibration scheme as time-interlaced calibration. If also the exposures containing both comb and sunlight are considered, the solar spectra can be calibrated from the overlaid comb. This concept is hereafter referred to as overlaid calibration. In the following sections we investigate the benefits and drawbacks of the two calibration schemes, and assess their performance.

The observations used for our analysis were made on May 29, 2012, from 12:18 to 17:16 coordinated universal time (UTC). During this time span, 2715 full cycles as described above were recorded. Unfortunately, the series was interrupted several times due to technical problems, and the telescope guiding was partly disturbed by passing clouds. Towards the end of the series, 86 minutes of uninterrupted operation with stable guiding were accomplished, which we use as our observed sample for the comb-Sun comparisons. However, to test the stability of the comb calibration on its own, all recorded comb spectra are usable. The observed solar spectrum also contained several O_2 lines of telluric origin, i.e. stemming from Earth's atmosphere[1]. Their line centers are independent of telescope guiding, and hence to compare the astro-comb with these lines, all recorded solar spectra are of use.

7.2 Calibration tests

7.2.1 Spectrograph calibration

Following the procedure described at the end of Sec. 2.2, we determine the sign of the offset frequency of the source comb to be positive (+50 MHz). The offset frequency of the comb after mode filtering depends on which set of comb modes is transmitted through the FPCs. This is clarified by measuring the frequency of the cw laser that locks the FPCs, which coincides with one of the transmitted comb modes. With the wavemeter in Fig. 7.1, that was calibrated with a stabilized He-Ne laser, we determine this frequency[2] to be 281.639 945 (40) THz, which indicates an offset frequency of +2.7725 GHz and confirms the positive offset frequency of the source comb. The frequency doubling of the filtered IR comb doubles the offset frequency, modulo the repetition rate, to +100 MHz.

The known offset frequency (+100 MHz) and mode spacing (5.445 GHz) allow to attribute

---

[1] In this context, "telluric" does not refer to the chemical element tellurium, but to "tellus", which is Latin for "Earth".

[2] This is often referred to as the anchor frequency.

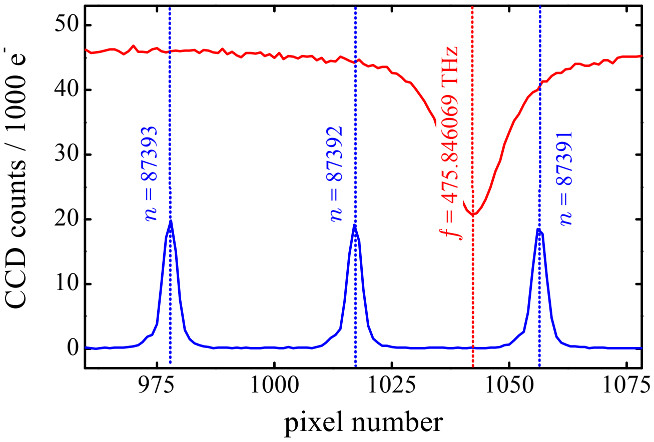

Figure 7.3 – Identification of comb lines. The graph shows a small portion of the comb spectrum (blue solid line near bottom) and of the solar spectrum (red solid line near top). The mode numbers n of the comb lines at the positions indicated by the blue dashed lines are derived from the known frequency f of a telluric O_2 line (red dashed line).

absolute frequencies to the observed comb lines, as soon as they have been assigned mode numbers. The latter can be derived from the known frequencies of the lines in the observed solar spectrum. The telluric O_2 lines are particularly well suited for this task, because they are fairly deep and much more narrow and stable than the lines originating from the solar photosphere. Their frequencies are listed in the HITRAN database [184], which we use to attribute mode numbers to the comb lines as shown in Fig. 7.3. The result is that the 101 observed comb lines have mode numbers ranging from 87 417 to 87 317.

As a next step, the comb lines are fitted with Gaussian functions using the Levenberg-Marquardt algorithm [148] (see Fig. 7.4(a)). The fit algorithm delivers uncertainties of the line centers from error propagation of the photon noise at each data point. The photon noise is assumed to be $\left[|N| + (R)^2\right]^{1/2}$, where N denotes the number of detected photoelectrons, and R the CCD readout noise. Subtraction of the dark and bias current of the CCD is included in N, as well as correction for different sensitivity of adjacent pixels (flat fielding). The centers of the fitted lines and their uncertainties are the basis for further analysis. The fact that the observed line profiles are not exactly Gaussian is uncritical for the further analysis, which merely requires a precise definition of the line center that leads to reproducible results.

An absolute calibration can be obtained from the line centers on the CCD and the known frequencies of the corresponding comb modes. With this information, the pixel-to-frequency relation can be mapped across the CCD, which is approximated by a third-order polynomial (Fig. 7.4(b)). According to the fitted polynomial, which is hereafter referred to as the frequency solution, an average CCD pixel spans 138.2 MHz or 87.09 m/s. The RMS deviation of the fit residuals of 0.87 m/s is close to the photon-noise limit of 0.60 m/s, but the discrepancy still requires an explanation. Using a higher-order polynomial for fitting does not significantly reduce the discrepancy. In [25, 26], remarkable deviations of the comb line centers from the frequency solution were observed, and attributed to irregularities of the pixelation caused by the manufacturing process of the CCD (see also Sec. 6.2.2). In particular, discontinuities in the pixel-to-frequency relation were found to occur every 512 pixels, which is equal to the width of the mask used for fabrication. In our case, the deviations are far less severe and do not display an obvious, periodically occurring pattern. However, after averaging the residuals from the frequency solution over all (>2700) comb spectra, their RMS still amounts

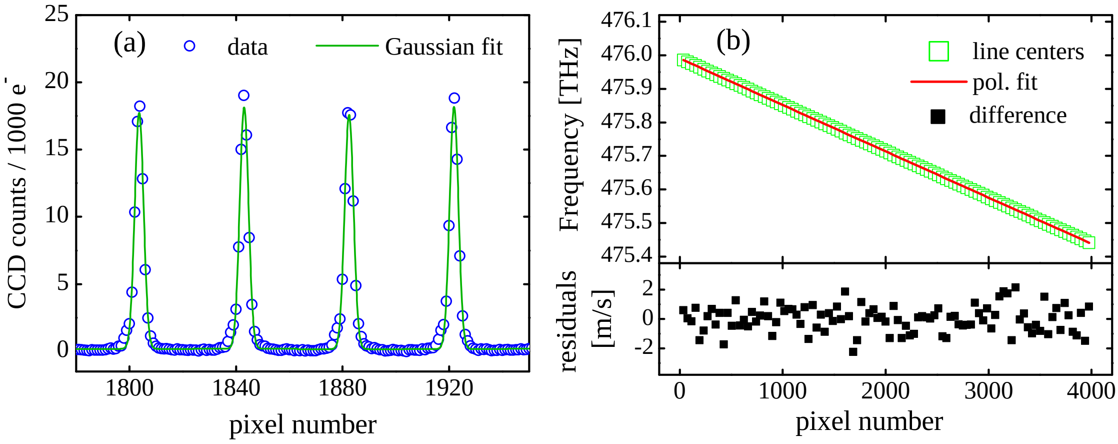

Figure 7.4 – (a) Small section of the observed comb spectrum, with a Gaussian function fitted to each comb line. The centers of the fitted Gaussians are assumed as the centers of the comb lines on the CCD. (b) Upper plot: Frequencies of the observed comb modes versus their line centers on the CCD. The data points are approximated by a third-order polynomial. Lower plot: Fit residuals, converted to m/s. Root-mean-square (RMS) of the fit residuals: 0.87 m/s. Photon noise: 0.60 m/s.

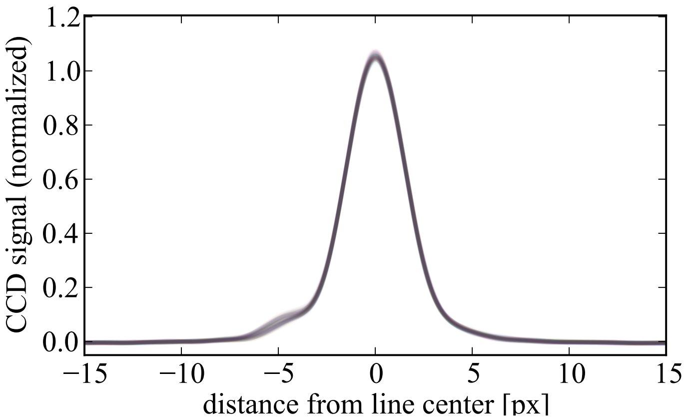

Figure 7.5 – Spectrograph instrumental profiles (superimposed, semi-transparent line plots), extracted from all comb lines in a single spectrograph exposure. Data points are interpolated with cubic splines. The positions of the data points at each comb line are measured relative to the position of the fitted Gaussian. The signal levels of the data points at each comb line are normalized to the amplitude of the fitted Gaussian.

to 0.50 m/s. Hence, the deviations above photon noise seem to be largely reproducible and of systematic nature. We thus attribute the largest portion of these deviations to irregularities in the CCD pixelation, even though the CCD was apparently not stitched together from smaller lithographic blocks of pixels, which is clearly preferable.

The astro-comb is a valuable tool to determine the instrumental profile (IP) of the spectrograph. This is the profile of a delta-shaped input spectrum as measured by the spectrograph. Knowledge of the IP is important e.g. when comparing spectra obtained from numerical computations to observed spectra. The numerical spectra need to be convolved with the IP to enable a meaningful comparison. As the comb modes are orders of magnitude more narrow in frequency than an optical resolution element of the spectrograph, they are ideal for measuring the IP. To this aim, the signal levels of the pixels around every comb line are normalized to the peak of the fitted Gaussian, and the pixel positions are measured relative to the center

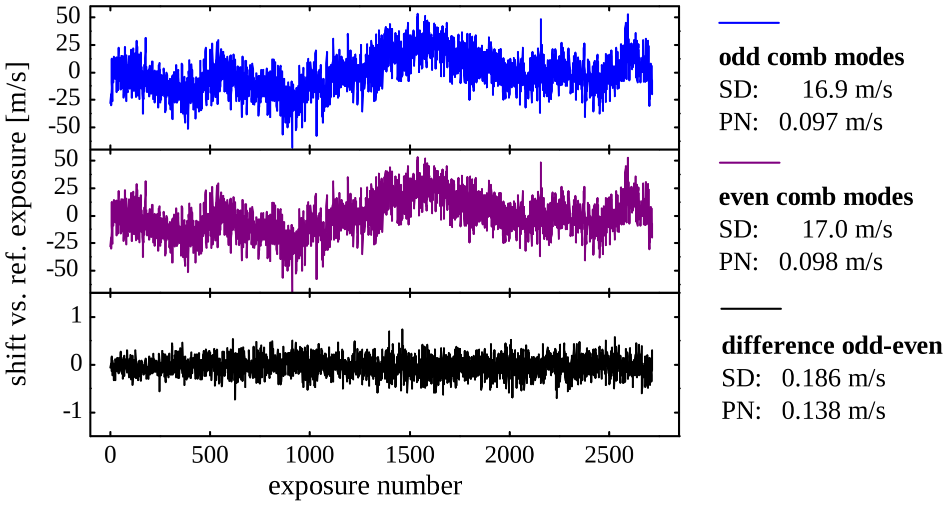

Figure 7.6 – Test of the calibration repeatability for overlaid calibration. The calibration shifts of two subsets of modes are compared, one formed by the lines with odd mode numbers (upper plot), and the other one formed by the lines with even mode numbers (central plot). The differential calibration shifts between the two subsets are shown in the lowest plot (notice the different vertical scale there). Next to each plot, the standard deviation (SD) and the photon-noise limit (PN) of the series are quoted. Integration time: 1 s. Cadence: 1 frame every 6 s.

of the Gaussian. The data points can be interpolated via cubic splines. Figure 7.5 shows the IPs obtained from all comb lines in a single exposure plotted on top of each other. In the left wing of the IPs, we see an asymmetric distortion that changes across the CCD. Therefore, using a single IP model for the complete observed spectral range is only possible in first order approximation. It is also worth noting, that the frequency solution and the IP must apply the same definition of the line center, as done here. This ensures, that a convolution (or deconvolution) with the IP does not imply a shift of the pixel-to-frequency relation. The IP shown in Fig. 7.5, understood as the average IP over the observed spectral range, has a full-width at half-maximum (FWHM) of 3.646 px, or 504 MHz, suggesting a spectrograph resolution of 1.06×10^6.

7.2.2 Calibration repeatability

In order to assess the calibration repeatability that the astro-comb provides in different calibration schemes, we consider only exposures with pure comb light, circumventing any limitations from the solar observation.

For testing the calibration repeatability provided by the aforementioned concept of an overlaid calibration, the observed comb lines are divided into two groups: One group is represented by the modes with odd mode numbers, and the other one by even mode numbers. We thus decompose the astro-comb into two interleaved combs with twofold mode spacing, and assess their relative stability. This mimics an overlaid calibration, with light from two sources simultaneously sent through the same fiber. For each exposure, we compute the shift of the comb lines relative to their position in a reference exposure, which is the first exposure of the series. The combined shift of all odd (even) modes is computed for every exposure by averaging the individual line shifts. The averaging of lines applies photon-noise weighting, which means that each line is weighted by its inverse variance given by photon noise. Figure 7.6 shows the result for the odd modes, the even modes, and the difference between the two. While the shifts of the

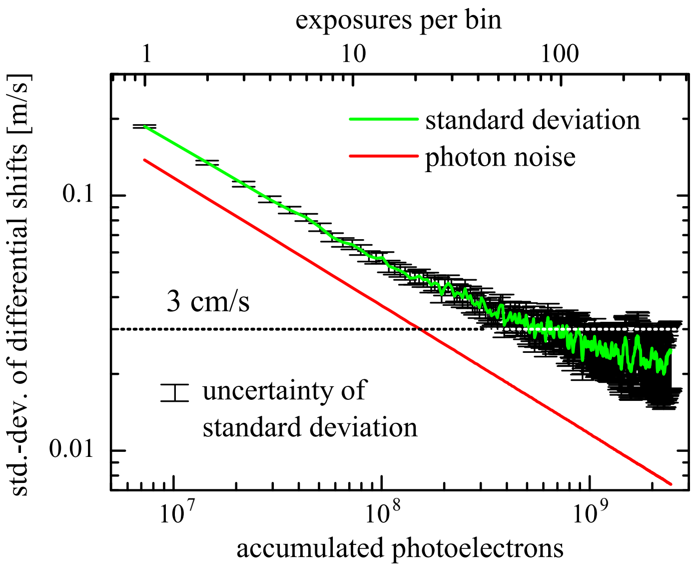

Figure 7.7 – Improvement of the calibration repeatability for overlaid calibration with increasing number of accumulated CCD counts. The number of counted photoelectrons is increased by summing up exposures into bins of increasing size (from just 1 exposure per bin to up to 360). The standard deviation (green line) of the differential shifts between odd and even comb modes is computed for each series of binned exposures. The uncertainty of the standard deviation (black error bars) increases with increasing number of accumulated counts because of the decreasing number of bins within the series. An exposure of 1 s was taken once every 6 s.

odd modes and the even modes mainly reflect spectrograph drifts, the difference between the two should not be larger than photon noise, if the two calibrations are consistent to that level. The standard deviation of both the odd and the even modes amounts to 17 m/s, whereas the standard deviation of the difference is only of 0.186 m/s (photon noise: 0.138 m/s).

The deviation from photon noise-limited statistics of the differential shifts, unlike in the case of the deviations from the frequency solution, can hardly be explained by some type of systematic uncertainty. Rather, we conclude that the scatter above photon noise is due to an excess noise source. Thermal noise certainly contributes to the excess noise, since the CCD was not cooled down to the very low temperatures reached by other astronomical CCDs (typically −90 °C to −120 °C). The largest portion of the excess noise is however most likely to be provoked by internal seeing within the spectrograph beam path, due to convection of air[3]. The convection elements have different air temperature, and therefore different refractive index, which disturbs the beam. This occurs because the VTT spectrograph is neither evacuated nor thermally stabilized. Nevertheless, for this calibration scheme, the improvement over the passive stability of the spectrograph amounts to about two orders of magnitude.

Even if the calibration repeatability obtained in a single exposure is limited by noise, it can still be further enhanced by combining several exposures into one. If an effect cannot be averaged down in this manner, it means that its influence displays some systematic behavior instead of being purely random. We test this by combining a given number of subsequent exposures into bins. We then carry out the same analysis as previously for the series of binned exposures. The result as a function of bin size is shown in Fig. 7.7. The standard deviation drops below 3.0 cm/s for bins of > 126 exposures. Again, the photon-noise limit is

---

[3] In later, so far unpublished tests conducted by H.-P. Doerr and coworkers it turned out, that the excess noise is drastically reduced 10 min after turning off all air-conditioning systems in the building. This supports our hypothesis on the origin of the excess noise.

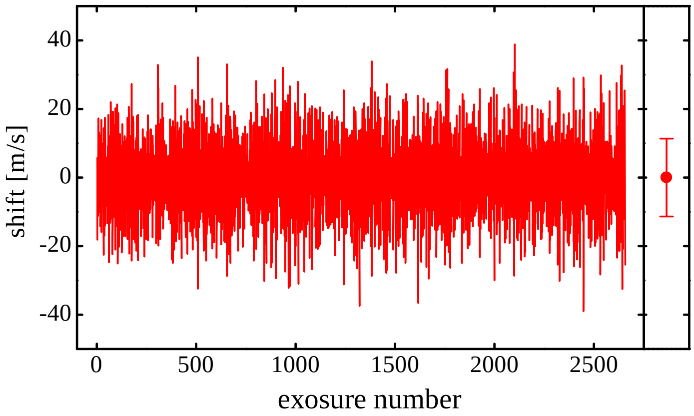

Figure 7.8 – Test of the calibration repeatability for time-interlaced calibration. Each calibration is compared to the interpolation of the preceding and subsequent one. The photon noise-weighted difference yields the calibration shifts as shown by the line plot. The error bar on the right represents the standard deviation of 11.3 m/s of the measured shifts. The photon-noise limit is 0.097 m/s. Integration time: 1 s. Cadence: 1 frame every 6 s.

not reached, which would allow an uncertainty as low as 1.2 cm/s at this point. The standard deviation seems to form a plateau near 2.3 cm/s. Strikingly, a plateau at approximately the same value was also found with an astro-comb on the two-channel spectrograph HARPS (see Sec. 6.2.1). As one of the world's most stable spectrographs, HARPS is passively stable to better than 1 m/s over at least many hours [20]. The VTT spectrograph in contrast, being neither evacuated nor temperature or pressure stabilized, can drift by up to 100 m/s over a day. The results thus show that with science light and calibration light simultaneously sharing the same spatial mode, spectrograph stabilization is of reduced importance, provided that seeing within the spectrograph is kept low enough.

We now turn to the repeatability as determined for time-interlaced calibration. In this calibration scheme, a science exposure is preceded and followed by a calibration exposure. From the two calibration exposures, two frequency solutions are derived, that are interpolated to calibrate the science exposure. To test this concept with comb light only, each calibration exposure is compared to the interpolation of the calibrations 6 s before and 6 s after it. The total calibration shift is computed as the photon noise-weighted average shift of the lines versus the interpolated calibration. The result is shown in Fig. 7.8. It displays a standard deviation of the calibration shifts of 11 m/s, which is only a rather modest improvement over the 17 m/s as obtained when considering the fully uncompensated spectrograph drifts (see upper two plots of Fig. 7.6). The uncertainties in this calibration scheme are known to arise from spectrograph drifts that occur on a sub-second time scale [153]. We expect a slightly better repeatability than demonstrated here for the calibration of the solar spectra, because of the twofold lower time span between the interpolated calibration exposures. Generally, the higher the frame rate, the better is the repeatability that we expect for this calibration scheme, as shown in [153] using a 10 Hz frame rate.

7.3 Calibrating solar spectra

7.3.1 Fitting procedures and noise limitations

We now show how our calibration methods can be applied to solar spectra. At first, we only consider exposures containing pure sunlight. The line centers of the absorption lines

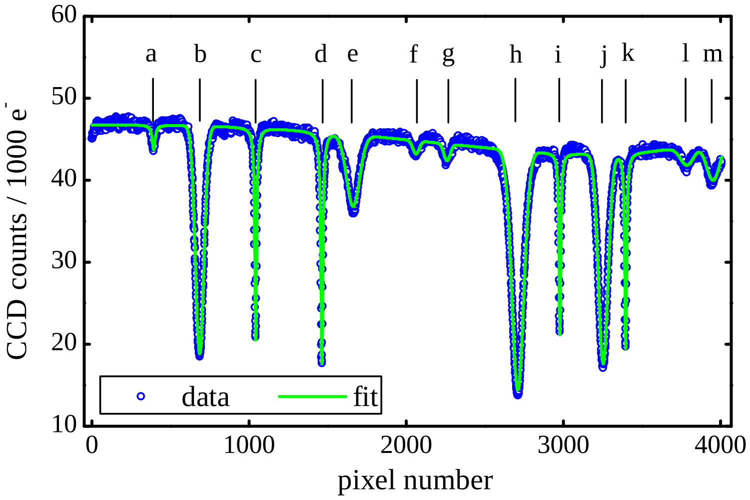

Figure 7.9 – Fit of the solar spectrum. The solar lines are fitted with Gaussian functions, while the telluric lines are fitted with Lorentzian functions. The global descent of the signal level from left to right is approximated by a fourth-order polynomial. The black dashes indicate the positions of fitted spectral lines labeled with the identifiers from Tab. 7.1.

are determined by fitting, similar to what was done in Sec. 7.2.1 for the comb lines. We approximate the solar lines with Gaussian functions, and the telluric lines with Lorentzian functions. Contrary to the analysis of the comb exposures, we do not perform the fit on a line-by-line basis, but fit the sum of the functions of all lines. The overall signal level is not constant along the echelle order, which is mainly because of the blaze function of the spectrograph grating. This is modeled by multiplying the sum of functions by a fourth-order polynomial, whose coefficients are adjusted by the fit. The result is shown in Fig. 7.9.

The positions of the line centers obtained in this way can be converted into frequencies using the frequency solution obtained from time-interlaced calibration. This permits the tracking of frequency changes (or RV changes) of the lines. Fitting a line model that accurately reflects the true line shapes is not needed here, since we are not interested in an accurate determination of absolute line frequencies. If the absolute frequency of a solar line needs to be specified, it is customary to determine its bisector, to account for the asymmetry of the line profile.

Determining line shifts in the overlaid exposures proves to be considerably more difficult. Here it is a strict necessity that the fit functions accurately reflect the true line shapes. This is not only the case for the solar lines, but for all lines, including the comb lines. If the model used for fitting does not fully match the measured lines, the fit residuals can influence the fit of the overlaid lines, and distort their measured line center. Since the relative signal strength of the two overlaid sources is not fixed, but can vary widely, the crosstalk between the two channels is not stable. Only if the fit functions perfectly match the measured line shapes can it be excluded, that the two fits influence one another in a systematic way. However, the two overlaid spectra will always be affected by each other's photon noise: The added photons from the comb bring in additional noise to the solar spectrum, but do not increase the signal of solar spectrum. Thus, the overlaid calibration usually comes at the price of decreasing the signal-to-noise ratio of the spectrum to be calibrated, and also the calibration itself is affected by a degraded signal-to-noise.

Because the line profiles have to be modeled so accurately, the approach of fitting simple mathematical functions to the spectral lines is given up when it comes to analyzing overlaid spectra. Instead, we use template spectra (as described below) for the Sun and for the comb,

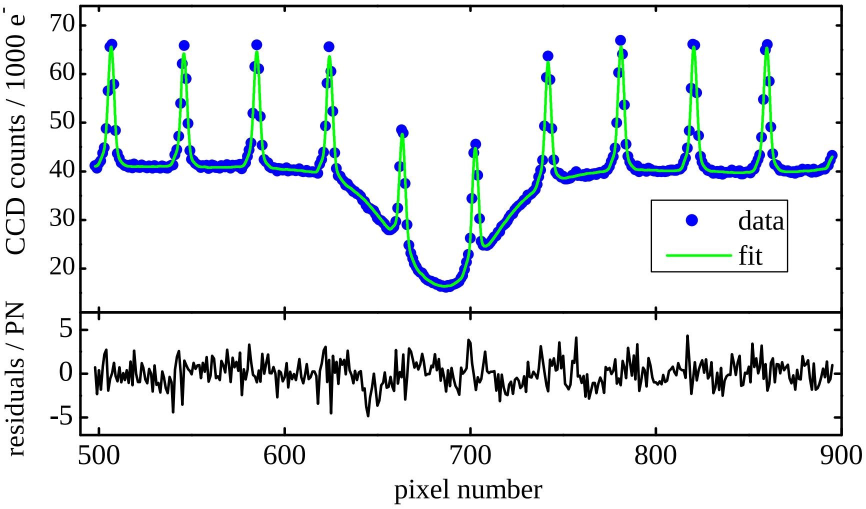

Figure 7.10 – Fit of a combined Sun and comb spectrum around a Fe I solar line. Upper plot: The measured data are fitted with a sum of templates for the solar spectrum and for the comb spectrum. Lower plot: Difference between measured data and model fit, expressed in terms of the photon noise (PN) of the data. The root-mean-square (RMS) of the distribution should be 1 if the model fits the lines within the limits given by photon noise. The actual RMS of the fit residuals is 1.47 times the photon noise.

whose sum (including an offset) is used to approximate the overlaid spectra. The sum of the two templates is matched to the overlaid spectra by shifting each template's position relative to the CCD pixels and by scaling its signal level. The square-sum of the fit residuals (χ^2), applying photon-noise weighting of the data points, is calculated by evaluating the templates at the positions of the pixels using cubic spline interpolation. The fit is designed such that the comb lines are scaled individually, since their relative signal strength is also subject to slight changes. Only a selected region around each line in the solar spectrum is fitted at a time. In this manner, lines in the solar spectrum can be tracked separately. Especially the telluric lines are expected to experience shifts that are quite different from the lines of solar origin. They also change in depth over the course of the day, owing to the varying air-mass along the line of sight.

In a first approach, a single comb exposure and a single solar exposure were used as templates for fitting. This however resulted in a very inaccurate localization of the line centers. The reason is, that if a noisy model is fitted to a noisy data set, the resulting χ^2 as a function of the fit parameters acquires finely structured noise, and thus loses its smoothness. This creates numerous local minima in the χ^2 landscape for the fit algorithm to get stuck in. The effect was found to be most pronounced for the broad solar lines, because their shallow slopes of the χ^2 valley can more easily acquire local minima through noise. For the comb, the effect turned out to be close to negligible, because of its narrow and numerous lines.

It was thus found to be essential to create templates with minimized noise. We therefore averaged the Sun and comb templates over all available comb and solar spectra. Each spectrum was shifted to match the line centers as indicated by the Gaussian/Lorentzian fits, before including it into the average. This was done separately for every line in the solar spectrum. In order to suppress the noise ever further, the templates for the lines in the solar spectrum were low-pass filtered by a fast-Fourier transform (FFT) filter. The cut-off of the filter had to be adjusted carefully depending on the line width, in order to achieve optimal noise suppression while still fully preserving the line shape. This yielded extremely smooth line templates es-

Table 7.1 – Photon noise of the fitted line centers in the solar spectrum. PN: Photon noise without overlaid comb. PN2: Photon noise with overlaid comb. The increase of photon noise induced by the overlay is listed in the rightmost column. The atomic/molecular species have been identified using [185–187].

identifier	species	origin	PN [m/s]	PN2 [m/s]	increase
a	H_2O	telluric	20.80	23.08	11 %
b	Fe I	solar	3.17	3.68	16 %
c	O_2	telluric	1.70	1.74	2 %
d	O_2	telluric	1.57	1.62	3 %
e	Si I	solar	14.09	15.97	13 %
f	O I / Ni I	solar	58.73	67.83	16 %
g	Sc II	solar	38.92	45.33	16 %
h	Fe I	solar	3.26	3.58	10 %
i	O_2	telluric	1.94	2.23	15 %
j	Fe I	solar	3.51	3.86	10 %
k	O_2	telluric	1.79	1.83	2 %
l	Fe I	solar	53.33	56.61	6 %
m	Ti I	solar	31.98	35.92	12 %

pecially for broad solar lines, where the noise suppression is most critical. Due to the narrow line width of the comb lines, the noise filter was neither applicable nor needed for the comb.

Figure 7.10 shows the fit and its residuals for a solar Fe I line. The quality of the fit can be judged from the distribution of the fit residuals normalized to the photon noise. The RMS of the residuals is 47 % above the photon noise of the data points, which is about equal to the usual level of excess noise, that was already observed and discussed in Sec. 7.2. The method therefore fulfills our expectations. All exposures with combined comb and sunlight are analyzed in this way to track the lines in the solar spectrum with respect to the overlaid comb.

A theoretical performance limitation is the photon noise of the solar lines. Even though the photon noise can always be reduced by collecting more exposures, it is useful to estimate the photon noise of the lines in a single exposure with the two calibration schemes. To this aim, we employ Monte-Carlo simulation, adding simulated photon noise to our templates for the solar spectrum to create artificial measurements. 25 000 simulated exposures were created in this manner, and subsequently fitted with the templates. The scatter of the line centers over the series reveals the photon noise of the line positions. For comparison, an analogous simulation was done for the overlay of comb and Sun. Table 7.1 lists the results. The characteristic lines all have a photon noise in the low m/s range. The O_2 lines have particularly low photon noise, because they are quite deep and narrow. The overlaid comb increases the photon noise of the solar lines by 10 to 16 %. It is striking though, that for the O_2 lines the increase can be as low as 2 %. The reason is, that the O_2 lines are narrow enough to fit between the comb lines, where they are hardly affected by the comb's photon noise. The impact of the comb is most pronounced if a comb line is located on the steepest slope of a line, which is most decisive for the localization of the line center.

7.3.2 Tracking solar lines

We demonstrate the usefulness of our calibration methods by detecting signatures of global solar oscillations in our time series of disk-integrated solar spectra. Most of the power of these oscillations is concentrated at frequencies of about 3 mHz, which is why they are often referred to as the “5-minute oscillations”. In integrated sunlight, only low-order oscillations with total velocity amplitudes of the order of 1 m/s are observed. Sensitive instruments with a stable wavelength calibration are required to detect these low-amplitude signals. Such global oscillations at a similar rate and amplitude are present in the spectra of other stars, and have to be temporally averaged for the detection of low-mass exoplanets. The measurement of the well-explored global solar oscillations, whose detection has first been published in 1979 [178], serves as a proof-of-concept for our technique. Future applications may then investigate more contemporary problems such as the influence of sunspots on radial velocity detection, which is of great interest for high-sensitivity exoplanet searches.

For detecting the solar oscillations, we track the average shift of the three strong Fe I lines, which are the most distinct features from the Sun within the spectral range of our observation. Besides the solar lines, we also track the shifts of the O_2 lines imprinted by Earth’s atmosphere. These lines are often used as a low-precision reference, but are restricted to certain spectral regions. Their line centers are affected by Doppler shifts through changing wind speeds and directions. At noon, they are expected to be stable within a few m/s. This is because when the Sun is near the zenith, the winds are approximately perpendicular to the line of sight. During the course of the afternoon, however, the stability of the lines is supposed to degrade, as the component of the wind speeds along the line of sight increases.

Time traces of the average shifts of the four O_2 lines, and of the three Fe I lines, are shown in Fig. 7.11, both with time-interlaced and overlaid calibration. The time series is longer for the O_2 lines than for the Fe I lines, since for the tracking of the O_2 lines, telescope guiding problems can be tolerated. Over the course of the series, all four O_2 lines experience about the same drift of approximately -17 m/s, similar to what found in earlier investigations [188,189]. The largest portion of the drift is assumed to be caused by winds [188, 189], with a weaker contribution arsing from the changing air-mass along the line of sight [189,190]. Time-interlaced calibration confirms the results obtained with overlaid calibration, but with $2-3$ times larger scatter. In the case of the overlaid spectra, the scatter is dominated by the measurement of the solar and telluric lines, rather than by the calibration. This limitation could be reduced by averaging a larger number of lines, e.g. with a spectrograph that records a wider spectral range.

The absolute frequencies of all four O_2 lines – determined with time-interlaced calibration – are within 100 MHz at the HITRAN values. Their accuracy is therefore sufficient to determine which set of modes of the source comb is transmitted through the FPCs of the astro-comb system. In Sec. 7.2 we have resolved the resulting ±250 MHz ambiguity, that turns into a ±500 MHz ambiguity after frequency doubling of the comb, by using a wavemeter. The comparison with the O_2 lines can either replace this piece of equipment or serve as a cross-check.

The time traces of the Fe I lines, as shown in Fig. 7.11, display a strong drift from the rotation of the Earth, which needs to be subtracted. We do this by fitting and subtracting a second-order polynomial to the time traces, leading to the curves shown in Fig. 7.12 (a) and (c). This ”quick-and-dirty” way of accounting for Earth’s rotation is sufficient for the aim of detecting solar oscillations, and partly also compensates other unwanted effects such as differential extinction of the solar disc [179] and telescope guiding errors. Besides the expected 5-minute oscillations, the time traces also display a slower component, which is probably caused by guiding errors. The graphs on the right-hand side of Fig. 7.12 represent the power spectra of the time traces to their left, computed by FFT. The 5-minute oscillations are represented by a peak at 3.3 mHz in the power spectra. The frequency and the signal strength are in good agreement with the results reported in [178]. Our series of acquisitions is not long enough in time to fully resolve the substructure of the peak at 3.3 mHz. However, the weak

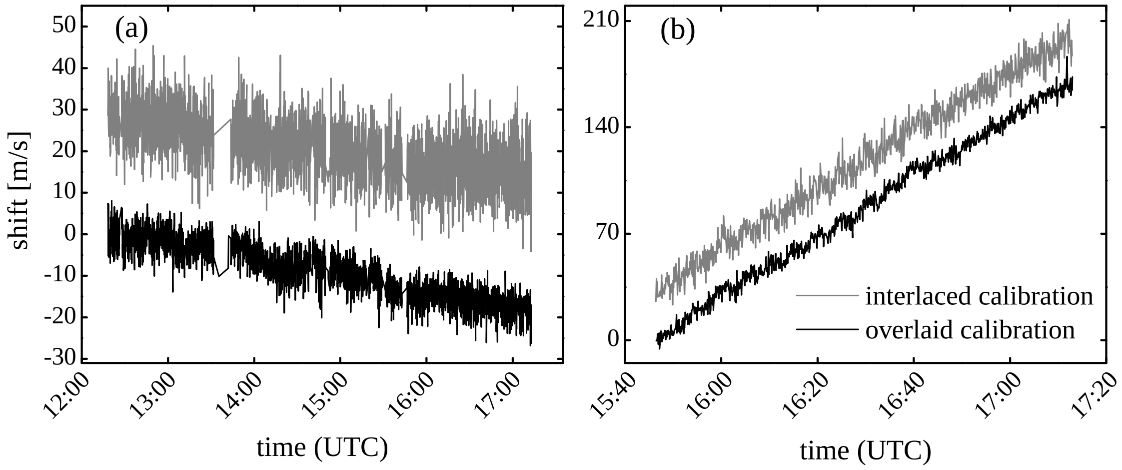

Figure 7.11 – Tracking lines in the solar spectrum using time-interlaced calibration (gray lines) and overlaid calibration (black lines). For clarity, the gray lines were given a vertical offset relative to the black lines. (a) Shift of the telluric lines with time, averaged over four O_2 lines. (b) Average shift of the three strongest Fe I lines.

side-lobes next to the central peak are likely to stem from partly resolved oscillation modes. The total oscillation power of the central peak at 3.3 mHz corresponds to an amplitude of 88 cm/s. Amplitudes of the globally averaged solar oscillations have also been characterized in [180] using the HARPS spectrograph, were the strongest component is reported to have an amplitude of 25 cm/s, confirming earlier findings. Since in our measurements, the peak at 3.3 mHz contains numerous unresolved components, our results are in unison with this. Supposed errors from telescope guiding appear below 1 mHz. It is not clearly seen in the power spectrum obtained from time-interlaced calibration, probably because it interferes with noise.

The peak detection threshold with time-interlaced and overlaid calibration can be estimated by regarding the noise floor of the power spectrum. For an oscillation signal of unresolved width and a 3 sigma confidence level, it is of 37 cm/s for overlaid calibration. The calibration tests in Sec. 7.2 yielded somewhat lower values with this scheme, but there only the standard deviation was specified, corresponding to merely 1 sigma. The guiding errors deteriorate the sensitivity of the measurement only at frequencies of below 1 mHz, where a signal would be masked by the guiding errors if its amplitude is below 63 cm/s. For time-interlaced calibration, the 3 sigma peak-detection threshold amounts to 69 cm/s. The performance is better than in Sec. 7.2 because of the higher frame rate, and because considering the time series through a frequency filter is a way of applying a temporal average.

On the time scale of the oscillations, the O_2 lines are relatively stable, and can thus also be used as a reference for their detection. Figure 7.12 (e) and (f) shows the analysis of the time trace of the Fe I lines as referenced to the O_2 lines. All findings derived from comb calibration are confirmed. Due to the lower photon noise, the 3 sigma peak detection threshold is of 28 cm/s. Our above analysis however clearly reveals that over longer time frames, the O_2 lines are unstable even on the 10 m/s scale, and are thus unsuited for sensitive detection of phenomena that occur on longer time horizons.

Disk-integrated solar oscillations have been measured for more than 3 decades by BiSON [179]. BiSON is a network of telescopes that observe solar oscillations via resonant scattering of a potassium line. This is a method very different from ours, which makes a comparison between the two all the more interesting. BiSON publicly provides data that also

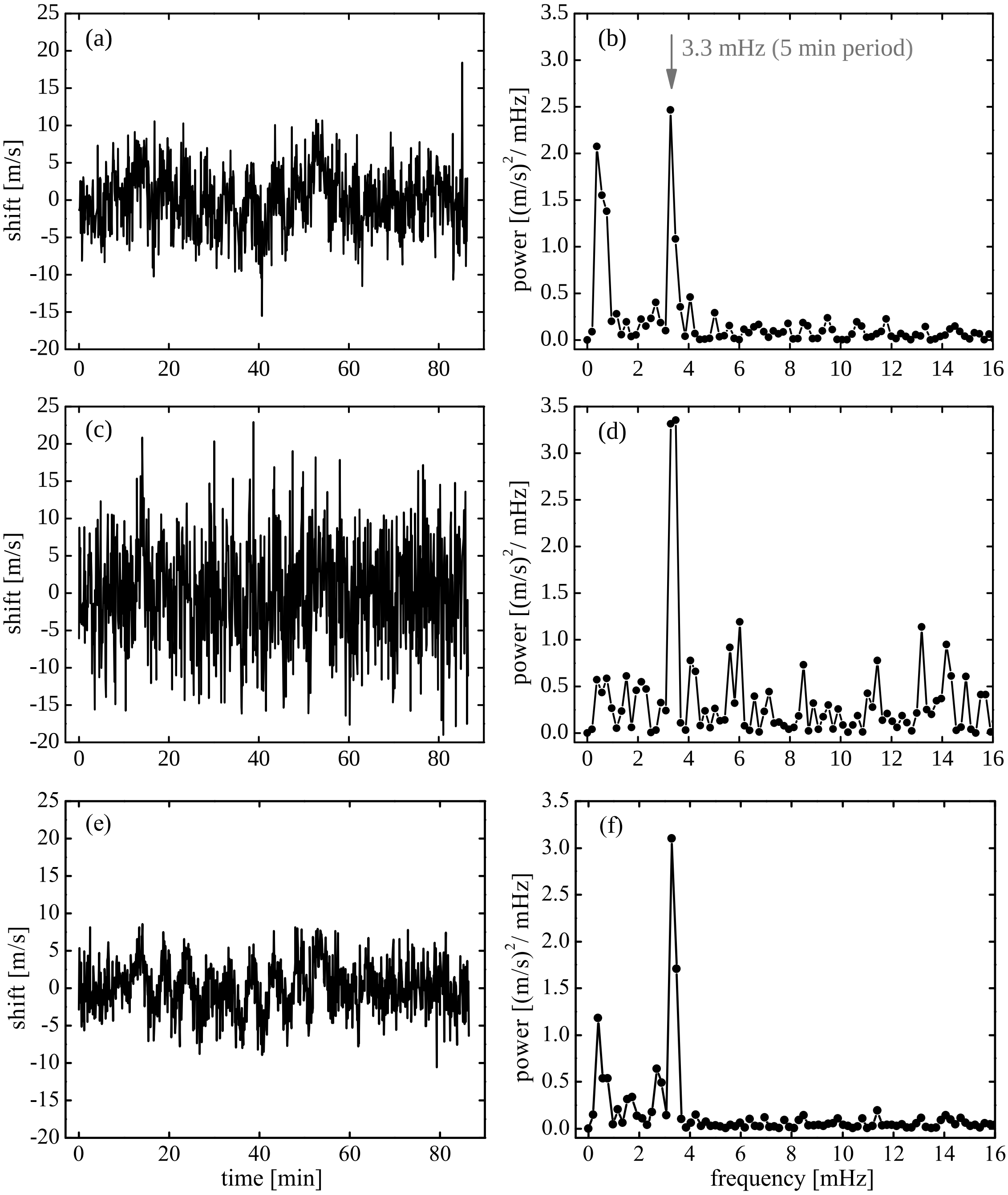

Figure 7.12 – Detection of solar oscillations using the three strongest Fe I lines of Fig. 7.9 / Tab. 7.1. Graphs on the left: Time traces with a second-order polynomial subtracted. Graphs on the right: Power spectra computed by fast Fourier transformation of the time traces. Note that these spectra scale quadratically in amplitude. Top: Overlaid calibration. Center: Time-interlaced calibration. Bottom: Calibration with telluric O_2 lines.

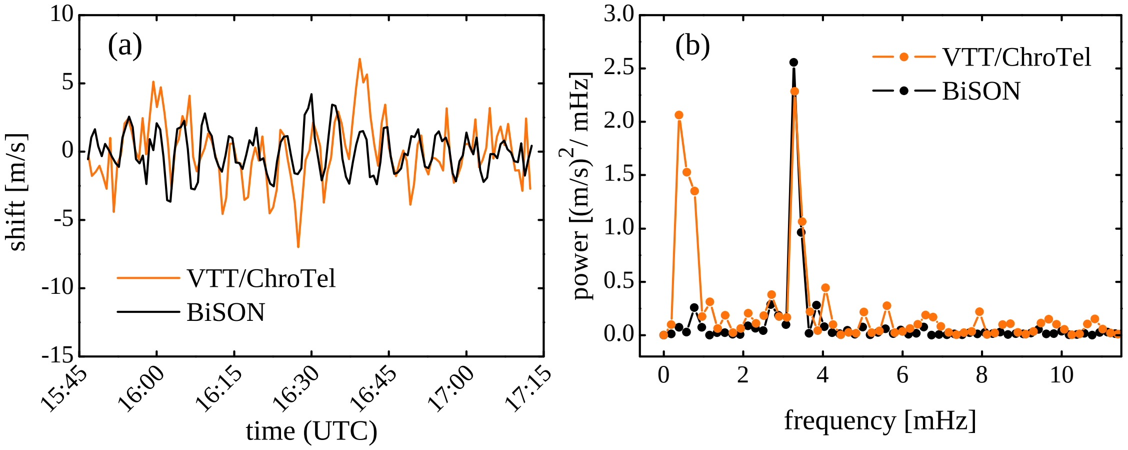

Figure 7.13 – Comparison of solar oscillation measurements from VTT/ChroTel to BiSON data of the same date and time. The VTT/ChroTel data were calibrated with the overlaid comb. Additionally, the time series was binned over 7 exposures (42 s), to match the temporal resolution of the BiSON data (40 s). (a) Time series of radial-velocity shifts. (b) Power spectra, computed by fast Fourier transformation.

cover the time period of our observation. To these data, we compare our observation using overlaid calibration with the astro-comb. We bin our data over 7 exposures (42 s), to match the temporal resolution of the BiSON data (40 s). The comparison is shown in Fig. 7.13. The measured phases of the oscillations nicely match each other. Also the overall powers of the 5-minute oscillations agree within the expected uncertainties. The most obvious differences come from the guiding errors in our data, that appear at frequencies below 1 mHz. More subtle differences might arise from the different weighting of the solar limb in our observation.

Chapter 8

Conclusion and Outlook

This work has demonstrated the generation of broadband, visible laser frequency combs for astronomical spectrograph calibration (astro-combs). The obtained spectral coverage was up to > 200 nm, centered at around 550 nm, with mode spacings of up to 18 GHz. The work has demonstrated reshaping of the astro-comb spectrum into a flat-top shape, which maximizes the overall signal-to-noise ratio of the calibration, and thus improves the calibration repeatability. The impact of nonlinear amplification of unwanted comb modes has been investigated, and restricted to allow a calibration accuracy of better than 1 cm/s.

In-field testing of the astro-comb has been carried out at the HARPS spectrograph at the La Silla Observatory (Chile), and at the VTT solar spectrograph at the Observatorio del Teide in Tenerife (Canary Islands). At HARPS, a calibration repeatability of 2.5 cm/s could be demonstrated over the course of a few hours − a factor of four better than with a state-of-the-art thorium-argon reference. At this point, the repeatability was apparently limited by unknown effects − possibly modal noise from the multimode fiber delivery to the spectrograph. At the VTT spectrograph, it was demonstrated how limitations from modal noise can be overcome by using single-mode fibers in different multiplexing schemes. This yielded a repeatability of 3 cm/s over several hours, equivalent to the results obtained on HARPS. Here, the repeatability was presumably limited by seeing within the spectrograph beam path, as it lacks temperature stabilization and evacuation as present in HARPS.

The demonstrated repeatability in the low cm/s-range enables intriguing new possibilities such as the detection of Earth-like exoplanets via radial-velocity measurements. The time span over which this repeatability could be maintained was however still insufficient for these applications, as they require years or even decades. Over time horizons longer than a few hours, systematic effects have been found to be important. This includes signal level-dependent effects that arise from the readout mechanism of the spectrograph CCD, and from the data extraction software. This has been characterized and found to be on the level of several m/s. Further investigation is required to eliminate the related systematic uncertainties and enable a few-cm/s precision over arbitrary time horizons.

Various astronomical applications of the astro-comb have also been demonstrated in this work, showing the applicability and value of astro-combs for astronomy. Radial-velocity measurements have been conducted on the exoplanet host star HD 75289 to reconstruct the orbit of its planetary companion. This was the first time that an astro-comb had been used for such an application. A comb-calibrated atlas of the solar lines in the 476−530 nm and 534−585 nm spectral range has been created from observations of moonlight, taking advantage of the highly accurate absolute calibration provided by the astro-comb. This atlas may serve as a secondary reference for calibration of ground or space-borne spectrographs within an uncertainty at the m/s-level. At the VTT solar spectrograph, the astro-comb was utilized to measure solar oscillations averaged over the full solar disk, considering the “Sun-as-a-star”. It was also used to assess the stability of absorption lines from Earth’s atmosphere as a low-precision reference. Numerous further scientific applications are planned at both the VTT spectrograph [152] and the HARPS spectrograph.

The astro-comb is now ready to be used for planet hunting, applications in solar physics, and for a more accurate search for a potential variability of fundamental constants on cosmological scales. Further investigations should be able to reduce the remaining uncertainties from the spectrograph and fiber delivery, which might ultimately lead to the first direct measurement of the acceleration of the cosmic expansion with next-generation telescopes. At the end of the present work, however, the limited lifetime of the tapered photonic crystal fibers used for spectral broadening remained an unsolved problem. This issue has been discovered and intensively studied in this work, and was found to be due to formation of color centers. Effective countermeasures have been proposed and tested, but the obtained lifetimes were still insufficient. During the completion of this work, continued efforts made by engineers and scientists at Menlo Systems have enabled them to manage this problem, by further elaborating the concept of direct spectral broadening as laid out in Sec. 3.2. The astro-comb is now ready for routine astronomy, and several installations of commercial versions of the astro-comb are currently being undertaken, including a permanent installation at HARPS in April 2015. It can be expected, that once the astro-comb is routinely accessible to the astronomical community, its scientific impact will even be greater than it already has been during the development and test phase.

The approach pursued in this work is technically the most mature concept for astro-comb generation, and the first one to make it into routine astronomical operation. Most contemporary astro-combs follow a similar basic design [31, 37]. However, there are a number of alternative concepts that might substantially reduce complexity, size, and cost of future astro-combs. For example, it might be possible to replace the Fabry-Pérot cavities for mode filtering by integrated waveguide components [191]. It would however be greatly preferable, if the required large mode spacing could be extracted directly from the oscillator that generates the frequency comb. Harmonic mode-locking has been proposed for this purpose [192], but it has turned out, that solely operating an oscillator in a multipulse regime does not necessarily widen the mode spacing of the emitted comb [193, 194]. Instead, an interferometer is required within the laser cavity to stabilize the sub-pulses relative to one another, which suppresses the unwanted cavity modes.

The simplest and most compact solution would be an oscillator that fundamentally offers a high repetition rate by its very short cavity length, which would completely eliminate the presence of side-modes. Such sources are continuously being developed, as large mode-spacing frequency combs are also of great interest for high-speed telecommunication [195] and for arbitrary waveform generation through line-by-line pulse shaping [155, 196]. Repetition rates of up to 100 GHz have been accomplished with a passively mode-locked Er:Yb:glass laser [197], and with a semiconductor laser [198], employing quantum well saturable absorbers. Multi-gigahertz waveguide lasers [199, 200] have been constructed with quantum dot saturable absorbers, and fiber lasers with repetition rates of 10 to 20 GHz have been built using graphene [90] and carbon nanotubes [89] as saturable absorbers. However, most of these lasers have pulse durations of about 1 ps. Pulse durations of significantly above 100 fs impede coherent spectral broadening [103], as required for self-referencing of the frequency comb and for broadband spectrograph calibration. The challenge thus lies in the reduction of the pulse duration. A sufficient shortening in pulse duration has recently enabled self-referencing of a mode-locked semiconductor laser, although at a relatively low repetition rate of 1.75 GHz [201].

Large-mode spacing frequency combs can also be generated by modulating a cw laser

[202–205], or from two beating cw lasers [206]. In [205], a coherently broadened 12.5 GHz frequency comb ranging from 1350 to 1750 nm has been obtained from a modulated cw laser. A stable offset frequency was achieved by stabilizing the cw laser to a molecular transition.

Another interesting possibility is the use of Kerr-combs from microresonators [207, 208]. These frequency combs are generated in a fairly compact and simple arrangement and intrinsically feature a broadband output. Their mode spacings lie between several tens of GHz and up to 1 THz. Such extremely large mode spacings are of great interest for survey spectrographs [209] and other low-resolution spectrographs.

As an alternative calibration technique, wavelength combs have been developed, that are generated by transmitting light of a continuum source such as an LED through a Fabry-Pérot or Mach-Zehnder interferometer [210–212]. The stability of the resulting line pattern can be enhanced by locking the interferometer to an atomic transition [210, 211]. These calibration sources can easily offer a large line spacing, and – although their basic idea is already much older – they emulate some properties of a laser frequency comb, such as its uniform line spacing and intensity. However, they do not represent an absolute frequency reference, and lack the ultra-high precision and low line width of a frequency comb. They are also likely to be prone to systematic uncertainties. However, for applications where simplicity and low cost are essential, and where accuracy and a very high precision are not needed, they may be a reasonable alternative.

Many of the concepts developed in this work such as spectral flattening, high repetition rate spectral broadening, and multiplexed single-mode fiber delivery, are highly relevant also for most alternative concepts for astro-comb generation. With the completion of this work, the first generation of astro-combs is now ready to move into commercial production, and to enter routine operation at observatories, paving the way to novel and exciting discoveries in astronomy.

Appendix A

Appendix

A.1 Derivations of formulas

The goal of this appendix is to derive Eqs. (4.1.5) and (4.1.7) from Eq. (4.1.4). This is done for the limiting case of large side-mode suppression. For this purpose, it is convenient to define $B \equiv 1-h$ and compute the leading order in B. The filter ratio is set to $m=2$, and the carrier frequency to $\omega_c = 0$. As explained in Sec. 4.1, the result in terms of spectral broadening and side-mode amplification is approximately independent of that choice. The initial side-mode suppression is given by $\varrho_i = (1+h)^2/(1-h)^2 \approx 4/B^2$. Using Eq. (4.1.4), the powers of the n^{th} principal mode and of the n^{th} side-mode are given by $P_n = S(2n\omega_r)$ and $S_n = S((2n+1)\omega_r)$, respectively. To describe the average side-mode suppression ϱ_{avg} after nonlinear propagation, we average the relative side-mode power S_n/P_n, weighted with the corresponding principal mode power P_n, and invert the result. This yields $\varrho_{\text{avg}} = \left(\sum_{n=-\infty}^{\infty} P_n\right) / \left(\sum_{n=-\infty}^{\infty} S_n\right)$. The average side-mode amplification A_{avg} is then given by:

$$A_{\text{avg}} = \frac{4}{B^2} \frac{\sum_{n=-\infty}^{\infty} S_n}{\sum_{n=-\infty}^{\infty} P_n} \tag{A.1.1}$$

Similarly, the RMS-bandwidth Δf_{RMS} can be expressed as:

$$2\pi\,\Delta f_{\text{RMS}} = \sqrt{\frac{\sum_{n=-\infty}^{\infty} (n\omega_r)^2\, S\,(n\omega_r)}{\sum_{n=-\infty}^{\infty} S\,(n\omega_r)} - \left(\frac{\sum_{n=-\infty}^{\infty} n\omega_r\, S\,(n\omega_r)}{\sum_{n=-\infty}^{\infty} S\,(n\omega_r)}\right)^2} \tag{A.1.2}$$

Taking advantage of the fact that the second term under the square root, which is the spectral center of mass, vanishes, and neglecting the side-modes, Eq. (A.1.2) simplifies to:

$$2\pi\Delta f_{\text{RMS}} = \sqrt{\frac{\sum_{n=-\infty}^{\infty} (2n\omega_r)^2\, P_n}{\sum_{n=-\infty}^{\infty} P_n}} \tag{A.1.3}$$

A_{avg} and Δf_{RMS} are determined by the three sums $\sum_{n=-\infty}^{\infty} S_n$, $\sum_{n=-\infty}^{\infty} P_n$ and $\sum_{n=-\infty}^{\infty} (2n\omega_r)^2\, P_n$. To calculate them in a compact way, we use the abbreviations:

$$f\,(T) = \exp\left[-\,(1+iC)\,\frac{T^2}{2T_0^2} + \frac{i}{2}A(T)\right], \qquad A\,(T) = \frac{2z}{L_{\text{NL}}} \exp\left(-\frac{T^2}{T_0^2}\right) \tag{A.1.4}$$

With the approximation $h^2 \approx 1-2B$, and $U\,(z,T)$ as defined by Eqs. (4.1.2) and (4.1.3), the power of the n^{th} principal mode becomes:

$$\begin{aligned} P_n = S(2n\omega_r) &= \int_{-\infty}^{\infty} \left[U(z,T) + (1-B)U((1-2B)z,T)\right] e^{+i4\pi nT/T_r} dT \\ &\quad \times \int_{-\infty}^{\infty} \left[U^*(z,T') + (1-B)U^*((1-2B)z,T')\right] e^{-i4\pi nT'/T_r} dT' \qquad \text{(A.1.5)} \\ &= \int_{-\infty}^{\infty} \left[f(T) + (1-B)f(T)e^{-iBA(T)}\right] e^{+i4\pi nT/T_r} dT \\ &\quad \times \int_{-\infty}^{\infty} \left[f^*(T') + (1-B)f^*(T')e^{+iBA(T')}\right] e^{-i4\pi nT'/T_r} dT'. \qquad \text{(A.1.6)} \end{aligned}$$

For the sum over all principal modes we obtain:

$$\begin{aligned} \sum_{n=-\infty}^{\infty} P_n &= \sum_{n=-\infty}^{\infty} \int_{-\infty}^{\infty}\int_{-\infty}^{\infty} f(T)f^*(T') \Big[1 + (1-B)(e^{-iBA(T)} + e^{+iBA(T')}) \\ &\qquad +(1-B)^2 e^{-iB(A(T)-A(T'))}\Big] e^{-i4\pi n(T-T')/T_r} dT dT' \qquad \text{(A.1.7)} \\ &\approx \frac{T_r}{2} \int_{-\infty}^{\infty}\int_{-\infty}^{\infty} f(T)f^*(T') \Big[1 + (1-B)(e^{-iBA(T)} + e^{+iBA(T')}) \\ &\qquad +(1-B)^2 e^{-iB(A(T)-A(T'))}\Big] \delta(T-T') dT dT' \qquad \text{(A.1.8)} \end{aligned}$$

where in the last step the sum over n has been replaced by an approximating integral leading to a δ-function. Expanding the term in square brackets yields $4-4B+(1-A(T)^2)B^2+O(B^3)$, which is independent of B in first order (undepleted principal modes). With the remaining integral over $|f(T)|^2 = \exp(-T^2/T_0^2)$ we readily obtain:

$$\sum_{n=-\infty}^{\infty} P_n = 2\sqrt{\pi}\, T_r T_0 \tag{A.1.9}$$

The sum over the side-modes is treated in the same way with the corresponding square brackets term $(1+A(T)^2)B^2+O(B^3)$. The remaining integral over $\exp(-T^2/T_0^2)B^2(1-A(T)^2)$ is again readily computed:

$$\sum_{n=-\infty}^{\infty} S_n = \frac{\sqrt{\pi}}{2}\, T_r T_0\, B^2 \left[1 + \frac{4}{\sqrt{3}}\left(\frac{z}{L_{\mathrm{NL}}}\right)^2\right] \tag{A.1.10}$$

Finally, the sum $\sum_{n=-\infty}^{\infty}(2n\omega_r)^2 P_n$ can be calculated in a similar manner using $\int_{-\infty}^{\infty} p^2 \exp(ipx)dp$ $= -2\pi\delta''(x)$, where $\delta''(x)$ denotes the second derivative of the Dirac delta function:

$$\begin{aligned} \sum_{n=-\infty}^{\infty} (2n\omega_r)^2 P_n &\approx 16\left(\frac{2\pi}{T_r}\right)^2 \int_{-\infty}^{\infty}\int_{-\infty}^{\infty} f(T)f^*(T') \sum_{n=-\infty}^{\infty} n^2 e^{-i4\pi n(T-T')/T_r} dT dT' \qquad \text{(A.1.11)} \\ &\approx -2T_r \int_{-\infty}^{\infty}\int_{-\infty}^{\infty} f(T)f^*(T')\delta''(T-T') dT dT' \qquad \text{(A.1.12)} \\ &= -2T_r \int_{-\infty}^{\infty} f(T) \left[\frac{d^2}{dT^2} f^*(T)\right] dT \qquad \text{(A.1.13)} \\ &= 2\sqrt{\pi}\frac{T_r}{T_0}\left[\frac{1}{2} + \frac{C^2}{2} + \frac{C}{\sqrt{2}}\frac{z}{L_{\mathrm{NL}}} + \frac{2}{3\sqrt{3}}\left(\frac{z}{L_{\mathrm{NL}}}\right)^2\right] \qquad \text{(A.1.14)} \end{aligned}$$

Inserting the results for $\sum_{n=-\infty}^{\infty} S_n$, $\sum_{n=-\infty}^{\infty} P_n$ and $\sum_{n=-\infty}^{\infty} (2n\omega_r)^2\, P_n$ into Eqs. (A.1.1) and (A.1.3) yields Eqs. (4.1.7) and (4.1.5).

A.2 List of abbreviations and acronyms

AC	alternating current
AOFS	acousto-optic frequency shifter
AU	astronomical unit(s)
BAO	baryon acoustic oscillations
BiSON	Birmingham Solar Oscillations Network
CCD	charge-coupled device
ChroTel	Chromospheric Telescope
COBE	Cosmic Background Explorer
CTI	charge-transfer inefficiency
cw	continuous wave
DC	direct current
ECDL	external-cavity diode laser
E-ELT	European Extremely Large Telescope
EOM	electro-optic modulator
Eq.	Equation
ESO	European Southern Observatory
FC	fiber collimator
FC/APC	ferrule connector for angled physical contact
FFT	fast Fourier transformation
Fig.	Figure
FPC	Fabry-Pérot cavity
FSR	free spectral range
FTS	Fourier-transform spectrometer
FWHM	full-width at half-maximum
GAWBS	guided acoustic-wave Brillouin scattering
GDD	group-delay dispersion
GPC	grating-prism compressor
GPS	global positioning system
GVD	group-velocity dispersion
HARPS	High Accuracy Radial velocity Planet Searcher
HIRES	High Resolution Echelle Spectrometer
HITRAN	high-resolution transmission
HOM	higher-order spatial mode
HWP	half-wave plate
IP	instrumental profile
IR	infra-red
iso	optical isolator
KIS	Kiepenheuer-Institut für Sonnenphysik
LBO	lithium triborate ($\mathrm{LiB_3O_5}$)
LC	liquid crystal
LCOS	liquid crystal on silicon
LFC	laser frequency comb
LMU	Ludwig-Maximilians-Universität
$\mathbf{M_\odot}$	mass of the Sun
MIT	Massachusetts Institute of Technology
MO	microscope objective
MPL	Max-Planck-Institut für die Physik des Lichts
MPQ	Max-Planck-Institut für Quantenoptik
NA	numerical aperture
NBOH	non-bridging oxygen hole
NIR	near-infrared
NIST	National Institute for Standards and Technology
NPE	nonlinear polarization evolution
OD	optical density
OSA	optical spectrum analyzer
PBS	polarizing beam splitter
PCF	photonic crystal fiber
PER	polarization-extinction ratio
PI	proportional-integral
PLL	phase-locked loop
PM	polarization-maintaining
PN	photon noise
PZT	lead zirconate titanate
QWP	quater-wave plate
RBW	resolution bandwidth
RF	radio frequency
RMS	root-mean-square
RV	radial velocity
S/N	signal to noise
SD	standard deviation

Sec.	Section
SHG	second-harmonic generation
SLM	spatial light modulator
SMF	single-mode fiber
SPM	self-phase modulation
SRS	stimulated Raman scattering
Tab.	Table
TEM	transverse electromagnetic
ThAr	thorium-argon
USM	Universitäts-Sternwarte München
UTC	coordinated universal time
UV	ultraviolet
UVES	Ultraviolet and Visual Echelle Spectrograph
VLT	Very Large Telescope
VTT	Vacuum Tower Telescope
WDM	wavelength-division multiplexer
WMAP	Wilkinson Microwave Anisotropy Probe

Bibliography

[1] R. Holzwarth, Th. Udem, T. W. Hänsch, J. C. Knight, W. J. Wadsworth, and P. St. J. Russell, "Optical frequency synthesizer for precision spectroscopy," Phys. Rev. Lett. **85**, 2264–2267 (2000).

[2] Th. Udem, R. Holzwarth, and T. W. Hänsch, "Optical frequency metrology," Nature **416**, 233–237 (2002).

[3] M. T. Murphy, Th. Udem, R. Holzwarth, A. Sizmann, L. Pasquini, C. Araujo-Hauck, H. Dekker, S. D'Odorico, M. Fischer, T. W. Hänsch, and A. Manescau, "High-precision wavelength calibration of astronomical spectrographs with laser frequency combs," Mon. Not. R. Astron. Soc. **380**, 839–847 (2007).

[4] H. R. Telle, "Frequency control of semiconductor lasers," in "Microwave and Optical Engineering," (Wiley, New York, 1996), pp. 137–167.

[5] C. G. Parthey, A. Matveev, J. Alnis, B. Bernhardt, A. Beyer, R. Holzwarth, A. Maistrou, R. Pohl, K. Predehl, Th. Udem, T. Wilken, N. Kolachevsky, M. Abgrall, D. Rovera, C. Salomon, P. Laurent, and T. W. Hänsch, "Improved measurement of the hydrogen 1S-2S transition frequency," Phys. Rev. Lett. **107**, 203001 (2011).

[6] B. J. Bloom, T. L. Nicholson, J. R. Williams, S. L. Campbell, M. Bishof, X. Zhang, W. Zhang, S. L. Bromley, and J. Ye, "An optical lattice clock with accuracy and stability at the 10^{-18} level," Nature **506**, 71–75 (2014).

[7] T. Rosenband *et al.*, "Frequency ratio of Al^{+} and Hg^{+} single-ion optical clocks; metrology at the 17th decimal place," Science **319**, 1808–1812 (2008).

[8] K. Predehl, G. Grosche, S. M. F. Raupach, S. Droste, O. Terra, J. Alnis, T. Legero, T. W. Hänsch, Th. Udem, R. Holzwarth, and H. Schnatz, "A 920-kilometer optical fiber link for frequency metrology at the 19th decimal place," Science **336**, 441–444 (2012).

[9] B. Bernhardt, "Dual comb spectroscopy," Ph.D. thesis, Ludwig-Maximilians-Universität München (2011).

[10] D. W. Peterson, M. A. Johnson, and A. L. Betz, "Infrared heterodyne spectroscopy of CO_2 on Mars," Nature **250**, 128–130 (1974).

[11] T. Kostiuk, F. Espenak, M. J. Mumma, and P. Romani, "Infrared studies of hydrocarbons on Jupiter," Infrared Phys. **29**, 199 – 204 (1989).

[12] J. J. Goldstein, M. J. Mumma, T. Kostiuk, D. Deming, F. Espenak, and D. Zipoy, "Absolute wind velocities in the lower thermosphere of Venus using infrared heterodyne spectroscopy," Icarus **94**, 45 – 63 (1991).

[13] G. Sonnabend, D. Wirtz, R. Schieder, and P. F. Bernath, "High-resolution infrared measurements of H_2O and SiO in sunspots," Sol. Phys. **233**, 205–213 (2006).

[14] G. Sonnabend, D. Wirtz, F. Schmülling, and R. Schieder, "Tuneable Heterodyne Infrared Spectrometer for atmospheric and astronomical studies," Appl. Opt. **41**, 2978–2984 (2002).

[15] P. Krötz, D. Stupar, J. Krieg, G. Sonnabend, M. Sornig, F. Giorgetta, E. Baumann, M. Giovannini, N. Hoyler, D. Hofstetter, and R. Schieder, "Applications for quantum cascade lasers and detectors in mid-infrared high-resolution heterodyne astronomy," Appl. Phys. B **90**, 187–190 (2008).

[16] G. Avila, P. Singh, and B. Chazelas, "Results on fibre scrambling for high accuracy radial velocity measurements," Proc. SPIE **7735**, 773588 (2010).

[17] T. R. Hunter and L. W. Ramsey, "Scrambling properties of optical fibers and the performance of a double scrambler," Publ. Astron. Soc. Pac. **104**, 1244–1251 (1992).

[18] G. W. Marcy and R. P. Butler, "Precision radial velocities with an iodine absorption cell," Publ. Astron. Soc. Pac. **104**, pp. 270–277 (1992).

[19] R. P. Butler, G. W. Marcy, E. Williams, C. Mccarthy, P. Dosanjh, and S. S. Vogt, "Attaining Doppler precision of 3 m s," Publ. Astron. Soc. Pac. **108**, pp. 500–509 (1996).

[20] M. Mayor *et al.*, "Setting new standards with HARPS," The Messenger **114**, 20–24 (2003).

[21] G. Rupprecht *et al.*, "The exoplanet hunter HARPS: performance and first results," Proc. SPIE **5492**, 148–159 (2004).

[22] B. N. Taylor and C. E. Kuyatt, "Guidelines for evaluating and expressing the uncertainty of NIST measurement results," NIST Technical Note **1297** (1994).

[23] B. A. Palmer and R. Engleman, "Atlas of the thorium spectrum," Los Alamos National Laboratory Report **9615** (1983).

[24] C. Lovis and F. Pepe, "A new list of thorium and argon spectral lines in the visible," A&A **468**, 1115–1121 (2007).

[25] T. Wilken, "Calibrating astronomical spectrographs with frequency combs," Ph.D. thesis, Ludwig-Maximilians-Universität München (2010).

[26] T. Wilken, C. Lovis, A. Manescau, T. Steinmetz, L. Pasquini, G. Lo Curto, T. W. Hänsch, R. Holzwarth, and Th. Udem, "High-precision calibration of spectrographs," Mon. Not. R. Astron. Soc. **405**, L16–L20 (2010).

[27] T. Steinmetz, T. Wilken, C. Araujo-Hauck, R. Holzwarth, T. W. Hänsch, L. Pasquini, A. Manescau, S. D'Odorico, M. T. Murphy, T. Kentischer, W. Schmidt, and Th. Udem, "Laser frequency combs for astronomical observations," Science **321**, 1335–1337 (2008).

[28] C.-H. Li, A. J. Benedick, P. Fendel, A. G. Glenday, F. X. Kärtner, D. F. Phillips, D. Sasselov, A. Szentgyorgyi, and R. L. Walsworth, "A laser frequency comb that enables radial velocity measurements with a precision of 1 cm s^{-1}," Nature **452**, 610–612 (2008).

[29] D. A. Braje, M. S. Kirchner, S. Osterman, T. Fortier, and S. A. Diddams, “Astronomical spectrograph calibration with broad-spectrum frequency combs,” Eur. Phys. J. D **48**, 57–66 (2008).

[30] F. Quinlan, G. Ycas, S. Osterman, and S. A. Diddams, “A 12.5 GHz-spaced optical frequency comb spanning >400 nm for near-infrared astronomical spectrograph calibration,” Rev. Sci. Instrum. **81**, 063105 (2010).

[31] G. G. Ycas, F. Quinlan, S. A. Diddams, S. Osterman, S. Mahadevan, S. Redman, R. Terrien, L. Ramsey, C. F. Bender, B. Botzer, and S. Sigurdsson, “Demonstration of on-sky calibration of astronomical spectra using a 25 GHz near-IR laser frequency comb,” Opt. Express **20**, 6631–6643 (2012).

[32] A. J. Benedick, G. Chang, J. R. Birge, L.-J. Chen, A. G. Glenday, C.-H. Li, D. F. Phillips, A. Szentgyorgyi, S. Korzennik, G. Furesz, R. L. Walsworth, and F. X. Kärtner, “Visible wavelength astro-comb,” Opt. Express **18**, 19175–19184 (2010).

[33] C.-H. Li, A. G. Glenday, A. J. Benedick, G. Chang, L.-J. Chen, C. Cramer, P. Fendel, G. Furesz, F. X. Kärtner, S. Korzennik, D. F. Phillips, D. Sasselov, A. Szentgyorgyi, and R. L. Walsworth, “In-situ determination of astro-comb calibrator lines to better than 10 cm s^{-1},” Opt. Express **18**, 13239–13249 (2010).

[34] C.-H. Li, G. Chang, L.-J. Chen, D. F. Phillips, F. Kärtner, and R. L. Walsworth, “Laboratory demonstration and characterization of a green astro-comb,” in “Advanced Solid-State Photonics,” (Optical Society of America, 2011), p. AME5.

[35] D. F. Phillips, A. G. Glenday, C.-H. Li, C. Cramer, G. Furesz, G. Chang, A. J. Benedick, L.-J. Chen, F. X. Kärtner, S. Korzennik, D. Sasselov, A. Szentgyorgyi, and R. L. Walsworth, “Calibration of an astrophysical spectrograph below 1 m/s using a laser frequency comb,” Opt. Express **20**, 13711–13726 (2012).

[36] C.-H. Li, A. G. Glenday, D. F. Phillips, G. Furesz, N. Langellier, M. Webber, A. Zibrov, A. J. Benedick, G. Chang, L.-J. Chen, D. Sasselov, F. Kärtner, A. Szentgyorgyi, and R. L. Walsworth, “Green astro-comb for HARPS-N,” Proc. SPIE **8446**, 84468X (2012).

[37] N. Langellier, C.-H. Li, A. G. Glenday, G. Chang, H.-W. Chen, J. Lim, G. Furesz, F. Kärtner, D. F. Phillips, D. Sasselov, A. Szentgyorgyi, and R. Walsworth, “Green astro-comb for HARPS-N,” Proc. SPIE **9147**, 91478N (2014).

[38] T. Steinmetz, T. Wilken, C. Araujo-Hauck, R. Holzwarth, T. W. Hänsch, and Th. Udem, “Fabry-Perot filter cavities for wide-spaced frequency combs with large spectral bandwidth,” Appl. Phys. B **96**, 251–256 (2009).

[39] T. Wilken, G. Lo Curto, R. A. Probst, T. Steinmetz, A. Manescau, L. Pasquini, J. I. Gonzalez Hernandez, R. Rebolo, T. W. Hänsch, Th. Udem, and R. Holzwarth, “A spectrograph for exoplanet observations calibrated at the centimetre-per-second level,” Nature **485**, 611–614 (2012).

[40] R. A. Probst, G. Lo Curto, G. Avila, B. L. Canto Martins, J. R. de Medeiros, M. Esposito, J. I. González Hernández, T. W. Hänsch, R. Holzwarth, F. Kerber, I. C. Leão, A. Manescau, L. Pasquini, R. Rebolo-López, T. Steinmetz, T. Udem, and Y. Wu, “A laser frequency comb featuring sub-cm/s precision for routine operation on HARPS,” Proc. SPIE **9147**, 91471C (2014).

[41] Y. Bhattacharjee and D. Clery, “A gallery of planet hunters,” Science **340**, 566–569 (2013).

[42] J. Schneider, “The Extrasolar Planets Encyclopaedia,” http://exoplanet.eu/catalog.php.

[43] A. W. Howard, “Observed properties of extrasolar planets,” Science **340**, 572–576 (2013).

[44] L. Wade, “And a glossary of their quarry,” Science **340**, 570–571 (2013).

[45] T. Sumi *et al.*, “ Unbound or distant planetary mass population detected by gravitational microlensing,” Nature **473**, 349–352 (2011).

[46] A. Cassan *et al.*, “One or more bound planets per Milky Way star from microlensing observations,” Nature **481**, 167–169 (2012).

[47] S. Seager, “Exoplanet habitability,” Science **340**, 577–581 (2013).

[48] N. J. Kasdin, D. Lisman, S. Shaklan, M. Thomson, D. Webb, E. Cady, G. W. Marks, and A. Lo, “Verifying occulter deployment tolerances as part of NASA’s technology development for exoplanet missions,” Proc. SPIE **8864**, 886417 (2013).

[49] P. Kalas, J. R. Graham, E. Chiang, M. P. Fitzgerald, M. Clampin, E. S. Kite, K. Stapelfeldt, C. Marois, and J. Krist, “Optical images of an exosolar planet 25 light-years from Earth,” Science **322**, 1345–1348 (2008).

[50] A.-M. Lagrange, M. Bonnefoy, G. Chauvin, D. Apai, D. Ehrenreich, A. Boccaletti, D. Gratadour, D. Rouan, D. Mouillet, S. Lacour, and M. Kasper, “A giant planet imaged in the disk of the young star β Pictoris,” Science **329**, 57–59 (2010).

[51] M. Mayor and D. Queloz, “A Jupiter-mass companion to a solar-type star,” Nature **378**, 355–359 (1995).

[52] C. Lovis, M. Mayor, F. Pepe, Y. Alibert, W. Benz, F. Bouchy, A. Correia, J. Laskar, C. Mordasini, D. Queloz, N. Santos, S. Udry, J. Bertaux, and J. Sivan, “An extrasolar planetary system with three Neptune-mass planets,” Nature **441**, 305–309 (2006).

[53] S. Udry, X. Bonfils, X. Delfosse, T. Forveille, M. Mayor, C. Perrier, F. Bouchy, C. Lovis, F. Pepe, D. Queloz, and J.-L. Bertaux, “The HARPS search for southern extra-solar planets - XI. Super-Earths (5 and 8 $M_\oplus$) in a 3-planet system,” A&A **469**, L43–L47 (2007).

[54] F. Pepe, C. Lovis, D. Segransan, W. Benz, F. Bouchy, X. Dumusque, M. Mayor, D. Queloz, N. C. Santos, and S. Udry, “The HARPS search for Earth-like planets in the habitable zone I. Very low-mass planets around HD 20794, HD 85512, and HD 192310,” A&A **534**, A58 (2011).

[55] F. Dumusque, Xavier and-Pepe, C. Lovis, D. Segransan, W. Sahlmann, Johannes and-Benz, F. Bouchy, M. Mayor, D. Queloz, N. Santos, and S. Udry, “An Earth-mass planet orbiting α Centauri B,” Nature **491**, 207–211 (2012).

[56] J. J. Lissauer *et al.*, “A closely packed system of low-mass, low-density planets transiting Kepler-11,” Nature **470**, 53–58 (2011).

[57] S. Perlmutter, “Nobel lecture: Measuring the acceleration of the cosmic expansion using supernovae,” Rev. Mod. Phys. **84**, 1127–1149 (2012).

[58] G. Börner, "Time and the universe," in "Astrophysics, Clocks, and Fundamental Constants," , vol. 648 of *Lect. Notes Phys.*, Karshenboim and Peik, eds. (2004), pp. 21–32.

[59] D. H. Weinberg, M. J. Mortonson, D. J. Eisenstein, C. Hirata, A. G. Riess, and E. Rozo, "Observational probes of cosmic acceleration," Phys. Rep. **530**, 87 – 255 (2013).

[60] J. Liske *et al.*, "Cosmic dynamics in the era of extremely large telescopes," Mon. Not. R. Astron. Soc. **386**, 1192–1218 (2008).

[61] A. Sandage, "The change of redshift and apparent luminosity of galaxies due to the deceleration of selected expanding universes," Astrophys. J. **136**, 319–333 (1962).

[62] A. Loeb, "Direct measurement of cosmological parameters from the cosmic deceleration of extragalactic objects," Astrophys. J. **499**, L111–L114 (1998).

[63] R. Tamai and J. Spyromilio, "European extremely large telescope: progress report," Proc. SPIE **9145**, 91451E (2014).

[64] F. M. Zerbi *et al.*, "HIRES: the high resolution spectrograph for the E-ELT," Proc. SPIE **9147**, 914723 (2014).

[65] J. D. Barrow, "Constants and variations: From alpha to omega," Astrophys. Space Sci. **283**, 645–660 (2003).

[66] A. I. Shlyakhter, "Direct test of the constancy of fundamental nuclear constants," Phys. Rev. C **264**, 340 (1976).

[67] T. Damour and F. Dyson, "The Oklo bound on the time variation of the fine-structure constant revisited," Nucl. Phys. B **480**, 37 – 54 (1996).

[68] Y. V. Petrov, A. I. Nazarov, M. S. Onegin, V. Y. Petrov, and E. G. Sakhnovsky, "Natural nuclear reactor at Oklo and variation of fundamental constants: Computation of neutronics of a fresh core," Phys. Rev. C **74**, 064610 (2006).

[69] Y. Fujii, A. Iwamoto, T. Fukahori, T. Ohnuki, M. Nakagawa, H. Hidaka, Y. Oura, and P. Möller, "The nuclear interaction at Oklo 2 billion years ago," Nucl. Phys. B **573**, 377 – 401 (2000).

[70] Y. Fujii, "Oklo constraint on the time-variability of the fine-structure constant," in "Astrophysics, Clocks and Fundamental Constants," , vol. 648 of *Lect. Notes Phys*, S. G. Karshenboim and E. Peik, eds. (2004), pp. 167–185.

[71] E. Menegoni, S. Galli, J. G. Bartlett, C. J. A. P. Martins, and A. Melchiorri, "New constraints on variations of the fine structure constant from CMB anisotropies," Phys. Rev. D **80**, 087302 (2009).

[72] P. P. Avelino, S. Esposito, G. Mangano, C. J. A. P. Martins, A. Melchiorri, G. Miele, O. Pisanti, G. Rocha, and P. T. P. Viana, "Early-universe constraints on a time-varying fine structure constant," Phys. Rev. D **64**, 103505 (2001).

[73] J. K. Webb, V. V. Flambaum, C. W. Churchill, M. J. Drinkwater, and J. D. Barrow, "Search for time variation of the fine structure constant," Phys. Rev. Lett. **82**, 884–887 (1999).

[74] J. K. Webb, M. T. Murphy, V. V. Flambaum, V. A. Dzuba, J. D. Barrow, C. W. Churchill, J. X. Prochaska, and A. M. Wolfe, “Further evidence for cosmological evolution of the fine structure constant,” Phys. Rev. Lett. **87**, 091301 (2001).

[75] M. T. Murphy, J. K. Webb, V. V. Flambaum, V. A. Dzuba, C. W. Churchill, J. X. Prochaska, J. D. Barrow, and A. M. Wolfe, “Possible evidence for a variable fine-structure constant from QSO absorption lines: motivations, analysis and results,” Mon. Not. R. Astron. Soc. **327**, 1208–1222 (2001).

[76] M. T. Murphy, J. K. Webb, V. V. Flambaum, C. W. Churchill, and J. X. Prochaska, “Possible evidence for a variable fine-structure constant from QSO absorption lines: systematic errors,” Mon. Not. R. Astron. Soc. **327**, 1223–1236 (2001).

[77] M. T. Murphy, J. K. Webb, and V. V. Flambaum, “Further evidence for a variable fine-structure constant from Keck/HIRES QSO absorption spectra,” Mon. Not. R. Astron. Soc. **345**, 609–638 (2003).

[78] M. T. Murphy, V. V. Flambaum, J. K. Webb, V. V. Dzuba, J. X. Prochaska, and A. M. Wolfe, “Constraining variations in the fine-structure constant, quark masses and the strong interaction,” in “Astrophysics, Clocks, and Fundamental Constants,” , vol. 648 of *Lect. Notes Phys.*, S. G. Karshenboim and E. Peik, eds. (2004), pp. 131–150.

[79] R. Srianand, H. Chand, P. Petitjean, and B. Aracil, “Limits on the time variation of the electromagnetic fine-structure constant in the low energy limit from absorption lines in the spectra of distant quasars,” Phys. Rev. Lett. **92**, 121302 (2004).

[80] H. Chand, R. Srianand, P. Petitjean, and B. Aracil, “Probing the cosmological variation of the fine-structure constant: Results based on VLT-UVES sample,” A&A **417**, 853–871 (2004).

[81] S. A. Levshakov, M. Centurión, P. Molaro, S. D’Odorico, D. Reimers, R. Quast, and M. Pollmann, “Most precise single redshift bound to $\Delta\alpha/\alpha$,” A&A **449**, 879–889 (2006).

[82] M. T. Murphy, J. K. Webb, and V. V. Flambaum, “Comment on ”Limits on the time variation of the electromagnetic fine-structure constant in the low energy limit from absorption lines in the spectra of distant quasars”,” Phys. Rev. Lett. **99**, 239001 (2007).

[83] R. Srianand, H. Chand, P. Petitjean, and B. Aracil, “Srianand et al. reply:,” Phys. Rev. Lett. **99**, 239002 (2007).

[84] J. K. Webb, J. A. King, M. T. Murphy, V. V. Flambaum, R. F. Carswell, and M. B. Bainbridge, “Indications of a spatial variation of the fine structure constant,” Phys. Rev. Lett. **107**, 191101 (2011).

[85] J. A. King, J. K. Webb, M. T. Murphy, V. V. Flambaum, R. F. Carswell, M. B. Bainbridge, M. R. Wilczynska, and F. E. Koch, “Spatial variation in the fine-structure constant – new results from VLT/UVES,” Mon. Not. R. Astron. Soc. **422**, 3370–3414 (2012).

[86] T. M. Evans, M. T. Murphy, J. B. Whitmore, T. Misawa, M. Centurion, S. D’Odorico, S. Lopez, C. J. A. P. Martins, P. Molaro, P. Petitjean, H. Rahmani, R. Srianand, and M. Wendt, “The UVES Large Program for testing fundamental physics – III. Constraints on the fine-structure constant from three telescopes,” Mon. Not. R. Astron. Soc **445**, 128–150 (2014).

[87] T. Wilken, M. Lezius, T. W. Hänsch, A. Kohfeldt, A. Wicht, V. Schkolnik, M. Krutzik, H. Duncker, O. Hellmig, P. Windpassinger, K. Sengstock, A. Peters, and R. Holzwarth, "A frequency comb and precision spectroscopy experiment in space," in "CLEO: 2013," (Optical Society of America, 2013), p. AF2H.5.

[88] H. M. Pask, R. J. Carman, D. C. Hanna, A. C. Tropper, C. J. Mackechnie, P. R. Barber, and J. M. Dawes, "Ytterbium-doped silica fiber lasers: versatile sources for the $1-1.2$ μm region," IEEE J. Sel. Top. Quant. Electron. **1**, 2–13 (1995).

[89] A. Martinez and S. Yamashita, "Multi-gigahertz repetition rate passively modelocked fiber lasers using carbon nanotubes," Opt. Express **19**, 6155–6163 (2011).

[90] A. Martinez and S. Yamashita, "10 GHz fundamental mode fiber laser using a graphene saturable absorber," Appl. Phys. Lett. **101**, 041118 (2012).

[91] A. Bartels, D. Heinecke, and S. A. Diddams, "10-GHz self-referenced optical frequency comb," Science **326**, 681 (2009).

[92] G. Chang, C.-H. Li, D. F. Phillips, R. L. Walsworth, and F. X. Kärtner, "Toward a broadband astro-comb: effects of nonlinear spectral broadening in optical fibers," Opt. Express **18**, 12736–12747 (2010).

[93] G. Chang, C.-H. Li, D. F. Phillips, A. Szentgyorgyi, R. L. Walsworth, and F. X. Kärtner, "Optimization of filtering schemes for broadband astro-combs," Opt. Express **20**, 24987–25013 (2012).

[94] R. A. Probst, T. Steinmetz, T. Wilken, H. Hundertmark, S. P. Stark, G. K. L. Wong, P. St. J. Russell, T. W. Hänsch, R. Holzwarth, and Th. Udem, "Nonlinear amplification of side-modes in frequency combs," Opt. Express **21**, 11670–11687 (2013).

[95] C.-H. Li, A. G. Glenday, N. Langellier, A. Zibrov, G. Chang, L.-J. Chen, G. Furesz, F. X. Kärtner, D. F. Phillips, D. Sasselov, A. Szentgyorgyi, and R. L. Walsworth, "A broadband green astro-comb for sub-10 cm/s calibration on astrophysical spectrographs," in "CLEO: 2013," (Optical Society of America, 2013), p. CTu1I.2.

[96] L.-J. Chen, G. Chang, C.-H. Li, A. J. Benedick, D. F. Philips, R. L. Walsworth, and F. X. Kärtner, "Broadband dispersion-free optical cavities based on zero group delay dispersion mirror sets," Opt. Express **18**, 23204–23211 (2010).

[97] I. N. Duling, C.-J. Chen, P. K. A. Wai, and C. R. Menyuk, "Operation of a nonlinear loop mirror in a laser cavity," IEEE J. Quantum Elect. **30**, 194–199 (1994).

[98] A. E. Siegman, *Lasers* (University Science Books, Sausalito, 1986).

[99] P. E. Ciddor, "Refractive index of air: new equations for the visible and near infrared," Appl. Opt. **35**, 1566–1573 (1996).

[100] P. E. Ciddor and R. J. Hill, "Refractive index of air. 2. group index," Appl. Opt. **38**, 1663–1667 (1999).

[101] C. Jauregui, J. Limpert, and A. Tunnermann, "High-power fibre lasers," Nat. Photon. **7**, 861–867 (2013).

[102] Y. Panbiharwala, B. Srinivasan, D. Venkitesh, and C. S. Kumar, "Investigation of self pulsing in ytterbium-doped high power fiber amplifiers," in "International Conference on Fibre Optics and Photonics," (Optical Society of America, 2012), p. TPo.15.

[103] J. M. Dudley, G. Genty, and S. Coen, “Supercontinuum generation in photonic crystal fiber,” Rev. Mod. Phys. **78**, 1135–1184 (2006).

[104] P. Russell, “Photonic crystal fibers,” Science **299**, 358–362 (2003).

[105] P. St. J. Russell, “Photonic-crystal fibers,” J. Lightwave Technol. **24**, 4729–4749 (2006).

[106] A. Bozolan, C. J. de Matos, C. M. B. Cordeiro, E. M. dos Santos, and J. Travers, “Supercontinuum generation in a water-core photonic crystal fiber,” Opt. Express **16**, 9671–9676 (2008).

[107] G. Genty, S. Coen, and J. M. Dudley, “Fiber supercontinuum sources (invited),” J. Opt. Soc. Am. B **24**, 1771–1785 (2007).

[108] H. C. Nguyen, B. T. Kuhlmey, E. C. Mägi, M. J. Steel, P. Domachuk, C. L. Smith, and B. J. Eggleton, “Tapered photonic crystal fibres: properties, characterisation and applications,” Appl. Phys. B **81**, 377–387 (2005).

[109] S. P. Stark, A. Podlipensky, N. Y. Joly, and P. St. J. Russell, “Ultraviolet-enhanced supercontinuum generation in tapered photonic crystal fiber,” J. Opt. Soc. Am. B **27**, 592–598 (2010).

[110] G. P. Agrawal, *Nonlinear Fiber Optics* (Academic Press, San Diego, 1989).

[111] S. P. Stark, “Novel aspects of pulse propagation in photonic-crystal fibers,” Ph.D. thesis, Friedrich-Alexander-Universität Erlangen-Nürnberg (2011).

[112] T. A. Birks and Y. W. Li, “The shape of fiber tapers,” J. Lightwave Technol. **10**, 432–438 (1992).

[113] S. Pricking and H. Giessen, “Tapering fibers with complex shape,” Opt. Express **18**, 3426–3437 (2010).

[114] L. Ding, C. Belacel, S. Ducci, G. Leo, and I. Favero, “Ultralow loss single-mode silica tapers manufactured by a microheater,” Appl. Opt. **49**, 2441–2445 (2010).

[115] T. X. Tran and F. Biancalana, “Dynamics and control of the early stage of supercontinuum generation in submicron-core optical fibers,” Phys. Rev. A **79**, 065802 (2009).

[116] S. Bardal, A. Kamal, and P. St. J. Russell, “Photoinduced birefringence in optical fibers: a comparative study of low-birefringence and high-birefringence fibers,” Opt. Lett. **17**, 411–413 (1992).

[117] P. St. J. Russell and D. P. Hand, “Rocking filter formation in photosensitive high birefringence optical fibres,” Electron. Lett. **26**, 1846–1848 (1990).

[118] H. Hosono, Y. Ikuta, T. Kinoshita, K. Kajihara, and M. Hirano, “Physical disorder and optical properties in the vacuum ultraviolet region of amorphous SiO_2,” Phys. Rev. Lett. **87**, 175501 (2001).

[119] A. Zoubir, M. Richardson, L. Canioni, A. Brocas, and L. Sarger, “Optical properties of infrared femtosecond laser-modified fused silica and application to waveguide fabrication,” J. Opt. Soc. Am. B **22**, 2138–2143 (2005).

[120] W. P. Leung, M. Kulkarni, D. Krajnovich, and A. C. Tam, "Effect of intense and prolonged 248 nm pulsed-laser irradiation on the properties of ultraviolet-grade fused silica," Appl. Phys. Lett. **58**, 551–553 (1991).

[121] M. Rothschild, D. J. Ehrlich, and D. C. Shaver, "Effects of excimer laser irradiation on the transmission, index of refraction, and density of ultraviolet grade fused silica," Appl. Phys. Lett. **55**, 1276–1278 (1989).

[122] N. Leclerc, S. Thomas, H. Fabian, C. Pfleiderer, H. Hitzler, R. Takke, W. Englisch, J. Wolfrum, and K.-O. Greulich, "Transient 210-nm absorption in fused silica induced by high-power UV laser irradiation," Opt. Lett. **16**, 940–942 (1991).

[123] K. Kajihara, "Improvement of vacuum-ultraviolet transparency of silica glass by modification of point defects (review)," J. Ceram. Soc. Jpn. **115**, 85–91 (2007).

[124] H. Hosono, M. Mizuguchi, L. Skuja, and T. Ogawa, "Fluorine-doped SiO_2 glasses for F_2 excimer laser optics: fluorine content and color-center formation," Opt. Lett. **24**, 1549–1551 (1999).

[125] Y. Ikuta, K. Kajihara, M. Hirano, and H. Hosono, "Correlation between oxygen-deficient center formation and volume compaction in synthetic SiO_2 glass upon ArF or F_2 excimer-laser irradiation," Appl. Opt. **43**, 2332–2336 (2004).

[126] S. M. Eaton, G. Cerullo, and R. Osellame, "Fundamentals of femtosecond laser modification of bulk dielectrics," in "Femtosecond Laser Micromachining," , vol. 123 of *Topics in Applied Physics* (2012), pp. 131–150.

[127] P. Dekker, M. Ams, G. D. Marshall, D. J. Little, and M. J. Withford, "Annealing dynamics of waveguide Bragg gratings: evidence of femtosecond laser induced colour centres," Opt. Express **18**, 3274–3283 (2010).

[128] W. W. Morey, G. Meltz, and W. H. Glenn, "Holographically generated gratings in optical fibers," Opt. Photon. News **1**, 14–16 (1990).

[129] R. M. Atkins, V. Mizrahi, and T. Erdogan, "248 nm induced vacuum UV spectral changes in optical fibre preform cores: support for a colour centre model of photosensitivity," Electron. Lett. **29**, 385–387 (1993).

[130] A. Kamal and P. St. J. Russell, "Physical origins and general dielectric tensor of photoinduced anisotropy in optical fibers and bulk glasses," J. Opt. Soc. Am. B **11**, 1576–1584 (1994).

[131] J. M. Stone, W. J. Wadsworth, and J. C. Knight, "1064 nm laser-induced defects in pure SiO_2 fibers," Opt. Lett. **38**, 2717–2719 (2013).

[132] M. Mizuguchi, L. Skuja, H. Hosono, and T. Ogawa, "F-doped and H_2-impregnated synthetic SiO_2 glasses for 157 nm optics," J. Vac. Sci. Technol. B **17**, 3280–3284 (1999).

[133] H. Hosono, M. Mizuguchi, H. Kawazoe, and O. Tohru, "Effects of fluorine dimer excimer laser radiation on the optical transmission and defect formation of various types of synthetic SiO_2 glasses," Appl. Phys. Lett. **74**, 2755–2757 (1999).

[134] V. E. Khazanov, Y. I. Kolesov, and N. N. Trofimov, "Glass fibres," in "Fibre Science and Technology," , vol. 5 of *Soviet Advanced Composites Technology Series*, V. I. Kostikov, ed. (Springer Netherlands, 1995), pp. 15–230.

[135] T. A. Michalske and S. W. Freiman, “A molecular mechanism for stress corrosion in vitreous silica,” J. Am. Ceram. Soc. **66**, 284–288 (1983).

[136] D. Wortmann, M. Ramme, and J. Gottmann, “Refractive index modification using fs-laser double pulses,” Opt. Express **15**, 10149–10153 (2007).

[137] Y. Colombe, D. H. Slichter, A. C. Wilson, D. Leibfried, and D. J. Wineland, “Single-mode optical fiber for high-power, low-loss UV transmission,” Opt. Express **22**, 19783–19793 (2014).

[138] M. Oto, S. Kikugawa, N. Sarukura, M. Hirano, and H. Hosono, “Optical fiber for deep ultraviolet light,” IEEE Photonics Technol. Lett. **13**, 978–980 (2001).

[139] M. Oto, S. Kikugawa, T. Miura, M. Hirano, and H. Hosono, “Fluorine doped silica glass fiber for deep ultraviolet light,” J. Non-Cryst. Solids **349**, 133–138 (2004).

[140] W. Wadsworth, A. Witkowska, S. Leon-Saval, and T. Birks, “Hole inflation and tapering of stock photonic crystal fibres,” Opt. Express **13**, 6541–6549 (2005).

[141] H. Hundertmark, S. Rammler, T. Wilken, R. Holzwarth, T. W. Hänsch, and P. St. J. Russell, “Octave-spanning supercontinuum generated in SF6-glass PCF by a 1060 nm mode-locked fibre laser delivering 20 pJ per pulse,” Opt. Express **17**, 1919–1924 (2009).

[142] G. Chang, L.-J. Chen, and F. X. Kärtner, “Highly efficient Cherenkov radiation in photonic crystal fibers for broadband visible wavelength generation,” Opt. Lett. **35**, 2361–2363 (2010).

[143] G. Chang, L.-J. Chen, and F. X. Kärtner, “Fiber-optic Cherenkov radiation in the few-cycle regime,” Opt. Express **19**, 6635–6647 (2011).

[144] V. Tombelaine, C. Buy-Lesvigne, P. Leproux, V. Couderc, and G. Mélin, “Optical poling in germanium-doped microstructured optical fiber for visible supercontinuum generation,” Opt. Lett. **33**, 2011–2013 (2008).

[145] R. H. Stolen and H. W. K. Tom, “Self-organized phase-matched harmonic generation in optical fibers,” Opt. Lett. **12**, 585–587 (1987).

[146] T. Wilken, R. Probst, T. W. Hänsch, Th. Udem, T. Steinmetz, R. Holzwarth, A. Manescau, G. L. Curto, L. Pasquini, S. Stark, H. Hundertmark, and P. St. J. Russell, “Suppressed mode recovery in nonlinear fibers of a Fabry-Perot-filtered frequency comb,” in “CLEO:2011 - Laser Applications to Photonic Applications,” (Optical Society of America, 2011), p. CWQ2.

[147] S. P. Stark, T. Steinmetz, R. A. Probst, H. Hundertmark, T. Wilken, T. W. Hänsch, Th. Udem, P. St. J. Russell, and R. Holzwarth, “14 GHz visible supercontinuum generation: calibration sources for astronomical spectrographs,” Opt. Express **19**, 15690–15695 (2011).

[148] W. H. Press, S. A. Teukolsky, W. T. Vetterling, and B. P. Flannery, *Numerical Recipes in C++* (Cambridge University Press, Cambridge, 2002).

[149] M. S. Kang, A. Nazarkin, A. Brenn, and P. S. J. Russell, “Tightly trapped acoustic phonons in photonic crystal fibres as highly nonlinear artificial Raman oscillators,” Nat. Phys. **5**, 276–280 (2009).

[150] L. Ricci, M. Weidemüller, T. Esslinger, A. Hemmerich, C. Zimmermann, V. Vuletic, W. König, and T. W. Hänsch, “A compact grating-stabilized diode-laser system for atomic physics,” Opt. Commun. **117**, 541–549 (1995).

[151] Z. F. Fan, P. J. S. Heim, and M. Dagenais, “Highly coherent RF signal generation by heterodyne optical phase locking of external cavity semiconductor lasers,” IEEE Photonics Technol. Lett. **10**, 719–721 (1998).

[152] H.-P. Doerr, T. Steinmetz, R. Holzwarth, T. Kentischer, and W. Schmidt, “A laser frequency comb system for absolute calibration of the VTT echelle spectrograph,” Sol. Phys. **280**, 663–670 (2012).

[153] H.-P. Doerr, T. J. Kentischer, T. Steinmetz, R. A. Probst, M. Franz, R. Holzwarth, Th. Udem, T. W. Hänsch, and W. Schmidt , “Performance of a laser frequency comb calibration system with a high-resolution solar echelle spectrograph,” Proc. SPIE **8450**, 84501G (2012).

[154] I. C. Chang, “Acousto-optic tunable filters,” Opt. Eng. **20**, 824–829 (1981).

[155] A. M. Weiner, “Ultrafast optical pulse shaping: A tutorial review,” Opt. Commun. **284**, 3669 – 3692 (2011).

[156] A. M. Weiner, “Femtosecond pulse shaping using spatial light modulators,” Rev. Sci. Instrum. **5**, 1929–1960 (2000).

[157] T. Brixner and G. Gerber, “Quantum control of gas-phase and liquid-phase femtochemistry,” Chem. Phys. Chem. **5**, 418–438 (2003).

[158] S.-H. Shim and M. T. Zanni, “How to turn your pump-probe instrument into a multidimensional spectrometer: 2D IR and Vis spectroscopies via pulse shaping,” Phys. Chem. Chem. Phys. **11**, 748–761 (2009).

[159] X. Yang, D. J. Richardson, and P. Petropoulos, “Broadband, flat frequency comb generated using pulse shaping-assisted nonlinear spectral broadening,” IEEE Photon. Technol. Lett. **25**, 543–545 (2013).

[160] J. Vaughan, T. Feurer, K. Stone, and K. Nelson, “Analysis of replica pulses in femtosecond pulse shaping with pixelated devices,” Opt. Express **14**, 1314–1328 (2006).

[161] E. Frumker and Y. Silberberg, “Phase and amplitude pulse shaping with two-dimensional phase-only spatial light modulators,” J. Opt. Soc. Am. B **24**, 2940–2947 (2007).

[162] La Silla Observatory, *HARPS User Manual* (European Southern Observatory, Chile, 2008).

[163] M. Imai and T. Asakura, “Evaluation of the mode scrambler characteristics in terms of the speckle contrast,” Opt. Commun. **30**, 299–303 (1979).

[164] S. Mahadevan, S. Halverson, L. Ramsey, and N. Venditti, “Suppression of fiber modal noise induced radial velocity errors for bright emission-line calibration sources,” The Astrophysical Journal **786**, 18 (2014).

[165] K. Horne, “An optimal extraction algorithm for CCD spectroscopy,” Publ. Astron. Soc. Pac. **98**, 609–617 (1986).

[166] Molaro, P. and Monai, S., "Solar atlas revised," A&A **544**, A125 (2012).

[167] P. Molaro, M. Esposito, S. Monai, G. Lo Curto, J. I. Gonzalez Hernandez, T. W. Hänsch, R. Holzwarth, A. Manescau, L. Pasquini, R. A. Probst, R. Rebolo, T. Steinmetz, Th. Udem, and T. Wilken, "A frequency comb calibrated solar atlas," A&A **560**, A61 (2013).

[168] S. Udry, M. Mayor, D. Naef, F. Pepe, D. Queloz, N. C. Santos, M. Burnet, B. Confino, and C. Melo, "The CORALIE survey for southern extra-solar planets. II. The short-period planetary companions to HD 75289 and HD 130322," A&A **356**, 590–598 (2000).

[169] M. Mugrauer, R. Neuhäuser, T. Mazeh, J. Alves, and E. Guenther, "A low-mass stellar companion of the planet host star HD 75289," A&A **425**, 249–253 (2004).

[170] F. Bouchy, J. Isambert, C. Lovis, I. Boisse, P. Figueira, G. Hébrard, F. Pepe, F. Bouchy, J. Isambert, C. Lovis, I. Boisse, P. Figueira, G. Hébrard, and F. Pepe, "Charge transfer inefficiency effect for high-precision radial velocity measurements," EAS Publications Series **37**, 247–253 (2009).

[171] P. Goudfrooij, R. C. Bohlin, J. Maíz-Apellániz, and R. A. Kimble, "Empirical corrections for charge transfer inefficiency and associated centroid shifts for STIS CCD observations," Publ. Astron. Soc. Pac. **118**, 1455–1473 (2006).

[172] C. Cavadore, "HARPS detector final design," http://www.eso.org/sci/php/optdet/instruments/harps/FDR-Harps-detectors.pdf.

[173] F. Zhao, G. Lo Curto, L. Pasquini, and G. Zhao, "Study of the harps line profile using a laser frequency comb," Proceedings of the International Astronomical Union **8**, 407–409 (2012).

[174] N. Jovanovic, O. Guyon, F. Martinache, C. Schwab, and N. Cvetojevic, "How to inject light efficiently into single-mode fibers," Proc. SPIE **9147**, 91477P (2014).

[175] C. H. Betters, S. G. Leon-Saval, J. G. Robertson, and J. Bland-Hawthorn, "Beating the classical limit: A diffraction-limited spectrograph for an arbitrary input beam," Opt. Express **21**, 26103–26112 (2013).

[176] I. Spaleniak, N. Jovanovic, S. Gross, M. J. Ireland, J. S. Lawrence, and M. J. Withford, "Integrated photonic building blocks for next-generation astronomical instrumentation II: the multimode to single mode transition," Opt. Express **21**, 27197–27208 (2013).

[177] A. G. Kosovichev, "Solar oscillations," AIP Conf. Proc. **1170**, 547–559 (2009).

[178] A. Claverie, G. R. Isaak, C. P. McLeod, H. B. van der Raay, and T. Roca Cortes , "Solar structure from global studies of the 5-minute oscillation," Nature **282**, 591–594 (1979).

[179] G. R. Davies, W. J. Chaplin, Y. Elsworth, and S. J. Hale, "BiSON data preparation: a correction for differential extinction and the weighted averaging of contemporaneous data," Mon. Not. R. Astron. Soc. **441**, 3009–3017 (2014).

[180] H. Kjeldsen, T. R. Bedding, T. Arentoft, R. P. Butler, T. H. Dall, C. Karoff, L. L. Kiss, C. G. Tinney, and W. J. Chaplin, "The amplitude of solar oscillations using stellar techniques," Astrophys. J. **682**, 1370–1375 (2008).

[181] E. H. Schröter, D. Soltau, and E. Wiehr, "The German solar telescopes at the Observatorio del Teide," Vistas Astron. **28**, 519–527 (1985).

[182] C. Bethge, H. Peter, T. J. Kentischer, C. Halbgewachs, D. F. Elmore, and C. Beck, “The Chromospheric Telescope,” A&A **534**, A105 (2011).

[183] T. J. Kentischer, C. Bethge, D. F. Elmore, R. Friedlein, C. Halbgewachs, M. Knölker, H. Peter, W. Schmidt, M. Sigwarth, and K. Streander, “ChroTel: a robotic telescope to observe the chromosphere of the Sun,” Proc. SPIE **7014**, 701413 (2008).

[184] “The HITRAN Database,” http://www.cfa.harvard.edu/hitran/.

[185] “SpectroWeb, the interactive database of spectral standard star atlases,” http://spectra.freeshell.org/spectroweb.html.

[186] “BASS2000 Solar Survey Archive,” http://bass2000.obspm.fr/home.php.

[187] R. L. Kurucz, “Kurucz Solar Atlas,” http://kurucz.harvard.edu/sun.html.

[188] H. Balthasar, U. Thiele, and H. Wöhl, “Terrestrial O_2 lines used as wavelength references - comparison of measurements and model computations,” A&A **114**, 357–359 (1982).

[189] P. Figueira, F. Pepe, C. Lovis, and M. Mayor, “Evaluating the stability of atmospheric lines with HARPS,” A&A **515**, A106 (2010).

[190] B. Caccin, F. Cavallini, G. Ceppatelli, A. Righini, and A. M. Sambuco, “Terrestrial O_2 lines used as wavelength references: experimental profiles and asymmetries vs. model computations,” A&A **149**, 357–364 (1985).

[191] G. Chang, C.-H. Li, D. Phillips, R. Walsworth, and F. X. Kärtner, “Broadband, large-spacing frequency-comb employing complementary interleavers for mode filtering,” in “CLEO:2011 - Laser Applications to Photonic Applications,” (2011), p. CWQ4.

[192] J. J. McFerran, “Échelle spectrograph calibration with a frequency comb based on a harmonically mode-locked fiber laser: a proposal,” Appl. Opt. **48**, 2752–2759 (2009).

[193] S. Herr, “High repetition rate frequency comb lasers,” diploma thesis, Ludwig-Maximilians-Universität München (2010).

[194] F. Quinlan, S. Ozharar, S. Gee, and P. J. Delfyett, “Harmonically mode-locked semiconductor-based lasers as high repetition rate ultralow noise pulse train and optical frequency comb sources,” J. Opt. A: Pure Appl. Opt. **11**, 103001 (2009).

[195] D. Hillerkuss *et al.*, “26 Tbit s^{-1} line-rate super-channel transmission utilizing all-optical fast Fourier transform processing,” Nat. Photonics **5**, 364–371 (2011).

[196] C.-B. Huang, Z. Jiang, D. Leaird, J. Caraquitena, and A. Weiner, “Spectral line-by-line shaping for optical and microwave arbitrary waveform generations,” Laser Photonics Rev. **2**, 227–248 (2008).

[197] A. E. Oehler, T. Südmeyer, K. J. Weingarten, and U. Keller, “100 GHz passively mode-locked Er:Yb:glass laser at 1.5 μm with 1.6-ps pulses,” Opt. Express **16**, 21930–21935 (2008).

[198] M. Mangold, C. A. Zaugg, S. M. Link, M. Golling, B. W. Tilma, and U. Keller, “Pulse repetition rate scaling from 5 to 100 GHz with a high-power semiconductor disk laser,” Opt. Express **22**, 6099–6107 (2014).

[199] A. Choudhary, A. A. Lagatsky, P. Kannan, W. Sibbett, C. T. A. Brown, and D. P. Shepherd, "Diode-pumped femtosecond solid-state waveguide laser with a 4.9 GHz pulse repetition rate," Opt. Lett. **37**, 4416–4418 (2012).

[200] A. Choudhary, A. A. Lagatsky, Z. Y. Zhang, K. J. Zhou, Q. Wang, R. A. Hogg, K. Pradeesh, E. U. Rafailov, W. Sibbett, C. T. A. Brown, and D. P. Shepherd, "A diode-pumped 1.5 μm waveguide laser mode-locked at 6.8 GHz by a quantum dot SESAM," Laser Phys. Lett. **10**, 105803 (2013).

[201] C. A. Zaugg, A. Klenner, M. Mangold, A. S. Mayer, S. M. Link, F. Emaury, M. Golling, E. Gini, C. J. Saraceno, B. W. Tilma, and U. Keller, "Gigahertz self-referenceable frequency comb from a semiconductor disk laser," Opt. Express **22**, 16445–16455 (2014).

[202] S. Xiao, L. Hollberg, and S. A. Diddams, "Generation of a 20 GHz train of subpicosecond pulses with a stabilized optical-frequency-comb generator," Opt. Lett. **34**, 85–87 (2009).

[203] A. Ishizawa, T. Nishikawa, A. Mizutori, H. Takara, S. Aozasa, A. Mori, H. Nakano, A. Takada, and M. Koga, "Octave-spanning frequency comb generated by 250 fs pulse train emitted from 25 GHz externally phase-modulated laser diode for carrier-envelope-offset-locking," Electron. Lett. **46**, 1343–1344 (2010).

[204] A. Ishizawa, T. Nishikawa, A. Mizutori, H. Takara, A. Takada, T. Sogawa, and M. Koga, "Phase-noise characteristics of a 25-GHz-spaced optical frequency comb based on a phase- and intensity-modulated laser," Opt. Express **21**, 29186–29194 (2013).

[205] K. Kashiwagi, S. Suzuki, Y. Tanaka, T. Kotani, J. Nishikawa, H. Suto, M. Tamura, and T. Kurokawa, "400-nm-spanning astro-comb directly generated from synthesized pump pulse with repetition rate of 12.5 GHz," in "CLEO: 2013," (2013), p. CTu1I.1.

[206] J. M. Chavez Boggio, T. Fremberg, D. Bodenmüller, M. Wysmolek, H. Sanyic, H. Fernando, J. Neumann, D. Kracht, R. Haynes, and M. M. Roth, "Astronomical optical frequency comb generation in nonlinear fibres and ring resonators: optimization studies," Proc. SPIE **8450**, 84501H (2012).

[207] T. J. Kippenberg, R. Holzwarth, and S. A. Diddams, "Microresonator-based optical frequency combs," Science **332**, 555–559 (2011).

[208] P. Del'Haye, A. Schliesser, O. Arcizet, T. Wilken, R. Holzwarth, and T. J. Kippenberg, "Optical frequency comb generation from a monolithic microresonator," Nature **450**, 1214–1217 (2007).

[209] Y. Hu and X. Wang, "Design of optical frequency comb for sky survey astronomical spectrograph calibration," Proc. SPIE **9042**, 90421F (2013).

[210] C. Schwab, J. Stürmer, Y. V. Gurevich, T. Führer, S. K. Lamoreaux, T. Walther, and A. Quirrenbach, "Stabilizing a Fabry-Perot etalon to 3 cm/s for spectrograph calibration," arXiv: **1404.0004**, [astro–ph.IM] (2010).

[211] T. Feger, M. J. Ireland, J. Bento, and C. Bacigalupo, "A stable and inexpensive wavelength reference for precise wavelength calibration of radial velocity spectrographs," Proc. SPIE **9147**, 914780 (2014).

[212] F. Wildi, F. Pepe, B. Chazelas, G. Lo Curto, and C. Lovis, "A Fabry-Perot calibrator of the HARPS radial velocity spectrograph: performance report," Proc. SPIE **7735**, 77354X (2010).

List of publications

Research articles in peer-reviewed journals

Comb-calibrated solar spectroscopy through a multiplexed single-mode fiber channel
R. A. Probst, L. Wang, H.-P. Doerr, T. Steinmetz, T. J. Kentischer, G. Zhao, T. W. Hänsch, Th. Udem, R. Holzwarth and W. Schmidt, New Journal of Physics 17, 023048 (2015).

A frequency comb calibrated solar atlas
P. Molaro, M. Esposito, S. Monai, G. Lo Curto, J. I. González Hernández, T. W. Hänsch, R. Holzwarth, A. Manescau, L. Pasquini, R. A. Probst, R. Rebolo, T. Steinmetz, Th. Udem, and T. Wilken, Astronomy & Astrophysics 560, A61 (2013).

Nonlinear amplification of side-modes in frequency combs
R. A. Probst, T. Steinmetz, T. Wilken, H. Hundertmark, S. P. Stark, G. K. L. Wong, P. St. J. Russell, T. W. Hänsch, R. Holzwarth, and Th. Udem, Optics Express 21, 11670–11687 (2013).

A spectrograph for exoplanet observations calibrated at the centimetre-per-second level
T. Wilken, G. Lo Curto, R. A. Probst, T. Steinmetz, A. Manescau, L. Pasquini, J. I. González Hernández, R. Rebolo, T. W. Hänsch, Th. Udem, and R. Holzwarth, Nature 485, 611–614 (2012).

14 GHz visible supercontinuum generation: calibration sources for astronomical spectrographs
S. P. Stark, T. Steinmetz, R. A. Probst, H. Hundertmark, T. Wilken, T. W. Hänsch, Th. Udem, P. St. J. Russell, and R. Holzwarth, Optics Express 19, 15690–15695 (2011).

Review articles

Laserlineal für den Kosmos
R. A. Probst, T. Wilken, T. Steinmetz, and Th. Udem, Physik in unserer Zeit 44 (2013).

Astronomical spectrograph calibration at the exo-Earth detection limit
G. Lo Curto, L. Pasquini, A. Manescau, R. Holzwarth, T. Steinmetz, T. Wilken, R. Probst, Th. Udem, T. W. Hänsch, J. González Hernández, M. Esposito, R. Rebolo, B. Canto Martins, and J. Renan de Medeiros, The Messenger 149, 2–6 (2012).

Conference proceedings

Spectrally flattened, broadband astronomical frequency combs
R. A. Probst, Y. Wu, T. Steinmetz, S. P. Stark, T. W. Hänsch, Th. Udem, and R. Holzwarth, in “2015 Conference on Lasers and Electro-Optics (CLEO),” (Optical Society of America, 2015), paper SW4G.7.

A laser frequency comb featuring sub-cm/s precision for routine operation on HARPS
R. A. Probst, G. Lo Curto, G. Avila, B. L. Canto Martins, J. Renan de Medeiros, M. Esposito, J. I. González Hernández, T. W. Hänsch, R. Holzwarth, F. Kerber, I. C. Leão, A. Manescau, L. Pasquini, R. Rebolo-López, T. Steinmetz, Th. Udem, and Y. Wu, Proceedings of the SPIE 9147, 9147-47 (2014).

Spectral flattening of supercontinua with a spatial light modulator
R. A. Probst, T. Steinmetz, T. Wilken, G. K. L. Wong, H. Hundertmark, S. P. Stark, P. St. J. Russell, T. W. Hänsch, R. Holzwarth, and Th. Udem, Proceedings of the SPIE 8864, 88641Z (2013).

Performance of a laser frequency comb calibration system with a high-resolution solar echelle spectrograph
H.-P. Doerr, T. J. Kentischer, T. Steinmetz, R. A. Probst, M. Franz, R. Holzwarth, Th. Udem, T. W. Hänsch, and W. Schmidt , Proceedings of the SPIE 8450, 84501G (2012).

Achieving a few cm/sec calibration repeatability for high resolution spectrographs: the laser frequency comb on HARPS
G. Lo Curto, A. Manescau, G. Avila, L. Pasquini, T. Wilken, T. Steinmetz, R. Holzwarth, R. Probst, Th. Udem, T. W. Hänsch, J. I. González Hernández, M. Esposito, R. Rebolo, B. Canto Martins, and J. Renan de Medeiros, Proceedings of the SPIE 8446, 84461W (2012).

14 GHz supercontinuum generation: calibration sources for astronomical spectrographs
S. Stark, H. Hundertmark, P. St. J. Russell, R. Probst, T. Wilken, T. W. Hänsch, Th. Udem, T. Steinmetz, and R. Holzwarth, in “2011 Conference on Lasers and Electro-Optics Europe and 12th European Quantum Electronics Conference (CLEO Europe/EQEC),” (Optical Society of America, 2011), paper JSIII_P1.

Suppressed mode recovery in nonlinear fibers of a Fabry-Perot-filtered frequency comb
T. Wilken, R. Probst, T. W. Hänsch, Th. Udem, T. Steinmetz, R. Holzwarth, A. Manescau, G. Lo Curto, L. Pasquini, S. Stark, H. Hundertmark, and P. St. J. Russell, in “2011 Conference on Lasers and Electro-Optics (CLEO),” (Optical Society of America, 2011), paper CWQ2.

Danksagung

Wissenschaftliche Arbeit lebt vom Austausch der Wissenschaftler untereinander, von Teamgeist und guter Zusammenarbeit. So hätte auch diese Arbeit niemals entstehen können, wenn nicht viele andere deren Gelingen durch ihre freundliche Zusammenarbeit unterstützt hätten. An dieser Stelle möchte ich mich deshalb bei all jenen bedanken, die auf diese Weise einen Beitrag geleistet haben.

Mein erster und wichtigster Dank gebührt Prof. Dr. Theodor W. Hänsch, der diese Arbeit überhaupt erst ermöglicht hat, und der für seine Doktoranden ein äußerst inspirierendes Umfeld geschaffen hat. Die Arbeit in seiner Gruppe war für mich eine große Ehre, und besonders die von ihm jährlich veranstalteten Symposien im Schloss Ringberg habe ich sehr genossen. Gleichfalls zu höchstem Dank verpflichtet bin ich Dr. habil. Thomas Udem und Dr. Ronald Holzwarth, die die Forschung über astronomische Frequenzkämme am Max-Planck-Institut für Quantenoptik (MPQ) bzw. bei Menlo Systems GmbH geleitet haben. Durch sie wurde auch meine eigene Arbeit angeleitet und geprägt. Meinen Kollegen, die mit mir an diesem Forschungsprojekt gearbeitet haben, steht ebenfalls großer Dank zu. Hierzu zählen Dr. Tilo Steinmetz und Dr. Tobias Wilken, die die Vorarbeit zur der vorliegenden Dissertation geleistet und beide mit mir dieses Thema bearbeitet haben. Dr. Tilo Steinmetz bleibt bis zum heutigen Tag weiterhin auf diesem Gebiet tätig, und es gibt wohl niemanden, der den Aufbau des astronomischen Frequenzkamms besser kennt und beherrscht als er. An unserem Projekt mitgewirkt hat außerdem Yuanjie Wu im Rahmen eines mehrjährigen Austauschs mit dem Nanjing Institute of Astronomical Optics & Technology. Auch ihm sei für die stets hervorragende Zusammenarbeit herzlich gedankt.

Der größte Teil der vorliegenden Arbeit fand am MPQ in Garching, und bei Menlo Systems GmbH in Martinsried statt. Ich möchte daher den Mechanikern Karl Linner und Wolfgang Simon, Helmut Brückner von der Elektronikwerkstatt, und den Verwaltungsmitarbeitern am MPQ und der LMU danken, die uns bei unserer Arbeit tatkräftig zur Seite standen. In gleicher Weise danken möchte ich allen Ingenieuren, die bei Menlo Systems den Aufbau des Astrokamms, der ursprünglich am MPQ entwickelt wurde, weiter verfeinert haben. Etwa zeitgleich mit der Beendigung dieser Arbeit haben sie den Astrokamm in ein auf Knopfdruck autonom arbeitendes System überführt. Dass schon bald eine Vielzahl von Observatorien mit einer kommerziellen Version des Astrokamms ausgestattet sein werden, ist nicht zuletzt ihr Verdienst. Besondere Erwähnung verdient außerdem Dr. Jens Dobrindt, der den Aufbau zum Tapern photonischer Kristallfasern (PCFs) bei Menlo Systems aufgebaut hat, den wir von ihm übernommen und weiterentwickelt haben.

Für die ausgesprochen angenehme Zusammenarbeit bei der Entwicklung der getaperten PCFs möchte ich mich bei Prof. Dr. Philip Russell und seiner Gruppe am Max-Planck-Institut für die Physik des Lichts (MPL) bedanken. Dies umfasst Dr. Sebastian Stark, Dr. Holger Hundertmark, Dr. Michael Frosz, Dr. Gordon Wong, Dipl.-Phys. Stanislaw Dörschner, und Dr. John Travers. Sie standen uns ebenfalls bei der Untersuchung ungewollter Phänomene wie Farbzentrenbildung und Frequenzverdopplung in getaperten PCFs mit Rat und Tat zur Seite.

Dr. Stark und Dr. Hundertmark wechselten vom MPL zu Menlo Systems und setzten diese Tätigkeit dort fort, ersterer von beiden bis zum heutigen Tag.

Unerlässlich für die vorliegende Arbeit war die Zusammenarbeit mit unseren astronomischen Kooperationspartnern. Sie haben es nicht nur ermöglicht, den Astrokamm in seiner Anwendung zu testen, sondern haben sowohl den Test als auch die Auswertung der gewonnenen Daten Hand in Hand mit uns durchgeführt. Eine besonders wichtige und langjährige Kooperation dieser Art hatten wir mit der Europäischen Südsternwarte (ESO). Hier haben Dr. Gaspare Lo Curto, Dr. Antonio Manescau, und Dr. Luca Pasquini mit uns über viele Jahre hinweg mit großem Einsatz und Begeisterung zusammengearbeitet. Bei allen dreien möchte ich an dieser Stelle für die freundliche und produktive Zusammenarbeit bedanken.

Des Weiteren danke ich unseren Kooperationspartnern vom Kiepenheuer Institut für Sonnenphysik (KIS) in Freiburg, die mit uns eine Variante des Astrokamms getestet haben, die speziell für das Vacuum Tower Telescope (VTT) auf Teneriffa optimiert wurde. Während der Installation, des Umbaus und des Tests dieses Systems entstanden die Ergebnisse in Kapitel 7. Mein herzlicher Dank hierfür gebührt Prof. Dr. Wolfgang Schmidt, Dr. Hans-Peter Doerr und Dr. Thomas Kentischer vom KIS. Bei der Auswertung der Daten vom VTT geholfen hat mir außerdem Dr. Liang Wang als Gastwissenschaftler an der Universitätssternwarte München (USM), dem ich hierfür herzlichst danken möchte.

Ebenfalls von Herzen danken möchte ich Dr. Frank Grupp von der USM, der mir während einer zweiwöchigen Summer School in Weihai (China) gleich zu Beginn meiner Promotion eine weitreichende Einführung in die Astronomie und deren Instrumentarik gewährt hat, und der mir in vielen persönlichen Gesprächen immer hilfsbereit als guter Ratgeber zur Seite stand.

Weiterhin möchte ich Dr. Paolo Molaro und Dr. Sergio Monai vom Osservatorio Astronomico di Trieste, und Dr. Massimiliano Esposito vom Instituto de Astrofísica de Canarias meine dankende Anerkennung aussprechen. Auf Basis der von uns gewonnenen Daten haben sie einen Frequenzkamm-kalibrierten Atlas solarer Linien erstellt, und diesen in Zusammenarbeit mit uns veröffentlicht.

Gedankt sei auch Dr. Anna Brucalassi von der USM und Dr. Gerardo Avila von der ESO für ihre Mithilfe bei der Entwicklung von Glasfasersystemen zum Anschluss des Astrokamms an den HARPS Spektrographen. Zu guter Letzt möchte ich Ankur Shringi aus Indien und Lucas Zeer-Wanklyn aus Kanada meinen lobenden Dank aussprechen, die im Rahmen ihrer Praktika an der spektralen Abflachung des Astrokamms mitgearbeitet haben.